DEVELOPMENT AND ELECTROCHEMICAL CHARACTERIZATION OF MULTIFUNCTIONAL POLYMERIC COATINGS FOR CORROSION MITIGATION IN METALLIC BIOMEDICAL IMPLANTS

by

HAMID ASADI

(Under the Direction of Ramaraja P. Ramasamy)

ABSTRACT

Metallic biomaterials are widely used for orthopedic and dental implant applications because of their superior mechanical strength, biocompatibility, and corrosion-resistant properties. The implantation of metallic devices in human body is always accompanied by corrosion phenomena due to the harsh and corrosive nature of the physiological environment. Metals may undergo different types of corrosion processes such as uniform, pitting, galvanic, and microbially-induced corrosion (MIC). Corrosion can adversely affect the mechanical integrity, functionality, and durability of implants and is a prime factor governing their biocompatibility. The principal paradigm of biocompatibility of metallic biomaterials has been “the more corrosion resistant, the more biocompatible.”. Therefore, protection of metallic implants against corrosion is very crucial. The application of protective coatings is a well-established strategy for separating metals from external aggressive environments. Among different types of protective coatings, polymeric coatings have been recognized as the most effective method to mitigate the corrosion of metallic substrates without changing their bulk properties, while providing them with other functionalities such as enhanced biocompatibility and cellular responses, ability to load small molecules, and antibacterial properties. This dissertation is focused on the development of multifunctional polymeric coatings to enhance the corrosion resistance properties of different types of metallic biomedical implants. The fabricated coatings were fully characterized through various physicochemical, electrochemical, and biological techniques to evaluate their potential as protective coating materials for bio-implant applications. In the first application, a polymeric coating based on polycaprolactone and lawsone, a natural plant extract obtained from Henna leaves, was fabricated on AZ31 Mg alloy to enhance its corrosion resistance and cytocompatibility for temporary orthopedic implant application. Incorporation of Lawsone provided the PCL coating with both corrosion inhibition properties and antibacterial activity. In the second application, a composite polymeric coating based on silk fibroin and cellulose nanocrystal was fabricated on AZ31 Mg alloy to enhance its corrosion resistance and biocompatibility for biodegradable bone implant application. In the third application, MIC of stainless steel was evaluated by using *Streptococcus mutans* as model microorganism for dental implant application. All the coatings were fully characterized through various physicochemical, electrochemical, and biological techniques to evaluate their potential as protective coating materials for bio-implant applications.

INDEX WORDS: Biomedical Implants, Corrosion, Protective Coatings, Antibacterial Activity, Cytocompatibility, Mg-based Alloys, Stainless Steel, Microbiologically-induced Corrosion

DEVELOPMENT AND ELECTROCHEMICAL CHARACTERIZATION OF MULTIFUNCTIONAL POLYMERIC COATINGS FOR CORROSION MITIGATION IN METALLIC BIOMEDICAL IMPLANTS

by

HAMID ASADI

B.S., Amirkabir University of Technology, Tehran, Iran, 2014

M.S., University of Tehran, Tehran, Iran, 2017

A Dissertation Submitted to the Graduate Faculty of The University of Georgia in Partial Fulfillment of the Requirements for the Degree

DOCTOR OF PHILOSOPHY

ATHENS, GEORGIA

2022

DEVELOPMENT AND ELECTROCHEMICAL CHARACTERIZATION OF MULTIFUNCTIONAL POLYMERIC COATINGS FOR CORROSION MITIGATION IN METALLIC BIOMEDICAL IMPLANTS

by

HAMID ASADI

Major Professor:	Ramaraja Ramasamy
Committee:	William Kisaalita
	Eric Freeman
	Yiping Zhao
	Ramana Pidaparti

Electronic Version Approved:

Ron Walcott
Vice Provost for Graduate Education and Dean of the Graduate School
The University of Georgia
May 2022

DEDICATION

To my beloved family.

ACKNOWLEDGEMENTS

I would like to express my gratitude and appreciation to Dr. Ramaraja Ramasamy for his guidance, support, and encouragement throughout my PhD. I would also like to thank my committee, Dr. William Kisaalita, Dr. Yiping Zhao, Dr. Eric Freeman, and Dr. Ramana Pidaparti for their thoughtful comments and recommendations on my PhD research. I gratefully acknowledge my lab mates for their friendship, support, and collaboration. My appreciation also goes out to my wife, family, and friends for their love, encouragement, and support all through my studies.

TABLE OF CONTENTS

Page

ACKNOWLEDGEMENTS v

LIST OF TABLES ix

LIST OF FIGURES xi

CHAPTER

1 INTRODUCTION 1

1.1 Metallic Biomedical Implants 1

1.2 Why Metals Corrode in Human Body? 3

1.3 Adverse Health Impact of Corrosion-failure of Implants 6

1.4 Corrosion Mitigation Strategies 8

1.5 Strategies to Enhance the Anti-corrosion Performance of Polymeric Coatings 9

1.6 Microbiologically-induced Corrosion 11

1.7 Mitigation Methods of Microbiologically-induced Corrosion 17

1.8 Corrosion Monitoring 27

1.9 Polymer Modified Electrodes for Biosensing applications 36

1.10 Specific Objectives and Organization of Chapters 37

2 A MULTIFUNCTIONAL POLYMERIC COATING INCORPORATING LAWSONE WITH CORROSION RESISTANCE AND ANTIBACTERIAL ACTIVITY FOR BIOMEDICAL MG ALLOYS 39

2.1 Introduction 42

2.2 Materials and methods 46
2.3 Results and discussion 52
2.4 Conclusion 88
3 CELLULOSE NANOCRYSTAL REINFORCED SILK FIBROIN COATING FOR ENHANCED CORROSION PROTECTION AND BIOCOMPATIBILITY OF MG-BASED ALLOYS FOR ORTHOPEDIC IMPLANT APPLICATIONS 90
3.1 Introduction 93
3.2 Materials and methods 97
3.3 Results and discussion 104
3.4 Conclusion 134
3.5 Supplementary data 135
4 MICROBIAL CORROSION OF STAINLESS STEEL DENTAL IMPLANT INDUCED BY STREPTOCOCCUS MUTANS BACTERIUM 141
4.1 Introduction 143
4.2 Materials and methods 144
4.3 Results and discussion 147
4.4 Conclusion 162
5 CONCLUSIONS AND FUTURE DIRECTIONS 163
REFERENCES 167

APPENDICES

A GRAPHENE-BASED ELECTROCHEMICAL BIOSENSOR FOR IMPEDIMETRIC DETECTION OF MICRO-RNA AS POTENTIAL CANCER BIOMARKER 184
B Nitric-oxide Releasing Coatings on Stainless Steel Sample 213

C Fixation of Biological Samples 215

D Bacterial Zone of Inhibition Test 216

LIST OF TABLES

Page

Table 1.1: Metallic biomaterials and their primary applications as implants 2

Table 1.2: The biological effects of certain metal ions that may be leached *in vivo* due to corrosion applications as implants 8

Table 2.1: Elemental composition of AZ31 Mg alloy (mass fraction, %) 47

Table 2.2: Composition of Hank's solution used for *in vitro* corrosion studies 50

Table 2.3: Thickness of the PCL-LS coating measured at different sites across the coated Mg samples 59

Table 2.4: The corrosion potentials (E_{corr}), corrosion current densities (i_{corr}), and corrosion inhibition efficiency (IE) of the Mg samples obtained from PP curves in Hank's solution by Tafel methods 68

Table 2.5: Representative fitting results of EIS spectra of Mg samples using appropriate equivalent electrical circuits 74

Table 2.6: Corrosion potentials (E_{corr}), corrosion current densities (I_{corr}), and corrosion rate values of the PCL-LS coated Mg samples with varying thicknesses performed in Hank's solution. 76

Table 2.7: Corrosion potentials (E_{corr}) and corrosion current densities (I_{corr}) values of the PCL-LS coated Mg samples performed in Hank's solutions containing varying NaCl concentrations…... 78

Table 3.1: Compositions of the solutions used for the fabrication of coatings...........................100

Table 3.2: Vibrational Band Assignments in the Amide I Region of SF 110

Table 3.3: Corrosion potentials (E_{corr}) and corrosion current densities (i_{corr}) values of the Mg samples obtained from PP curves in Hank's solution by Tafel methods...................................117

Table 3.4: Representative fitting results of EIS spectra of Mg samples using appropriate equivalent electrical circuits 124

LIST OF FIGURES

Page

Figure 1.1: Main factors causing corrosion of metallic implants in the physiological environments..6

Figure 1.2: Two possible toxicity routes for metal ions released into body fluids due to corrosion and wear 7

Figure 1.3: Schematic representation for the steps of biofilm formation on titanium dental implants...12

Figure 1.4: Schematic illustration of different types of iron corrosion by SRB 15

Figure 1.5: Formation of oxygen concentration cell caused by biofilm 16

Figure 1.6: Schematic (left) and the actual (right) three-electrode setup used for electrochemical corrosion experiments.. 28

Figure 1.7: Schematic polarization curve showing Tafel extrapolation. 30

Figure 1.8: Typical Bode-Impedance (red) and Bode-phase (blue) plots....................................32

Figure 1.9: Expressing the Impedance Magnitude in terms of x and y components 32

Figure 1.10: Typical Nyquist Plot...33

Figure 1.11: Observation of putting corrosion by SEM (A) and the working principle of FTIR machine (B) … 36

Figure 2.1: Schematic of the PCL-LS coating on the AZ31 Mg substrate 46

Figure 2.2: Surface SEM images of AZ31 (A), AZ31-OH (B) PCL (C), and PCL-LS (D)..........53

Figure 2.3: Cross-sectional morphology of PCL-LS/substrate interface with the corresponding elemental analysis mapping and EDS spectra 54

Figure 2.4: Paint thickness gauge (A) and micrometer (B) that initially used for the measurement of coating uniformity but were abandoned due to the lack of accuracy and repeatability 55

Figure 2.5: Schematic (A), photograph (B), and microscopic image (C) of the PCL-LS sample prepared for uniformity analysis by the profilometer 56

Figure 2.6: Typical surface profile obtained from probing the sample surface by profilometer...57

Figure 2.7: Spin coating setup used to prepare PCL-LS coated Mg substrates 58

Figure 2.8: Thickness of the PCL-LS coating measured at different sites across the coated Mg samples (M1-M8)..60

Figure 2.9: Thickness dependence of the PCL-LS coatings on the volume of drop casted solution …………………………………………………………………………………………61

Figure 2.10: ATR-FTIR spectra of bare, alkaline treated, and coated Mg samples 63

Figure 2.11: Water contact angle values of bare, alkaline treated, and coated Mg samples 64

Figure 2.12: Photographs of the PCL-LS coating on (A) untreated and (B) alkaline-treated AZ31 substrate before and after the cross-cut adhesion test..65

Figure 2.13: Open circuit potential curves (A) and potentiodynamic polarization curves (B) of bare, alkaline treated, and coated Mg samples performed in Hank’s solution 67

Figure 2.14: EIS spectra of Mg samples performed in Hank’s solution; Nyquist plots (A) and (B) (Insets: EC models employed for EIS data fitting), Bode-impedance plots (C), and Bode-phase plots (D) 70

Figure 2.15: Evolution of Bode plots spectra of the coated Mg samples performed in Hank's solution; Nyquist plots (A) and (B) (Insets: EC models employed for data fitting), Bode-impedance plots (C), and Bode-phase plots (D) 73

Figure 2.16: Tafel curves of the PCL-LS coated Mg samples with varying thicknesses performed in Hank's solution 76

Figure 2.17: Tafel curves of the PCL-LS coated Mg sample obtained in Hank's solutions containing varying NaCl concentrations..78

Figure 2.18: SEM images of bare, alkaline treated, and coated Mg samples before and after immersion in Hank's solution for 7 days at 37 °C..80

Figure 2.19: Variation in hydrogen evolution volume (A) and pH value (B) of each group during immersion in Hank's solution at 37 °C for 7 days..83

Figure 2.20: ATR-FTIR spectra (C) of sample after 7 days of immersion in Hank's solution.....84

Figure 2.21: Antibacterial activity of AZ31 (a), AZ31-OH (b), PCL (c), and PCL-LS (d) against *E. coli* and *S. aureus* evaluated by measuring the diameter of inhibitory zones 86

Figure 2.22: Viability of hFOB cells exposed to sample extracts of 1, 3, and 5 days compared to control cells grown in pure media measured by CCK-8 assay kit...88

Figure 3.1: Schematic illustration of the fabrication steps of SF-CNC coating on PD-modified AZ31 Mg substrate. 97

Figure 3.2: TEM image (A) and particle size distribution (B) of CNCs 105

Figure 3.3: Surface SEM images of AZ31 (A), AZ31-OH (B) AZ31-PD (C), SF (D), and SF-CNC (E); Cross-sectional morphology of SF-CNC/substrate interface (F) with the corresponding elemental analysis mapping (G) 107

Figure 3.4: ATR-FTIR spectra of AZ31 (a), AZ31-OH (b) AZ31-PD (c), SF (d), and SF-CNC (e) 108

Figure 3.5: Deconvoluted FTIR spectra of the amide I band of non-treated SF (A), methanol-treated SF (B), and methanol-treated SF-CNC (C); B = β-sheets 111

Figure 3.6: Water contact angle values of bare, pretreated, and coated Mg samples 113

Figure 3.7: Photographs of the SF and SF-CNC coatings on alkaline-treated AZ31 with and without the intermediary PD layer before and after the cross-cut adhesion test 115

Figure 3.8: Open circuit potential (A) and potentiodynamic polarization (B) curves of bare, pretreated, and coated Mg samples performed in Hank's solution 117

Figure 3.9: EIS spectra of Mg samples performed in Hank's solution; Nyquist plots (A and B), Bode-impedance plots (C), and Bode-phase plots (D) 119

Figure 3.10: Nyquist EIS spectra of SF-CNC coating on non-treated (A) and PD-modified (B) AZ31-OH surface and the corresponding cross-sectional SEM images of the coating/substate interfaces; Red arrows point to the interfacial gaps between the coating and the substrate 121

Figure 3.11: Electrical equivalent circuits employed for fitting the EIS spectra of AZ31 and AZ31-OH (EEC1), AZ31-PD (EEC2), and SF and SF-CNC (EEC3) 123

Figure 3.12: Variation of log |Z|0.01Hz values of the samples over 7 days of immersion in Hank's solution 126

Figure 3.13: Variation in pH value (A) and hydrogen evolution volume (B) of each group of the samples during immersion in Hank's solution at 37 °C for 14 days 128

Figure 3.14: SEM images of bare, pretreated, and coated Mg samples before and after immersion in Hank's solution for 7 and 14 days at 37 °C 130

Figure 3.15: Viability of hFOB cells exposed to sample extracts of 3 and 5 days compared to control cells grown in pure media measured by CCK-8 assay kit 132

Figure 3.16: Fluorescence images of actin-nucleus stained hFOB cells cultured on AZ31 (A), AZ31-OH (B), AZ31-PD (C), SF (D), and SF-CNC (E) for 24 h; Blue: DAPI; Green: F-actin...134

Figure S3.1: Surface SEM images (higher magnification) of as-prepared AZ31 (A), AZ31-OH (B) AZ31-PD (C), SF (D), and SF-CNC (E)...135

Figure S3.2: Nyquist (A), Bode-phase (B), and Bode-impedance (C) plots of bare AZ31 at different time intervals during 7 days of immersion in the Hank's solution 136

Figure S3.3: Nyquist (A), Bode-phase (B), and Bode-impedance (C) plots of AZ31-OH at different time intervals during 7 days of immersion in the Hank's solution 137

Figure S3.4: Nyquist (A), Bode-phase (B), and Bode-impedance (C) plots of AZ31-PD at different time intervals during 7 days of immersion in the Hank's solution 138

Figure S3.5: Nyquist (A), Bode-phase (B), and Bode-impedance (C) plots of SF at different time intervals during 7 days of immersion in the Hank's solution 139

Figure S3.6: Nyquist (A), Bode-phase (B), and Bode-impedance (C) plots of SF-CNC at different time intervals during 7 days of immersion in the Hank's solution 140

Figure 4.1: Experimental setup used for electrochemical studies. (A) anerobic chamber with GasPak, (B) electrochemical cells containing sterile AS (left) and AS-*S.mu* (right), (C) electrochemical measurement under sterile hood. 148

Figure 4.2: Surface SEM images of (A) bare SS and (B) PU-coated SS....................................149

Figure 4.3: ATR-FTIR spectra of bare and PU-coated SS samples..................................... 150

Figure 4.4: Formation of *S. mutans* Biofilm on SS surface after 14 days of immersion in AS-*S.mu*. 151

Figure 4.5: Formation of *S. mutans* Biofilm on PU-SS surface after 14 days of immersion in AS-S.mu. .... .152

Figure 4.6: Post-corrosion surface morphology of SS immersed in AS (A) and AS-*S.mu* (B) for 28 days after removal of the biofilm....................154

Figure 4.7: Post-corrosion surface morphology of PU-SS immersed in AS (A) and AS-*S.mu* (B and C) for 28 days after removal of the biofilm.................... .155

Figure 4.8: pH measurement of the corrosion media after 7 days of immersion....................156

Figure 4.9: OCP values of SS immersed in AS with and without the presence of *S. mutans*.................... .157

Figure 4.10: OCP values of PU-SS immersed in AS with and without the presence of *S. mutans*.................... .158

Figure 4.11: $|Z|_{0.01Hz}$ values of SS immersed in AS with and without the presence of *S. mutans*.................... .160

Figure 4.12: $|Z|_{0.01Hz}$ values of PU-SS immersed in AS with and without the presence of *S. mutans*.................... .161

CHAPTER 1

INTRODUCTION

1.1 Metallic Biomedical Implants

Metals are extensively being used for load-bearing dental and orthopedic applications as biomedical implants due to their excellent biocompatibility, mechanical properties including high yield, fatigue, tensile, compressive, and shear strength along with sufficient ductility, hardness, and fracture toughness. Therefore, metals have shown great advantages over ceramic and polymeric biomaterials to be used in biomedical implant application. There are two main types of metallic implant devices: 1) temporary implants such as bone plates, screws, and pins; and 2) permanent implants such as total joints replacement and dental implants. Despite the presence of numerous types of metals and alloy systems, only a few of them possess requirements needed for bioimplant application. The most commonly used metallic biomaterials are titanium and its alloys, 316L stainless steel (316L SS), and cobalt-based (Co-Cr) alloys. Besides, a few other metals such as nickel titanium (NiTi) and tantalum (Ta) have been recently gained attention for bioimplant application because of their shape memory properties. Magnesium (Mg)-based alloys are another important type of metallic implant materials that have shown great promise to be used in temporary implant application such as fixation plates, pins, and screws. Mg-based alloys have the ability to biodegrade under physiological condition to fully bioresorbable and non-toxic products, while the damaged bone tissue is being reconstructed and substituted. Such a unique property eliminates the need for a second surgery to remove the implant after the full healing of the bone tissue [1]. Four main classes of metallic implants and their primary applications are listed in Table 1.1.

Table 1.1. Metallic biomaterials and their primary applications as implants [2].

Materials	Application	Primary utilizations	Application status
Stainless steels	Orthopedic Orthodontic Cardiovascular	Temporary devices (screws, plates and hip nails), total hip replacements	Routinely applied
Co-based alloys	Orthopedic Orthodontic Cardiovascular	Total joints replacements, dental implants, removable partial dentures, orthodontic wire leads, femoral stems, bone implant applications, load-bearing implants	Routinely applied
Ti-based alloys	Orthopedic Orthodontic Cardiovascular	Dental implants, orthodontic wire leads, cardiovascular, vascular stents, heart valve parts, stem, total hip replacements	Routinely applied
Miscellaneous			
NiTi	Orthodontic Cardiovascular	Vascular stents, Vena cava filter, Intracranial aneurysm clips, catheter guide wires, orthopedic staples, orthodontic dental arch wires	FDA approved
Mg	Orthopedic Craniofacial	Biodegradable orthopedic implants	Animal test
Ta		A radiographic marker, wire structures for neurosurgery and plastic surgery	FDA approved

1.2 Why Metals Corrode in Human Body?

The corrosion resistance is an important aspect of implant materials and has a great impact on their functionality, durability, and biocompatibility. The body environment is harsh and raises several challenges with respect to corrosion of metallic implants. Corrosion is considered as the gradual degradation of materials as a result of electrochemical attack by a hostile electrolytic environment with the passage of time. Water constitutes between 40-60% of total human body mass and can be subdivided into two major fluid compartments, namely the extracellular and the intracellular fluids. Extracellular fluids (ECFs) consist of the plasma found in the blood vessels, the interstitial fluid that surrounds the cells, the lymph and transcellular fluids. Intracellular fluid (ICF) refers to the water inside the cells. The major cations present in body fluid are hydrogen, sodium, potassium, calcium and magnesium ions, while the major anions include hydroxide, bicarbonate, chloride, phosphate and sulphate ions. Moreover, there are other organic substances of low-molecular-weight species and relatively high molecular-weight polymeric components, and dissolved oxygen in the body fluid. Dissolved salts are known to be the most influential components for implant corrosion *in vivo*, while chloride ions (and other halides) have been widely reported to induce corrosion in almost all types of metals. Temperature and pH are other two important parameters that can aggravate the corrosion behavior of metallic implants. The temperature of body fluids in the human body is 37 ºC under normal condition which imposes an elevated temperature on the implant throughout its lifespan and can generally accelerate the electrochemical reactions of corrosion [3]. There is always a high chance of pathological infection following an implantation surgery because of hospital-acquired infection or disrupted blood supply around the implantation site. Such infections may result in a significant pH drop sometimes as low as 4.0 around the inserted implant which in turn can cause severe localized corrosion of the metallic implant. It's worth mentioned that such acidic environment may last for several weeks to fully be recovered by the human body. Inflammatory response of human body following implementation and the production of corrosives compounds such as H_2O_2 is another factor that can create electrochemical cells and cause localized corrosion of the implant. The severity of such inflammatory responses is defendant on the implant size and shape along with the biological effects of corrosion products released from the implant surface [4]. Another important factor leading to implant corrosion is the level of dissolved oxygen. The level of oxygen in body fluids is often lower than the typical artificial solutions (exposed to air atmosphere) that are being used to study implants corrosion *in vitro*, and that is mainly because of the presence of hemoglobin (main component of red blood cells) and its combination with oxygen molecules. The partial pressure of oxygen in blood varies between 100 to 40 mmHg for arterial and venous blood, respectively, while the corresponding value in air is 160 mmHg. This oxygen deficiency reduces the re-passivation ability of metals and formation of natural oxide layer on their surfaces, which is known to play an important role in corrosion resistance of metals. Besides, the different partial pressure of oxygen across the human body may result in formation of aeration cell and induce implant corrosion [5]. In the case of dental implants, saliva contains aggressive anions such as chlorides which causes dissolution of the natural protective oxide layer. Moreover, high concentration of fluorides present in toothpastes and mouthwashes exerts detrimental effect on dental implants. For instance, the TiO_2 surface oxide layer of Ti based dental implants reacts with fluoride solutions and forms titanium-fluoride molecules (such as titanium fluoride or sodium titanium fluoride) and forms a porous layer with many structural defects, making the bulk material prone to electrochemical attack [6]. Once the passive surface layer is disrupted, corrosion proceeds and metal ions/debris are released continuously. The metal ions released from bioimplants can result in potentially biological side effects, serious type of infection and other health issues in the patients. Release of metal debris into the peri-implant region can also activate a cascade of signaling molecules that result in the activation and differentiation of osteoclast cells and leads to bone resorption/osteolysis of the peri-implant region. As a result, the bonding between the bone and implant is lost and results in implant loosening [2]. Biological macromolecules present in the body fluids can also contribute to the corrosion of implants by upsetting the equilibrium of the corrosion reactions of the implant through consumption of the products due to anodic or cathodic reaction. For instance, proteins can form complex with metal ions and change their concentration around the implant surface and change the equilibrium across the surface double layer that is formed by the electrons on the surface and cations present in the solution [7]. Bacteria are also able to induce and cause an accelerated type of corrosion, namely known as microbiologically-induced corrosion (MIC) which recently has been widely investigated for its adverse impact on corrosion of metallic implants. MIC in implants, its mechanism of action, and mitigation strategies will be discussed in the following sections. Uniform, stress corrosion cracking, galvanic, pitting, and fatigue corrosion are the most common types of that metallic implants undergo in the human body. They can occur simultaneously or in some cases, be an extension to an existing type of corrosion. A figurative summary of the aforementioned factors is shown in Figure 1.1.

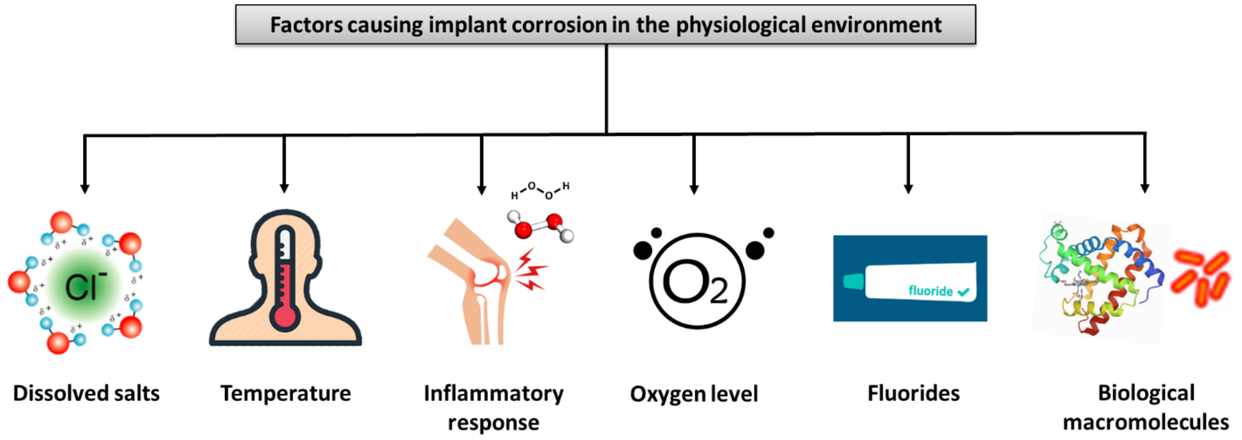

Fig 1.1. Main factors causing corrosion of metallic implants in the physiological environments.

1.3 Adverse Health Impact of Corrosion-failure of Implants

Corrosion of implant materials can significantly decrease their life span and lead to repeated surgeries in some cases. Corrosion and erosion corrosion are responsible for 42% of implant failures in the two most used implant materials 316L stainless steel and Ti-6Al-4V [8]. The release of corrosion products and leaching of metal ions lead to adverse biological reactions in the tissues surrounding the implants in three different ways: 1) electrical current produced form corrosion can change cellular behavior, 2) corrosion alters the chemical environment around the cells, and 3) cellular metabolism is affected by released metallic ions. Apart from the local toxicity, corrosion products and released metal ions can be transferred and accumulated in other body parts and damage organs leading to their malfunctioning, which are known as systemic remote effects of corrosion. Some of the common symptoms of mild corrosion include acute pain, reddening, and swelling near the implantation site. Previous studies have shown there are elevated concentrations of metallic ions in blood, organs (e.g., kidney and liver), serum, and urine of patients with either stainless steel or cobalt-base orthopedic total joint replacement components. These metallic ions may not be harmful by themselves if they react with water molecules and anions; however, they can form complexes when combined with other biomolecules such as proteins and induce very intense immune responses mediated by macrophages resulting in production of reactive oxygen intermediates and pro-inflammatory cytokines that affect a host of local cell types and induce a widening zone of soft-tissue damage and inflammation (Figure 1.2). Cobalt, chromium, and nickel are the most common examples, while nickel has the most adverse effect (Table 1.2).

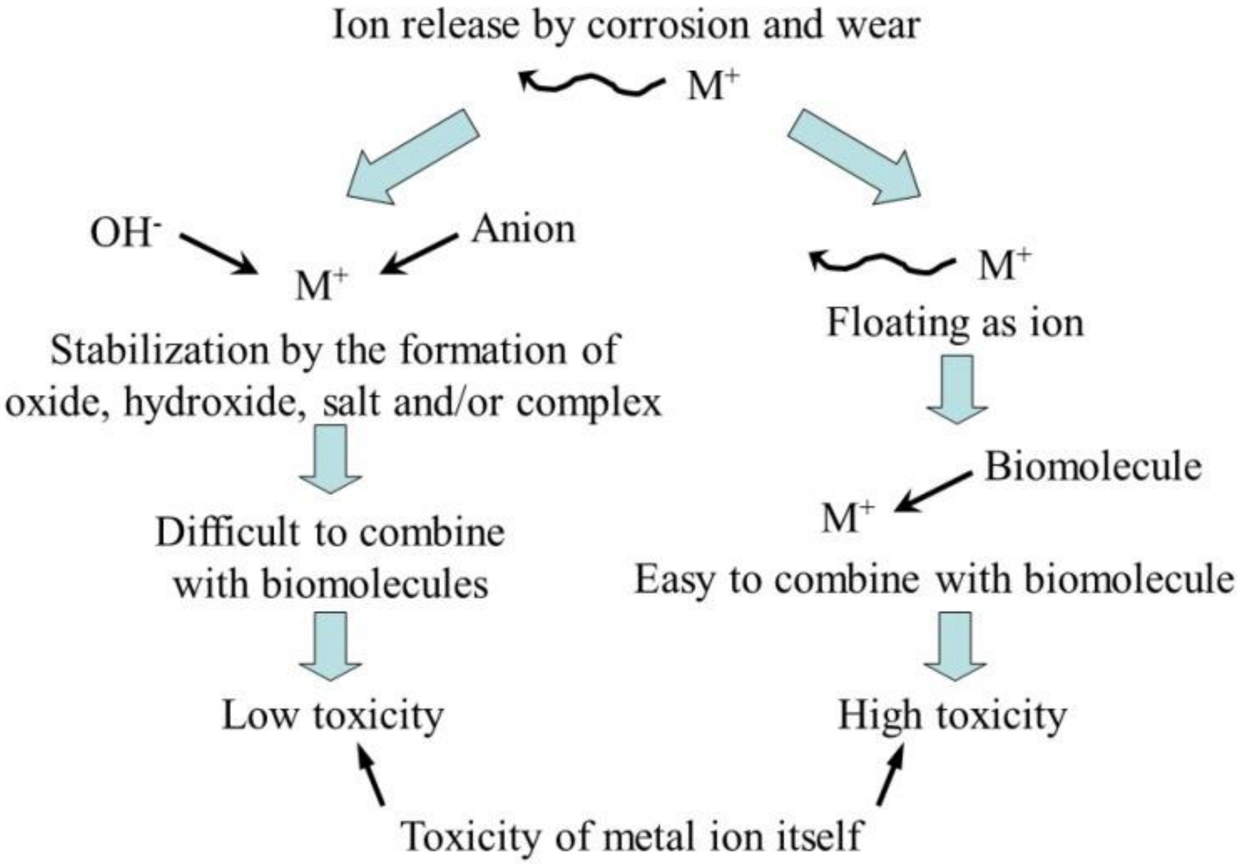

Fig 1.2. Two possible toxicity routes for metal ions released into body fluids due to corrosion and wear [9].

Table 1.2. The biological effects of certain metal ions that may be leached *in vivo* due to corrosion [5].

Metal	Effects
Nickel (Ni)	The major cause of allergic contact dermatitis. The significant biological parameter is the amount released to the skin during exposure to human sweat. Has toxic effects with cellular damage in cell cultures at high concentrations. Harmful to bone in tissue cultures, although less than Co or V. Has a potency for carcinogenicity.
Cobalt (Co)	Inhibits iron (Fe) from being absorbed into the blood stream causing anaemia B
Chromium (Cr)	Ulcers and central nerve system disturbances
Aluminium (Al)	Epileptic effects and Alzheimer's disease
Vanadium (V)	Toxic in the elementary state
Molybdenum (Mo)	Is toxic in large doses; symptoms include diarrhoea, coma and cardiac failure and inhibition of activity of ceruloplasmin, cytochrome oxidase, glutaminase, choline esterase and sulphite oxidase. High levels of Mo can also interfere with Ca and P metabolism.

1.4 Corrosion Mitigation Strategies

Considering the adverse effects of corrosion on implant performance and human body, it is critical to identify approaches to enhance the corrosion resistance of metallic implant materials that are aimed to be used in highly corrosive physiological environment. First approach is to improve the material properties by alloying. However, alloying is often accompanied by introducing of toxic elements such as aluminum, vanadium, and niobium to the metallic materials which can potentially compromise their biocompatibility [10]. Surface modification has been recognized as a promising approach to enhance the surface properties and corrosion resistance of materials without changing their bulk properties, while overcoming the adverse effects of alloying.

Apart from corrosion, surface modification can impart the underlying implant substrate with other features such as enhanced bioactivity, cytocompatibility, osteointegration, antibacterial properties. The most common surface modification techniques include deposition of a thin uniform coating, development of stable passivation oxide layer, ion beam processing for surface modification and surface texturing [2]. Among the various methods that have been attempted to protect metallic implant from corrosion, the application of polymeric polymers has attracted a great deal of attention over the past few years. Polymeric coatings can act as a physical barrier and protect the underlying metals by separating them from the external aggressive environments of human body. Besides, they can provide other functionalities to the substrate such as enhanced biocompatibility and cellular responses, ability to load small molecules, self-healing, and antibacterial properties. Although these polymeric coatings can improve the corrosion resistance of metals to some degree, they are still susceptible to damage by the highly corrosive environment of the human body, which results in polymer degradation and deterioration of protective barrier properties. Following the emergence of defects and micro-cracks within a coating, corrosive species and water penetrate through the defected areas and reach the metal surface, leading to the occurrence of corrosion [11].

1.5 Strategies to Enhance the Anti-corrosion Performance of Polymeric Coatings

Several approaches have been attempted to ameliorate the corrosion protection performance of polymeric coatings. These include the incorporation of corrosion inhibitors/organic salts [12-14] and anticorrosive fillers [15] into polymeric coatings, hybridization with other polymers (copolymerization, blending, and layer-by-layer) [16, 17], surface pretreatment/activation [18, 19], and applying intermediate layers [20, 21]. Introduction of corrosion inhibitors and anticorrosive nanofillers into polymeric matrices are among the most well-established and promising approaches to enhance the corrosion resistance and durability of polymeric coatings.

1.5.1 Introduction of Corrosion Inhibitors into Polymeric Matrix

Introducing corrosion inhibitors into the polymeric coatings have shown great potential to improve their durability and anti-corrosion properties [22, 23]. Generally, a composite polymer/corrosion inhibitor coating consists of a polymeric coating as a passive physical barrier, hosting an active corrosion inhibitor within the coating matrix. When the barrier coating is damaged by corrosive species, the loaded corrosion inhibitor can be released into the defected sites and mitigate the corrosion progression by forming insoluble metal complexes [24, 25]. Several inorganic and organic corrosion inhibitors such as cerium ion [26], 8-hydroxyquinoline [27], vanadate [28], molybdate [29], and benzotriazole [30] have been proposed for corrosion protection of metals so far. Although being effective in corrosion mitigation, most of these synthetic inhibitors are not suitable for implantable biomedical applications due to their potential cytotoxic and carcinogenic effects in the physiological environment [31, 32]. Eco-friendly corrosion inhibitors also known as “green” inhibitors have emerged as promising alternatives to hazardous synthetic inhibitors [33]. Among all the green alternatives, plant-derived corrosion inhibitors have gained considerable attraction, as they possess desired biocompatibility while being inexpensive and available through renewable resources, making them suitable choices to be used in biomedical applications [34, 35].

1.5.2 Introduction of Anti-corrosive fillers into Polymeric Matrix

Addition of anticorrosive nanofillers can improve the barrier properties of polymeric coatings against the aggressive physiological environment by increasing the tortuosity of corrosive species permeation pathways, creation of microcapillaries with high capillary pressure for penetration of liquid species, as well as other mechanisms related to filler-matrix and filler-metal interface interactions [36]. A variety of anticorrosive nanofillers such as graphene and its derivatives [37], hydroxyapatite [38], ZnO [39], silica [40], TiO_2 [41], $Mg(OH)_2$ [42], and layered double hydroxide [43] have been incorporated into protective polymeric coatings to enhance their corrosion protection performance. Over the past decade, bio-based nanofillers such as cellulose nanocrystals (CNC) and lignin have gained extensive attention due to their low-price, renewability, biocompatibility, and biodegradability [44]. Taking all the desired properties into account, bio-based nanofillers promise to be novel and renewable reinforcement materials for fabrication of anticorrosive coatings on metallic biomedical implants.

1.6 Microbiologically-induced Corrosion

Metals are widely used in many engineering as well as medical applications (mainly as an important class of biomaterials/implants) because of their superior mechanical strength and corrosion-resistant properties. Microorganisms have a strong tendency to populate on any surfaces including metals, giving rise to a complex and strongly adhering microbial community, called “biofilm”. Formation of biofilms on metals is highly detrimental to the underlying substrates and may cause physical degradation or biodeterioration of metal surfaces, thus presenting many industrial problems [45]. Generally, accelerated deterioration/corrosion of metals by processes directly or indirectly related to the activity of microbiological organisms is defined as microbiologically influenced corrosion (MIC) or bio-corrosion. One of the sectors that is highly impacted by bio-corrosion and its negative consequences is the aquatic and maritime industry. Steel is widely utilized material for building platforms and transport systems in oil/gas sector. Despite the abundance and economic value, the largest capital loss in oil/gas operations is resulting from steel corrosion. About 20% of the annual corrosion damages of metals may be induced by

MIC in anaerobic environments, at a direct cost of 30-50 billion dollars annually worldwide [46]. Therefore, protection of metallic structures against MIC is of great importance for prolonging the service life of maritime structures and equipment. In the field of biomedical engineering, dental implants are most vulnerable to MIC and its adverse consequences. For instance, titanium (Ti) and its alloys are widely used for dental implants because of their excellent biocompatibility and corrosion resistance. These beneficial properties are due to the presence of stable and compact titanium oxide, mainly TiO_2, formed on the surface of Ti implants. However, this protective passive film can be destroyed by the biofilm formation and bacterial cell metabolism on the implant surface (Figure 1.3) [47]. As a result, Ti^{4+} ions are generated which can accumulate into the surrounding soft and bone tissues and lead to localized corrosion of Ti and, in extreme cases, implant failure [48]. Since Ti surface does not exhibit any obvious antibacterial properties, they are prone to undergo microbial colonization in the oral environment and subsequently MIC. So, it is crucial to develop practical approaches which can effectively prevent MIC for broad clinical applications of Ti as a dental material.

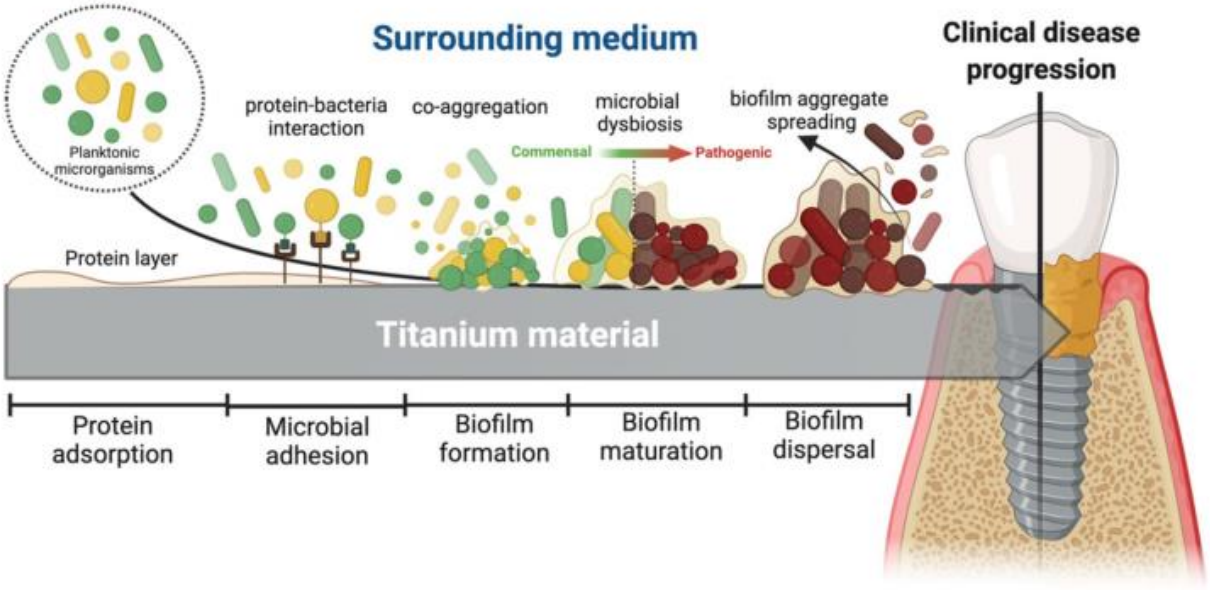

Fig. 1.3. Schematic representation for the steps of biofilm formation on titanium dental implants [49].

1.6.1 Mechanisms of MIC in Marine Industry

Generally, microorganisms such as bacteria, algae, and fungi have been known as a main cause of accelerated metal corrosion, even where the environment is not highly corrosive. They can accelerate the corrosion process of many metals by their physical presence, metabolic activities, and direct involvement in the corrosion reaction, resulting in a severe metal corrosion accompanied by the deposition of a thick layer of corrosion products and in often, the odor of hydrogen sulfide. The main bacteria associated with MIC are slime-forming bacteria, acetate-producing bacteria, acetate-oxidizing bacteria, iron/manganese oxidizing bacteria, methane producers, organic acid-producing bacteria, sulfur/sulfide-oxidizing bacteria, and sulfate-reducing bacteria (SRB) that may coexist with each other in the biofilm. Among them, SRB, a diverse group of bacteria that are active in an anaerobic environment and the most common in petroleum operations because of the prevailing anaerobic environment, have been known as the principle cause of MIC and induced corrosion and degradation of many metals, particularly steel-based structures [45, 50]. SRB such as *desulfovibrio* and *desulfotomaculum* are able to survive and grow fast under anaerobic (no oxygen) conditions, for instance, deep in soil and below a pile of corrosion deposits. SRB are highly resistant and can withstand and grow over wide ranges of pH (4-8), temperatures (10-90 °C), and at pressures up to 500 atm. Low molecular weight compounds such as lactate and fumarate provide the main source of carbon needed for different cellular activities of SRB. SRB are equipped with hydrogenase enzyme helping them to derive energy from the oxidation of hydrogen molecules [51]. Although there is no universally accepted mechanism behind the corrosive action of SBR, it can be explained from two perspectives: 1) the general MIC mechanism based on the metabolic activity of bacteria, and 2) chemical reactions between extracellular polymer substances (EPS) and the steel substrate, which induce MIC (Fig. 1.4)

1) SRB tend to form a biofilm layer on the steel substrate and generate hydrogen sulfide (H_2S) by conversion of sulfates. H_2S reacts with Fe and forms FeS-product deposits. FeS products formed on the metal surface is an efficient cathodic site for the reduction of hydrogen, thus accelerating the whole corrosion process by cathodic depolarization. Another viewpoint suggests that oxygen made available from the sulfate reduction reaction may react with the evolved hydrogen and speed up the cathodic reaction [50]. The overall reaction of the of the anaerobic corrosion of iron induced by SRB can is described below:

$$SO_4^{2-} \rightarrow S^{2-} + 2O_2$$

$$4Fe + SO_4^{2-} + 4H_2O \rightarrow FeS + 3Fe(OH)_2 + 2OH^-$$

It is also proposed that H_2S along with the existent CO_2 can react with water and produce a mild acidic condition. This acidic condition accelerates the corrosion process by itself, while providing a more favorable environment for SRB growth and therefore, inducing a more rapid corrosion. Besides, SOB may release aggressive compounds such as acetic or sulfuric acid during their metabolic activities, which are hazardous to the integrity of steel and cause severe corrosion. For example, Thiobacillus is a type of SOB that releases H_2SO_4 and corrodes the steel substrate [52].

2) chemical interaction between EPS of the biofilm and the steel substrate may be another mechanism behind the MIC of steels. The secreted EPS from bacteria consists many anionic macromolecules such as protein, polysaccharide, uronic acid, nucleic acid, and lipids with metal-binding capacity. Metal ions such as Fe^{3+} can form electron-shuttling compounds through interaction with the anionic macromolecules present in EPS and create new redox pathways. These newly formed pathways can result in cathodic depolarization and corrosion of the steel substrate.

Considering the key role of SBR, it is crucial to prevent the bio-corrosion induced by SRB in order to prolong the service life of maritime structures and equipment [53, 54].

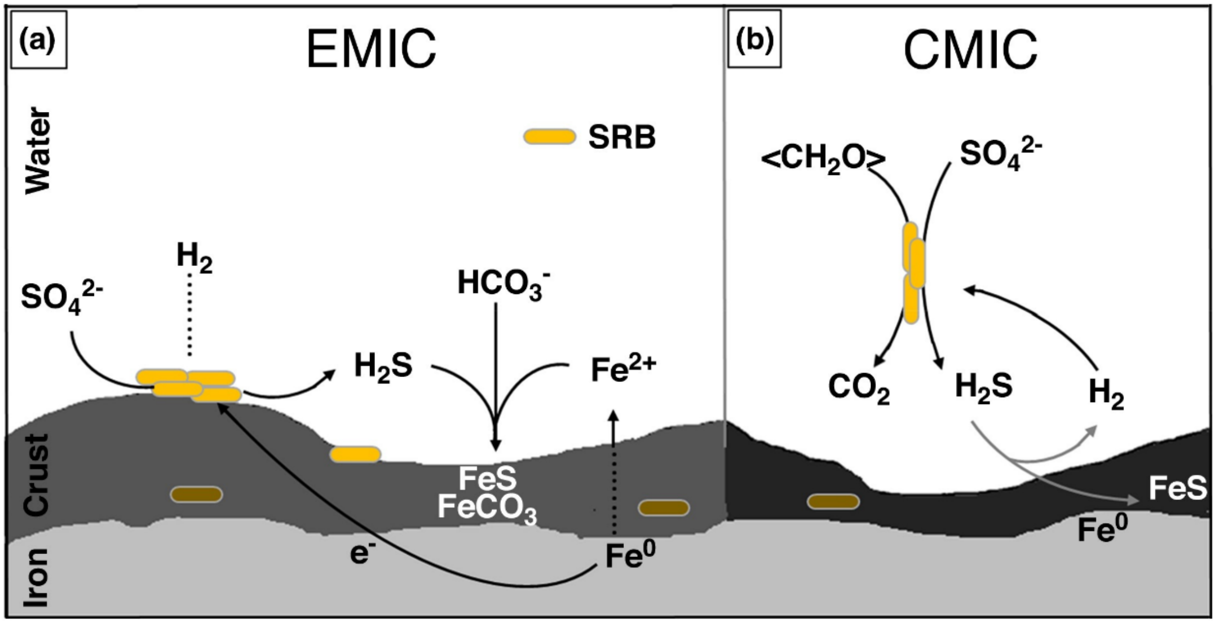

Current Opinion in Chemical Engineering

Fig. 1.4. Schematic illustration of different types of iron corrosion by SRB. (a) In EMIC, SRB takes electrons from iron oxidation and utilizes them for the conversion of sulfate to sulfide followed by the formation of H_2S. Then H_2S and HCO^{3-} reacts with Fe^{2+} and forms FeS and $FeCO_3$ respectively. (b) In CMIC, the sulfidogenic degradation of organic matter in anoxic environments which produces bicarbonate ion and FeS. Intracellular oxidation of organic compounds by SRB results in the formation of sulfide, which stoichiometrically reacts with metallic iron and forms FeS [55].

1.6.2 Mechanisms of MIC in Dental Implants

The complex oral environment is a perfect culture medium for the microbial colonization promoting preferential growth of aerobic or anaerobic microorganisms. MIC of dental implant, particularly Ti-based implants, is known to be a result of metabolic activity of living microorganisms in biofilm and can be linked to microbial metabolites such as organic acids, acidic environment, the formation of local electrochemical cells due to a potential difference in the concentrations of chemicals such as oxygen, and direct or indirect electron transfer reactions with microorganisms. *S. mutans* has been reported to be the main microorganism in oral biofilms [56]. The adverse effect of microbial metabolites such as lactic acid and hydrogen peroxide on the corrosion of Ti has been reported previously [47]. *S. mutans*, *A. viscosus*, and *P. gingivalis* can metabolize carbohydrates to lactic acid and create a localized corrosive condition for Ti implant, leading to discoloration and pitting corrosion of the surface [48, 57]. Moreover, bacterial metabolism can create a locally anaerobic environment and forms anode and cathode regions on the metal surface, resulting in the formation of oxygen concentration cells and causes local electrochemical corrosion (Figure 1.5). It is also suggested that the corrosive properties of Ti can be induced by the formation of oxygen concentration cells due to oxygen consumption along with bacterial metabolism [47].

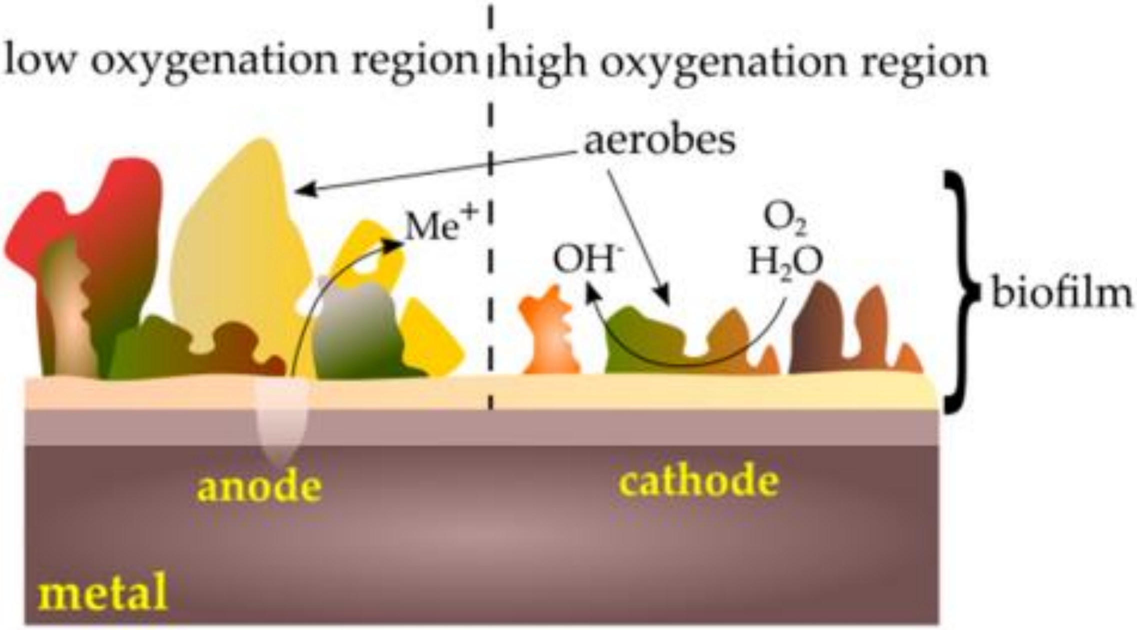

Fig 1.5. Formation of oxygen concentration cell caused by biofilm [58].

1.7 Mitigation Methods of Microbiologically-induced Corrosion

Considering the negative impact of MIC on both marine and biomedical industries, protection of metallic substates against MIC has therefore become very important and the subject of many studies over the last few decades. In both applications, the formation of bacterial biofilm on the metal surfaces is the first and foremost step toward MIC problem and the detrimental consequences associated with that. The bacteria present in a biofilm can be several orders of magnitude more resistant to any antibacterial agents than their planktonic counterparts, making eradication of a formed/established biofilm very difficult or even impossible [59]. Therefore, most of the effort and attentions have been focused on developing preventive strategies to make metal surfaces more resistant against bacterial colonization and biofilm formation in both marine and medical applications. Each application has its own requirements and constraints, dictating the choice of preventive strategies that can be applied, which will be discussed in detail in the following sections.

1.7.1 Mitigation Approaches in Marine Industry

Strategies to combat bio-corrosion are classified to four main categories including 1) biocides, 2) cathodic protection, 3) beneficial application of bacterial biofilms, and 4) application of protective coatings.

1.7.1.1 Biocides

Various oxidizing (e.g., chlorine, bromine, ozone) or nonoxidizing (e.g., formaldehyde, glutaradehyde, quaternary ammonium compounds, isothiazolines) biocides have been widely used in marine industry to prevent MIC, mostly in closed systems such as pipelines. Because of enhanced resistance of biofilms to antimicrobial agents, biocides are much less effective against sessile organisms within biofilms as compared to planktonic population. The lack of efficiency against biofilms along with the adverse environmental hazards (e.g., inhibiting the growth of non-targeted organisms) and high-cost have highly limited the application of biocides in practice, particularly in open flow systems [60].

1.7.1.2 Cathodic Protection

Cathodic protection is another method that have been employed to mitigate bio-corrosion of steel-based structures, however, it does not have any preventive effect on the adhesion of aerobic bacteria and formation of biofilms on the surfaces. Hence, the localized corrosion induced by SRB still remains as a detrimental issue in cathodic protected systems [61]. In CP, an active sacrificial metal (anode) or an external current source is applied to limit the corrosion reaction of a target metal, by making it the cathode of the electrochemical corrosion cell [52]. CP can be employed individually or with other corrosion mitigation techniques such as protective coatings. The most important parameter in any CP systems is the protection potential. Protection potential is in fact the minimum required potential needed to obtain a satisfactory level of protection for a metallic structure. For instance, the protection potential to protect an iron structure buried and submerged in aqueous environment is -0.850 V vs. a copper/copper sulfate ($Cu/CuSO_4$ [CSE]) reference electrode (-0.536 V vs. standard hydrogen electrode (SHE)) [62]. CP is accompanied by the current transfer across the metal/electrolyte interface as per one of the below reduction reactions [63]:

1) $2H_2O + O_2 + 4e^- \rightarrow 4OH^-$ (dissolved oxygen (O_2) reduction in aerobic environments)

2) $2H^+ + 2e^- \rightarrow H_2$ (proton (H^+) reduction in anaerobic or acidic environments)

3) $2H_2O + 2e^- \rightarrow H_2 + 2OH^-$ (reaction (2) in a neutral or basic media)

Reactions (1) and (3) lead to alkalization (increase in the concentration of OH^- ions) at the metal/electrolyte interface and precipitation of insoluble salts such as $CaCO_3$. Deposition of calcareous (calcium-containing) corrosion products result in mitigation of oxygen reduction reaction, as they are very weak electron conductors, therefor, imparting corrosion protection to the system. A drawback associated with CP is that the deposition of corrosion products may block pipes and tubes, especially the smaller ones [64]. Another limitation arises from the alkalized media by CP, which may result in accelerated proliferation of some microorganisms including SBR, as have been reported in several studies. For instance, Olivares et al. have reported that under cathodic polarization, SRB populations on coupons at protection potentials were twice as large as populations on non-protected coupons [65]. Similarly, it was demonstrated that the alkalinity resulted from a CP of XL 52 steel substates at a protection potential of -0.950 V vs. CSE did not negatively affect the SRB growth. In has been also proposed that some MIC-causing SBR are able to use cathodes as sources of electrons for their metabolism, particularly under anaerobic conditions. The presence of SRB can also affect CP and its efficacy. SRB are well-known for generation of H_2S chemical, which may dissociate to H^+, to bisulfide (HS^-) and sulfide (S_2^-), depending on the pH of the environment. Therefore, in the presence of SRB, some chemical compounds such as insoluble ferrous sulfide (FeS) may form, which have been reported to shift the needed protection potential to more negative values (in some cases more than 200-300 mV) than the normal reference conditions [66]. Another potential issue of CP is the generation of is the production of atomic hydrogen (H^o). H^o atoms are such small that they can easily diffuse through steel-based structures and cause hydrogen blistering/embrittlement. There are several studies reported that the presence of MIC-inducing SBR can increase the risk of hydrogen attack by increasing the permeation rate of hydrogen and imposing a more negative protection potential to the system [63]. As mentioned earlier, CP can be accompanied by other corrosion mitigation techniques such as protective coatings. However, the strong electrical fields along with the alkaline media generated by CP may cause detachment/delamination of the protective coating from the underlying metal substrate (cathode) [67]. In summary, despite being effective in corrosion mitigation to some extent, there are still several key drawbacks associated with CP, limiting its application for MIC. First, not only CP cannot prevent biofilm formation, but also it may even boost the growth and proliferation of SBR in some cases, worsening the chance of biofouling on the metal surface. Once biofilms are formed on the metal surface, it increases the required protection potential for an effective cathodic protection, which in turn results in other issues including higher operating costs, higher chance of hydrogen attack/embrittlement, and higher delamination rate of the applied protective coatings.

1.7.1.3 Bacterial Biofilm

Recently, the application of biofilms constituted by specific types of microorganisms has been investigated as a bio-inspired method for prevention of MIC and reported to be effective for a number of metals and alloys, including steels. However, the uncertainty about the formation of biofilm and the unpredictable nature of that have made this approach still far from being practical in industrial applications and therefore, much more research and investigation are needed to be done in this area to fully understand and discriminate between the bacterial extracellular materials that induce bio-corrosion and those that are able to inhibit the bio-corrosion process [68].

1.7.1.4 Protective Coatings

The most common strategy for prevention of bio-corrosion is the use of protective coatings with about 90% of total corrosion prevention costs being spent on that. Different types of protective coatings including organometallic (e.g., tributyltin (TBT)-based paints), inorganic (e.g., titanium oxides and zinc), and organic (e.g., polymers) have been developed so far to combat MIC of metallic structures. Traditionally, organometallic coatings such as tributyltin (TBT)-based paints had been widely applied as anti-fouling surfaces, however, despite being effective in the marine environment, their application have been globally banned since 2008 by International Maritime Organization mainly because of their detrimental effect on non-targeted marine organisms [69]. Despite being effective against MIC to some extent, inorganic coatings such zinc and titanium oxide are very prone to bacterial adhesion and therefore, formation of biofilm due to the lack of antibacterial activity. The last and likely the most important class of protective coatings is organic coatings, which are generally referred as polymeric coatings. Among different types of protective coatings, accumulated studies and evidences have shown that polymer coatings with anticorrosion and antimicrobial properties can be novel and effective approaches to prevent bio-corrosion [70]. Polymeric coatings such as polyurethanes, fluorinated compounds, epoxy resins, polyimides, silicones, coal-tar epoxies, and polyvinyl chlorides have been shown to be very effective to combat regular corrosion, since they usually possess high barrier and anti-corrosion properties and can isolate the underlying corrosion-prone substrate from the surrounding corrosive environment [71]. However, in the case of bio-corrosion, their effectivity may be limited because of the following reasons [72]:

1) Like any other types of protective coatings, polymeric coatings are prone to mechanical damages such as cracks, defects, and crevices. These types of heterogenous damaged sites are highly favorable for the occurrence of localized corrosion and preferential microbial colonization.

2) Interfacial delamination of a poorly bonded coating can create a highly favorable condition for anaerobic growth of microorganisms, including MIC-causing types, and diminishes the long-term stability and durability of the coating.

3) Polymeric coatings are susceptible to undergo biodegradation processes, as some of the microorganisms may rely on them a source of nutrition for their physiological activities. The biodegradation process along with the production of corrosive biproducts can lead to a significant loss of barrier and protection properties within a short period of time.

Therefore, aiming to address all the above mentioned concerns over the use of polymeric coatings as protective layer in MIC application, different modifications have been attempted to inhibit the attachment of bacterial cells and the subsequent microbial degradation of polymeric coatings through induction of strong antibacterial and anti-biofouling properties, while providing them with other beneficial functionalities such as enhanced resistance against mechanical damages and interfacial delamination. Having a dual functionality (both anti-corrosion and antibacterial) is crucial for any MIC protective coating, as none of these features (anti-corrosion and antibacterial) are able to solely combat against MIC and both of them should be present in an ideal coating system and complement each other to obtain an effective protection for the underneath metallic substrate. Most of the antimicrobial polymeric coatings we have already discussed have some levels of barrier and anti-corrosion properties, as they can isolate the covered corrosion-susceptible substrate from the surrounding corrosive environment. The barrier and antimicrobial properties of the coatings can be further augmented by preparing inorganic–organic hybrid composite coatings.

Several nanoparticles (NPs) such as titanium dioxide (TiO_2), silicon dioxide (SiO_2), silver (Ag), and graphene-based NPs have been reported with dual anti-corrosion and antimicrobial functionality that can serve as ideal coating materials for inhibiting MIC [73]. These nanomaterials can be used either blended with other protective coatings or in the format of a thin layer of inorganic coating on the metallic substrates. In a study by Krishnamurthy et al. [74], they have applied a 3-4 monolayered graphene coatings with minimal defect density on a nickel (Ni)-foam substrate against SRB induced corrosion and compared its performance with two other polymeric coatings based on parylene and polyurethane. They reported that only a minimum Ni corrosion was detected over an 800 hours of exposure test, and the performance of graphene coating was found to be superior than those traditional polymeric coatings for the prevention of MIC. TiO_2 NP is another nanostructured material that can provide both anti-corrosion and antibacterial functions. TiO_2 is known to have a broad-spectrum bactericidal activity with an excellent corrosion resistance. Activation of TiO_2 particles with adequate UV light generates electrons and holes that react with adsorbed water and dioxygen molecules to form reactive oxygen species (ROS), killing or inhibiting the growth of bacteria by penetrating their cell walls [75]. Moreover, numerous studies have demonstrated that the inclusion of TiO_2 in coatings can result in a correlated change in surface energy and its components, which has a significant influence on bacterial adhesion. Zhang et al. [76], fabricated a nanocomposite coating based on polytetrafluorethylene (PTFE) and TiO_2 NPs on stainless steel substrate using a sol-gel dip coating technique. The result of bacterial studies showed that the UV-activated TiO_2 nanoparticles could remarkably inhibit bacterial growth. Besides, the TiO_2-PTFE coatings showed an excellent corrosion resistance in Hank's solution, much higher than pure TiO_2 or PTFE coatings, proving the anti-corrosive properties of TiO_2 NPs. Despite the great potential of nanomaterials, their practical application as coating material to inhibit MIC is still limited and further studies are needed for the commercialization of nanomaterial coatings against MIC, notably into reducing cost and simplifying application to the surface being protected.

Currently, the polymeric coatings being used to combat MIC can be classified to three main categories: 1) traditional polymeric coatings incorporated with biocides, 2) antimicrobial polymeric coatings, and 3) electroactive polymeric coatings [70]. The commonly used polymers in protective coating application such as have been incorporated with different types of biocides to impart the coatings antibacterial activity and minimize their microbial degradation. Stobie et al. doped silver ions into the perfloropolyether–urethane coatings reported a remarkable antibacterial activity as a result of silver ions release [77]. In another study by Haque et al., silicone-based coatings were doped with sodium benzoate and exhibited a good resistance against bacterial adhesion [78]. In view of the complex environmental, ecological, and economical issues, attentions have been shifted from those traditionally pollutant and detrimental coatings to more environmental-friendly antimicrobial coatings to prevent biofouling, bacterial adhesion, and biofilm formation on metallic substrate. Regarding this issue, non-leaching antimicrobial coatings hold a great promise as alternatives to those of environmentally harmful coatings. Most of the non-leaching antimicrobial coatings contain quaternary ammonium moieties in their structures. Quaternary ammonium compounds are able to kill bacterial cells by attacking their plasmic membranes, resulting in the dissolution of lipids and the release of intracellular materials. In addition to their bactericidal activity, the detergent-like properties of quaternary ammonium compounds protect the polymeric coating against the formation of polysaccharidic materials, which are released during the process of bacteria colonization. All these properties together have made quaternary ammonium compounds a promising class of materials to be utilized in MIC protective coatings. Quaternary ammonium compounds-containing antimicrobial coatings are often fabricated via covalently grafting of the polymeric layer onto the substrate surface by either simple coupling reactions or surface-initiated free-radical polymerization [70]. Lastly, electroactive polymeric coatings are the third category of organic protective coatings for MIC. Conductive polymers such as polypyrrole (PPy), polyaniline (PANI), and polythiophene (PBT) have been extensively employed to fabricate anticorrosion coating on various metallic substrates. The corrosion protection of conductive polymers is attributed to their ability to act as barrier and inhibitors, protect anodic dissolution, and mediate oxygen reduction [79]. Recently, strong antibacterial activities have been reported by several groups for some of these conductive polymers such as PANI and poly(N-methylaniline) (PNMA) against different types of bacteria including SRB [80]. Owing to their excellent corrosion protection along with a strong antibacterial activity, conductive polymers are, therefore, a very promising choice for combating MIC.

1.7.2 Mitigation Approaches of MIC in Dental Implants

One of the effective strategies to combat MIC can be the prevention of biofilm formation on the implant surface, as the formation of biofilms is widely recognized as the key step in initiating bio-corrosion. Thus, it is pivotal to develop modified surfaces with enhanced antimicrobial potential. Various surface modification of metallic implants to provide antimicrobial behavior as well as additional corrosion resistance has become the subject of extensive studies. Currently, surface antibacterial coating and surface topographic modification are the main strategies to prevent or reduce bacterial adhesion and biofilm formation on implant surfaces. Since different studies demonstrate inconsistent results, the exact antibacterial effect of topographic-modified implant surfaces is still disputed. Contrarily, surface antibacterial coatings show an exact effect on inhibiting biofilm formation on implant surfaces [81]. In a study by Zhang et al, they developed a tantalum nitride (TaN)-decorated titanium surface via depositing a layer of TaN onto pure Ti using magnetron sputtering for dental implant application. The microbial corrosion behaviors of the TaN-coated Ti and unmodified Ti surfaces were evaluated and compared by various electrochemical techniques as well as morphological and chemical characterization of the corrosive surfaces. After 14 days incubation, TaN-decorated Ti exhibited a satisfactory *in vitro* antibacterial activity toward the mixed bacteria including *S. mutans*, *A. viscosus*, and *P. gingivalis*. Potentiodynamic polarization and electrochemical impedance spectroscopy studies indicated that TaN coating exhibited higher MIC resistance in comparison to bare Ti in two bacteria-containing artificial saliva solutions [82].

Among all antibacterial coatings, polymeric coatings have gained considerable attention due to their intrinsic advantages. Some polymers such as chitosan possess bactericidal activity and can kill bacteria adhering to the surface. Besides, polymeric coatings can be used as a local antibacterial drug/agent delivery system to combat bacterial colonization. Conventional antibiotics can be released from these coatings to prevent the surface from recolonization [83]. Multifunctional composite polymeric coatings also allow the incorporation of nanoparticles with different application. For example, Graphene-based nanoparticles as antibacterial agents and calcium phosphates as bioactive components have been incorporated into polymeric coatings [84]. Apart from antibacterial properties, polymeric coating can also play an important role as a corrosion protection of metallic implants. The polymeric outer layer prevents metal from corrosion or exposure to oxidation. Additionally, presence of a coating on top of the implant surface helps to prevent the release of harmful metal ions into the human body surrounding [85]. It’s worth mentioning that there are several techniques available to coat a metallic surface with polymeric materials including spin-coating, dip-coating, layer-by-layer self-assembly, electrophoretic deposition, photo-grafting, etc.

1.8 Corrosion Monitoring

1.8.1 Electrochemical Techniques

Electrochemical techniques are widely used for corrosion monitoring because of their advantages over other traditional monitoring techniques including but not limited to fast measurement, the ability to provide insight on the corrosion mechanism/behavior of the tested sample, repeatability, and accuracy. A three-electrode setup (Figure 1.6) is usually needed to perform electrochemical corrosion studies. The setup consists of three electrodes with the metal sample as the working electrode, a reference electrode, and a platinum wire/graphite rod as the counter electrode. For the electrochemical measurements, an electrolyte/corrosion media is needed which its composition must be determined based on the nature of the experiment and the intended application of the metal according to the available standards (such as ASTM) for that specific application. The electrolyte must be able to simulate the corrosion media where the metal sample is supposed to function in. Electrochemical measurements are performed by an instrument called electrochemical workstation /potentiostat/electrochemical analyzer which is connected to the electrodes and run by a controlling software. The most commonly used electrochemical corrosion techniques include linear polarisation resistance (LPR), potentiodynamic polarization (PP), open circuit potential (OCP), electrochemical noise (EN) technique, EIS, harmonic distortion analysis (HDA), Potentiometric, Amperometry measurements and so forth. Here, we focus on three electrochemical techniques, OCP vs time, PP, and EIS that are frequently used in this dissertation for corrosion monitoring purposes.

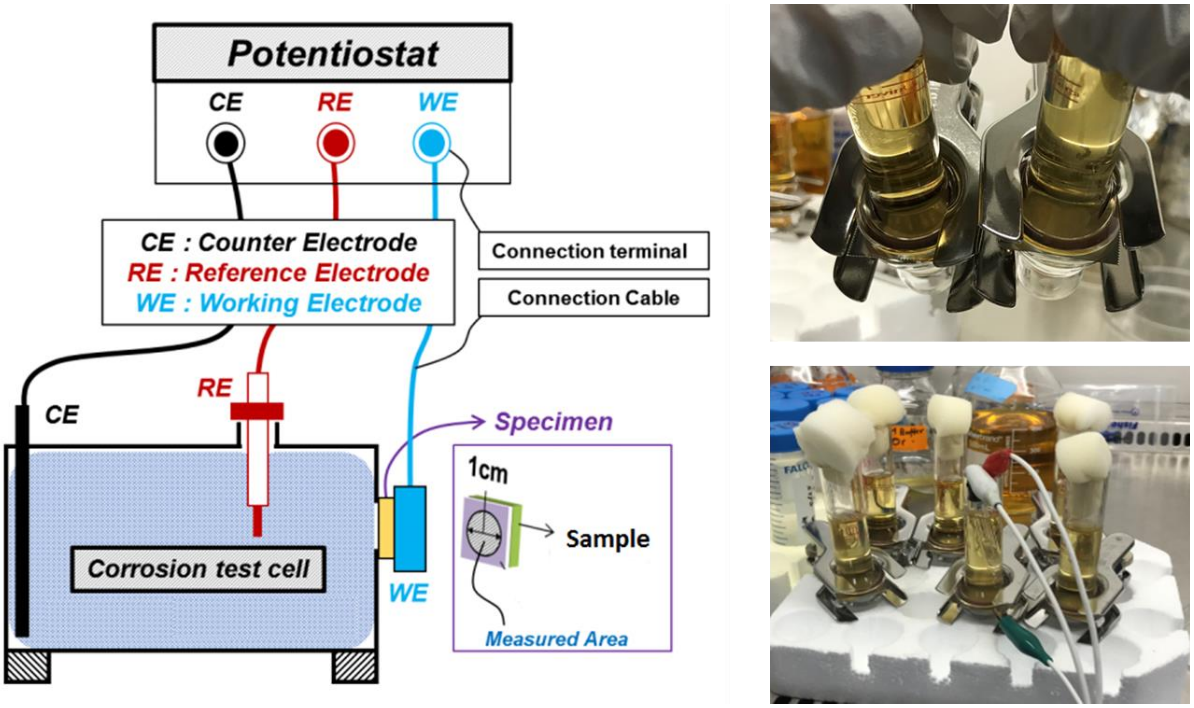

Fig. 1.6. Schematic (left) and the actual (right) three-electrode setup used for electrochemical corrosion experiments.

1.8.1.1 Open Circuit Potential

OCP is the first EC characterization that is usually carried out on metallic simples before conducting other tests such as EIS, LPR, PDP and so forth. In OCP, the potential of the metallic sample as the working electrode, is recorded with respect to a reference electrode without applying any external potential or current to the electrochemical cell. This recorded potential is called OCP. The OCP experiment specifies either a low or high corrosion probability, but it does not provide the corrosion rate [59]. Generally, a more positive OCP value means the surface is nobler and therefore, less susceptible to corrosion.

1.8.1.2 Potentiodynamic Polarization

The scanning of the current potential domain to characterize a material medium pair can be carried out using the LPR method, which is a non-destructive technique. In this method, minimal voltage variations (< ±30 mV to its corrosion potential) are applied to a metal. In this narrow potential range, the obtained current response is linear and therefore, the corresponding polarization resistance (Rp), defined as the slope of the current vs. potential curve, is constant. Rp is inversely related to the instantaneous corrosion rate and can be described by the Stern-Geary equation:

$R_p = B/I_{corr}$ with $B = (\beta a \beta c / 2.3 (\beta a+\beta c))$

where, I_{corr} represents the corrosion current and βa and βc represent Tafel coefficients. If the constant B is known, then by using Faraday's law, the corrosion rate can be determined from I_{corr}. Similarly, the PP technique can also measure the corrosion rate by using the same LPR equation. Nevertheless, the PP technique applies the metal wide voltage variations (> ±300 mV vs. OCP) and is considered a destructive process. PP is perhaps the most widely used polarization testing technique to measure corrosion resistance. From PP, a plot of applied potential (or overpotential) versus logarithm of current density is obtained and called Tafel plot in which the values of Tafel slopes, corrosion potential E_{corr}, and corrosion current density I_{corr} can be determined using extrapolation (Figure 1.7) [86]. In general, a more positive E_{corr} and a lower I_{corr} reflect a higher corrosion resistance of a sample.

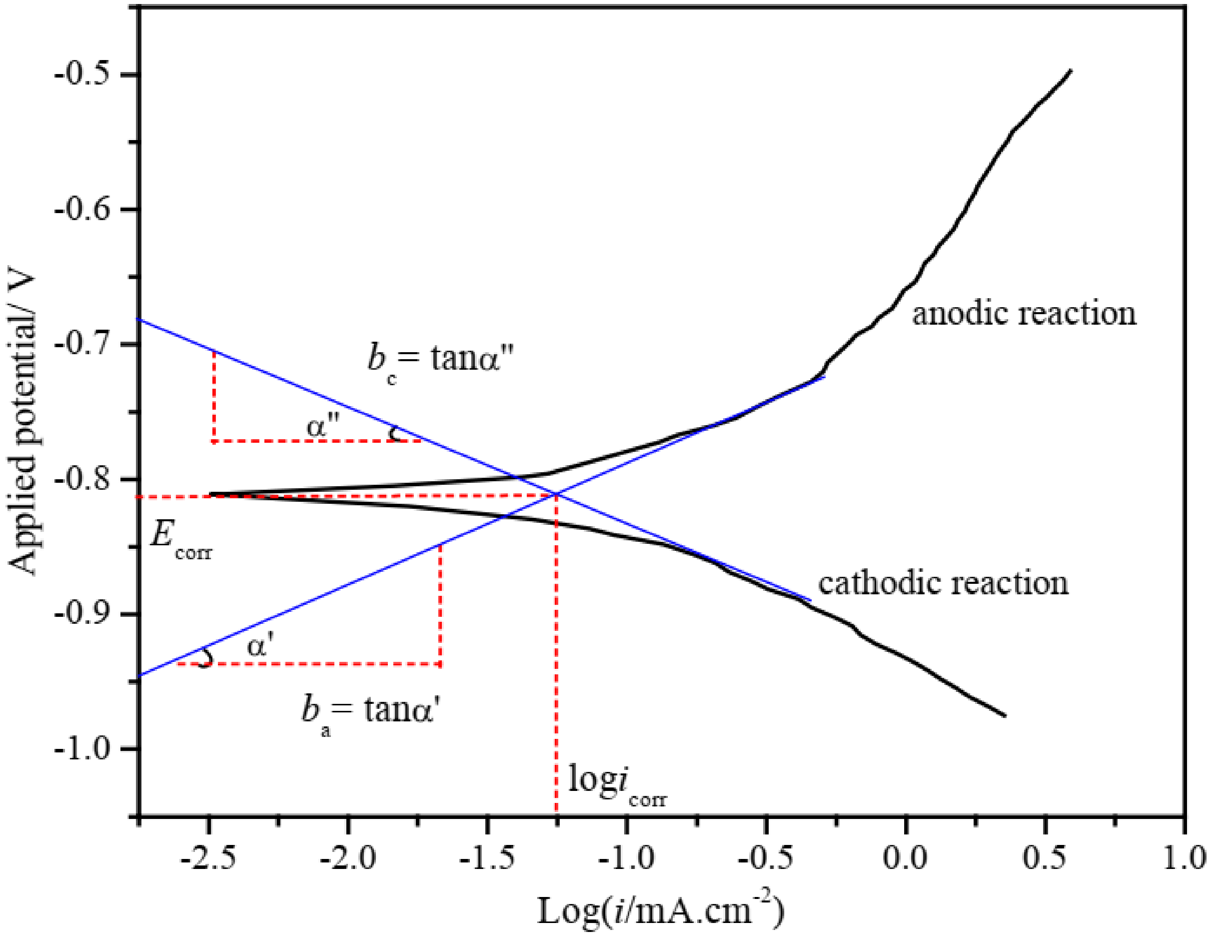

Fig. 1.7. Schematic polarization curve showing Tafel extrapolation [86].

1.8.1.3 Electrochemical impedance spectroscopy

EIS is one of the most important electrochemical techniques where the impedance in a circuit is measured by ohms (as resistance unit). Over the other electrochemical technique, EIS offers several advantages reliant on the fact that it is a steady-state technique, that it utilizes small signal analysis, and that it is able to probe signal relaxations over a very wide range of applied frequency, from less than 1 mHz to greater than 1 MHz. In EIS, an alternating voltage with varying frequencies (from MHz to μHz) is applied to the working electrode and the resulting current is measured in EIS measurements. The frequency sweep enables access to all processes taking place at the electrode: charge transfer and mass transport. Any other electrical contribution and artefacts are visible with EIS. Many impedances (Z) are recorded against each frequency range due to the phase differences of applied voltages and the resulting currents. Once the potentiostat collects the potential vs. time and the current vs. time data at each frequency, a Fast Fourier Transform (FFT) is applied to the data. The FFT converts the potential vs. time and current vs. time into potential magnitude vs. frequency and current magnitude vs. frequency. The potential amplitude E_0, current amplitude i_0, and the phase angle ϕ at each frequency f are determined from the FFT analysis. With these data we can describe the different plotting conventions associated with EIS. The magnitude of the impedance is equal to the potential amplitude E_0 divided by the current amplitude i_0, as shown in the below:

$$|Z| = \frac{E_0}{i_0}$$

If we plot the magnitude of the impedance |Z| and the phase angle ϕ as a function of frequency on a double-axis plot, we get what is called a Bode plot (Figure 1.8).

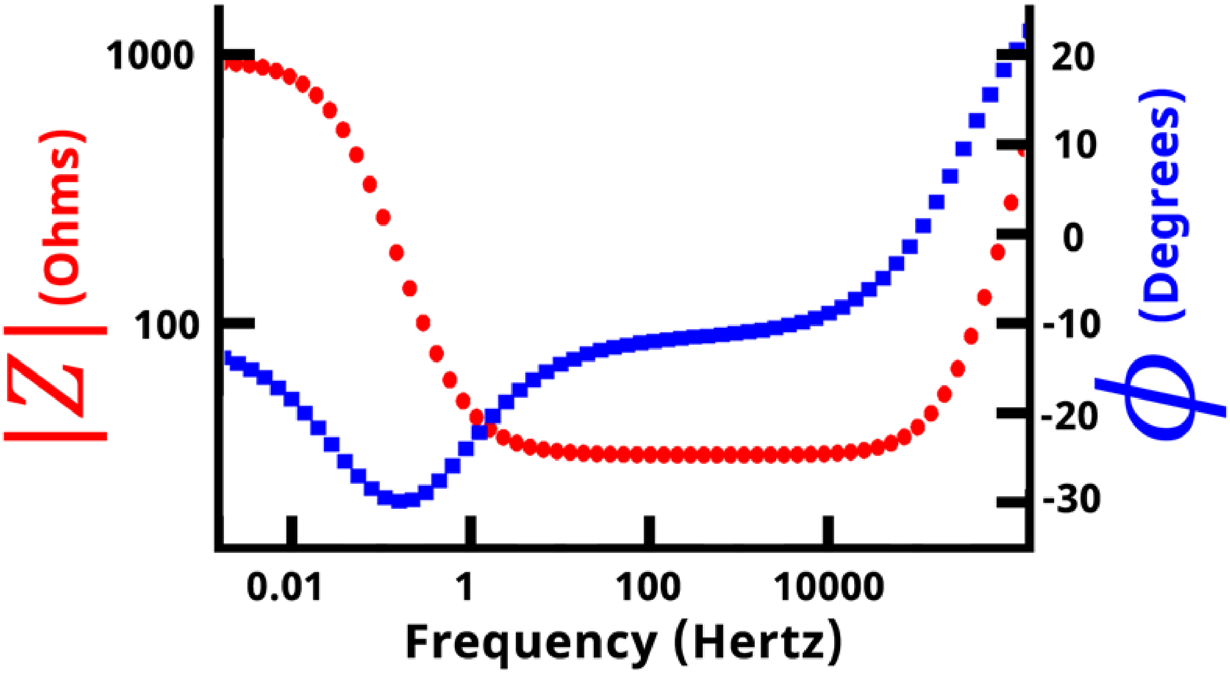

Fig. 1.8. Typical Bode-Impedance (red) and Bode-phase (blue) plots.

In a Bode plot, |Z| vs. f is displayed on the primary vertical axis and ϕ vs. f is displayed on the secondary vertical axis. Frequency and impedance magnitude are normally plotted on a logarithmic scale, while the phase angle is displayed linearly. We can also break the impedance magnitude into its x and y components (Figure 1.9).

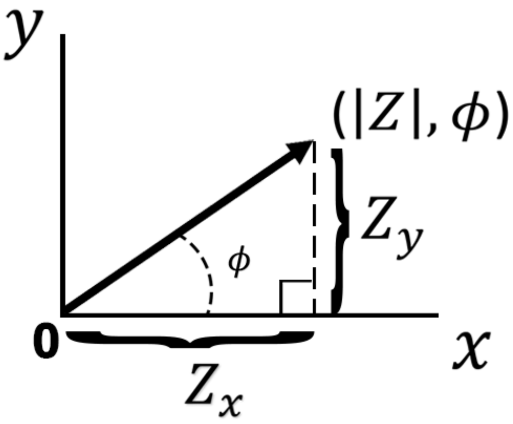

Fig 1.9. Expressing the Impedance Magnitude in terms of x and y components.

The impedance associated with the x-axis is referred to as the real impedance, Z_r, and the impedance associated with the y-axis is referred to as the imaginary impedance, Z_i. If we plot the real impedance Z_r on the x-axis and the negative imaginary impedance $-Z_i$ on the y-axis we obtain a plot known Nyquist plot (Figure 1.10).

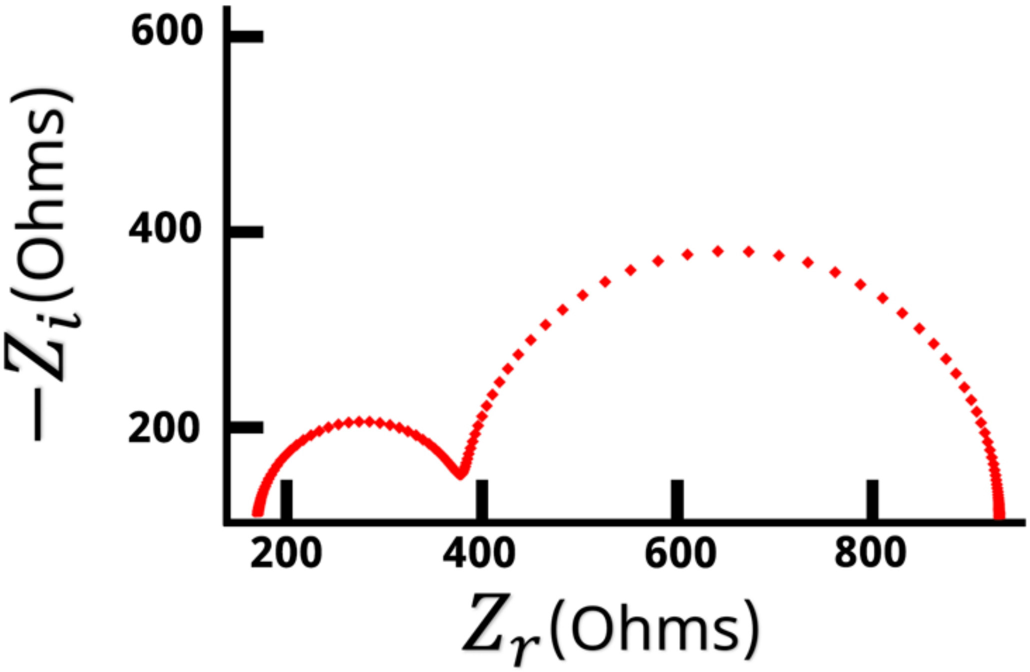

Fig. 1.10. A typical Nyquist Plot [87]

Nyquist plots are the most common form of displaying impedance data, followed by Bode plots. Bode plots allow easy determination of frequency values, compared with Nyquist plots where frequency values are not plotted. Generally, the lower-leftmost points on a Nyquist plot correspond to the highest frequencies and following the trace to the right moves from high to low frequency. Generally, a higher semi-circular diameter in Nyquist plots reflects more corrosion resistance and therefore, less corrosion rate of a tested sample.

1.8.2 Surface Analytical Methods

1.8.2.1 Scanning Electron Microscopy

SEM produces images by scanning the sample with a high-energy beam of electrons. Electrons are produced at the top of the column, accelerated down and passed through a combination of lenses and apertures to produce a focused beam of electrons which hits the surface of the sample. The sample is mounted on a stage in the chamber area and specimens are observed in high vacuum. When the electron beam hits the surface of the sample, it penetrates the sample to a depth of a few microns, depending on the accelerating voltage and the density of the sample. Accelerated electrons in an SEM carry significant amounts of kinetic energy and when they interact with the sample a variety of signals are produced. These signals include secondary electrons (that produce SEM images, most valuable for showing morphology and topography on samples), backscattered electrons (BSE) (most valuable for illustrating contrasts in composition in multiphase samples), diffracted backscattered electrons (EBSD that are used to determine crystal structures and orientations of minerals), photons (characteristic X-rays that are used for elemental analysis and continuum X-rays), visible light (cathodoluminescence-CL), and heat. These signals are collected by one or more detectors to form images which are then displayed on the computer screen. In corrosion monitoring, the surface of a tested sample before and after corrosion experiment can be imaged by SEM to visualize the changes on the surface because of corrosion phenomena. SEM imaging can provide valuable information about the surface morphological changes of the sample (either coated or non-coated) as well as the formation of corrosion products [88].

1.8.2.2 Fourier-transform Infrared Spectroscopy (FTIR)

FTIR Analysis can be used to identify unknown materials, additives within polymers, surface contamination on a material, and more. The results of the test provide information on a sample’s molecular composition and structure. FTIR analysis measures the range of wavelengths in the infrared region that are absorbed by a material. This is done by applying infrared radiation (IR) to a material. The sample’s absorbance of the infrared light’s energy at various wavelengths is measured to determine the material’s molecular composition and structure. The basic theory at work is that the bonds between different elements absorb light at different frequencies. Therefore, unknown materials are identified by searching the spectrum against a database of reference spectra. An FTIR instrument uses a system called an interferometer to collect a spectrum. The interferometer consists of a source, beam-splitter, two mirrors, and a detector. The energy goes from the source to the beam-splitter which splits the beam into two parts. One part is transmitted to a moving mirror which moves back and forth at a constant velocity; and one part is reflected to a fixed mirror. The two beams are reflected from the mirrors and recombined at the beam-splitter. The beam from the moving mirror has traveled a different distance than the beam from the fixed mirror. When the beams are combined an interference pattern is created, since some of the wavelengths recombine constructively and some destructively. This interference pattern is called an interferogram. This interferogram then goes from the beam-splitter to the sample, where some energy is absorbed, and some is transmitted. The transmitted portion reaches the detector. The detector reads information about every wavelength in the infrared range simultaneously. To obtain the infrared spectrum, the detector signal is sent to the computer, and an algorithm called a Fourier transform is performed on the interferogram to obtain the full spectrum as a function of wavenumber (Figure 1.11). In corrosion monitoring, FTIR analysis can be used to determine the chemical compositions of the formed corrosion products on the sample surface during the corrosion experiment. Although FTIR is considered as a semi-quantitative technique, measuring the intensity of characteristic peaks of the corrosion products can provide some information on the severity of the corrosion process the sample has undergone, where a higher characteristic peak intensity reflects a higher amount of corrosion product formed on the sample surface, and therefore a more severe corrosion process.

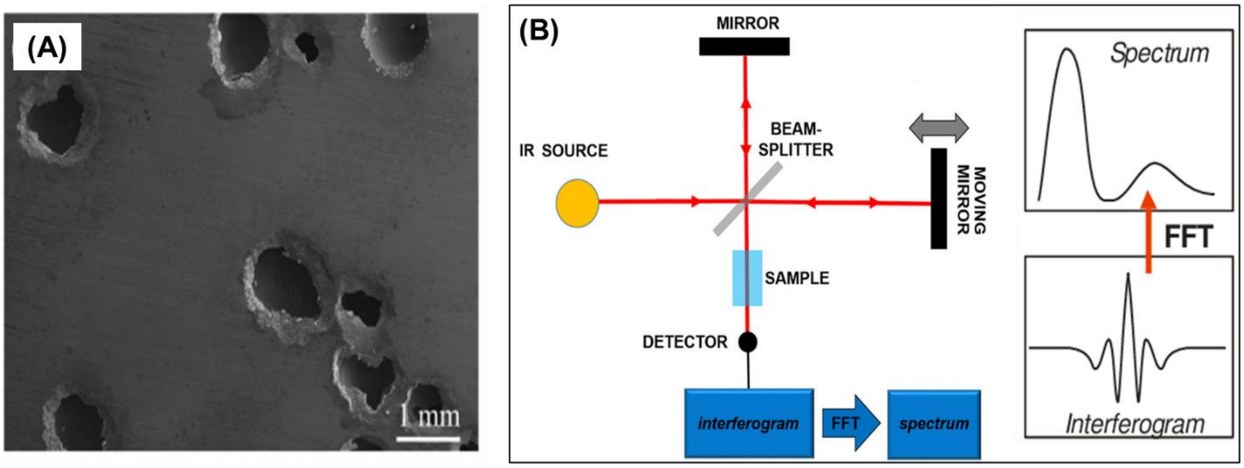

Fig 1.11. Observation of putting corrosion by SEM (A) and the working principle of FTIR machine (B) [89].

1.9. Polymer Modified Electrodes for Biosensing applications

The application of polymers (natural and synthetic) either alone or in composite form for modification of electrodes (mostly metals) have been widely discussed so far as a promising approach for enhancing the corrosion resistance properties of the modified electrode against different types of corrosion. In addition to the corrosion protection properties, polymer modified electrodes offer great promise as biosensing platforms that can be used for detection of various chemical and biological targets. DNA is a polymer that can be synthesized both naturally and artificially with huge potential in biosensing application. The monomer units of DNA are nucleotides, and the polymer is known as a "polynucleotide." Each nucleotide consists of a 5-carbon sugar (deoxyribose), a nitrogen containing base attached to the sugar, and a phosphate group. There are four different types of nucleotides including adenine, guanine, cytosine, and thymine found in DNA, differing only in the nitrogenous base. DNA has been widely used as a functional polymer to modify different types of electrodes for fabrication of nucleic acid biosensors, where the hybridization events between target nucleic acids and the probe DNA strand is converted into a quantifiable signal that is proportional to the concentration of the target molecule. In a project focusing on the detection of miRNAs as potential cancer biomarkers, we modified glassy carbon electrode surface with DNA polymer to serve as the biorecognition element to selectively interact and recognize miRNA-21, a biomarker for early detection of prostate cancer. The results of this project are presented in the appendices (APPENDIX A) at the end of the dissertation.

1.10 Specific Objectives and Organization of Chapters

Chapter 2: A multifunctional polymeric coating incorporating lawsone with corrosion resistance and antibacterial activity for biomedical Mg alloys

a) Physicochemical characterization of composite polycaprolactone / lawsone composite coating on AZ31 Mg alloy
b) *In vitro* corrosion characterization (pH change, hydrogen evolution, and post-corrosion surface morphology and ATR-FTIR)
c) Evaluating the corrosion protection performance of the coating by electrochemical techniques
d) Biological characterization of the coating in terms of antibacterial activity and cellular viability

Chapter 3: Cellulose nanocrystal reinforced silk fibroin coating for enhanced corrosion protection and biocompatibility of Mg-based alloys for orthopedic implant applications

a) Physicochemical characterization of composite polycaprolactone / lawsone composite coating on AZ31 Mg alloy
b) *In vitro* corrosion characterization (pH change, hydrogen evolution, and post-corrosion surface morphology)
c) Evaluating the corrosion protection performance of the coating by electrochemical techniques
d) Cytocompatibility of the coating (cellular viability and adhesion) toward human fetal osteoblast cells

Chapter 4: Microbial corrosion of stainless steel dental implant induced by *streptococcus mutans* bacterium

a) Preparation of bare and polyurethan-coated SS substrates
b) Culture of *Streptococcus mutans* and formation of biofilm on SS substrates
c) Investigation the corrosive effect of *S. mutans* by electrochemical and surface analysis techniques

Chapter 5. Conclusion and future directions

CHAPTER 2

A MULTIFUNCTIONAL POLYMERIC COATING INCORPORATING LAWSONE WITH CORROSION RESISTANCE AND ANTIBACTERIAL ACTIVITY FOR BIOMEDICAL MG ALLOYS

This chapter contains text from the following publication:

Hamid Asadi, Baviththira Suganthan, Sama Ghalei, Hitesh Handa, and Ramaraja P. Ramasamy. Progress in Organic Coatings 153 (2021): 106157.106157.

Reprinted here with permission of the publisher.

Abstract

The clinical application of magnesium (Mg)-based alloys as temporary orthopedic implants is highly limited by their rapid corrosion rate in the physiological environment. Herein, an anti-corrosive polymeric coating based on polycaprolactone (PCL) and lawsone was prepared on AZ31 Mg alloy to improve its corrosion resistance. Lawsone was incorporated into the coatings as a corrosion inhibitor to enhance the passive corrosion protection of the PCL coating through its strong chelation ability of dissolving Mg^{2+}. Anti-corrosion properties of the coatings were assessed by electrochemical techniques and *in vitro* immersion tests, and the results demonstrated a remarkable improvement in corrosion resistance of the bare Mg alloy. In addition to the corrosion inhibition effect, incorporation of lawsone provided the coatings with a strong antibacterial activity against *Escherichia coli* and *Staphylococcus aureus* bacterial strains. Moreover, the fabricated coatings were cytocompatible (viability of > 85%) toward human fetal osteoblast cells. The findings of this work highlighted the great potential of lawsone as a natural corrosion inhibitor for fabrication of corrosion protective, antibacterial, and biocompatible coatings on Mg-based biodegradable implants.

Graphical Abstract

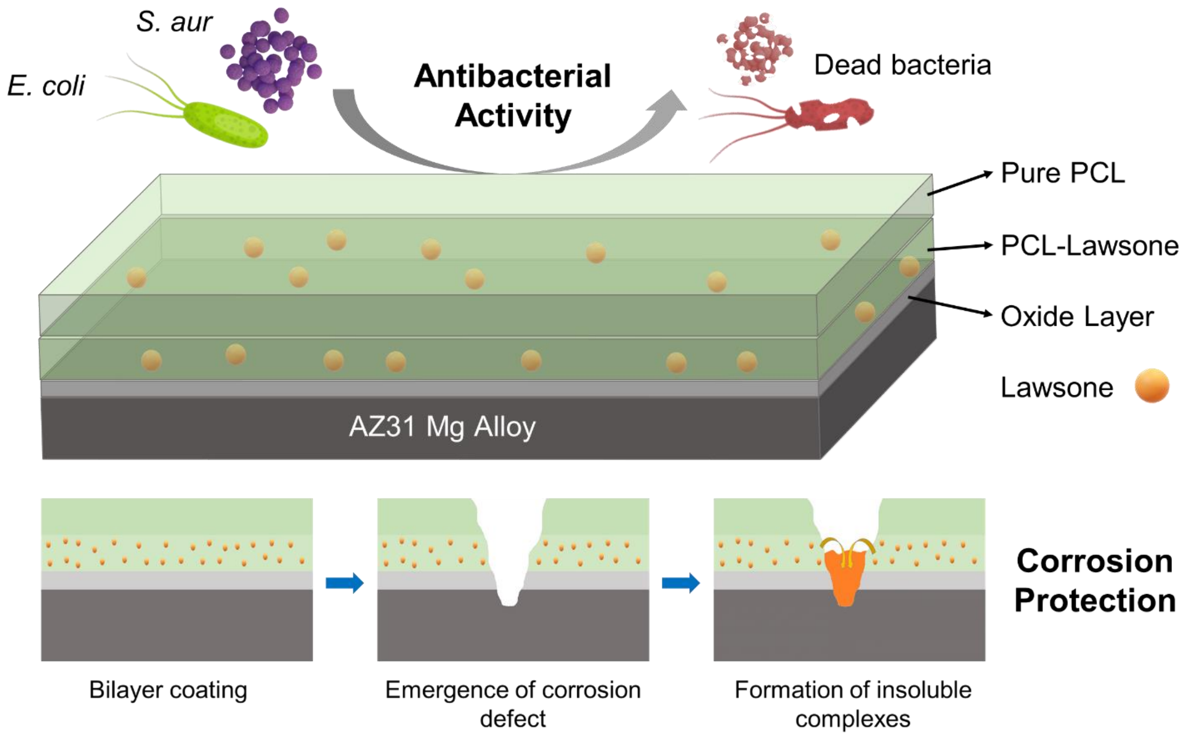

2.1. Introduction

Magnesium (Mg) alloys have emerged as a new class of biodegradable metallic biomaterials in recent years. Particularly, they have gained extensive attention as potential temporary orthopedic bone implants such as fixation screws, plates and pins for the healing of bone defects owing to their biocompatibility and biodegradability, and mechanical properties suitable to natural human bones [90]. In the physiological environment, Mg alloy can be degraded and safely adsorbed by the human body with no inflammatory responses, while the damaged bone tissue is being reconstructed and substituted. This eliminates the need for a second surgery to remove the implant from the body after full healing of the bone defect [91].

Despite all the desirable properties of Mg alloys, their practical application is still limited because of their poor corrosion resistance and rapid degradation rate [92]. Fast corrosion results in excessive H_2 generation at the implant site, local alkalization, and deteriorated mechanical integrity of the implant, which in turns may cause severe complications such as pneumoderma, delayed healing process, and even tissue necrosis [13, 93]. Together, these issues emphasize the need for novel strategies to tailor the corrosion/degradation rate of Mg alloys and expand their clinical application as bioimplants.

Numerous corrosion protection methods including surface chemical treatments [94], phosphate coatings [95], conversion coatings [93], anodization [96], micro-arc oxidation [97, 98], and polymeric coatings [99-101] have been adopted for Mg alloys so far. Among them, polymeric coatings have been recognized as the most effective method to tailor the corrosion rate of Mg alloys without changing their bulk properties [102]. Besides, they can provide other functionalities to the substrate such as enhanced biocompatibility and cellular responses, ability to load small molecules, self-healing, and antibacterial properties [103].

Several synthetic polymers such as polylactic acid (PLA) [104], poly(lactic-co-glycolic) acid (PLGA) [105], polydopamine [43], and polycaprolactone (PCL) [99] as well as natural polymers like chitosan [106] and silk fibroin [13] have been used as protective coatings on Mg alloys in biomedical applications. Although these polymeric coatings can improve the corrosion resistance of Mg alloys to a certain degree, they are susceptible to damage by the highly corrosive environment of the human body, which results in polymer degradation and deterioration of protective barrier properties [107]. Following the emergence of defects or micro-cracks within a coating, corrosive species and water penetrate through the defected areas of the coating and reach the Mg alloy surface, leading to the occurrence of localized corrosion (mainly pitting corrosion) and rapid degradation of Mg alloys [108].

Introducing corrosion inhibitors into the polymeric coatings have shown great potential to improve their durability and anti-corrosion properties [22, 23]. Generally, a composite polymer/corrosion inhibitor coating consists of a polymeric coating as a passive physical barrier, hosting an active corrosion inhibitor within the coating matrix. When the barrier coating is damaged by corrosive species, the loaded corrosion inhibitor can be released into the defected sites and mitigate the corrosion progression by forming insoluble metal complexes [24, 25]. Several inorganic and organic corrosion inhibitors such as cerium ion [26], 8-hydroxyquinoline [27], vanadate [28], molybdate [29], and benzotriazole [30] have been proposed for corrosion protection of Mg alloys so far. Although being effective in corrosion mitigation, most of these synthetic inhibitors are not suitable for implantable biomedical applications due to their potential cytotoxic and carcinogenic effects in the physiological environment [31, 32].

Eco-friendly corrosion inhibitors also known as “green” inhibitors have emerged as promising alternatives to hazardous synthetic inhibitors [33]. Among all the green alternatives, plant-derived corrosion inhibitors have gained considerable attraction, as they possess desired biocompatibility while being inexpensive and available through renewable resources [34, 35]. Lawsone (2-hydroxy-1,4-napthoquinone) is a natural red-orange dye and extracted from the leaves of *Lawsonia inermis* plant, which is known as “Henna”. As the main active ingredient of Henna, lawsone has well-known corrosion inhibition properties based on the chelation of metal cations [109]. It has been used as a corrosion inhibitor for different metal substrates such as steel and aluminum alloys, by either adding it to a corrosion solution or incorporating it in a coating formulation [110, 111]. In a comprehensive study by Lamaka *et al.* [112], inhibition efficiencies of multiple corrosion inhibitors on Mg and its alloys were examined through hydrogen evolution test. Lawsone (0.04 M in corrosion solution) showed excellent inhibition efficiencies of 97% and 90% for high-purity Mg (Fe % 51 ppm) and Mg alloy AZ31, respectively. In addition to the corrosion inhibition properties, lawsone is non-toxic to the human body and has been widely used in various biomedical applications such as wound healing [113], antibacterial coating [114], and cancer treatment [115]. Moreover, it has been reported that lawsone possesses antibacterial and antibiofilm activities against gram-positive and gram-negative bacteria [116]. Such antibacterial effects can be helpful in the prevention of microbial infection and failure of the implant especially at early stages after implantation [117]. Taken together, lawsone is an attractive candidate to be used in the fabrication of protective coatings on biodegradable Mg-based orthopedic implants.

Herein, we present a composite coating on a Mg alloy for biodegradable bone implant application. For the first time in this study, lawsone was incorporated into a coating formulation to improve the corrosion resistance properties of a Mg-based alloy. The structure of the proposed composite coating on the AZ31 Mg substrate is schematically presented in Figure 2.1. AZ31 is one of the Mg–Al–Zn alloys with a comparatively lower Al content (~ 3 wt%) than other Mg alloys (with typical Al contents of 3–13 wt%). This makes AZ31 more suitable for biomedical applications, as excessive Al contents may be harmful to neurons and the osteoblast cells [118, 119]. Before coating, the AZ31 substrate was alkaline treated to form a temporary passive layer of $Mg(OH)_2$ on the surface. This layer protects the active surface of AZ31 against corrosion during the coating process and ensures the formation of a homogenous coating with no bubbles and pores [120]. PCL, a bioresorbable semi-crystalline polyester, was selected as the polymeric matrix in the proposed coating, due to its excellent biocompatibility and slow degradation rate [121]. Previous studies have shown that PCL coatings can effectively hinder the initial rapid degradation of Mg alloys [122]. Our proposed coating has a bi-layered structure consisting of a PCL/lawsone inner layer and a pure PCL top layer. The top layer serves as a physical barrier to minimize the excessive leaching of the loaded inhibitor. The PCL/lawsone is the functional layer of the coating, in which lawsone was embedded as a natural and non-toxic corrosion inhibitor, to improve the corrosion inhibition ability. Such bilayer coating structure benefits from the biocompatibility and barrier properties of PCL, and the corrosion inhibition and antibacterial activity of lawsone. The morphological and physicochemical properties of the fabricated coating were characterized by scanning electron microscope (SEM), attenuated total reflectance-Fourier transform Infrared analysis (ATR-FTIR), and contact angle measurement. The corrosion protection effect of the coating was assessed by electrochemical tests and immersion experiments in Hank's solution. Finally, the antibacterial properties and cell compatibility of the coating were evaluated.

Our central hypothesis is that the incorporation of lawsone corrosion inhibitor into the PCL polymeric matrix will enhance the corrosion protection of PCL coating through its strong chelation ability of dissolving Mg^{2+} and impart it with antibacterial properties. We also expect the composite coating not to show any cytotoxic effect due to the well-known cytocompatibility of PCL and the natural origin of lawsone as a plant extract. Application of such coating on AZ31 Mg alloy is expected to improve its corrosion resistance, cytocompatibility, and bactericidal activity, making it a better candidate to be used as biodegradable orthopedic implant material.

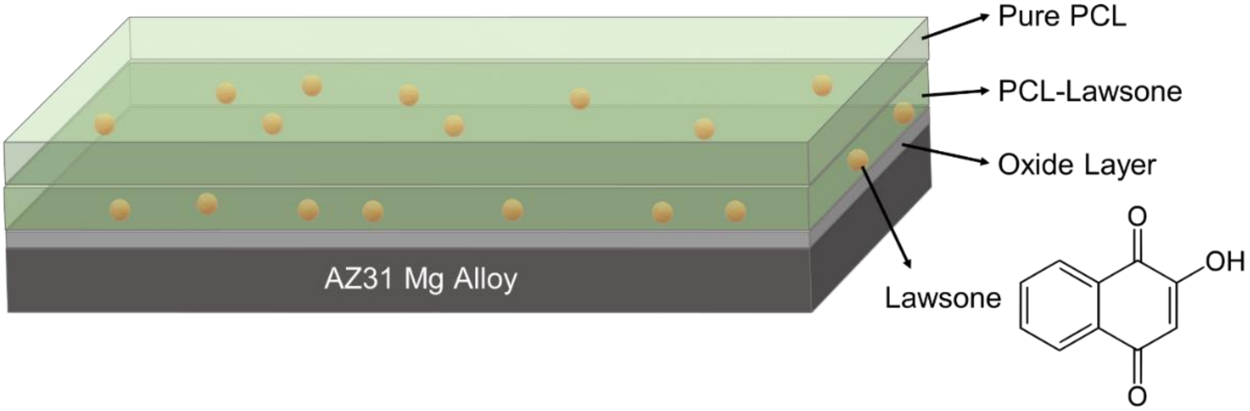

Fig. 2.1. Schematic of the PCL-LS coating on the AZ31 Mg substrate.

2.2 Materials and methods

2.2.1 Chemicals and Reagents

Poly(ε-caprolactone) (PCL) with the average molecular weight of 80,000 g/mol and lawsone (2-Hydroxy-1,4-naphthoquinone, 97%) were purchased from Sigma-Aldrich. Dichloromethane was obtained from EMD chemicals. All other reagents, unless otherwise specified, are of reagent grade. Milli-Q water (resistivity = 18 MΩ.cm) was used for the preparation of all electrolytes and aqueous solutions.

2.2.2 Preparation of AZ31 Substrates

AZ31 Mg alloy sheet with a thickness of 1 mm was cut into the pieces of 2×2 cm. AZ31 samples were first mechanically polished by 2000-grit silicon carbide abrasive paper to remove contamination and native oxides layer. Then, they were ultrasonically cleaned in ethanol and distilled water each for 5 min, and finally dried in an oven at 60 °C. The chemical composition of the AZ31 alloy is shown in Table 2.1.

Table 2.1. Elemental composition of AZ31 Mg alloy (mass fraction, %).

Al	Zn	Mn	Si	Cu	Fe	Ni	Others	Mg
2.5-3.5	0.7-1.3	0.2-1	0.05	0.01	>0.05	>0.05	0.4	remaining

2.2.3. Alkaline Pretreatment

Before applying the polymeric coating on the Mg alloy surface, it is necessary to provide the Mg sample with primary protection against possible corrosion during the coating process. In this study, alkaline treatment was used to form a passive layer of $Mg(OH)_2$ on the Mg surface to enhance its corrosion resistance. To do so, all Mg samples were immersed in 1 M NaOH solution at 80 °C for 4 h. After the reaction was completed, samples were thoroughly rinsed with deionized (DI) water and dried at 80 °C. This sample was labeled as "AZ31-OH".

2.2.4. Fabrication of PCL-Lawsone Coatings

PCL solution (1% w/v) was prepared by dissolving PCL in dichloromethane using a magnetic stirrer for 1 h. Lawsone powder was added to the PCL solution and stirred to obtain a homogenous solution with 1% w/w of lawsone with respect to PCL weight. The resulting PCL/lawsone solution (200 μL) was pipetted on alkaline pretreated Mg samples and dried under the hood for 24 h at room temperature. During the drying process, all samples were placed on glass Petri dishes with closed lids to control the solvent evaporation rate. The same process was repeated for the other side of the samples. To prepare the top coating, a pure PCL solution (200 μL) was pipetted on both sample sides. The lawsone-interbedded samples were labeled as "PCL-LS". Meanwhile, specimens coated with pure PCL were also prepared as controls under the same condition and denoted as "PCL".

2.2.5. Coating Characterization

The surface and cross-section morphologies of the coatings were visualized by a scanning electron microscope (SEM, FEI Teneo, FEI Co.). Before SEM observation, all samples (except for those prepared for cross-sectional imaging) were gold-sputtered to improve conductivity. The elemental analysis across the coating/substrate interface was obtained by an energy dispersive x-ray spectrometer (EDS) connected to the SEM. The functional groups of the coatings were recognized by attenuated total reflectance-Fourier transform Infrared analysis (ATR-FTIR, Nicolet 6700, Thermo Electron Corporation, MA, USA). The spectra were recorded from 4000 to 800 cm^{-1} in wavenumber and 128 scans with a resolution of 4 cm^{-1}. The surface wettability of samples was measured using a Krüss DSA 100 drop shape analyzer at room temperature. The static contact angle was measured by the dropwise addition of Hank's solution (1 μL) onto the sample surface. Adhesion of the protective coatings to the AZ31 substrate was examined by the cross-cut tape test according to ASTM D3359. A lattice of 100 squares of 1 mm^2 area each was formed on the coated samples using a sharp blade and a cross-cut guide. An adhesive tape (SEMicro CHT) was applied to the cross-cut area, rubbed with an eraser to ensure a firm contact between the tape and the test area, and quickly pulled off at an angle of 180° after 90 s. Depending on the percentage damage of the coatings, adhesion was graded according to ASTM standard chart, where 5B represents excellent adhesion (0% of coating detachment) and 0B represents very poor adhesion (> 65% of coating detachment).

2.2.6. *In vitro* Corrosion Evaluation

2.2.6.1. Electrochemical Measurements

Hank's solution (the compositions are listed in Table 2.2) was used for electrochemical and immersion experiments (according to ASTM-G31-72) to mimic the main inorganic components of the corrosive aqueous media in the human body [123]. Electrochemical measurements were conducted in a custom-made corrosion cell in Hank's solution using CHI-920c model potentiostat (CH Instruments Inc., Austin, TX). The set-up consists of three electrodes with Mg samples exposing a surface area of 1 cm^2 as the working electrode, a silver/silver chloride (Ag/AgCl 3 M) reference electrode, and a platinum wire as the counter electrode. First, the open circuit potential (OCP) values of samples were recorded for 30 min without any external disturbance. Then, electrochemical impedance spectroscopy (EIS) measurement was carried out at OCP between frequencies of 10^{-2} to 10^5 Hz with an AC amplitude of ±10 mV. Immediately, after the EIS test, a potentiodynamic polarization (PP) test was performed from − 250 mV to + 250 mV vs OCP at a scan rate of 1 mV/s to evaluate the corrosion behavior of the of the coated samples. The EIS data were quantitatively simulated using appropriate equivalent circuit (EC) models. EIS measurements of coated samples after 1, 3, and 7 days of immersion in Hank's solution were also carried out under the same conditions. All electrochemical corrosion experiments were carried out in triplicates, and the average values was used for analyses. The corrosion potential (E_{corr}) and corrosion current density (I_{corr}) were determined from PP curves by Tafel extrapolation method. The inhibition efficiency (IE) of each sample was calculated using Eq. 1 as below [124]:

$$\% IE = \frac{I_o - I_i}{I_o} \times 100 \qquad (Eq. 1)$$

Where I_o and I_i are the corrosion current densities of AZ31 (control sample) and the tested sample, respectively.

Table 2.2. Composition of Hank's solution used for *in vitro* corrosion studies.

NaCl	KCl	$CaCl_2$	$MgSO_4.7H_2O$	$MgCl_2.6H_2O$	$Na_2HPO_4.2H_2O$	KH_2PO_4	D-Glucose	$NaHCO_3$
8 g/L	0.4 g/L	0.14 g/L	0.1 g/L	0.1 g/L	0.06 g/L	0.06 g/L	1 g/L	0.35 g/L

2.2.6.2. Immersion Experiments

Samples were immersed in a sealed vial containing Hank's solution at 37 °C with a volume-to-sample area ratio of 20 mL/cm2 (ASTM G31-72). For each sample, the volume of evolved hydrogen generated by Mg samples was measured every 24 h up to 7 days. The experimental set-up for this test consists of an inverted funnel-burette system above the sample, immersed in a solution-filled container. Meanwhile, the pH values of the immersion solutions were recorded during the immersion test. After immersion for 7 days, all samples were taken out and thoroughly rinsed with DI water to remove the corrosion products on the surface and quickly dried. Post-corrosion surface morphology was characterized using SEM and surface compositions were analyzed using ATR-FTIR analysis.

2.2.7. Antibacterial Activity Assay

Escherichia coli (*E. coli*) and *Staphylococcus aureus* (*S. aureus*) bacterial strains were used to study the antibacterial activities of the coatings using the Kirby-Bauer disk diffusion test [125]. Briefly, a pure bacterial culture is suspended in a phosphate buffer saline (pH 7.4), adjusted to a turbidity of 0.5 McFarland standard, and swabbed uniformly across a culture plate. Mg samples were cut into pieces of 1×1 cm in diameter, sterilized under UV light for 1 h each side, and placed on the culture plates. After, incubating the plates at 37 °C for 24 h, the antibacterial activity was evaluated by measuring the diameter of the inhibitory zone formed around the samples.

2.2.8. Cytocompatibility

2.2.8.1. Cell Culture

Fetal Osteoblast cells (hFOB 1.19-ATCC 11372) were cultured in 75 cm^2 T-flasks with a 1:1 mixture of Ham's F12 Medium and Dulbecco's Modified Eagle's Medium, containing 0.3 mg/mL Geneticin (Gibco Life Technologies) and supplemented by 10% fetal bovine serum (FBS) in a humidified incubator at 37 °C with 5% CO_2. The culture medium was replenished with fresh media every 2 days until cells were 90% confluent. Thereafter, the cells were detached from the T-flask using 0.18% trypsin and 5 mM EDTA for 5 min.

2.2.8.2. Cell Viability

The effect of leach outs from the Mg samples in hFOB media were tested against fetal osteoblast cell proliferation. The sample leachates were obtained using cell culture media with an extraction media/surface area ratio of 1.25 mL/cm^2 in a humidified atmosphere with 5% CO_2 at 37 °C for 1,3, and 5 days according to ISO 10993-12 [126]. Around 5000 cells/well were seeded in a cell culture grade 96-well plate and incubated for 24 h in a humidified incubator with 5% CO_2 at 37 °C. The manufacturer’s protocol (Sigma-Aldrich) was followed to perform the cytocompatibility test using a CCK-8 kit on hFOB. After 24 h of cell culture incubation in a 96-well plate, 10 μL of the leachates from the samples were added (n = 6) to the cells. The cells were allowed to respond to the leachates during a separate 24 h incubation period inside a cell culture incubator at physiological temperature. Then, 10 μL of the WST-8 solution was added to the resulting solution and incubated for 2 h. During this time, dehydrogenase enzymes from live cells acted on the WST-8 solution, converting it to an orange product, formazan, measurable at 450 nm [127, 128]. The relative viability (%) of the cells in response to sample leachates was reported relative to the control (without leachate exposure) using Eq. 2 [129]:

$$\%\, cell\ viability = \frac{absorbance\ of\ the\ test\ samples}{absorbance\ of\ the\ control\ samples} \times 100 \qquad (Eq. 2)$$

2.2.9. Statistical analysis

All data in this study were expressed as mean ± standard deviation with n = 3. One-way analysis of variance (ANOVA) tests was used to determine statistical significance, where significance was defined as $p < 0.05$.

2.3. Results and discussion

2.3.1. Coating Characterizations

2.3.1.1. Surface Morphology

Figure 2.2A-D exhibits the SEM surface morphologies of as-prepared Mg samples. The bare AZ31 substrate showed a flat and smooth surface with some orderly aligned scratches on that, remained from the mechanical polishing step. After alkaline treatment and formation of a dense oxide layer, the scratches became shallower on AZ31-OH surface. The coated Mg samples (both PCL and PCL-LS) evidently exhibited smooth and uniform polymeric layers on their surfaces, which was distinct from the surface morphologies of those uncoated Mg samples. Moreover, no obvious defects were observed on the coating, suggesting that the coatings can fully cover the substrates and protect them against corrosive environment. Figure 2.3 shows the cross-sectional morphology of the PCL-LS/substrate interface with the corresponding elemental analysis mapping and EDS spectra. The bi-layered structure of the polymeric coating composed of an inner PCL-Lawsone and a top pure PCL layer along with the formed oxide layer on the AZ31 substrate surface were clearly observed. The PCL-LS coating was quite compact and uniformly covered the pretreated AZ31 substrate with no distinct gap across the interface, indicating the success in coating strategy. The thicknesses of the polymeric coating and the oxide layer were found to be about 10 μm and 4 μm, respectively. EDS analysis was conducted to confirm the elemental composition of each layer. As expected, section A from the AZ31 substate showed a sharp peak related to Mg element. In the EDS spectrum of section B, a new O peak was emerged, confirming the nature of oxide layer. Additionally, the highest content of C element was observed in section C, corresponding to the PCL structure.

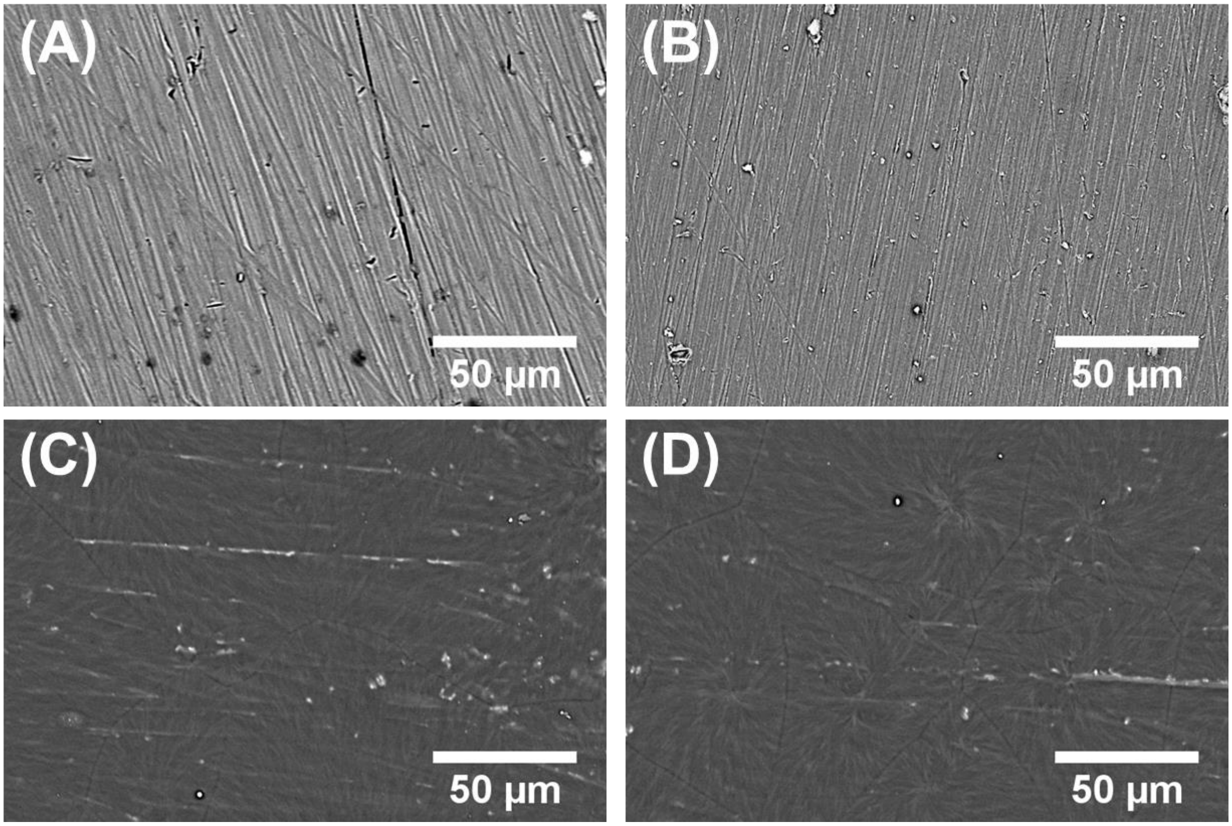

Fig. 2.2. Surface SEM images of AZ31 (A), AZ31-OH (B) PCL (C), and PCL-LS (D

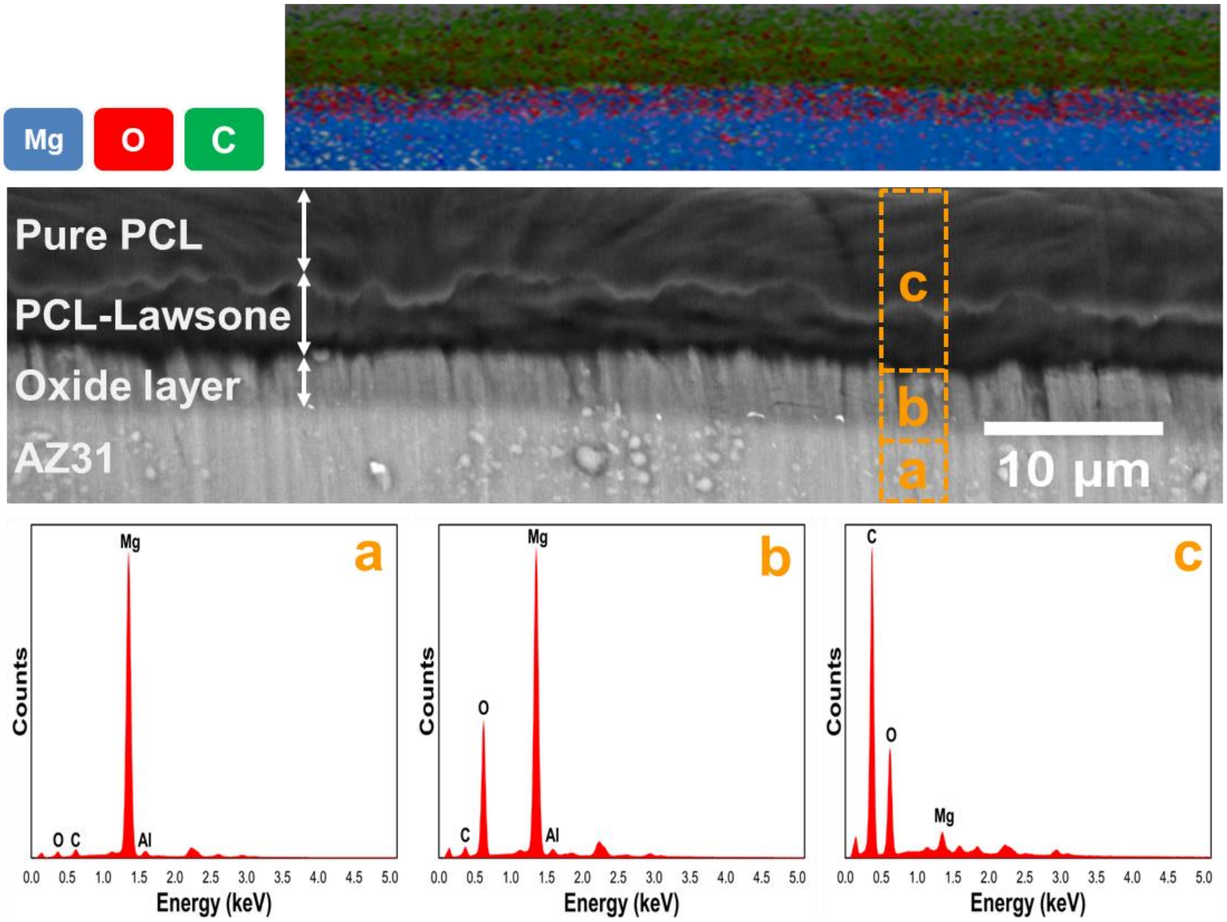

Fig. 2.3. Surface Cross-sectional morphology of PCL-LS/substrate interface with the corresponding elemental analysis mapping and EDS spectra.

2.3.1.2 Coating Uniformity

Coating uniformity, defined by the variation of coating thickness across the underlying substrate, is among the most important parameters that needs to be examined for any corrosion protective coating. In this project, the drop-casting method was utilized to coat AZ31 substrate with the PCL-LS coating. Although the drop-casting method offers a simple, straightforward, and cost-effective coating process, there are some concerns over the uniformity of the coatings fabricated by this method. The uniformity of the PCL-LS coating was evaluated using a surface profilometer (BRUKER Dektak XT). Profilometer measures the surface profile by physically tracing the surface with a stylus and is ideal for evaluation of coating thickness and surface roughness at nano scale without damaging the sample. Before using a profilometer, other instruments such as a simple paint thickness gauge and micrometer were used to evaluate the coating uniformity, however none of these instruments had the sufficient accuracy and repeatability needed for this objective (Figure 2.4). The thickness gauge and micrometer work best for ferrous substate and rigid materials, respectively, and are not suitable to be used for Mg alloys substrates and compressible polymeric coatings.

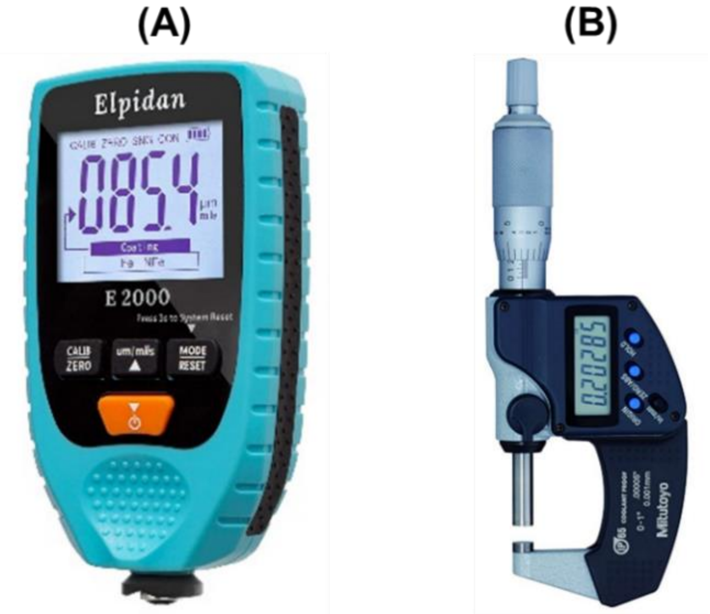

Fig. 2.4. Paint thickness gauge (A) and micrometer (B) that initially used for the measurement of coating uniformity but were abandoned due to the lack of accuracy and repeatability.

For uniformity measurement by the profilometer, a stripe of the coating was detached from the surface using a sharp blade cutter to create a non-coated area adjacent to the coating (Figure 2.5). Having a non-coated area is needed for measurement of the coating thickness by the profilometer is required to serve as a point of reference when measuring the thickness of the coating. The profilometer physically probes the sample surface with a stylus starting from the non-coated area and moving toward the coated section of the sample.

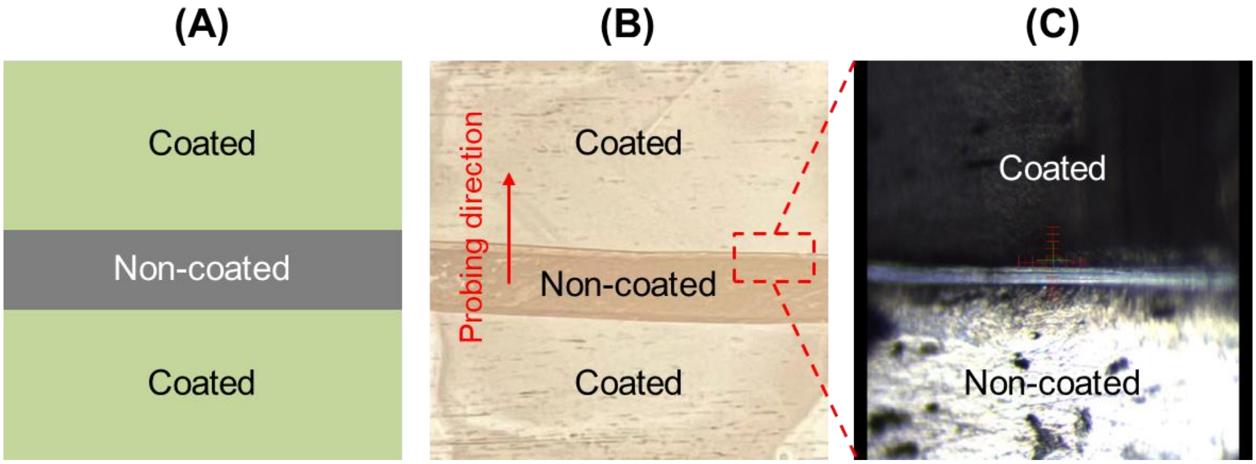

Fig. 2.5. Schematic (A), photograph (B), and microscopic image (C) of the PCL-LS sample prepared for uniformity analysis by the profilometer.

The typical surface profile obtained by this method is shown in Figure 2.6. The left section of the profile is related to the non-coated area showing lower height values. Moving toward coated area, a sudden drop in height value was observed which is due to the blade cutter used for detachment of the coating form the Mg alloy surface causing a dent on the metal surface, known as “Knife effect”. Following that, a jump in height value appeared in the surface profile which was attributed to the coating edge coming off the surface after detachment of the coating. The next section of the profile where the height values reach plateau represent the thickness of the coating with respect to the non-coated area can be used for measurement. Thickness of the coating was determined by measuring the difference of levels between the coated area and the underlying substrate.

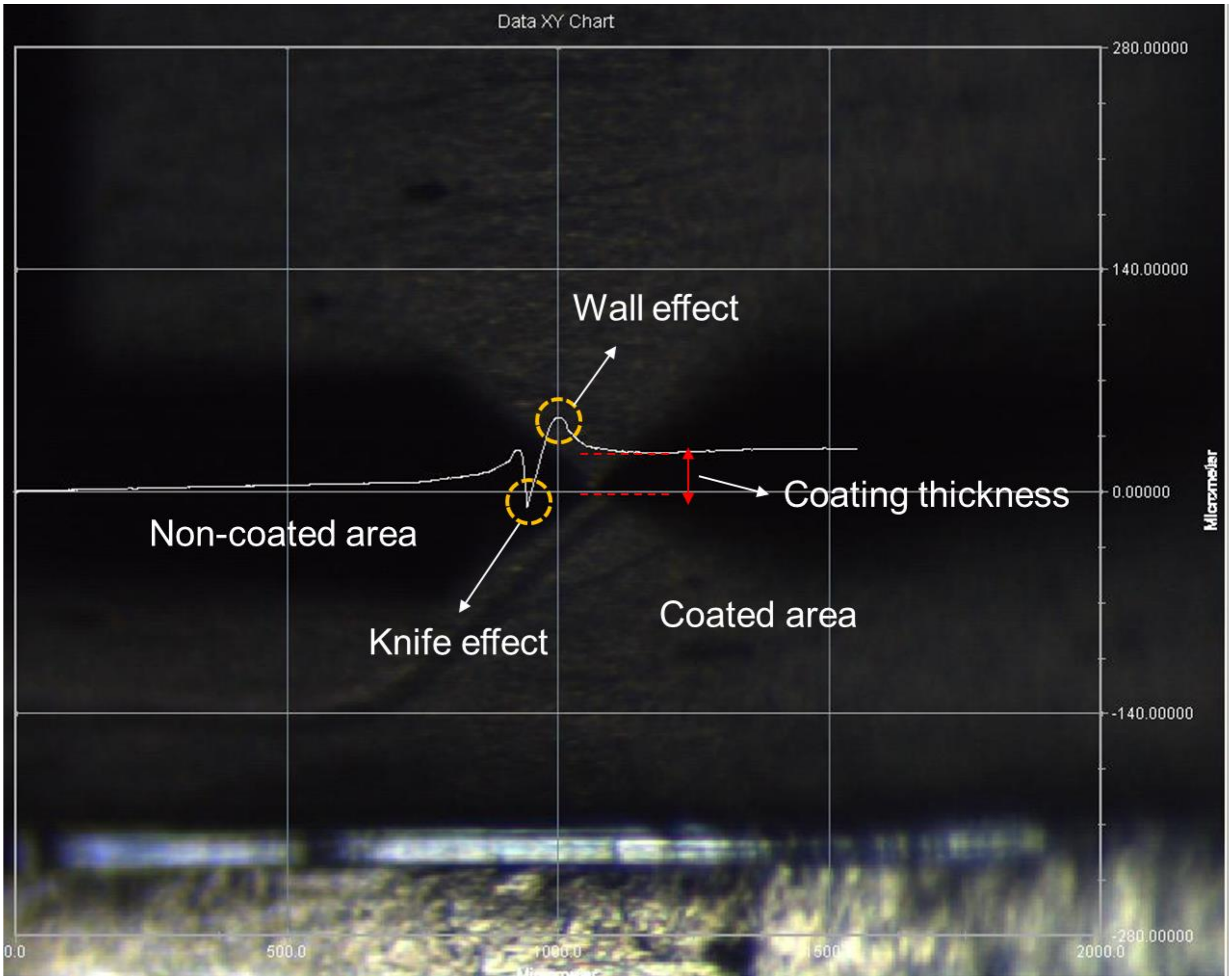

Fig. 2.6. Typical surface profile obtained from probing the sample surface by profilometer.

In addition to the drop-casted PCL-LS sample, PCL-LS coated Mg alloy sample was prepared by spin-coating method for comparison as shown in Figure 2.7. Spin coating is known for its ability to produce very uniform coatings quickly and easily. Spin coated Mg samples were prepared by pipetting 500 µL of PCL-LS solution on the samples and spin coating at 500 rpm and 3100 rpm for 15s and 25s, respectively. This process was repeated one more time with a blank

PCL solution to obtain a thick and fully covering PCL coating. A higher concentration of PCL solution (8% w/v) was used in the spin coating process to obtain thicker coatings to be comparable with the original PCL-LS sample, which was not possible to obtain using 1% w/v PCL solutions that were used in fabrication of the drop-casted PCL-LS coatings.

Fig. 2.7. Spin coating setup used to prepare PCL-LS coated Mg substrates.

8 measurements (M1-M8) were made at different sites on each sample across the coating by probing from one side (M1) to the ultimate opposite side (M8) of the sample. In contrast to cross-sectional SEM imaging where the result is limited to a small part of the sample, this method measures the thickness of the coating all across the sample at different points and provides a better and more accurate insight on the thickness uniformity. The thickness values of samples measured at different sites are listed in Table 2.3 and their corresponding graph is plotted in Figure 2.8. In both drop-casted and spin coated samples, the thickness of the coating at the edges of the samples (M1 and M8) were found to be significantly higher than those obtained in the middle of the samples (M2-M7). There are several behind the thickness variation at the edges of spin coated samples.

First, surface tension effects make it difficult for solution that is flowing radially outward to detach from the substrate. Thus, a small "bead" of liquid can stay attached around the entire perimeter and result in thicker coatings in this rim zone. In addition, if substrates are not exactly round and especially if they are square or rectangular, then the air flows over the protruding parts (corners) will be perturbed. Although the flow may still be laminar, it will have different flow history and will usually result in non-uniformity in coating thickness in these corner areas. Although the edges of the coatings could potentially be the areas of concern in terms of uniformity, only the central area of the samples were used and involved in the electrochemical measurements, where the highest uniformity was observed. It's worth mentioning that the thickness of PCL-LS coating (excluding the edges, M2-M7) showed RSD of 17.85% when drop casted and 8.77% when spin coated, respectively, indicating the relatively higher uniformity of the spin coated coating compared to the drop casted one.

Table 2.3. Thickness of the PCL-LS coating measured at different sites across the coated Mg samples.

	M1	M2	M3	M4	M5	M6	M7	M8	RSD% (M2-M7)
Drop casted	18.6	8.76	6.67	5.37	8.96	7.88	7.76	30.78	17.85
Spin coated	34.88	5.3	5.07	4.52	5.13	5.88	4.91	20.45	8.77

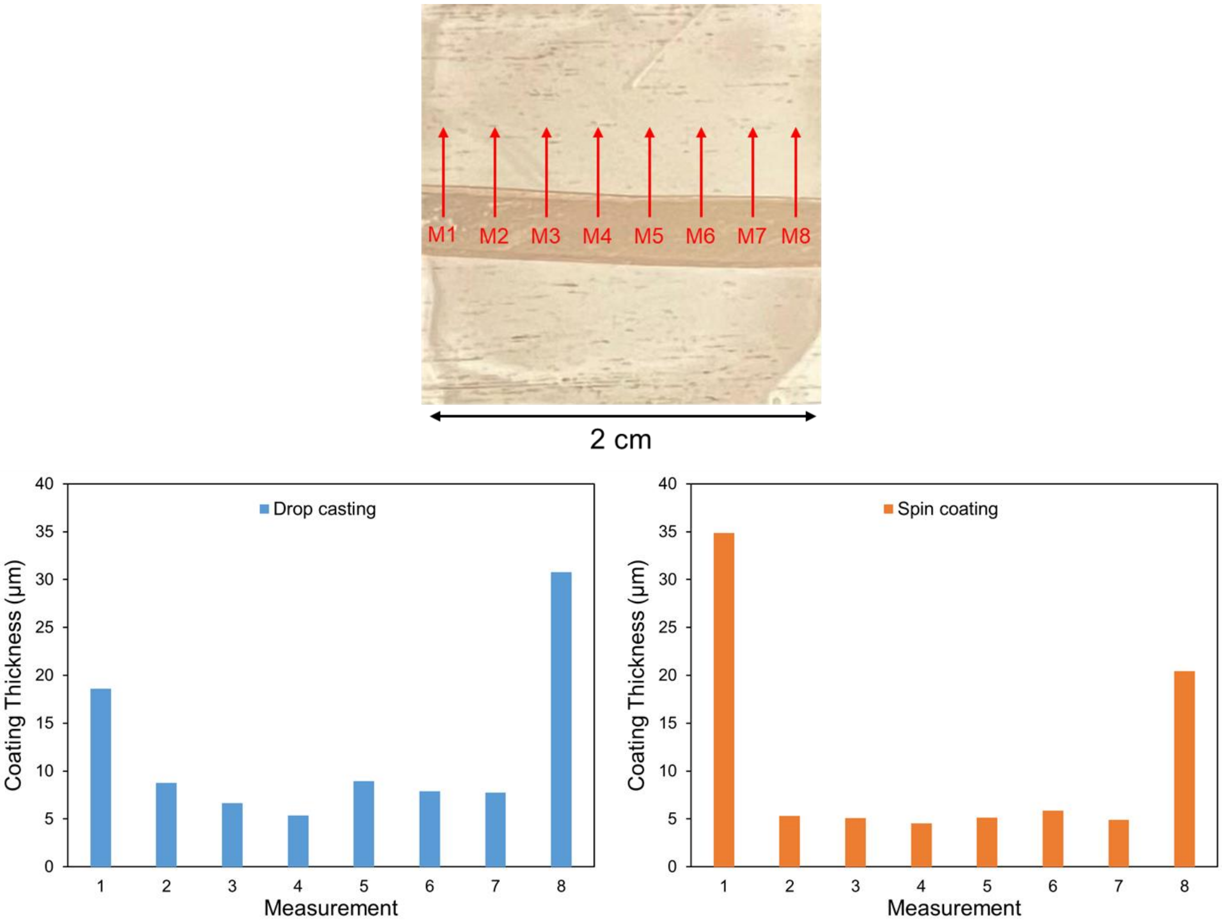

Fig. 2.8. Thickness of the PCL-LS coating measured at different sites across the coated Mg samples (M1-M8).

2.3.1.3 Repeatability of the Fabrication Method

For any protective coating applications, its crucial to assure that the fabrication method used in coating preparation has sufficient repeatability and produces coatings with known thickness every time. To evaluate the repeatability of fabrication methods, PCL-LS coated Mg samples were prepared by drop casting using different solution volumes with different number of layers. The original PCL-LS coating has a bi-layered structure consisting of a PCL/lawsone inner layer and a pure PCL top layer. Two other samples were prepared with 6 (3 PCL/lawsone + 3 PCL) and 10 (5 PCL/lawsone + 5 PCL) layers and the coating thicknesses were measured using the same profilometer as above. Figure 2.9 shows drop casted solution volume versus the obtained coating thickness. It was observed that the coating thickness increased linearly with the increasing of the volume of PCL solution deposited on the substrate. The obtained linear relationship can be used to fabricate coatings with known thickness if needed in future experiments. Besides, the relative standard deviation (RSD) values were all found to be below 10% indicating that the fabrication method has a satisfactory level of repeatability to create coatings with different thicknesses.

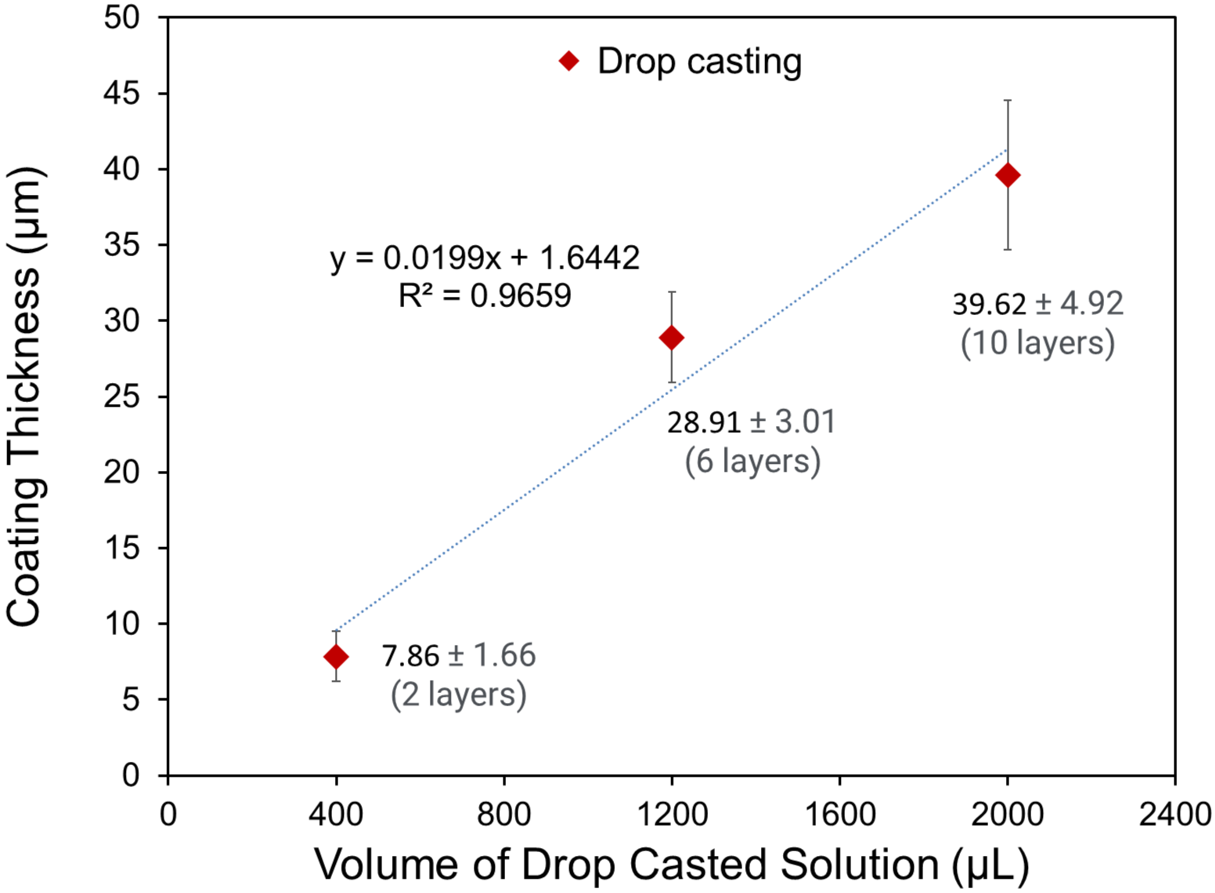

Fig. 2.9. Thickness dependence of the PCL-LS coatings on the volume of drop casted solution

2.3.1.4. Chemical Composition of the Coatings

ATR-FTIR was employed to analyze the chemical compositions of the sample surfaces resulted from pretreatment and coatings. As shown in Figure 2.10, the bare AZ31 surface did not show any distinctive peak, indicating that no chemical groups were present on the surface. After alkaline treatment, a sharp peak at 3700 cm^{-1} corresponding to hydroxyl groups appeared in the spectrum, showing that the $Mg(OH)_2$ layer was formed on the Mg alloy surface [130]. Formation of the oxide layer is necessary to protect the highly susceptible Mg alloy surface against corrosion during the coating procedure. Moreover, the emerged hydroxyl groups on the Mg alloy surface may enhance the adhesion strength of the coatings to the substrate through chemical interaction with coating molecules [120]. The FTIR spectrum of PCL coating presented the characteristic absorption peaks of PCL. The peaks at 2944 cm^{-1}, 2865 cm^{-1}, and 1723 cm^{-1} were assigned to asymmetric CH_2 stretching, symmetric CH_2 stretching, and C=O stretching of PCL, respectively, verifying the presence of PCL coating [131]. The spectrum of PCL-LS composite coating did not show discernible differences compared to the pure PCL spectrum. This might be due to the presence of pure PCL top coatings and a limited penetration depth of ATR-FTIR (less than 1 μm), suppressing the emergence of lawsone characteristic peaks in the spectrum [132, 133].

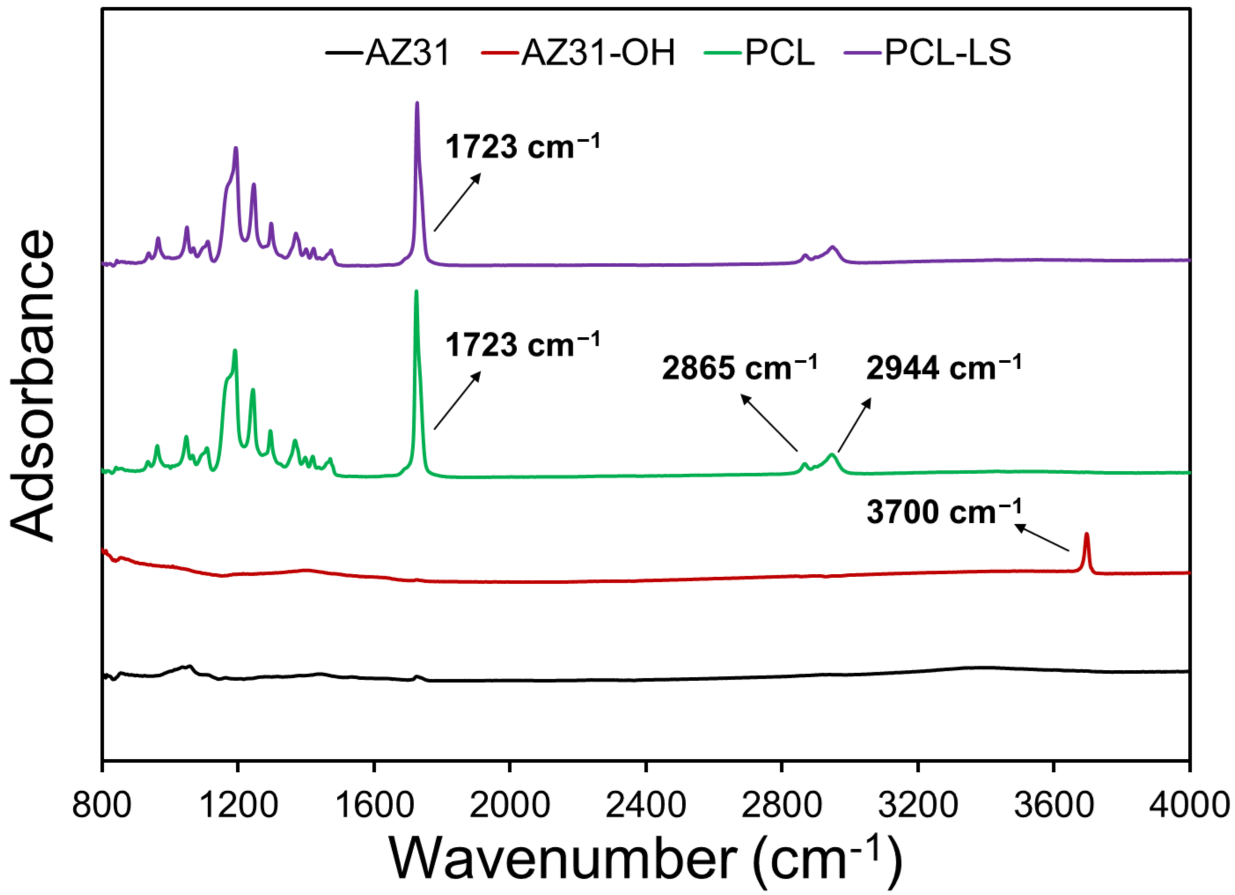

Fig. 2.10. ATR-FTIR spectra of bare, alkaline treated, and coated Mg samples.

2.3.1.5. Wettability Measurement

The wettability of the Mg samples was investigated by the contact angle measurement test with Hank's solution. Figure 2.11 shows the measured contact angles and their representative images. Pristine AZ31 Mg alloy showed a relatively hydrophilic surface with a contact angle of 3.9 ± 1.4°. After alkaline treatment, the contact angle was reduced to 30.5 ± 0.9° due to the presence of abundant hydroxyl groups of the formed $Mg(OH)_2$ layer on the AZ31 surface, showing improved hydrophilicity [134]. In contrast, PCL coated Mg samples clearly exhibited a more hydrophobic surface (nearly round-shaped droplet) with a contact angle value of 96.1 ± 1.6° compared to the uncoated Mg samples. The lawsone entrapment in the PCL (PCL-LS) brought about no significant difference in contact angle, since the PCL top coating is the one that interacts with water molecules. The results of surface morphologies, ATR-FTIR, and contact angle measurement confirmed that all surface modification and coating steps were successfully carried out on the Mg alloy surface.

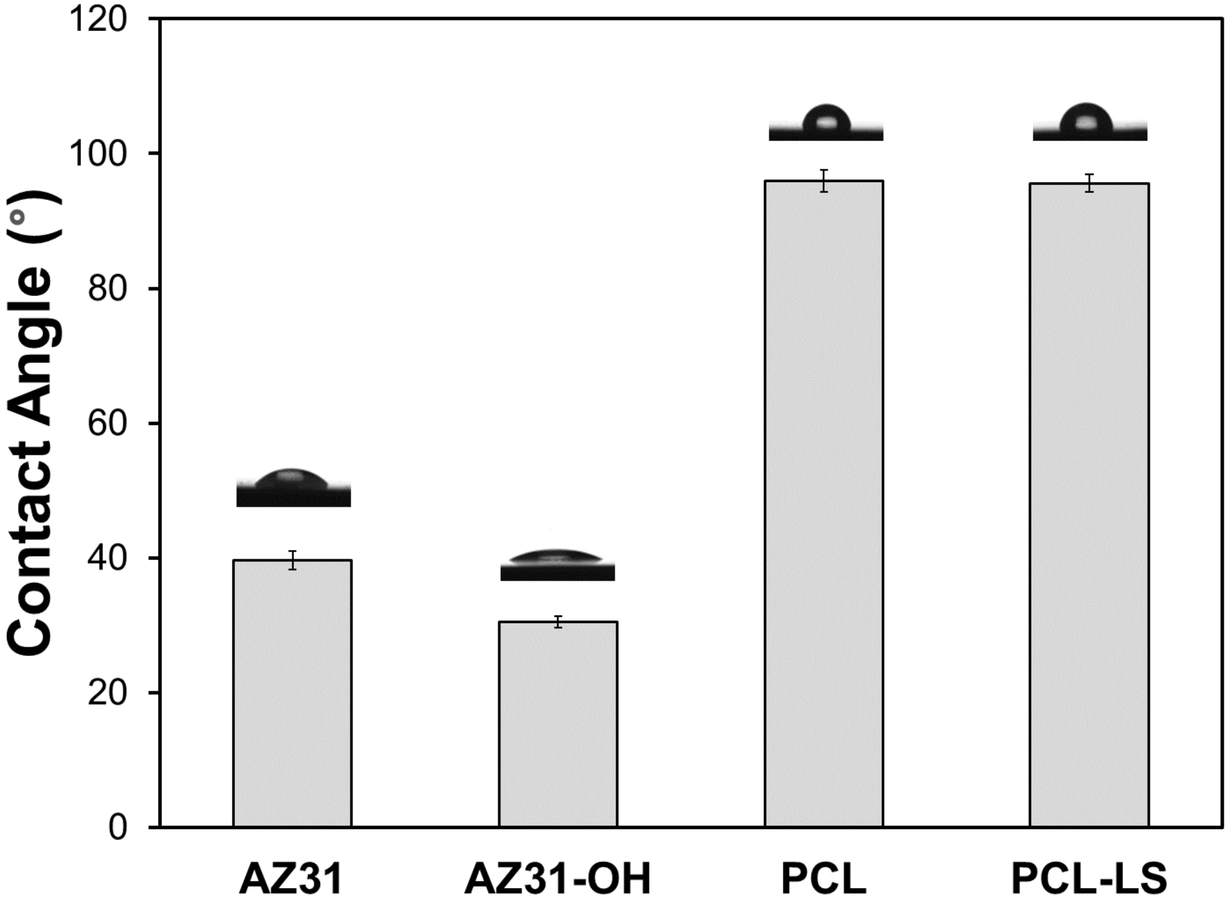

Fig. 2.11. Water contact angle values of bare, alkaline treated, and coated Mg samples.

2.3.1.6. Coating Adhesion Test

Having an adequate adhesion strength to the underlaying substrate is critical for any protective coatings as it determines the functionality and durability of the coating for the intended period of application. Interfacial adhesion between the Mg substrates and the PCL-LS coating was evaluated by the cross-cut adhesion test. Figure 2.12 shows the surface of the PCL-LS coating on Mg alloy substrates before and after tape test. From the photographs after the tape removal, the adhesion strength of the PCL-LS to untreated AZ31 and AZ31-OH were classified as 3B and 4B, respectively. Compared to bare AZ31, AZ31-OH showed an improved adhesiveness to the PCL-LS coating. This is most likely due to the emerged numerous hydroxyl groups on the metal surface resulted from the alkaline pretreatment, which in turns can chemically interact with COOH groups of PCL and improve the coating/substrate interfacial adhesion [135]. The results suggested that the PCL-LS coating has acceptable adhesion strength on the alkaline treated AZ31substrate for biomedical applications.

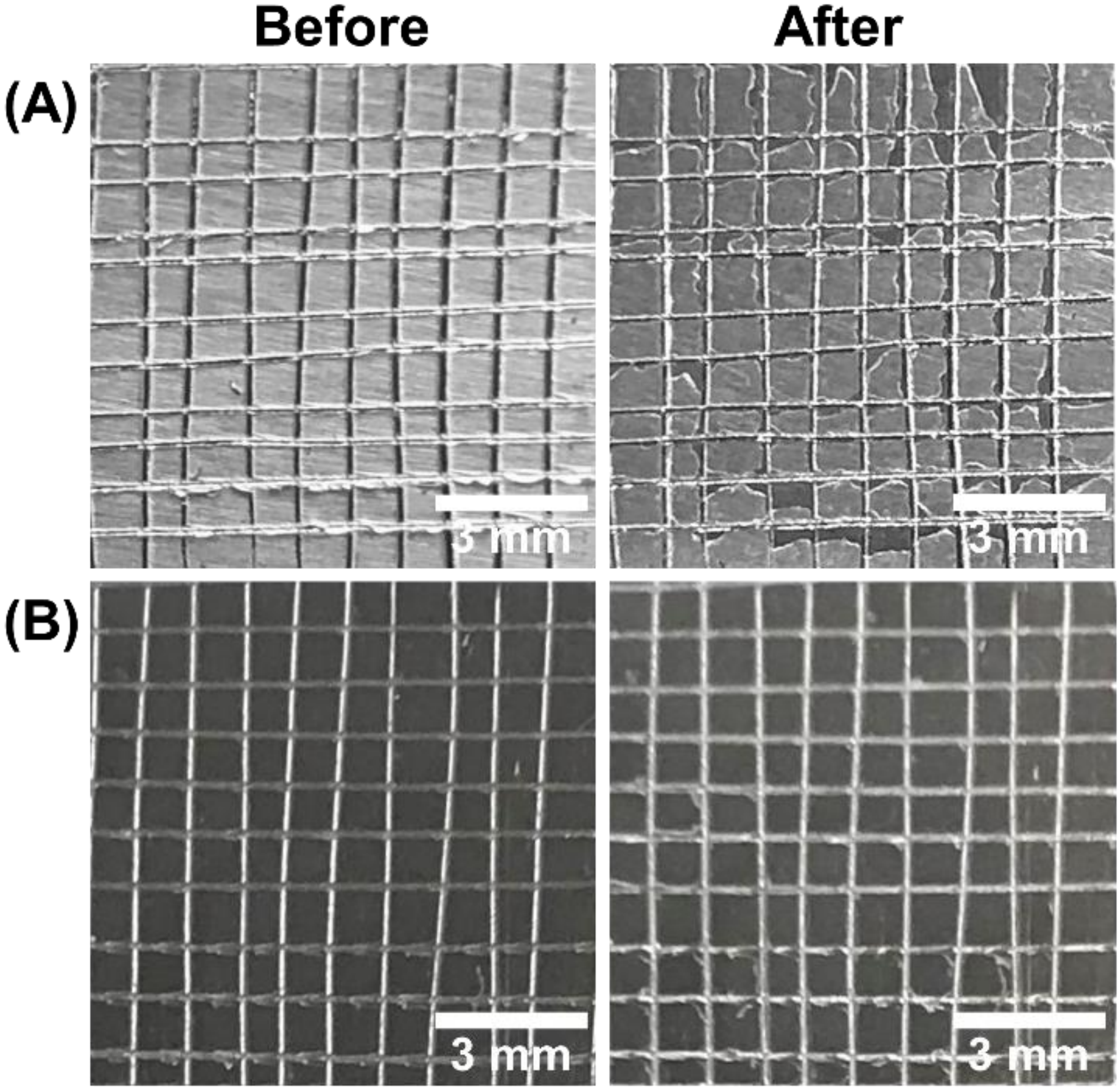

Fig. 2.12. Photographs of the PCL-LS coating on (A) untreated and (B) alkaline-treated AZ31 substrate before and after the cross-cut adhesion test.

2.3.2. *In vitro* Corrosion Studies

2.3.2.1. Open Circuit Potential and Polarization Measurements

The electrochemical measurements were performed in Hank's solution to further investigate the corrosion resistance of each sample using OCP and PP (Tafel plot) measurements. Figure 2.13A displays the OCP spectra of all samples for 30 min. The OCP curves reflect the potential change of the electrode surface in electrolyte without externally applied voltage [136]. Generally, a more positive OCP value means the surface is nobler and therefore, less susceptible to corrosion [137]. Bare AZ31 sample showed some fluctuation and finally stabilized at a quite cathodic/negative OCP value of -1.448 V. The fluctuating of OCP is associated with the active corrosion and product formation/dissolution taking place on the AZ31 surface [138]. The final OCP of AZ31-OH and the PCL increased to more positive values of -1.412 and -1.401, respectively, implying the more stable surfaces of these samples compared to the AZ31 sample. The OCP values were further going up toward more positive value by adding the inhibitor to the PCL coatings and reached to the highest value of -1.279 V for the PCL-LS coating. The more positive OCP values achieved by the incorporation of lawsone can slow down the cathodic hydrogen evolution and subsequently, the overall rate of corrosion reaction [139].

Potentiodymanic polarization curves can provide invaluable information about the corrosion process as well as the corrosion rate of the substrate being tested. The Tafel curves of AZ31, alkaline treated, and coated samples are shown in Figure 2.5B, and the corresponding values of E_{corr}, I_{corr}, and IE are listed in Table 2.4. The pristine AZ31 substrate exhibited a typical curve of active metals corrosion with a low E_{corr} of -1.456 V and a high I_{corr} of 3.71×10^{-6} A.cm^{-2}. After alkaline treatment, the curve of AZ31-OH slightly shifted toward more positive potentials and showed a decreased I_{corr} of 8.92×10^{-7} A.cm^{-2}. This is mainly because of the formed $Mg(OH)_2$

protective layer that can isolate the bulk substrate from the corrosion medium. The presence of sharp current changes on the polarization curves of AZ31 (at -1.41 V) and AZ31-OH (at -1.331 V), indicated the breakdown of the substrates due to the possible pitting corrosion [120]. No sign of pitting corrosion was observed on the Tafel plots of coated samples. The PCL coated sample showed an I_{corr} value of 5.34×10^{-7} A.cm^{-2}, which was much lower than that of the uncoated Mg substrates. This is because of the physical barrier effect of the PCL coating against the penetration of the corrosive electrolyte, resulting in enhanced corrosion resistance of the sample [140]. Incorporation of lawsone into the PCL coating, remarkably shifted the E_{corr} values toward a more positive potential of -1.288 V. A more positive E_{corr} values implies that the surface has become nobler and therefore, higher potential driving forces are required to initiate the corrosion on the sample [141]. This suggests that the addition of the inhibitor can further improve the corrosion resistance of the PCL coating. As listed in Table 2.4, PCL-LS exhibited the highest IE of 98.3% and the lowest I_{corr} of 5.98×10^{-8} A.cm^{-2} among all samples, which is about two orders of magnitude lower than that of AZ31.

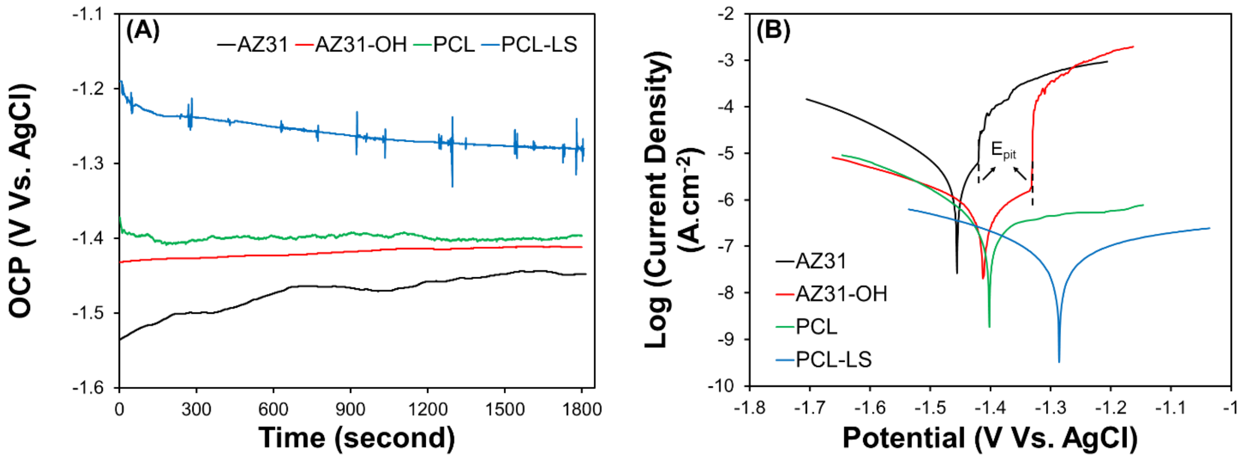

Fig. 2.13. Open circuit potential curves (A) and potentiodynamic polarization curves (B) of bare, alkaline treated, and coated Mg samples performed in Hank's solution.

Table 2.4. The corrosion potentials (E_{corr}), corrosion current densities (i_{corr}), and corrosion inhibition efficiency (IE) of the Mg samples obtained from PP curves in Hank's solution by Tafel methods.

Samples	E_{corr} (V)	I_{corr} (A/cm^2)	IE (%)
AZ31	-1.45	3.7×10^{-6}	-
AZ31-OH	-1.41	8.9×10^{-7}	75.9
PCL	-1.39	5.3×10^{-7}	85.6
PCL-LS	-1.28	5.9×10^{-8}	98.3

2.3.2.2. EIS measurements

EIS was utilized as a powerful technique to further investigate the corrosion protection performance of the coatings and corrosion mechanism [142]. Nyquist plots and Bode plots (impedance and phase angle plots) of EIS spectra for the tested samples are presented in Figure 2.6. Generally, the diameter of the semicircle in the Nyquist plot has been associated with the corrosion resistance of a sample, wherein a larger arc means superior corrosion protective properties [143]. As shown in Figure 2.14A-B, the PCL showed a much larger capacitive loop compared to that of AZ31 and AZ31-OH samples, indicating the enhancement of corrosion resistance by applying the PCL coating on AZ31 surfaces. The diameter of the capacitive loop of PCL-LS was furthered increased, suggesting that the incorporation of lawsone enhances the corrosion resistance of the coating more effectively than pure PCL. It is well known that the value of impedance modulus at the lowest-frequency region ($|Z|_{0.01\ Hz}$) of the Bode impedance plot can be used as a semi-quantitative indicator of the anti-corrosive properties of a sample [144]. As shown in Figure 2.6C, the $|Z|_{0.1Hz}$ values of the tested samples are in the following order: AZ31 < AZ31-OH < PCL < PCL-LS, which was consistent with the I_{corr} values obtained from PP tests.

From the Bode-phase plots in Figure 2.14D, it can be noted that the broad peak at medium-frequency range is more pronounced for AZ31-OH that that of bare AZ31, which reflects the improvement of the oxide layer [145]. Besides, both PCL and PCL-LS showed high phase angles at the initial high-frequency region, which are generally attributed to the coating layers and indicate the barrier performance of the coatings [146]. Compared with PCL coating, PCL-LS exhibited a broader high-frequency phase and kept higher impedance values over a wider frequency range, which indicates the superior barrier performance of the PCL-LS coating [147]. Two equivalent electrical circuits (EECs) applied to fit the EIS data are shown in Figure 2.14A-B (insets). The EIS responses of the bare AZ31 and AZ31-OH were fitted with one time constant, indicating that only one kinetic process occurred during the corrosion process. The EEC was expressed as $R_s(CPE_{dl}\ R_{ct}\ R_LL)$, where R_s and R_{ct} represent the electrolyte and interfacial charge transfer resistance, while CPE_{dl} reflects the capacitive behavior of the electric double layer. Besides, an R_L-L component was implemented to reflect the pseudo-inductive behavior at the low-frequency region associate with dissolution and pitting corrosion [148]. In case of the coated samples, the EIS spectra were described by three time constants and the employed ECC consists of three equivalent circuits in series expressed as $Rs(CPE_{out}\ R_{out})(CPE_{in}\ R_{in})(CPE_{dl}\ R_{ct})$. The resistance and capacitive behavior of the polymeric coatings were divided into outer and inner parts shown by R_{out}/CPE_{out} and R_{in}/CPE_{in}, respectively, to account for their high thicknesses. In all EEC models, constant-phase elements were introduced instead of ideal capacitors to take the intrinsic inhomogeneity of the coating and metal surface into account and minimize the fitting error [149]. Each CPE element consists of two other parameters; Y0 (admittance) and n (exponent) [150]. The obtained electrochemical parameters from each model are presented in Table 2.5. As listed in Table 2.5, the

PCL-LS showed the highest value of R_{ct} (50.2 kΩ.cm^2) and the lowest value of CPE_{dl} (2.20×10^{-9} F.cm^2) among all samples, suggesting the best corrosion protection performance of PCL-LS [27].

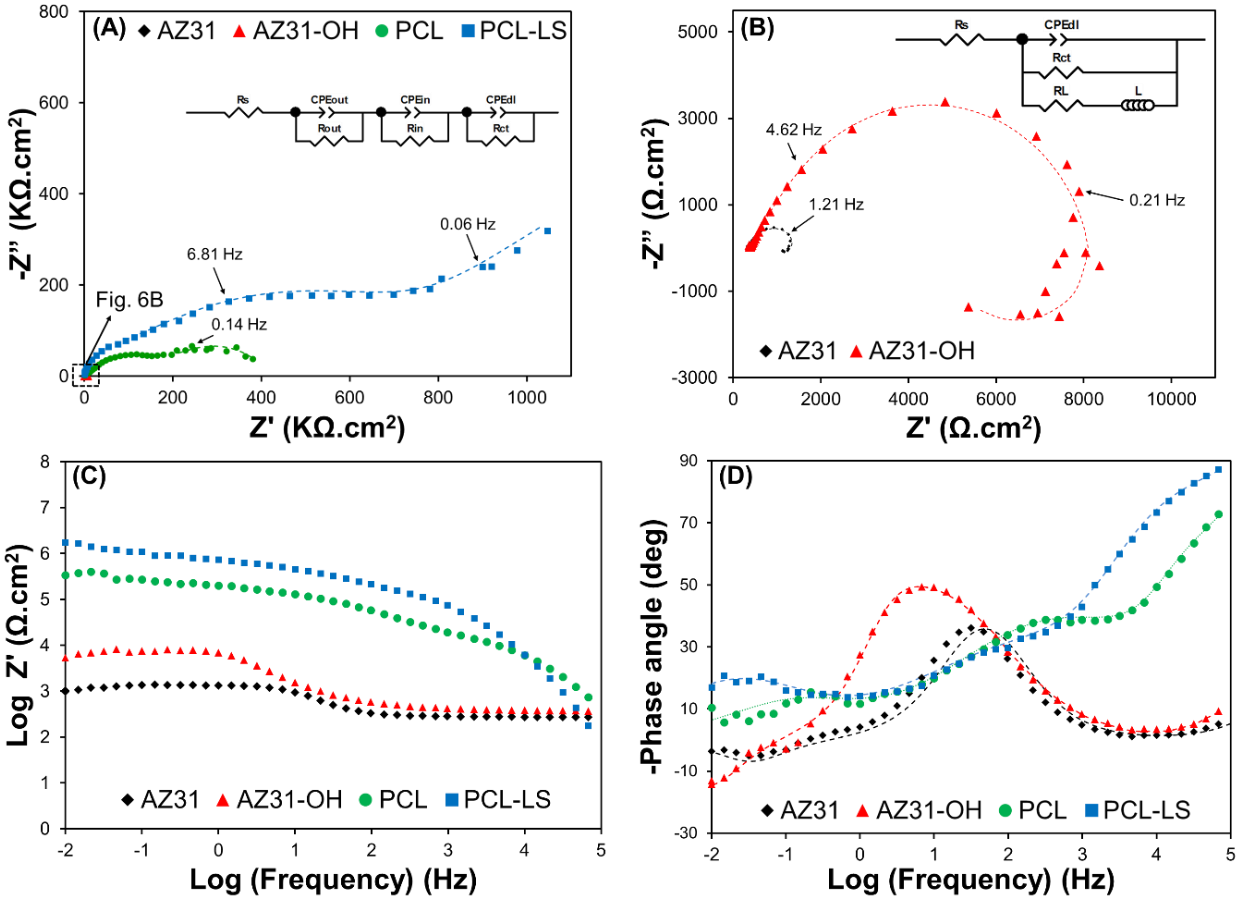

Fig. 2.14. EIS spectra of Mg samples performed in Hank's solution; Nyquist plots (A) and (B) (Insets: EC models employed for EIS data fitting), Bode-impedance plots (C), and Bode-phase plots (D).

EIS, as a non-destructive technique, can allow us to continuously monitor the corrosion resistance properties of a sample over a long period, as it does not perturb the system significantly due to its steady state measurement [151]. The effect of lawsone inhibitor on long-term protection performance of the coatings was studied through EIS measurements by comparing barrier properties of PCL and PCL-LS coatings during a 7-day immersion period in Hank's solution. Bode plots of PCL and PCL-LS coatings after 1,3, and 7 days of immersion and the corresponding fitted

EIS parameters are presented in Figure 2.15A-D and Table 2.5, respectively. As can be seen in Figure 2.15A, the phase angle of PCL at the high-frequency region started to sharply decline with increasing the immersion time, indicating diffusion of water and corrosive species into the PCL film and thus, rapid deterioration of barrier properties [152]. As immersion continued, a broad time constant in the medium-frequency range became more visible (at about 1-10 Hz), which is attributed to two combined time constants belong to the pore resistance of the coating and the oxide layer on the Mg alloy [145]. Moreover, an inductive loop appeared on the PCL spectra (at about 10^{-2} Hz), which is attributed to the pitting corrosion and adsorption/desorption of intermediates on the metal substrate during immersion [151]. The Bode plot of the PCL-LS (Figure 2.15C) showed a completely different trend. In contrast to the PCL, the phase angles of PCL-LS coating at the high-frequency region remained quite stable with much less variation during the immersion period. Besides, no inductive loop was observed in the PCL-LS spectra even after 7 days of immersion, proving the presence of a stable corrosion protective layer on the metal surface [153].

Variation of log $|Z|_{0.01Hz}$ for the PCL and PCL-LS over immersion time can be seen from Bode-impedance plots, which can reflect the overall corrosion resistance of the coated samples. For the PCL coating (Figure 2.15B), the $|Z|_{0.01Hz}$ value continued to decrease over 7 days of immersion test. With the increase of immersion time, PCL coating started to gradually lose it barrier properties due to the penetration of corrosive electrolyte into the coatings, resulting in a steady decrease of $|Z|_{0.01Hz}$ during the test [124]. It should be mentioned that the final $|Z|_{0.01Hz}$ value was still higher compared to uncoated Mg samples at the end of the immersion test. In contrast to PCL coating, PCL-LS (Figure 2.15D) could maintain stable corrosion resistance and showed a better performance with a much lower reduction in $|Z|_{0.1Hz}$ values during 7 days of immersion. The results suggest that the lawsone inhibitor could effectively mitigate the development of corrosion and provide durable protection with long-term stability.

According to Table 2.5, the R_{ct}, R_{out}, and R_{in} values of PCL coatings all declined during the whole immersion time, reveling the successive deterioration of the physical barrier properties of the pure PCL coating over time [147]. In the case of PCL-LS coating, R_{out} increased from 2.48×10^6 to 6.84×10^6 $\Omega.cm^2$ after 24 h of immersion. Moreover, as the exposure time prolonged, n values related to CPE_{dl} continuously rose, indicating that the Mg alloy surface is becoming smoother by time. That is most likely due to the formation of insoluble metal-lawsone complexes upon the release of lawsone and filling of the active corroding sites on the Mg substrate [154]. It should be also noted that, at the end of 7-day immersion time, the R_{ct} value of PCL-LS coating is much higher than those of uncoated Mg samples and the pure PCL coating.

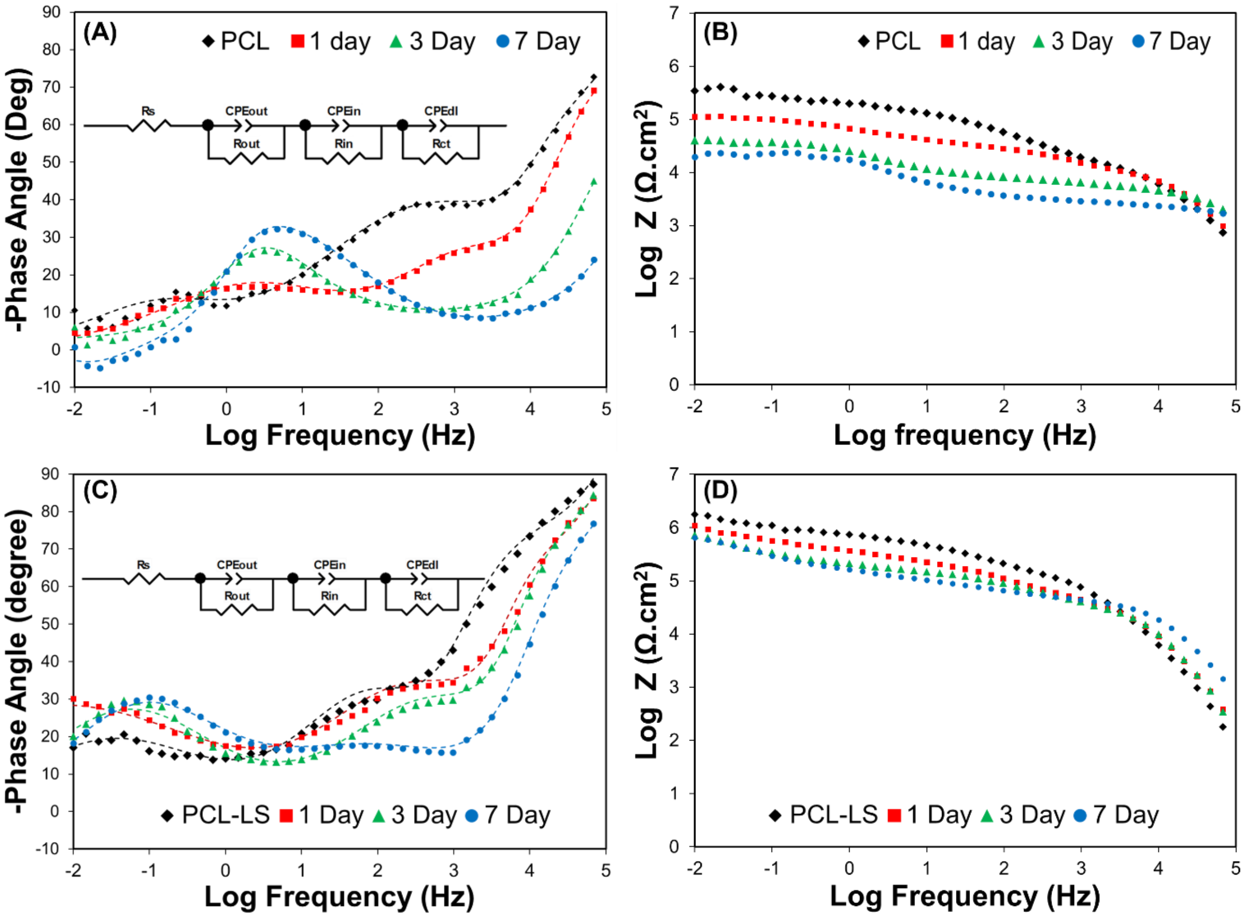

Fig. 2.15. Evolution of Bode plots spectra of the coated Mg samples performed in Hank's solution; Nyquist plots (A) and (B) (Insets: EC models employed for data fitting), Bode-impedance plots (C), and Bode-phase plots (D).

Table 2.5. Representative fitting results of EIS spectra of Mg samples using appropriate equivalent electrical circuits.

Samples	Time (day)	R_{outer} (Ω.cm^2)	Q_{outer} (F.cm^{-2})	n_1	R_{inner} (Ω.cm^2)	Q_{inner} (F.cm^{-2})	n_2	R_{ct} (Ω.cm^2)	Q_{dl} (F.cm^{-2})	n_3	R_L (Ω.cm^2)	L (H.cm^2)	Chi^2
AZ31	-	-	-	-	-	-	-	1.34×10^{3}	5.81×10^{-5}	0.78	1.94×10^{3}	3.61×10^{2}	0.0067
AZ31-OH	-	-	-	-	-	-	-	6.82×10^{3}	9.80×10^{-6}	0.6	4.23×10^{3}	1.24×10^{4}	0.0206
PCL	-	1.84×10^{5}	2.99×10^{-7}	0.96	2.30×10^{5}	7.59×10^{-6}	0.61	1.56×10^{4}	3.98×10^{-9}	0.96	-	-	0.0047
	1	9.43×10^{4}	5.61×10^{-6}	0.52	2.3040×10^{4}	2.46×10^{-7}	0.64	1.35×10^{4}	2.00×10^{-9}	0.96	-	-	0.0005
	3	9.15×10^{4}	4.45×10^{-5}	0.27	2.30×10^{4}	7.69×10^{-6}	0.82	1.09×10^{4}	4.56×10^{-9}	0.88	-	-	0.0013
	7	5.25×10^{4}	1.56×10^{-8}	0.28	1.30×10^{4}	8.13×10^{-6}	0.97	5.84×10^{3}	9.68×10^{-6}	0.68	-	-	0.0074
PCL-LS	-	2.48×10^{6}	2.01×10^{-6}	0.53	5.24×10^{5}	6.52×10^{-8}	0.69	5.02×10^{4}	2.20×10^{-9}	0.94	-	-	0.0044
	1	6.84×10^{6}	2.16×10^{-6}	0.47	3.96×10^{5}	6.77×10^{-8}	0.68	3.33×10^{4}	1.14×10^{-9}	0.99	-	-	0.0028
	3	1.17×10^{6}	2.89×10^{-6}	0.59	1.43×10^{5}	1.47×10^{-7}	0.61	2.11×10^{4}	8.61×10^{-10}	0.99	-	-	0.0014
	7	8.63×10^{5}	4.64×10^{-6}	0.63	1.01×10^{5}	8.76×10^{-7}	0.48	2.05×10^{4}	1.00×10^{-9}	0.93	-	-	0.0006

2.3.2.3 Effect of Coating Thickness

The effect of coating thickness on the corrosion resistance properties of the PCL-LS coated sample was evaluated by PP in Hank's solution. Tafel plots of PCL-LS coated Mg alloy with different coating thicknesses are shown in Figure 2.16, and the corresponding analysis results are listed in Table 2.6. It can be seen that the corrosion current I_{corr} values decreased when the coating thickness increased from 7.86 ± 1.66 µm to 28.91 ± 3.01 µm µm and further to 39.63 ± 4.92 µm µm. No obvious trend was observed between E_{corr} values, and the thickness of the PCL-LS coating applied on the Mg samples. Overall, the results suggested that the protection effect of the PCL-LS coating on the Mg alloy was enhanced with the increasing of the coating thickness, which in turn can slow down the degradation rate of AZ31 alloy in Hank's solution. The enhancement effect of thickness on corrosion degradation rate of AZ31 alloy can be employed to design and fabricate Mg-based implants with tailored corrosion degradation rates based on the implantation site and the intended application which is a great advantage for the developed PCL-LS protective coating.

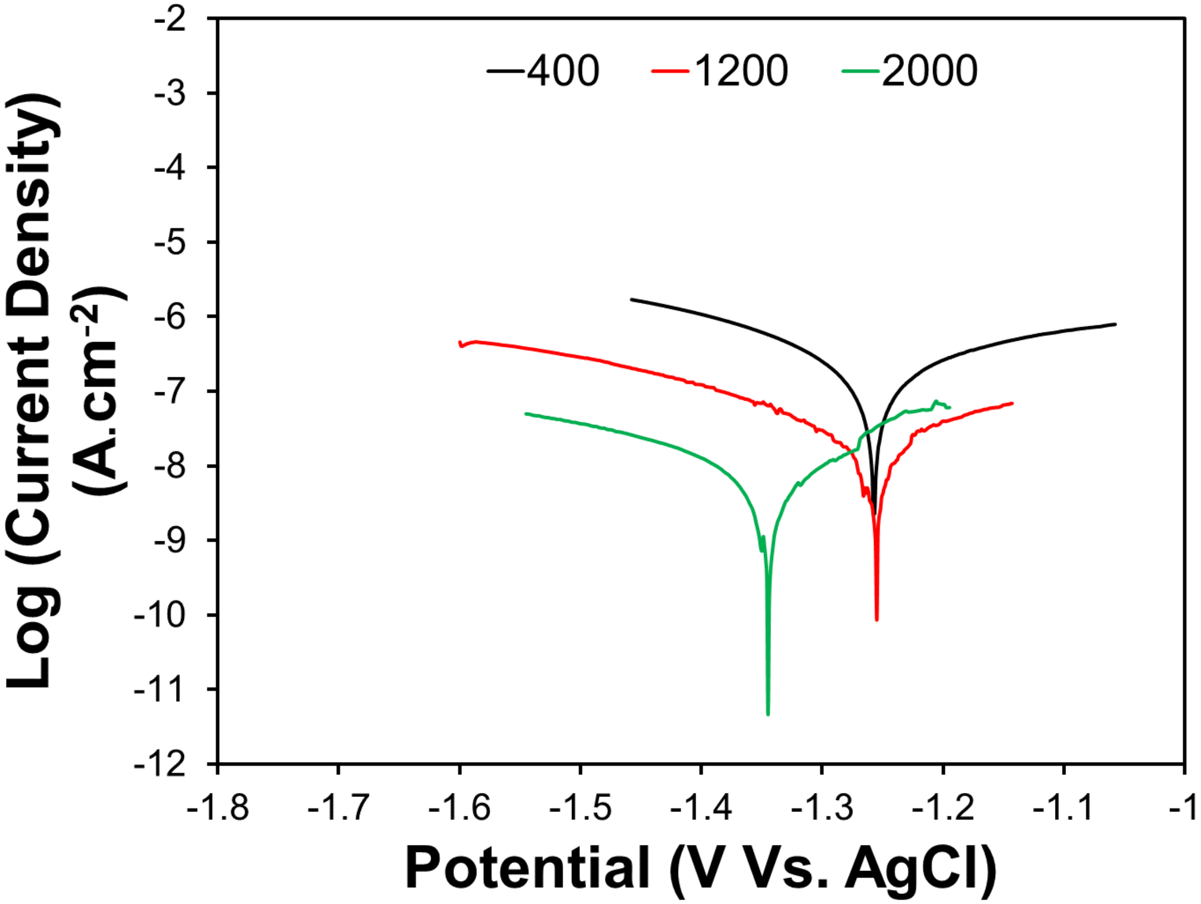

Fig. 2.16. Tafel curves of the PCL-LS coated Mg samples with varying thicknesses performed in Hank's solution.

Table 2.6. Corrosion potentials (E_{corr}), corrosion current densities (I_{corr}), and corrosion rate values of the PCL-LS coated Mg samples with varying thicknesses performed in Hank's solution.

Thickness (µm)	7.8	28.9	39.6
E_{corr} (V)	-1.258	-1.255	-1.345
I_{corr} (A/cm^2)	6.8×10^{-8}	1.8×10^{-8}	5.1×10^{-9}

2.3.2.4 Effect of Electrolyte

The effect of electrolyte corrosiveness on the corrosion resistance of the AZ31 alloy was investigated by PP test. Chloride ions are known to be the most aggressive ions present in the physiological environment and Hank's solution that can dissolve the natural protective oxide layers and induce corrosion in almost all types of metals including Mg alloys. Hank's solution, the electrolyte used in the electrochemical and *in vitro immersion* tests, contains 8 g/L NaCl in its composition. To create electrolytes with different levels of corrosiveness, we added 16, 40, and 80 g/L NaCl to the original recipe of Hank's solution and labeled them as Hank-16, Hank-40, and Hank 80, respectively. Tafel plots of PCL-LS coated Mg alloy performed in different electrolytes are shown in Figure 2.17, and the corresponding results are summarized in Table 2.7. I_{corr} was increased with the increased NaCl concentrations. The increase in I_{corr} often can be related to the persisting hydrogen evolution process. The anodic dissolution process of Mg alloys includes the formation and breakdown of protective surface film as well as the exposure of the dissolved surface. The adsorption of Cl^{-} on the weak part of the surface film layer accelerates the dissolution of the surface film during the anodic polarization, leading to the accelerations of Mg dissolution [155]. Besides, the E_{corr} values shifted toward more negative potential when the concentration of NaCl was increased in the Hank's solution, indicating the higher tendency of the samples to be corroded at increased levels of NaCl.

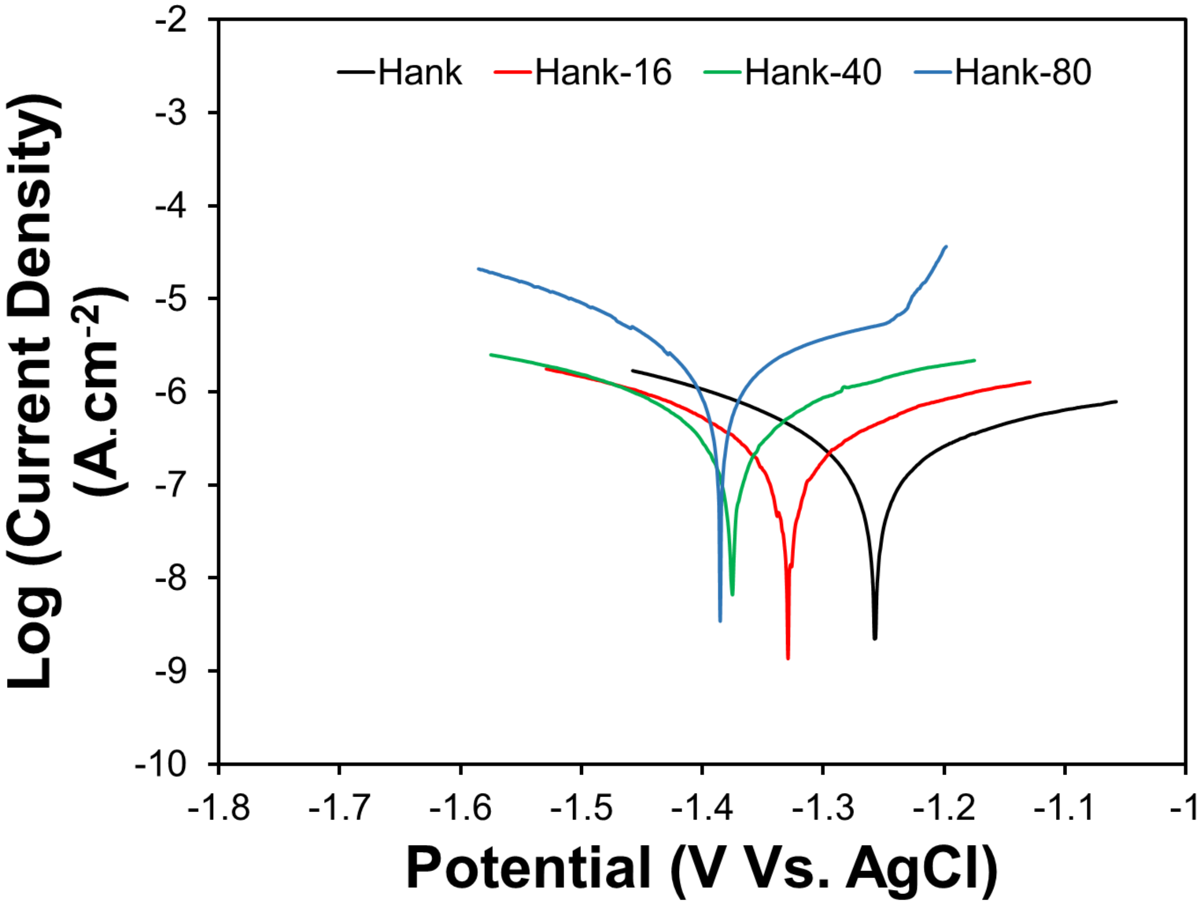

Fig. 2.17. Tafel curves of the PCL-LS coated Mg sample obtained in Hank's solutions contaning varying NaCl concentrations.

Table 2.7. Corrosion potentials (E_{corr}) and corrosion current densities (I_{corr}) values of the PCL-LS coated Mg samples performed in Hank's solutions containing varying NaCl concentrations.

	Hank	Hank-16	Hank-40	Hank-80
E_{corr} (V)	-1.258	-1.329	-1.375	-1.385
I_{corr} (A/cm^2)	6.8×10^{-8}	2.2×10^{-7}	5.0×10^{-7}	2.2×10^{-6}

2.3.2.5. Immersion Corrosion Tests

Figure 2.18 exhibits the post-corrosion SEM surface morphologies of Mg samples. After being immersed in Hank's solution for 7 days, the uncoated AZ31 and AZ31-OH samples displayed highly cracked surfaces with the presence of accumulated corrosion products on them, indicating that both samples underwent severe corrosion during the immersion test. Similarly, a high amount of corrosion products was observed on the PCL surface at the end of the immersion period, showing an insufficient corrosion protection performance by the pure PCL coating on the Mg alloy. Remarkably, the PCL-LS surface remained almost intact after 7 days of immersion and showed the least sign of corrosion with very minor defects on the polymer coating. The SEM observations suggested that the presence of lawsone mitigates the corrosion damages of the PCL coating during immersion and improved the barrier properties against the penetration of water and corrosive specious through the coating.

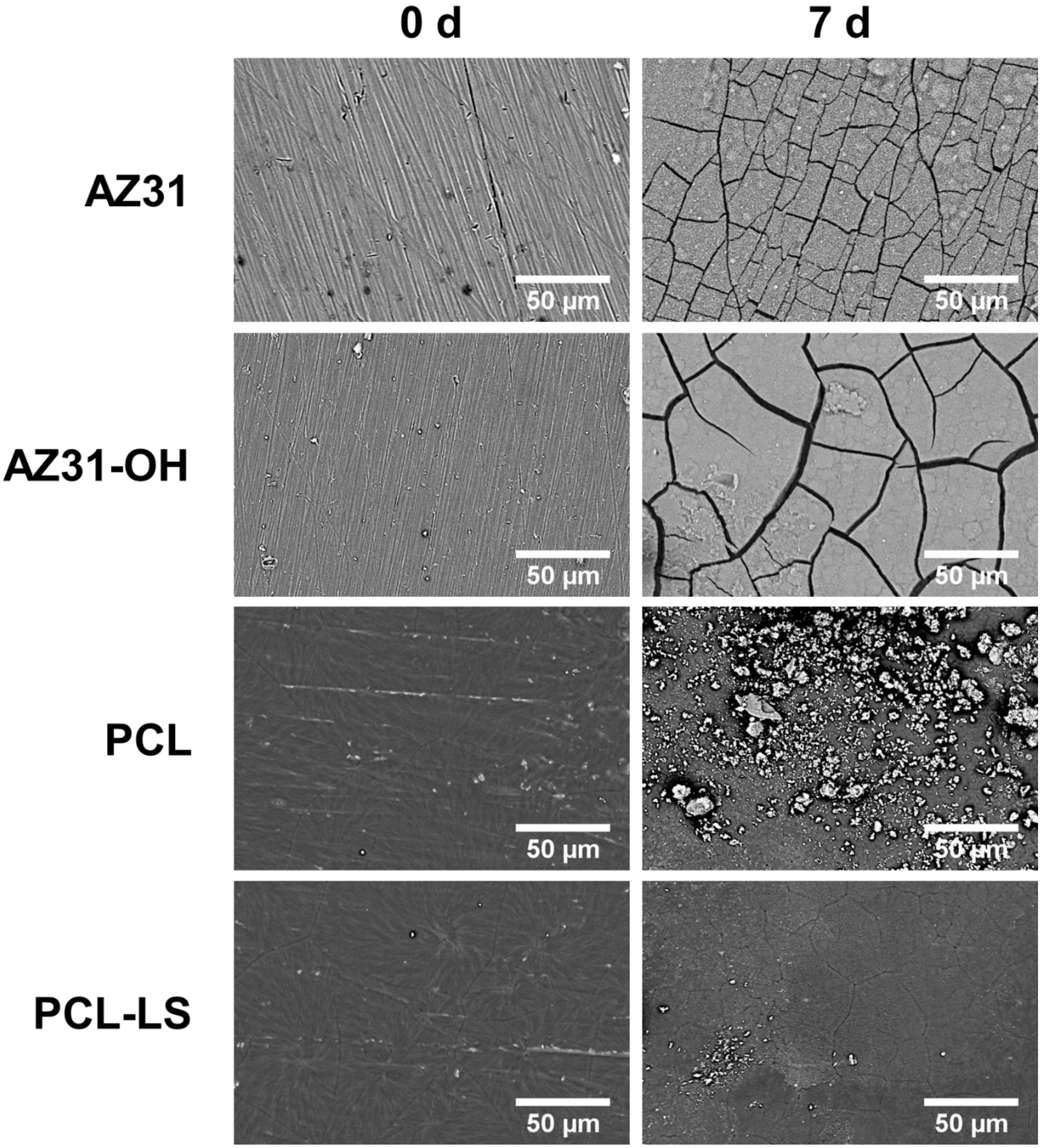

Fig. 2.18. SEM images of bare, alkaline treated, and coated Mg samples before and after immersion in Hank's solution for 7 days at 37 °C.

To further evaluate the long-term degradation of Mg samples, *in vitro* immersion studies were performed as a reliable measurement in addition to the typical electrochemical corrosion tests [156]. Corrosion of Mg alloys in aqueous electrolytes co-occurs with the generation of hydrogen gas and increment of pH value as per the below equation [157]:

$$Mg + 2H_2O \rightarrow Mg^{2+} + 2OH^{-} + H_2\,(g)$$

It means the corrosion of each mole of Mg atom, results in the generation of one mole of hydrogen gas and two moles of OH^- anions. Therefore, monitoring the hydrogen evolution and pH value variation can provide precise information about the Mg corrosion as well as the protection efficiency of a coating on the Mg surface. Figure 2.19A-B presents the variation in the hydrogen evolution volume and pH value during the immersion period of all experimental samples. As shown in Figure 2.19A, the pristine AZ31 substrate showed a quick increase in the volume of evolved hydrogen and culminated to 7.92 ± 0.67 $mL.cm^{-2}$ after 7 days of immersion, showing a very high reactivity and degradation rate of bare AZ31. For the AZ31-OH sample, the average of H_2 evolution rate within the first two days (0.41 ± 0.19 $mL.cm^{-2}.day^{-1}$) was much slower than that of the pristine AZ31 substrate (1.20 ± 0.17 $mL.cm^{-2}.day^{-1}$). After 2 days, it started to increase, and the evolved hydrogen reached a final volume of 6.10 ± 0.84 $mL.cm^{-2}$ at the end of 7-day immersion. The slower rate at the initial stages is attributed to the presence of the protective $Mg(OH)_2$ layer resulted from alkaline treatment. However, in the presence of chloride ions, this layer will be converted into $MgCl_2$, which is less stable in aqueous solutions than $Mg(OH)_2$, increasing the corrosion rate [102]. PCL displayed a total hydrogen evolution volume of 3.025 ± 0.31 $mL.cm^{-2}$ after 7 days, which was much lower compared to bare AZ31 and AZ31-OH samples. This implies the PCL coating can provide steady corrosion protection by acting as a barrier layer to inhibit the water/electrolyte diffusing into the substrate. The accumulated hydrogen volume of PCL-LS further decreased to 1.25 ± 0.28 $mL.cm^{-2}$ in, showing the highest corrosion protection of PCL-LS coating among all tested samples.

The trend of pH changes (Figure 2.19B) was consistent with the hydrogen evolution results. The AZ31 exhibited a sharp rise in pH from about 7.4 to above 8.8 within the first day of immersion and reached to 10.88 ± 0.19 at the end. Although being successful in suppressing hydrogen generation at initial stages, the AZ31-OH sample did not show noticeably lower pH values than the AZ31 over the whole testing period. This might be due to the dissolution of the passive $Mg(OH)_2$ layer into the media, resulting in OH^- release and increase in pH values [158]. The pH values of the PCL and PCL-LS at the end of the immersion period were 8.57 ± 0.26 and 8.16 ± 0.10, respectively, which are much lower than that of uncoated Mg samples. It indicates that these coated samples were stable and did not undergo severe corrosion during immersion. Overall, the results of hydrogen evolution and pH change tests demonstrated that the corrosion resistance of Mg alloy was effectively improved by PCL coating and more significantly after incorporation of lawsone into the coating formulation.

ATR-FTIR was used to investigate the compositions of corrosion products after immersion for 7 days in Hank's solution. As displayed in Figure 2.20, the characteristic peaks for PO_4^{3-} appeared in the spectra of all samples at 991 cm^{-1}, indicating that the corrosion products are mainly phosphate [159, 160]. The intensities of these peaks are less pronounced in the alkaline treated and coated Mg samples, indicating the better anti-corrosion properties of them compared to AZ31. Moreover, the presence of sharp characteristic peaks at 1723 cm^{-1} confirmed the existence of PCL coatings on the Mg samples after 7 days of immersion. It is worth mentioning that the intensity of the characteristic peak was higher in PCL-LS sample compared to the pure PCL coating. This indicates that in the absence of lawsone and its corrosion inhibition capability, the PCL coating degrades more rapidly within the immersion period.

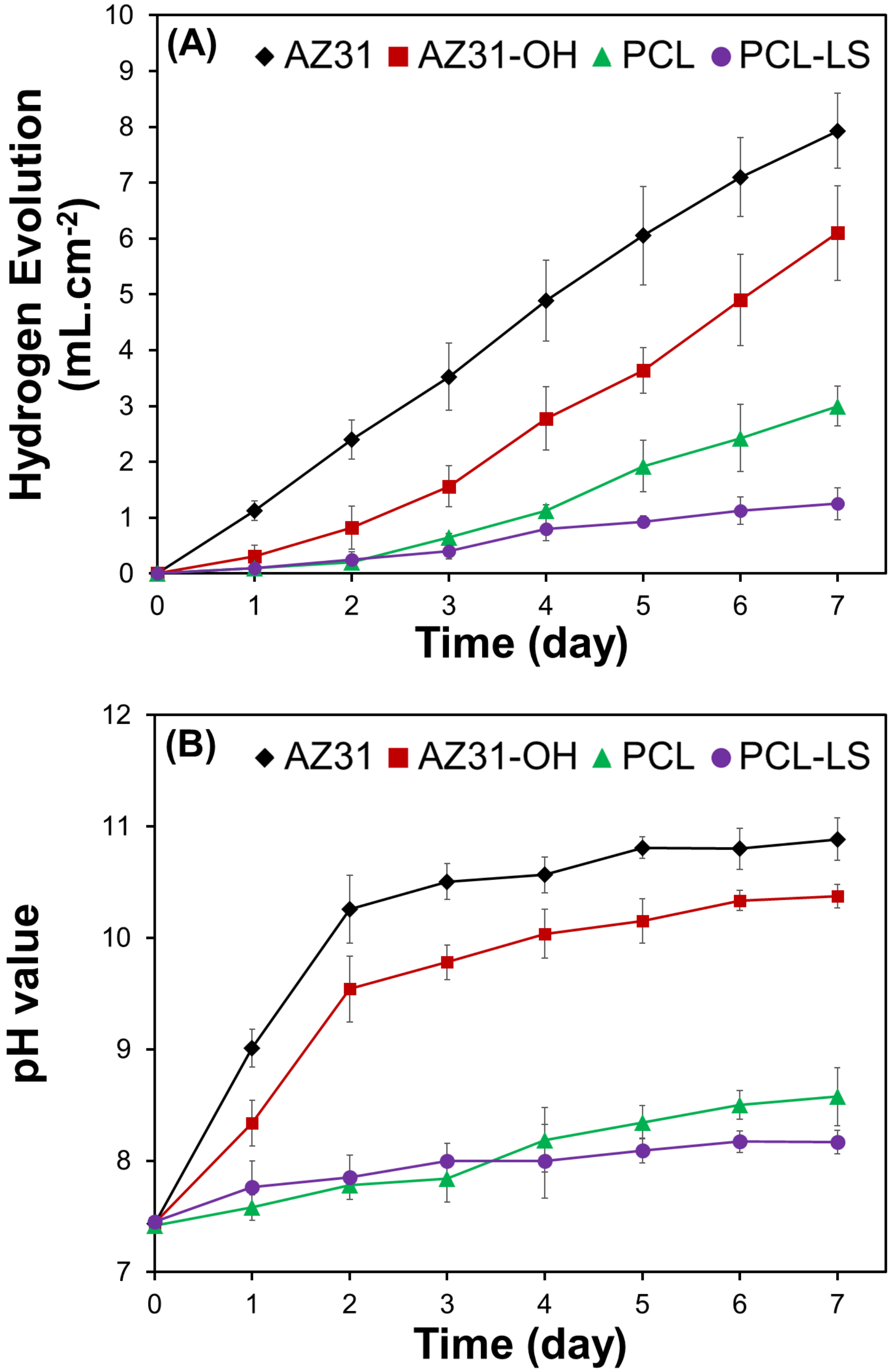

Fig. 2.19. Variation in hydrogen evolution volume (A), pH value (B) of each group during immersion in Hank’s solution at 37 °C for 7 days.

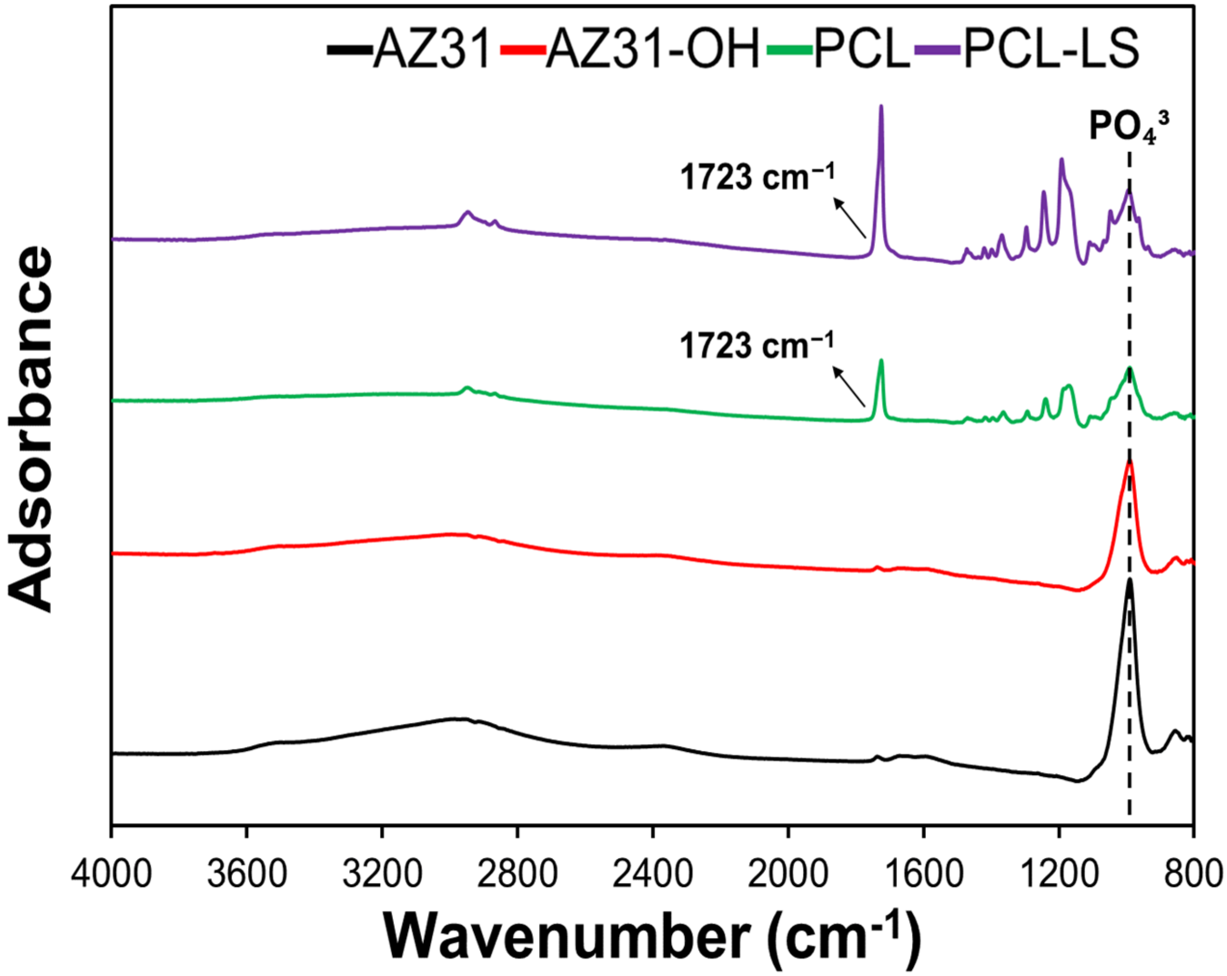

Fig. 2.20. ATR-FTIR spectra of the samples after 7 days of immersion in Hank's solution.

2.3.3. Mechanism of Corrosion Inhibition of PCL-LS Coating

The corrosion inhibition property of the PCL-LS coating was verified by electrochemical corrosion studies as well as *in vitro* immersion tests. Lawsone is initially entrapped within the inner layer of the coating as the corrosion inhibitor, while a top PCL layer is coated on that as a barrier layer to minimize the leaching of the inhibitor. Once a defect appears within the PCL coating, the lawsone molecule is released from the inner layer into the damaged area. The anticorrosive properties of lawsone mainly rely on its ability to chelate metal cations - in our case Mg^{2+} - to form a protective barrier on top of the underlying Mg substrate [111]. Exposing to a saline electrolyte like Hank’s solution, the lawsone molecule undergoes a chemical rearrangement by delocalization of a pair of electrons on its hydroxyl group and then can form a complex with Mg^{2+} ions [14]. These insoluble complexes produced by lawsone molecules will be adsorbed onto the damaged area of the Mg surface and block the active sites of corrosion. The formed organic layer can seal and isolate the damaged substrate form the corrosive electrolyte and thus prevents further corrosion at the metal surface [109].

2.3.4. Antibacterial Studies

Antibacterial properties the coatings were evaluated against *E. coli* and *S. aureus*, two bacterial strains mainly associated with the biomedical implant-related infections [161]. Figure 2.21 shows the results of the disc diffusion test after 24 h of incubation at 37 °C. As can be seen, no zone of inhibition was observed around AZ31, AZ31-OH, and PCL samples on agar plates, implying that these samples do not possess any antibacterial activity. In contrast, PCL-LS displayed clear zones of inhibition against *E. coli* and *S. aureus* with diameters of 26 ± 0.5 mm and 22 ± 0.8 mm, respectively. The ability of lawsone to inhibit bacterial growth has been reported previously in several studies [114, 116]. The bactericidal property of lawsone arises from its molecular structure (2-hydroxy-1,4 napthoquinone). The highly reactive quinone groups of lawsone interact with the nucleophilic amino acids of surface proteins and polypeptides present on the bacterial cell membrane and inactivate them by disturbing their functionalities, therefore induce antibacterial properties [162, 163]. The results suggest that the PCL-LS composite coating has a great potential for Mg alloys, as it offers both corrosion-protective and antibacterial functions.

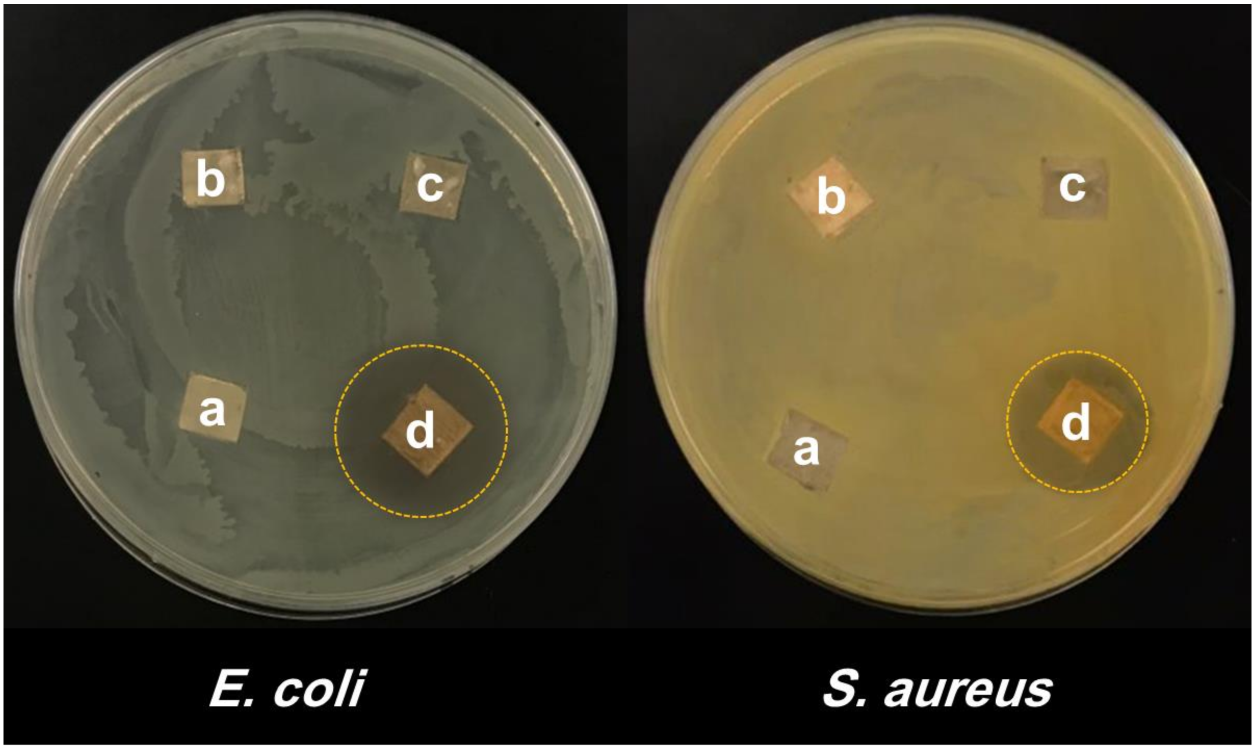

Fig. 2.21. Antibacterial activity of AZ31 (a), AZ31-OH (b), PCL (c), and PCL-LS (d) against *E. coli* and *S. aureus* evaluated by measuring the diameter of inhibitory zones.

2.3.5. *In vitro* Cytocompatibility

To investigate the biosafety of coatings for bio-implant applications, the *in vitro* cytocompatibility of Mg samples were examined toward hFOBs using CCK-8 test. Figure 2.22 shows the viability percentage of hFOBs exposed to different Mg samples extractions for 1, 3, and 5 days. No significant difference was observed among the viability of samples after 1 day of incubation (P-value > 0.05). However, as the incubation time prolonged, the viability of coated samples was significantly higher (P-value < 0.05) than those of uncoated samples at 3-day and 5-day time intervals, indicating the improved cytocompatibility of the Mg substrates after applying the coatings. It should be mentioned that the viability values of both PCL and PCL-LS were 88.6

± 8.2 % and 86.1 ± 10.2 % after 5 days of incubation, respectively, which was notably higher that those of uncoated samples. This demonstrates the acceptable cytocompatibility of the coatings, which is a primary requirement for bio-implant application [161]. The enhanced cell viability of coated samples can be attributed to their lower degradation rate [164]. It has been reported that the rapid degradation of bare Mg alloys leads to the formation of air gas pockets along with an increase in pH value of the culture environment. This will result in the altered cellular osmolality and damage of the cell membranes, which ultimately lead to cell death [165]. The cytocompatibility results indicated that applying PCL coatings promoted the cell viability on AZ31 substrates. Moreover, incorporation of lawsone as corrosion inhibitor into the PCL coating not only did not compromise the cytocompatibility but also remarkably improved the corrosion properties of the pure PCL coating and endowed it with a remarkable antibacterial property.

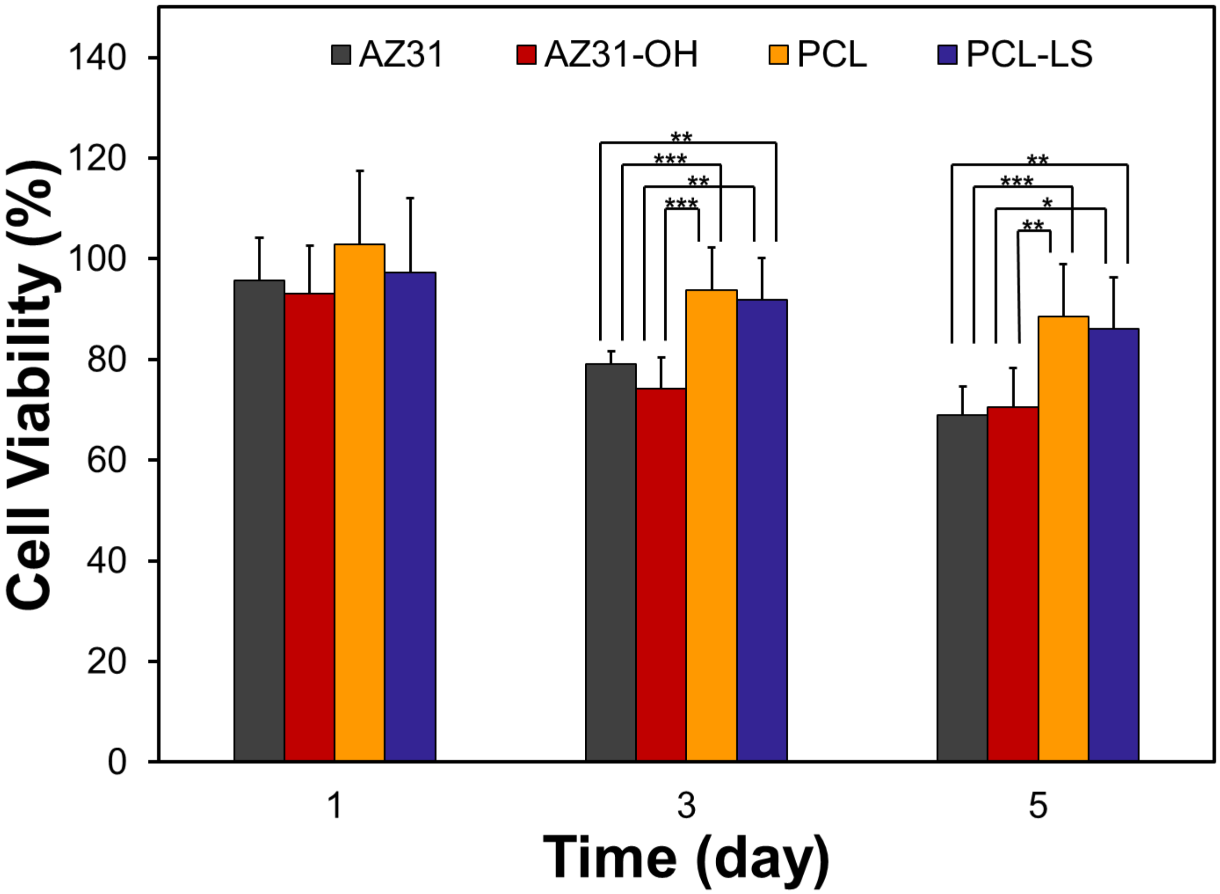

Fig. 2.22. Viability of hFOB cells exposed to sample extracts of 1, 3, and 5 days compared to control cells grown in pure media measured by CCK-8 assay kit. The difference in cell viabilities at each day was considered statically significant with $^{*}p < 0.05$, $^{**}p < 0.01$, $^{***}p < 0.001$, as denoted with asterisks.

2.4. Conclusions

In this study, lawsone was used a natural corrosion inhibitor and incorporated into the biocompatible PCL polymeric coating to improve the corrosion resistance of biodegradable AZ31 Mg alloy. The fabricated coatings were fully characterized with surface and cross-sectional SEM imaging, ATR-FTIR, and wettability tests. A compact and uniform PCL-LS coating with the thickness of ~ 10 µm was formed on the alkaline pretreated AZ31 substrate using a drop-casting method. Alkaline treatment of AZ31 substrates improved the adhesion strength of the PCL-LS coating, resulting in an excellent adhesion strength of 4B according to ASTM D3359. The corrosion resistance of the AZ31 substrate was increased by almost two order of magnitudes (IE of 98.3%) after being coated with PCL-LS. The results of long-term EIS studies clearly indicated that the PCL coatings incorporated with 1% (w/w) lawsone better maintained their protective barrier properties in Hank's solution, which is explained by the strong chelation ability of lawsone molecule against dissolving Mg cations. Moreover, coating of AZ31 alloy with the PCL-LS significantly hampered local alkalization and excessive H_2 generation. In addition to the anticorrosion properties, lawsone-containing coatings showed a strong antibacterial activity against *E. coli* and *S. aureus*, which can be highly beneficial for bio-implant applications as it minimizes the risk of implant-related infection at the early stages. While most of commonly used Mg corrosion inhibitors have limited biomedical applications due to the concerns over their cytocompatibility, no cytotoxic effect was observed for PCL-LS coating toward hFOB cells (viability of > 85%). The results of this study suggested the proposed polymeric coating based on lawsone has great potential as a protective coating to expand the applicability of Mg alloys for biodegradable implant applications.

CHAPTER 3

CELLULOSE NANOCRYSTAL REINFORCED SILK FIBROIN COATING FOR ENHANCED CORROSION PROTECTION AND BIOCOMPATIBILITY OF MG-BASED ALLOYS FOR ORTHOPEDIC IMPLANT APPLICATIONS

This chapter contains text from the following publication:

Hamid Asadi, Sama Ghalei, Hitesh Handa, and Ramaraja P. Ramasamy. Progress in Organic Coatings 161 (2021): 106525.

Reprinted here with permission of the publisher.

Abstract

In this work, a novel coating material based on silk fibroin (SF) and cellulose nanocrystals (CNCs) was developed on biodegradable AZ31 Mg alloy and assessed for corrosion resistance and biocompatibility. Before the application of the coating, AZ31 substrate was modified with a layer of polydopamine to enhance the adhesion of the protective coating to the metal surface as confirmed by the adhesion tape test. SEM images revealed the formation of a defect-free and uniform SF-CNC coating with a thickness of 11.2 ± 2.5 µm on AZ31 alloy. The results of the electrochemical corrosion and *in vitro* immersion tests clearly demonstrated an enhanced corrosion resistance of the SF coating after the incorporation of CNCs. Compared to the unmodified Mg alloy, the SF-CNC coated AZ31 exhibited a remarkably improved cytocompatibility with a viability of 114% and excellent adhesion and spreading of human fetal osteoblast cells onto the coating surface. The findings of this work highlight the great potential of SF and CNC as bio-based nature-derived anticorrosive nanofillers for fabrication of protective and biocompatible coatings on Mg-based biodegradable orthopedic implants.

Graphical Abstract

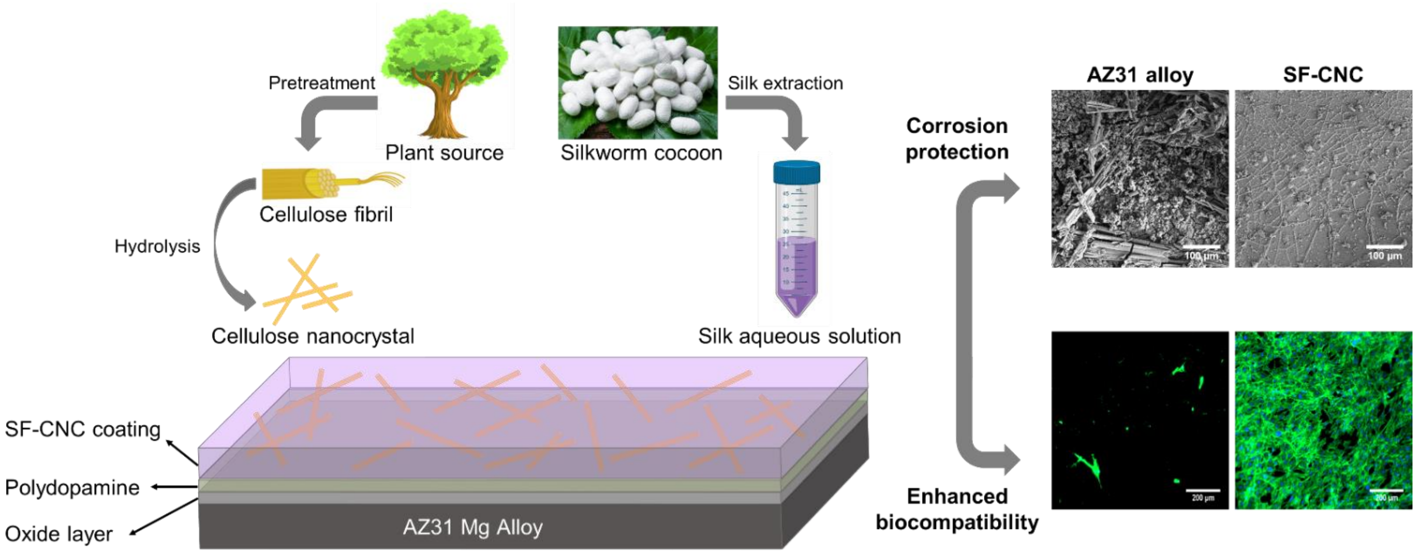

3.1 Introduction

Over the past few years, a variety of natural and synthetic polymers have been used for fabrication of corrosion protective coatings on biomedical Mg alloys [103]. Predominantly, synthetic polymers such polylactic acid (PLA), poly(lactic-co-glycolic) acid (PLGA), polyethylene imine (PEI), and polycaprolactone (PCL) have been proven to offer good anticorrosion properties, however, the cellular responses toward these coatings are not often as satisfactory mainly because of their hydrophobic characteristics and lack of bioactivity [107, 166]. On the other hand, natural polymer-based coatings possess enhanced biocompatibility (e.g. conductive to enhanced cell attachment and growth) compared to synthetic polymer-based coatings. However, most biopolymer-based coatings are highly susceptible to the permeation of water and other corrosive species in the physiological environment because of their porous structure and limited barrier properties [123]. In order to take advantage of the desired biocompatibility properties of biopolymers for application as protective coatings on Mg-based implants, their corrosion resistance must be improved in order to be competitive against synthetic polymers.

Several approaches have been attempted to ameliorate the corrosion resistance properties of polymeric coatings on Mg alloys including the incorporation of corrosion inhibitors/organic salts [12-14], hybridization with other polymers (copolymerization, blending, and layer-by-layer) [16, 17], surface pretreatment/activation [18, 19], and applying intermediate layers [20, 21]. Introduction of anticorrosive nanofillers into polymeric matrix is another well-established approach to enhance the corrosion resistance and durability of polymeric coatings. Addition of anticorrosive nanofillers can improve the barrier properties of polymeric coatings against the aggressive physiological environment by increasing the tortuosity of corrosive species permeation pathways, creation of microcapillaries with high capillary pressure for penetration of liquid species, as well as other mechanisms related to filler-matrix and filler-metal interface interactions [36]. A variety of anticorrosive nanofillers such as graphene and its derivatives [37], hydroxyapatite [38], ZnO [39], silica [40], TiO_2 [41], $Mg(OH)_2$ [42], and layered double hydroxide [43] have been incorporated into protective polymeric coatings on Mg alloys in previous reports.

Over the past decade, bio-based nanofillers have gained extensive attention due to their low-price, renewability, biocompatibility, and biodegradability [44]. Cellulose nanocrystal (CNC) is a needle-like nanoparticle with the size of 5-50 nm in diameter and hundreds of nanometers in length, which are produced from various plant sources through strong acid hydrolysis [167]. Having high aspect ratio, biocompatibility, excellent mechanical properties, dispersibility in aqueous and organic solvents, and formation of strong interfacial bonding with polymeric matrices through its abundant surface hydroxyl groups are some properties that have made CNC a popular reinforcing agent for fabrication of polymeric composites in various biomedical applications [167]. Recently, the anticorrosion properties of CNC have gained interest and have been reported in a few studies [168-172]. Taking all the desired properties of CNC into account, it promises to be a novel and renewable reinforcement material for fabrication of anticorrosive coatings on Mg biodegradable implants.

In the previous chapter, we developed and characterized a polymeric coating based on synthetic PCL loaded with lawsone corrosion inhibitor. In this project, we aimed at developing a protective coating on Mg alloys based on natural polymers in order to take advantage of their excellent cellular response and biological properties. Here, we developed a composite coating consisting of silk fibroin (SF) and CNC on the AZ31 Mg alloy to improve its corrosion resistance and biocompatibility for biodegradable bone implant applications. SF is a natural protein extracted from Bombyx mori silkworm [173]. Owing to its excellent biocompatibility, controllable biodegradability, and superior mechanical properties, SF films and coatings have been extensively researched in diverse biomedical applications [129]. Specifically, SF has been used as surface coating on bone implants in several studies and showed high osteogenic activities both *in vitro* and *in vivo* [174]. Compared to the commonly used synthetic polymeric coatings such as polyhydroxybutyrate (PHB), PCL, polyamide, PLA, and PGA, which degrade into acidic products, SF shows less immunogenicity (the human body's immune response provoked by a foreign material) as it decomposes to its constituent biocompatible amino acids [175]. Considering all the above advantages, SF shows great potential as a coating material for biodegradable Mg alloys.

In this study, CNC nanoparticles were incorporated into the SF coating as anticorrosion nanofillers for the first time in reported literature with the aim of improving the barrier and corrosion protection properties of the SF film. The schematic of the proposed coating is shown in Figure 3.1. AZ31 was selected as model biodegradable Mg substrate due to its lower content of Al (~ 3 wt%), an element known to be harmful for neural system and bone cells, among all other Mg alloys with typical Al content of 3-13 wt% [119]. Adequate interfacial adhesion is a primary requirement for any protective coating, which is often difficult to achieve on bare metallic surfaces with no functional groups and poor adhesiveness. To address this issue, before applying the polymeric coating, the AZ31 substrates were modified with a thin layer of polydopamine (PD) to serve as intermediary layer and to improve the coating/substrate adhesion. PD possesses outstanding adhesiveness to almost any type of material, numerous functional groups, and excellent biocompatible, which make it a very suitable platform for modification of biomedical Mg alloys surfaces before applying a secondary protective coating [176]. Finally, the composite CNC-reinforced SF coating was applied onto the PD-pretreated AZ31 surface by the drop-cast method. The proposed composite coating was characterized through various physiochemical techniques. The corrosion resistance of the coating and the effect of CNC inclusion on the corrosion protection performance of the coating were investigated through extensive electrochemical techniques and *in vitro* immersion tests. Finally, the biocompatibility of the coating in terms of cellular toxicity and adhesion was assessed. Our central hypothesis is that the incorporation of CNC as bio-based nanofiller into SF matrix can improve its corrosion resistance and barrier properties by inducing desired conformational changes in the secondary structure of SF. We expect a composite coating based on SF and CNC will benefit from the excellent biological properties of SF and anticorrosion properties of CNC, which can endow the underlying AZ31 Mg alloy with an enhanced corrosion resistance, comparable to those obtained by synthetic polymers, and cytocompatibility.

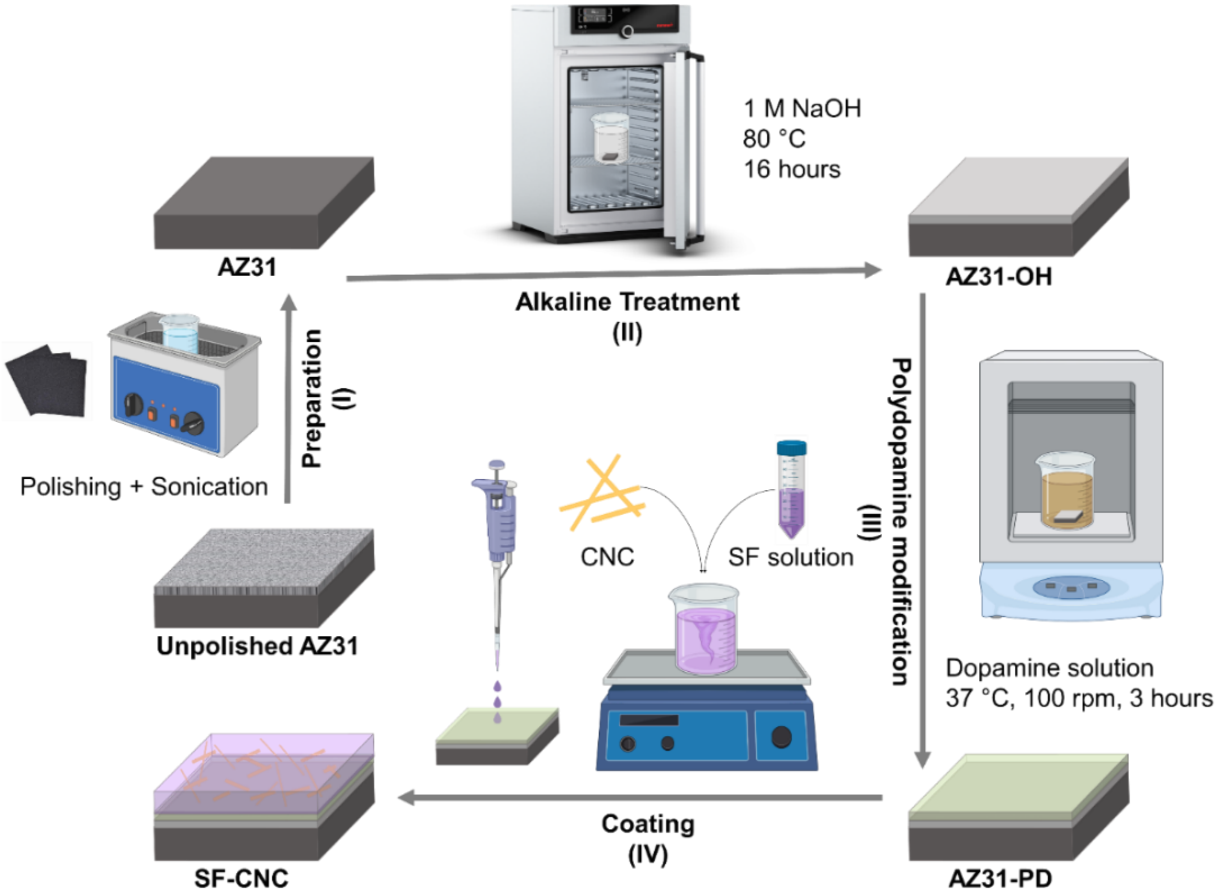

Fig. 3.1. Schematic illustration of the fabrication steps of SF-CNC coating on PD-modified AZ31 Mg substrate.

3.2. Materials and Methods

3.2.1 Materials

Bombyx mori silk cocoons were obtained from Paradise Fibers (USA). Spectra/Por 3 regenerated cellulose dialysis membrane tubing (3.5 kDa, molecular weight cut-off) was obtained from Fisher Scientific (USA). Concentrated aqueous suspension of CNC was kindly provided by Dr. Sudhagar Mani, University of Georgia, USA. Polyethylene glycol with a molecular weight of 200 (PEG_{200}) was purchased from Sigma-Aldrich (Cat# P3015). Trypsin−EDTA was obtained from Corning (Manassas, VA 20109). The Cell Counting Kit-8 (CCK-8) was purchased from

Sigma-Aldrich (St. Louis, MO 63103). Mixture of Dulbecco's Modified Eagle's Medium and Ham's F-12 Medium (DMEM/F-12), geneticin, and fetal bovine serum (FBS) were bought from Gibco-Life Technologies (Grand Island, NY 14072). The phalloidin (Alexa Fluor 488) and DAPI (diamidino-2-phenylindole) reagents were purchased from Thermo Fisher Scientific (Thermo Fisher Scientific Inc., USA). Fetal Osteoblast cells were purchased from American Type Culture Collection (hFOB 1.19-ATCC 11372). All aqueous solutions were prepared using ultrapure water purified with a Milli-Q Millipore system. All other reagents, unless otherwise specified, are of reagent grade.

3.2.2 Silk Fibroin Extraction

Aqueous SF solution was extracted from bombyx mori cocoons following a previously established procedure [177]. The cocoons were first boiled in a 0.02 M sodium carbonate solution for 30 min to remove the sericin. After drying the degummed SF at room temperature overnight, it was dissolved in 9.3 M lithium bromide solution for 4 h at 60 °C. Then, the SF solution in lithium bromide was dialyzed against water for 48 h to obtain the aqueous SF solution which was further filtered and stored at 4 °C until used. The final concentration of SF solution was 7% w/v.

3.2.3 Preparation of AZ31 Substrates

AZ31 Mg alloy sheets ((wt%): Mg (balance), Al (2.5-3.5), Zn (0.7-1.3), Mn (0.2-1), Si (0.05), Cu (0.01), Fe (>0.05), Ni (>0.05), others (0.4)) with dimension of 2×2 cm and thickness of 1 mm were polished by 2000, 2500, and 3000-grit SiC abrasive papers to remove the natural metal oxides layer and obtain a uniform roughness. Then, they were sonicated in absolute ethanol and water each for 5 min to remove any surface contaminations, and finally dried at 60 °C.

3.2.4 Pretreatment of AZ31 Substrates

AZ31 samples were treated with 1 M NaOH at 80 °C for 16 h to form a passive layer of $Mg(OH)_2$ on the Mg alloy surface. Afterward, they were thoroughly rinsed with water, dried at 80 °C for 1 h, and labeled as "AZ31-OH". The alkaline treatment of AZ31 substrates promotes the deposition of a homogenous PD layer by mitigating the generation and adhesion of H_2 to the Mg surface [178]. The PD modified samples were obtained by placing the alkaline treated Mg substrates in a 6-well plate filled with 10 mL of 2 mg/mL dopamine hydrochloride solution in Tris-HCl buffer (25 mM, pH 8.5). The reaction was carried out in a shaker incubator 37 °C and 100 rpm for 3 h at dark. After completion of the reaction, the samples were sonicated with water for 1 min, and labelled as “AZ31-PD”

3.2.5 Fabrication of the SF and SF-CNC coatings

SF-based protective coatings on the Mg alloy were prepared by the solution casting method from aqueous SF and CNC solutions. First, CNC dispersion with a concentration of 7 mg/mL was obtained by adding a certain amount of water to the stock CNC, followed by stirring and bath sonication each for 15 min. The obtained solution was filtered (5 µm) to remove the big particles from the solution. In this study, we employed never-dried aqueous dispersions of CNC over its lyophilized powder form to reduce the chance of CNC aggregation, which is known to be a common issue in producing CNC-reinforced polymeric composites [179]. A certain volume of CNC suspension was added to the SF solution and stirred for 15 min to obtain a well-dispersed and homogenous solution. To obtain better mechanical properties and prevent surface crack formation on the coatings, PEG_{200} was also added into the solution. Finally, the pH of the solution was brought up to 10 using a 1 M NaOH solution. The detailed composition of the coating solutions is listed in Table 3.1. To prepare the top coatings, 200 µL of either SF or SF-CNC solution was pipetted on the pretreated AZ31 substrates and dried at room temperature for 24 h. Afterward, the SF-based coatings were cross-linked by immersion in 80 wt% methanol for 1 h to become more water stable and corrosion resistant, as reported previously [180]. The coated samples with the blank SF and CNC-containing solution were denoted as “SF” and “SF-CNC”, respectively. A batch of SF-CNC coatings were also made on AZ31-OH substrates without PD modification under the same condition to be used as control samples in adhesion tape and electrochemical corrosion tests.

Table 3.1. Compositions of the solutions used for the fabrication of coatings.

Solutions	7% w/v SF (μL)	7 mg/mL CNC dispersion (μL)	PEG_{200} (μL)	1 M NaOH (μL)	Water (μL)
SF	1000	0	10	10	100
SF-CNC	1000	100	10	10	0

3.2.6 Material Characterization

TEM imaging was performed for morphological and size analyses of CNCs using a JEOL JEM-2100 transmission electron microscope. Dynamic light scattering (DLS; Zetasizer, Malvern Instrument) was performed to measure the particle size and surface charge (zeta potential) of CNC particles. Dilute CNC dispersions (0.1 mg/mL in water) were used to avoid multiple scattering [133]. The surface and cross-sectional morphologies of the samples were observed using a field emission scanning electron microscope (SEM, FEI Teneo, FEI Co.). The elemental analysis across the coating/substrate interface was obtained by an energy dispersive x-ray spectrometer (EDS) connected to the SEM. The chemical structures of the coatings were characterized by attenuated total reflectance-Fourier transform Infrared (ATR-FTIR) analysis using a Nicolet 6700 spectrometer (Thermo Electron Corporation, MA, USA). The spectra were recorded over the wavenumber range of 4000-800 cm^{-1} with 128 scans and a resolution of 1 cm^{-1} for each measurement. Amid I band deconvolution was performed for each spectrum to measure the crystallinity (β-sheet content) using OriginPro 8 software according to previous studies [181]. Water contact angle (WCA) measurements were performed using a Krüss DSA 100 drop shape analyzer at room temperature. The static contact angle was measured by the dropwise addition of water (1 μL) onto 2×2 cm samples. Measurements were taken at 3 different areas for each sample. Adhesion strength of the coatings were evaluated by ASTM D3359 cross-cut tape test. Two series of 11 cuts with 1 mm distance apart were made perpendicular to each other using a sharp blade and a cross-guide to form a lattice pattern of 100 squares on the coatings. An adhesive tape (SEMicro CHT) was applied to the cross-cut area, rubbed with an eraser to ensure a firm contact between the tape and the test area, and quickly pulled off at an angle of 180° after 90 s. The percentage of the coating detached by the tape was quantified and the coating adhesion was graded according to ASTM standard chart, with 5B indicative of the highest level of adhesion (0% detachment) and 0B indicative of the worst adhesin (> 65% detachment).

3.2.7 *In vitro* Corrosion Evaluation

3.2.7.1 Electrochemical Corrosion Measurements

All the electrochemical and *in vitro* corrosion studies were carried out in Hank's solution ($NaCl$ 8.00 g/L, KCl 0.40 g/L, $CaCl_2$ 0.14 g/L, $NaHCO_3$ 0.35 g/L, $MgSO_4.7H_2O$ 0.10 g/L, $MgCl_2.6H_2O$ 0.1 g/L, $Na_2HPO_4.2H_2O$ 0.06 g/L, KH_2PO_4 0.06 g/L, D-Glucose 1 g/L, $NaHCO_3$ 0.35 g/L, pH 7.4) in order to simulate the corrosive physiological environment according to ASTM-G31-72 standards [123]. Electrochemical corrosion tests were performed in a custom-made three-electrode cell consisting of Mg samples with an exposing surface area of 1 cm^2 served as working electrode, a silver/silver chloride (Ag/AgCl 3 M) reference electrode, and a platinum wire as the counter electrode connected to an electrochemical workstation (CHI-920c, CH Instruments Inc., Austin, TX). The open circuit potential (OCP) plot versus time were recorded over a course of 3 h under no external potential. Potentiodynamic polarization (PP) test was performed from − 200 mV to + 200 mV vs OCP at a scan rate of 1 mV/s and the values of corrosion potential (E_{corr}) and corrosion current density (I_{corr}) for each sample were calculated using the Tafel extrapolation method. For electrochemical impedance measurement (EIS), the samples were allowed to stabilize for 30 min in the electrolyte before the test. Then, EIS measurement was run at the OCP over a scanning frequency range of 10^5 to 10^{-2} Hz with an AC amplitude of ± 10 mV. All EIS data were fitted and analyzed using Zview software by adopting appropriate electrical equivalent circuit (EEC) models. For each of OCP, PP, and EIS studies, a new batch of samples were used, all in triplicates, and the average result was reported and shown in the figures.

3.2.7.2 *In vitro* Corrosion Tests

Each sample was individually placed in a sealed test containing Hank's solution with a volume to sample area ratio of 20 mL/cm^2 (ASTM G31-72). An inverted funnel-burette system was placed above the samples inside the solution to collect the generated hydrogen every day up to 14 days. Meanwhile, the pH value of the corrosion media was also measured at the same time intervals. At the end of the immersion test, the specimens were removed from the solution, rinsed thoroughly with water, and dried at 70 °C. The post-corrosion morphologies of the samples were imaged by SEM.

3.2.8 Cytocompatibility

3.2.8.1 Cell Culture

Fetal Osteoblast cells were cultured in 75 cm^2 T-flsks with a 1:1 mixture of Ham's F12 Medium and Dulbecco's Modified Eagle's Medium, containing 0.3 mg/mL Geneticin and supplemented by 10% fetal bovine serum (FBS) in a humidified incubator at 37 °C with 5% CO_2. The culture medium was refreshed every day until cells reached 90% confluency. Thereafter, the cells were detached from the T-flask surface by treating them with 0.18% trypsin and 5 mM EDTA for 5 min.

3.2.8.2. Cell Viability

The samples leachates were obtained using cell culture media with an extraction media/surface area ratio of 1.25 mL/cm^2 in a humidified atmosphere with 5% CO_2 at 37 °C for 3 and 5 days according to ISO 10993-12 [126]. The leachates were then exposed to hFOB cells to evaluate any potential cytotoxic response. Cells were seeded in a 96-well plate at a concentration of 50,000 cells/mL and incubated for 24 h in a humidified incubator with 5% CO_2. After formation of a cell monolayer on the bottom of the wells, the medium in each well was replaced with 100 µL of the sample leachates (n=6) and incubated for another 24 h. The cytotoxicity assay was performed based on the manufacturer's protocol (Sigma-Aldrich) using a CCK-8 kit. After 24 h of cells exposure to the leachates, 10 µL of WST-8 solution was added to each well and incubated for 4 h. Afterwards the UV absorbance of the orange formazan produced by the live cells was measured at 450 nm and the relative cell viability was calculated according to the following equation [182]:

$$\% \, cell \, viability = \frac{absorbance \, of \, the \, test \, samples}{absorbance \, of \, the \, control \, samples} \times 100$$

3.2.8.3 Cell Adhesion

Samples with a size of 1×1 cm were sterilized by UV radiation for 2 h on each side prior to cell seeding. Osteoblast cells at a concentration of 15,000 cells/cm^2 were seeded on each sterilized sample and kept for 24 h in an incubator (T = 37 °C, 5% CO_2). The cell-seeded samples were washed with a PBS solution, fixed with 4% formaldehyde for 10 min, and permeated with 0.2% Triton X-100 for 10 min. After several washing with PBS, the cells cytoplasm and nuclei were stained using phalloidin and DAPI reagents, respectively, to observe their morphology and adhesion on different samples. An inverted fluorescent microscope (AMG EVOS FL) was used to image the stained cells.

3.2.9 Statistical analysis

All data in this study were expressed as mean ± standard deviation with n = 3. One-way analysis of variance (ANOVA) was adopted for statistical analysis, where P-value < 0.05 was considered statistically significant.

3.3 Results

3.3.1 CNC Characterization

CNC nanoparticles were observed by TEM (Figure 3.2A) and showed the typical rod-like structure with cross-sectional dimension of 21 ± 5 nm and length of 147 ± 45 nm. Additionally, the CNC dispersion was analyzed by DLS (Figure 3.2B). The rod-like morphology of CNCs resulted in emergence of two peaks at 132 and 26 nm, where the smaller one represents the diameter and the larger one represents the length of the CNCs. The sizes were consistent with the

TEM results and comparable with the previous reports [183]. Besides, the zeta-potential of CNCs were found to be -31.4 ± 2.1 mV, implying the anionic surface of CNC particles [172].

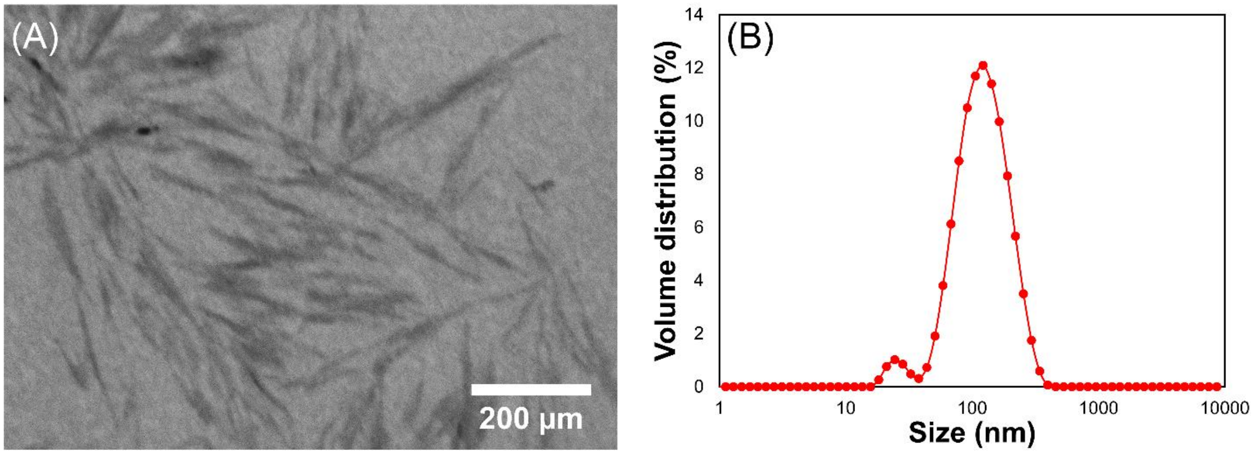

Fig. 3.2. TEM image (A) and particle size distribution (B) of CNCs.

3.3.2 Coating Characterization

3.3.2.1 Surface Morphology

The surface morphologies of Mg substrates before and after modifications were investigated by SEM as shown in Figure 3.3. SEM images with a higher magnification can be also found in the supplementary material (Figure S3.1). Untreated AZ31 substrate showed a quite flat surface with some aligned scratches remained form the mechanical polishing step with SiC papers. After alkaline treatment with NaOH, those aligned scratches faded from the surface due to the formation of a dense $Mg(OH)_2$ oxide layer. AZ31-PD exhibited a rougher surface with some small PD aggregations formed on the surface by self-assembly during the deposition process. Nevertheless, the coating was still aligned with the polishing grooves underneath, implying the relatively low thickness of the PD coating [176]. The surface morphology of the pure SF coating was smooth and homogenous with no cracks or defects on the surface. Being defect-free is a crucial factor for any protective coating, as it ensures the complete isolation of the covered metal against corrosive environment. Similarly, the SF-CNC coating was flat and uniform with no apparent big size CNC agglomeration on the surface, showing that the CNCs were homogeneously distributed within the SF coating. In addition, the cross-sectional SEM image of the SF-CNC coated sample (Figure 3.3) displayed a distinct and compact polymeric layer covering the underlying AZ31 substrate with no void or cleavage at the interface, along with an oxide layer formed on the surface during alkaline treatment. The thicknesses of the SF-CNC coating and the oxide layer were measured to be 11.2 ± 2.5 µm and 20.3 ± 1.8 µm, respectively. The results of EDS analysis (Figure 3.3) further confirmed the elemental composition of each layer, where the highest concentrations of Mg, O, and C elements were observed withing the AZ31 substrate, inner oxide layer, and the outer organic layer composed of SF-CNC coating and PD layer, respectively.

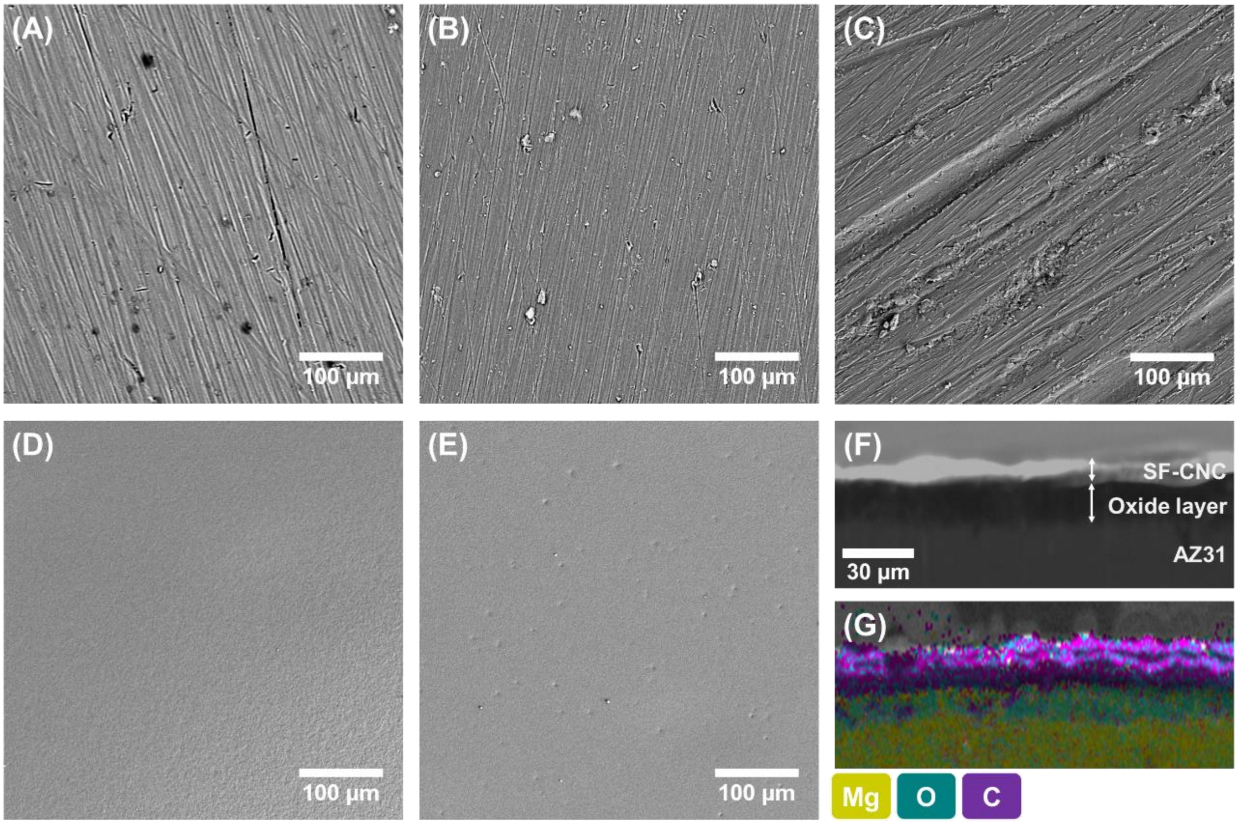

Fig. 3.3. Surface SEM images of AZ31 (A), AZ31-OH (B) AZ31-PD (C), SF (D), and SF-CNC (E); Cross-sectional morphology of SF-CNC/substrate interface (F) with the corresponding elemental analysis mapping (G).

3.3.2.2 Chemical Composition of the Coatings

Figure 3.4 displays the ATR-FTIR spectra of the bare and modified Mg alloy samples. No distinctive peaks were observed in the spectrum of AZ31, as there is no functional group on the surface of bare AZ31 alloy. AZ31-OH showed an adsorption peak at 3700 cm^{-1}, which is related to the hydroxyl groups of the formed $Mg(OH)_2$ layer during alkaline treatment process [130]. The formation of intermediary PD layer was confirmed by the emergence of the adsorption peaks in the range of 1450-1625 cm^{-1} corresponding to the C=C stretching vibration of benzene rings and the N-H bending [184], as well as a broad band centered at 3215 cm^{-1} related to stretching vibrations of -NH (catechol groups) and -OH (hydrogen bonding of PD molecules) groups [185].

The SF coating showed the typical characteristic peaks of SF at 1624 cm^{-1} and 1524 cm^{-1}, corresponding to the amide I (N−H deformation) and amide II (C−N stretching), respectively. Meanwhile, a broad peak centered at 3300 cm^{-1} was also observed, which could be attributed to the hydroxyl groups [186]. The SF-CNC coating exhibited a similar spectrum as the SF coating, with some variations. Compared to the pure SF coating, the characteristic bands of SF-CNC shifted to higher wavenumbers and became less pronounced. These alterations suggested the formation of strong intermolecular hydrogen bonding between the SF matrix and CNCs [125, 187].

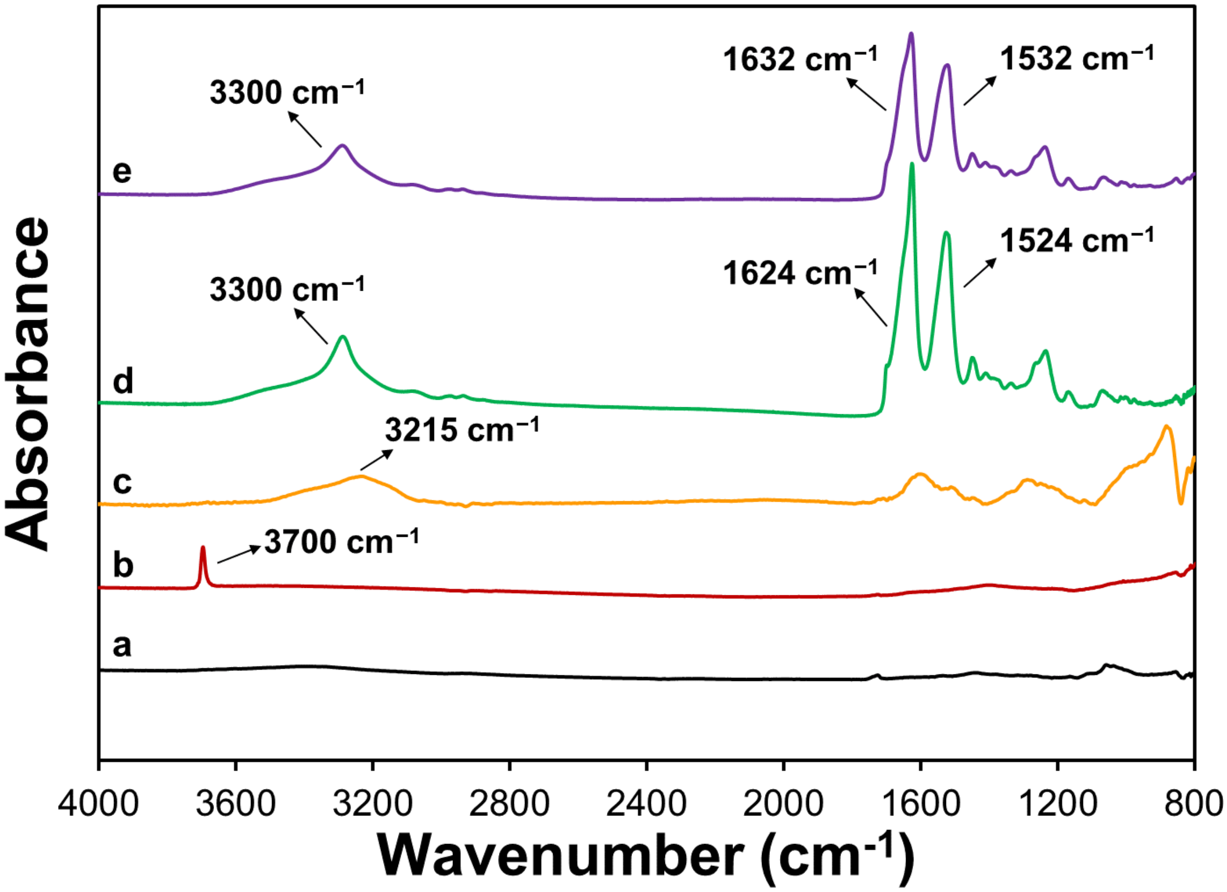

Fig. 3.4. ATR-FTIR spectra of AZ31 (a), AZ31-OH (b) AZ31-PD (c), SF (d), and SF-CNC (e).

SF has various secondary structures including random coils, α-helices, β-sheets, and β-turns that can be adjusted by change in solvent, pH, applied shearing force, metal ion content as well as post-treatment. The secondary structure determines some of the characteristics of SF such as stability, wettability, mechanical properties, and biodegradability, which are among the most important properties in coating applications [13]. The effect of methanol treatment and CNC incorporation on the secondary structures of the SF coating was quantitively studied by deconvolution of amide I band (1590-1700 cm^{-1}) according to the wavenumber ranges listed in Table 3.2, and the results are shown in Figure 3.5. As expected, the methanol treatment of SF coatings led to a significant increase in β-sheet percentage from 16% to 23%. Moreover, incorporation of CNCs into the SF coatings was found to further increases the β-sheet content to 31% in the SF-CNC coating. A similar increasing trend in β-sheets content by nanocellulose has been previously reported and attributed to the strong interaction between CNCs and SF through hydrogen bonding, leading to conformational changes of SF from random coil/helix to β-sheet [188, 189]. The higher content of β-sheet has been reported to be more preferable in protective coating applications, as it improves the water stability and barrier properties of the SF coatings, resulting in higher corrosion protection properties in the physiological environment [190].

Table 3.2. Vibrational Band Assignments in the Amide I Region of SF [191].

Wavenumber range (cm^{-1})	Assignment
1605−1615	(Tyr) side chains/aggregated strands
1616−1621	Aggregate beta-strand/ beta-sheets (weak)
1622−1627	Beta-sheets (strong)
1628−1637	Beta-sheets (strong)
1638−1646	Random coils/extended chains
1647−1655	Random coils
1656−1662	Alpha-helices
1663−1670	Turns
1671−1685	Turns
1686−1696	Turns
1697−1703	Beta-sheets (weak)

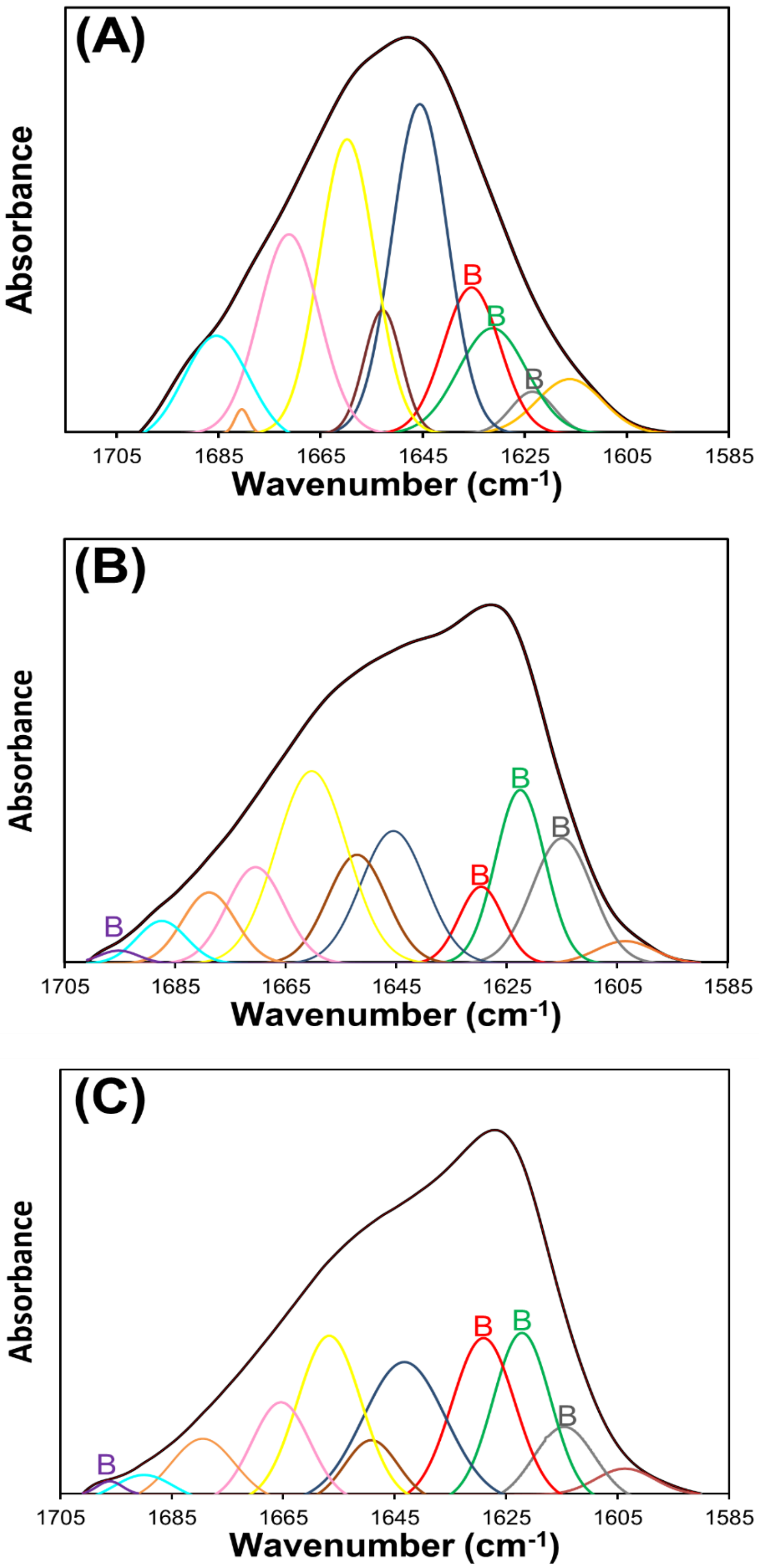

Fig. 3.5. Deconvoluted FTIR spectra of the amide I band of non-treated SF (A), methanol-treated SF (B), and methanol-treated SF-CNC (C); B = β-sheets.

3.3.2.3 Wettability Measurement

Figure 3.6 displays the measured water contact angle (WCA) values of the samples and their representative images. Bare AZ31 substrate showed a relatively hydrophilic surface with an average contact angle of 42.9 ± 3.0°. The contact angle value of AZ31 substrates dropped to 29.1 ± 2.3° after alkaline treatment due to the emergence of numerous hydroxyl groups on the AZ31 surface during alkaline treatment process [134]. No significant change in WCA values was observed following the modification of AZ31-OH surface with PD. Meanwhile, the SF-coated Mg sample showed an apparently less hydrophilic surface with a contact angle value of 77.7 ± 1.6°, which is in agreement with the reported values for methanol-treated SF coatings in previous studies [192]. Incorporation of CNCs into the SF coating did not bring about a significant change in WCA value. Despite the presence of numerous hydrophilic hydroxyl and sulfate groups of CNCs [172] along with the slightly increased surface roughness of SF-CNC coating, which may further drives it toward a more hydrophilic surface [193, 194], the higher β-sheet content of the SF-CNC coating reduced hydrophilicity and counterbalances the effect of CNC addition, thus resulted in no significant change ($P\text{-value} > 0.05$) in the WCA value [195]. Taking the results of SEM morphological analysis, ATR-FTIR and wettability measurements into consideration, it can be concluded that all the surface modification and coating processes were successfully carried out on the AZ31 alloy substrates.

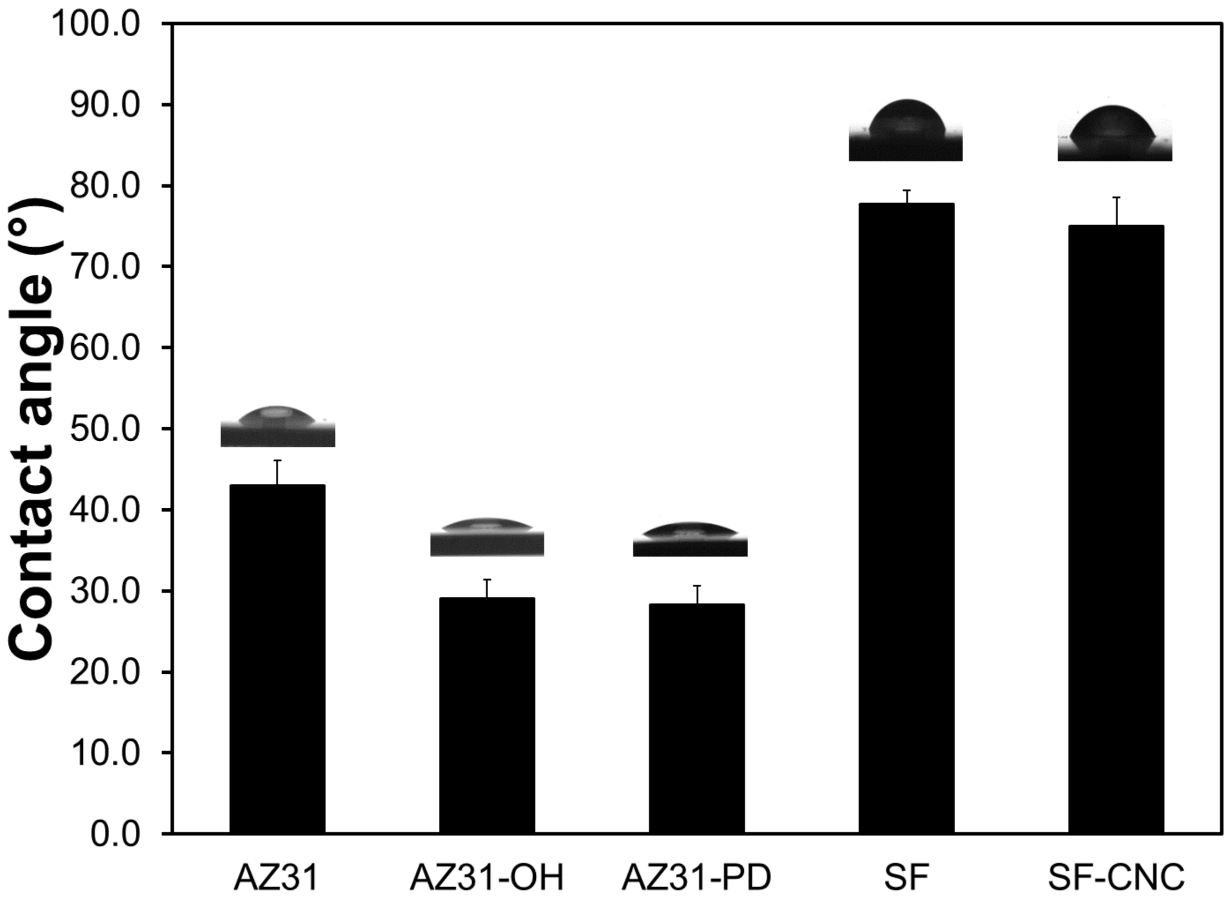

Fig. 3.6. Water contact angle values of bare, pretreated, and coated Mg samples.

3.3.3 Coating Adhesion Test

The performance and reliability of any protective coating highly relies on the adhesion strength of the coating to the underlying substrate. Poor bonding between the polymeric layer and the Mg implant may result in interfacial delamination under mechanical shearing (while inserting the implant) or long-term corrosive environment, which in turn compromises the protective properties of the coating [196]. The adhesion strength of SF and SF-CNC coatings to the AZ31 substrate and the effect of PD pretreatment on that was examined by ASTM D3359 cross-cut tape test. Figure 3.7 depicts the photographs of cross-cut areas of SF and SF-CNC coated AZ31-OH and AZ31-PD substrates taken before and after the tape test. In the case of SF and SF-CNC coated AZ31-OH without PD, a relatively high percentage of the coatings were detached from the surface after tape removal, indicating an insufficient adhesion strength between the coatings and alkaline treated Mg alloy. In contrast, SF and SF-CNC coatings on PD-modified AZ31 showed superior adhesion, where the edges of the cuts were completely smooth and none of the squares were detached. Considering the number of detached squares (fully or partially), the adhesion strength of SF and SF-CNC coatings on AZ31-OH and AZ31-PD were graded as 2B and 5B, respectively. The improved adhesion of the SF and SF-CNC to the AZ31-PD can be attributed to the extraordinary robust adhesion of the PD to the Mg surface along with the existence of numerous functional groups (hydroxyl and amine) that can react with the coatings [197]. The application of PD as an intermediary layer to improve the adhesion of an external polymeric layer has been previously reported in several other studies [121, 176]. The results indicated that the SF and SF-CNC coatings have excellent adhesion strength on the PD pretreated AZ31 substrate, making them more feasible for clinical application.

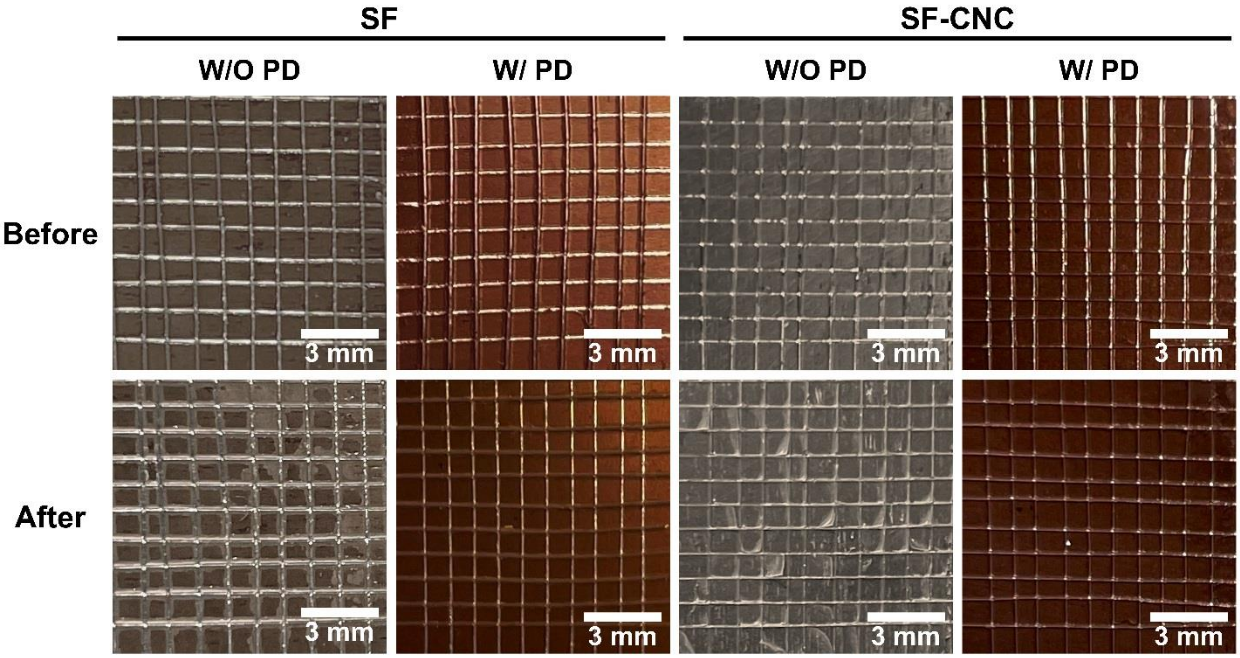

Fig. 3.7. Photographs of the SF and SF-CNC coatings on alkaline-treated AZ31 with and without the intermediary PD layer before and after the cross-cut adhesion test.

3.3.4 *In vitro* Corrosion Studies

3.3.4.1 Electrochemical Measurements

Electrochemical corrosion tests including open circuit potential, potentiodynamic polarization, and electrochemical impedance spectroscopy were conducted in Hank's solution to evaluate the corrosion resistance properties of the coated samples. Figure 3.8A shows the OCP vs. time plots of the samples during 3 h of immersion. Generally, a more positive OCP value represents a nobler surface with less susceptibility to corrosion [137]. As expected, the bare AZ31 stabilized at a quite negative OCP of -1.49 V (vs. Ag/AgCl), which was the lowest value among all tested samples. For AZ31-OH, the steady OCP value was found to be -1.43 V, showing a more stable surface was achieved after alkaline treatment of Mg substrates. Deposition of PD film on the AZ31-OH did not noticeably change the final OCP value. The OCP of the SF-coated sample started from -1.33 V and finally reached -1.40 V at the end of test period. Although being much more positive than those uncoated Mg samples, the decreasing trend of OCP values during immersion time implies the deterioration of pure SF coating barrier properties, which ultimately may lead to the breakdown of the coating upon long exposure to Hank's solution [171]. Incorporation of CNC into the SF coating further increased the final OCP toward more positive value of -1.34 V, while mitigating the reduction trend of OCP during immersion time compared to that of pure SF coating. The OCP results suggested that CNC can act as an anodic protector, slowing down the cathodic hydrogen evolution and therefore, the overall anodic dissolution rate of the Mg alloy [139].

Figure 3.8B displays the PP curves (Tafel plots) of uncoated and coated Mg samples, while the values of corrosion potential (E_{corr}) and corrosion current density (I_{corr}) derived from the Tafel plots are summarized in Table 3.3. Generally, curves with more positive E_{corr} and lower I_{corr} represent a sample with less corrosion tendency and corrosion rates [198]. The pristine AZ31 substrate had the lowest E_{corr} of -1.44 V and the highest I_{corr} of 2.8×10^{-6} A.cm^{-2} among all the tested samples. Alkaline treatment of AZ31 resulted in a shift of E_{corr} toward a more positive potentials and reduction of I_{corr} to 8.9×10^{-7} A.cm^{-2}. This improvement in corrosion resistance is associated to the formed $Mg(OH)_2$ conversion layer [199]. Formation of PD on the AZ31-OH surface did not bring about any protective effect as no significant changes in E_{corr} and I_{corr} values were observed. It's worth mentioning that for all uncoated samples (AZ31, AZ31-OH, and AZ31-PD), sharp increases in the current density were observed in the anodic region of the polarization curves, implying these samples underwent pitting corrosion during the polarization test leading to sudden oxidation [120]. After deposition of SF coating, E_{corr} remarkably shifted to a more positive value of -1.35 V and I_{corr} was decreased to 5.7×10^{-7} A.cm^{-2}. This reflects the superior corrosion resistance of the SF coated sample, which is originated from the barrier properties of the compact silk film against the corrosive environment [126]. Incorporation of CNCs into the SF coating further shifted the E_{corr} value to -1.31 V and resulted in the lowest I_{corr} value of 2.5×10^{-7} $A.cm^{-2}$, which was approximately an order of magnitude lower than that of bare AZ31. The results of PP test clearly confirmed the superior effectiveness of the composite SF-CNC coating in retarding the rapid corrosion of the Mg substrate.

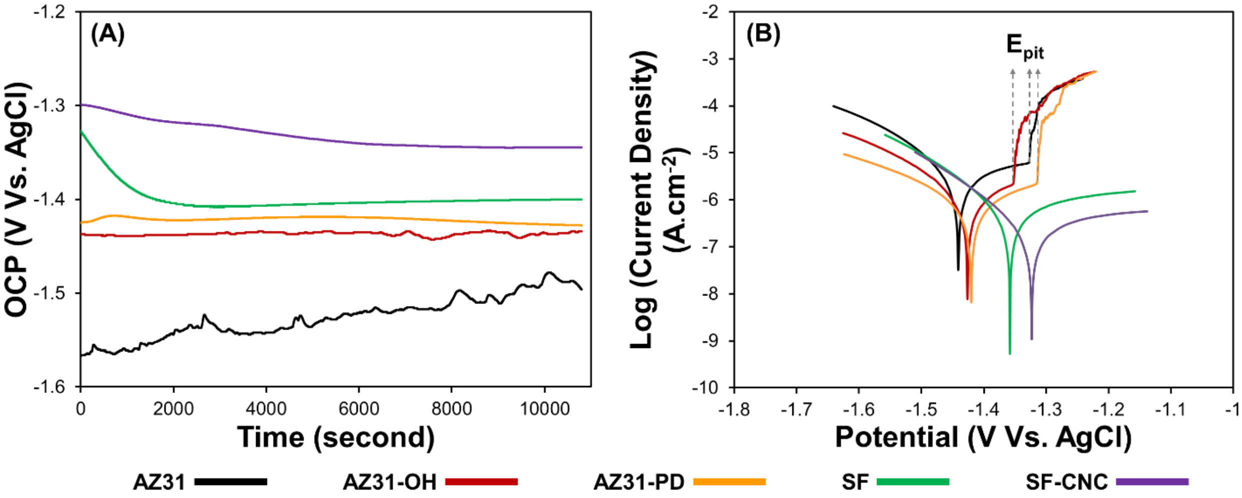

Fig. 3.8. Open circuit potential (A) and potentiodynamic polarization (B) curves of bare, pretreated, and coated Mg samples performed in Hank's solution.

Table 3.3. Corrosion potentials (E_{corr}) and corrosion current densities (i_{corr}) values of the Mg samples obtained from PP curves in Hank's solution by Tafel methods.

Samples	E_{corr} (V)	I_{corr} (A/cm^2)
AZ31	-1.44	2.8×10^{-6}
AZ31-OH	-1.42	8.9×10^{-7}
AZ31-PD	-1.41	8.7×10^{-7}
SF	-1.35	5.7×10^{-7}
SF-CNC	-1.31	2.5×10^{-7}

EIS was employed as a powerful, non-intrusive tool to further evaluate the corrosion protection properties of the coated samples. Figure 3.9 exhibits the Nyquist plots and Bode plots (both impedance and phase angle plots) of EIS spectra of the samples. In a typical Nyquist plot, a higher diameter of the impedance arc represents the superior corrosion resistance of a tested sample [12]. As can be seen in Figure 3.9A-B, the arc diameters were found to be in the following order: AZ31 < AZ31-OH ≈ AZ31-PD < SF < SF-CNC. Moreover, the impedance values at the lowest-frequency region ($|Z|_{0.01\ Hz}$) of the Bode-impedance plots (Figure 3.9C), which is also known to be a semi-quantitative indicative of anticorrosion performance, followed the same order. The results were consistent to those of observed in OCP and PP tests and clearly showed the protective properties of the SF coating on the Mg alloy, while confirming the enhancement effect of CNCs on the anticorrosion properties of the SF coating. As can be seen in the Bode-phase plots (Figure 3.9D), the peak at the medium-frequency range became more eminent following the alkaline treatment of AZ31, indicating the enhancement of the oxide layer [145]. Moreover, coating the sample with the SF and SF-CNC resulted in loftier and wider phase angles, confirming the success of coating process [190]. Compared to the SF, SF-CNC exhibited broader time constants and kept higher impedance values over the low- and medium-frequency ranges (10^{-2}-10^{2} Hz), implying the superior corrosion protection performance of the SF-CNC coating [12].

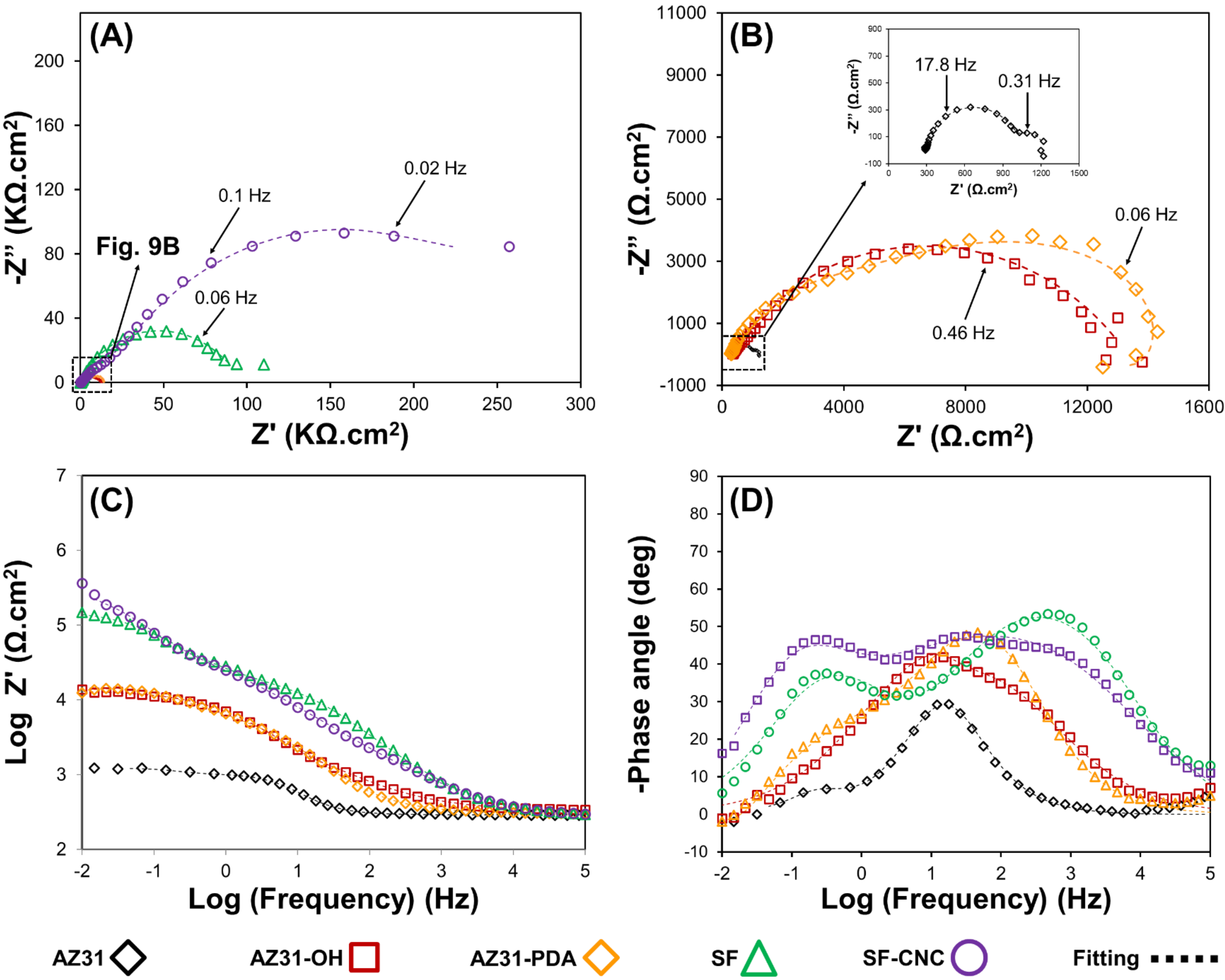

Fig. 3.9. EIS spectra of Mg samples performed in Hank's solution; Nyquist plots (A and B), Bode-impedance plots (C), and Bode-phase plots (D).

The effect of PD modification on the corrosion protection properties of the SF-CNC coating was also investigated through EIS measurement. Figure 3.10 shows the Nyquist EIS spectra of SF-CNC coating on the AZ31-OH surface with and without subsequent PD modification with the corresponding cross-sectional SEM images of the coating/substate interfaces. As can be seen, the diameter of semicircle only slightly increased following the application of SF-CNC coating on AZ31-OH, implying a very limited improvement in corrosion protection offered by the coating. Moreover, an inductive loop appeared on the Nyquist spectrum at the low-frequency region, which is attributed to the pitting corrosion and adsorption/desorption of intermediates on the metal substrate [148]. The poor corrosion resistance of the SF-CNC coating on AZ31-OH is most likely because of the weak bonding between the polymer layer and the underneath metal substrate, which could result in interfacial delamination and loss of corrosion protection properties [200]. This assumption is further supported by the high magnified cross-sectional SEM images of the SF-CNC coating, where several cleavages were observed sporadically along the metal/coating interface, when the SF-CNC coating was applied on the AZ31-OH surface with no subsequent PD modification. In contrast, in the case of SF-CNC coating on the PD-modified AZ31-OH, the diameter of impedance arc was remarkably increased. Besides, no inductive loop was observed at the lower frequencies, suggesting the presence of a stable corrosion protective layer on the metal surface [153]. A similar enhancement effect of intermediary PD layer on the corrosion protection performance of an externally applied polymeric coating has been previously reported in several studies and attributed to the higher adhesion at substrate/coating interface resulted from the chemical interactions as well as mechanical anchoring between the organic coating and the PD surface [121, 200-202]. The results clearly indicated that the presence of the intermediary PD layer with improved adhesiveness to the secondary coating is decisive to acquire a notable corrosion protection offered by the SF-CNC coating.

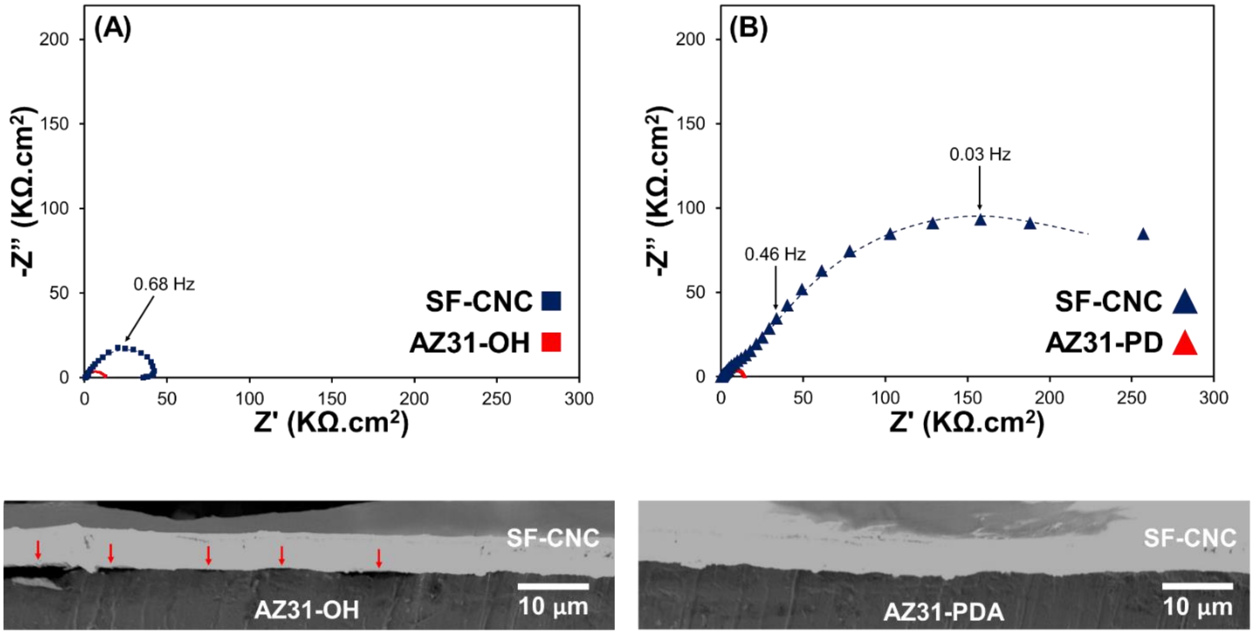

Fig. 3.10. Nyquist EIS spectra of SF-CNC coating on non-treated (A) and PD-modified (B) AZ31-OH surface and the corresponding cross-sectional SEM images of the coating/substate interfaces; Red arrows point to the interfacial gaps between the coating and the substrate.

Appropriate electrical equivalent circuits (EECs) (Figure 3.11) were employed for each group of the samples to further analyze the EIS results, and the electrochemical parameters from using equivalent circuit fitting of each model are summarized in Table 3.4. The EEC1 used for bare AZ31 and AZ31-OH was expressed as $R_s(CPE_1(CPE_{dl}\ R_{ct})R_1)$ to describe a surface with an outer oxide layer due to natural oxidation of the Mg alloy or alkaline treatment [203], where R_s represents the electrolyte resistance, R_1 and CPE_1 represent the resistance and capacitance of the outer layer, and R_{ct} and CPE_{dl} appear for the interfacial charge transfer resistance and electric double-layer capacitance, respectively. In the case of AZ31-PD, an R_L-L component was implemented and the EEC2 was expressed as $R_s(CPE_1(CPE_{dl}\ R_{ct}\ R_L\text{-}L)R_1)$ to account for the pseudo-inductive behavior at the low-frequency region, which is reported to be associated with the adsorption/desorption of intermediates on the metal substrate dissolution and pitting corrosion

[151]. For the SF and SF-CNC coated samples, the employed EEC3 consists of two equivalent circuits in series expressed as $R_s(CPE_1\ R_1)(CPE_{dl}\ R_{ct})$, where CPE_1 and R_1 represent capacitive behavior and the resistance of the barrier coatings, respectively. It should be mentioned that constant-phase elements were implemented in all EEC models instead of ideal capacitors to reflect the intrinsic inhomogeneity of the coatings and the metal surface as well as minimizing the fitting error [12]. According to Table 3.4, the highest R_{ct} value (31.2 $k\Omega.cm^2$) was found for SF-CNC, implying the highest impedance of the corrosion reaction and therefore the best corrosion protection performance. Moreover, SF-CNC had also the highest R_1 among all the samples, indicating the superior barrier properties of the composite SF-CNC coating.

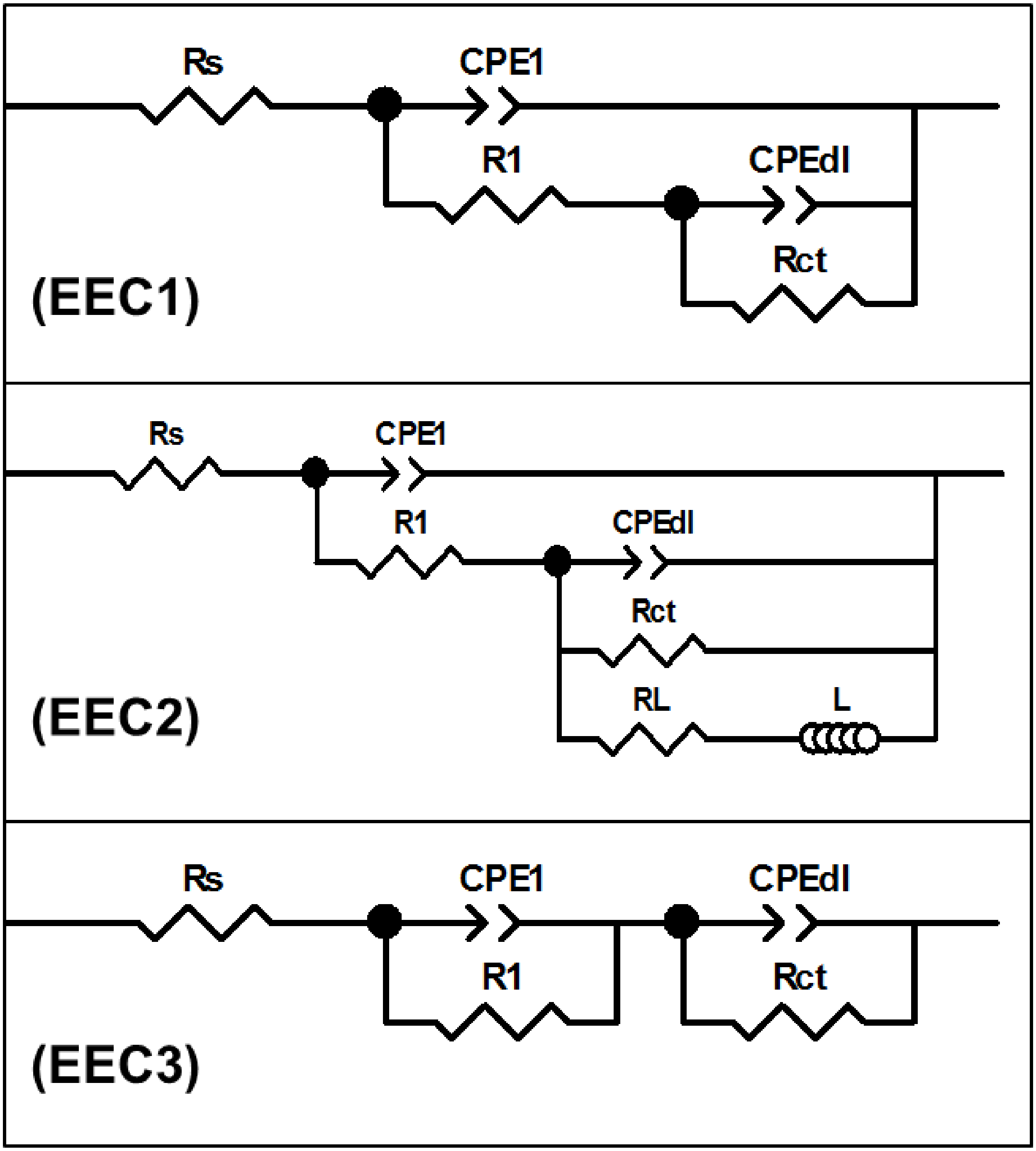

Fig. 3.11. Electrical equivalent circuits employed for fitting the EIS spectra of AZ31 and AZ31-OH (EEC1), AZ31-PD (EEC2), and SF and SF-CNC (EEC3).

Table 3.4. Representative fitting results of EIS spectra of Mg samples using appropriate equivalent electrical circuits.

Samples	R_s ($\Omega.cm^2$)	R_1 ($\Omega.cm^2$)	Q_1 ($F.cm^{-2}$)	n_1	R_{ct} ($\Omega.cm^2$)	Q_{dl} ($F.cm^{-2}$)	n_2	R_L ($\Omega.cm^2$)	L ($H.cm^2$)	Chi^2
AZ31	2.91×10^2	7.56×10^2	4.26×10^{-5}	0.89	1.71×10^2	4.36×10^{-3}	0.99	-	-	0.0050
AZ31-OH	3.28×10^2	6.75×10^3	2.37×10^{-5}	0.61	6.22×10^3	1.19×10^{-6}	0.99	-	-	0.0027
AZ31-PD	3.02×10^2	6.84×10^3	1.14×10^{-5}	0.75	8.27×10^3	8.63×10^{-5}	0.75	3.04×10^4	2.31×10^5	0.0021
SF	2.69×10^2	1.41×10^5	1.19×10^{-5}	0.71	1.56×10^4	2.19×10^{-6}	0.70	-	-	0.0021
SF-CNC	2.54×10^2	2.63×10^6	1.33×10^{-5}	0.78	3.12×10^4	8.52×10^{-6}	0.57	-	-	0.0014

To further understand the long-term corrosion behavior, the samples were studied by EIS as a non-destructive technique during a 7-day immersion test in Hank's solution. Nyquist and Bode plots of the samples after 0, 1, 3, and 7 days of immersion are presented in Figures S3.2-S3.6. $|Z|_{0.01Hz}$ values were employed to investigate the overall corrosion resistance of the sample at different time intervals, while a higher $|Z|_{0.01Hz}$ value generally reflects a lower corrosion rate of the corroding metal [144]. As shown in (Figure 3.12), the $|Z|_{0.01Hz}$ of bare AZ31 surface slightly increased by time and kept the same level of resistance until the end of the test, which can be attributed to the formation of surface corrosion products (mainly phosphates [12]) that can serve as a barrier against the corrosion medium. However, this layer is not strong enough to resist the aggressive corrosion process because of its loose and porous structure [160]. For AZ31-OH, the $|Z|_{0.01Hz}$ values continuously dropped within the immersion time. Although the formed $Mg(OH)_2$ layer from the alkaline treatment can initially improve the corrosion resistance by isolating the Mg substrate from the corrosion medium, with the presence of chloride ions in the corrosion electrolyte, the oxide layer will be converted into a much less stable $MgCl_2$ layer with poor barrier properties, resulting in a constant drop of impedance value over time [102]. AZ31-PD showed also a similar decreasing trend in corrosion resistance like AZ31-OH, indicating that the deposited PD layer is not able to protect the metal surface against the corrosive ions and species present in the media. In the case of coated samples (SF and SF-CNC), the $|Z|_{0.01Hz}$ values started to decline with prolonged immersion time most likely due to the gradual diffusion of water and corrosive species into the coatings and decrement of the physical barrier properties over time. Similar observations have been reported in previous studies for Mg alloys coated with SF-based coatings [13, 108, 123, 190]. Compared to the SF, the SF-CNC showed less variations in $|Z|_{0.01Hz}$ values during the immersion period while it had the highest $|Z|_{0.01Hz}$ among all the samples at the end of the immersion test, showing its superior long-term barrier properties and durable corrosion protection. The degradation mechanism of the coated samples can be explained as follows. Following the immersion of coated samples in Hank's solution, water and corrosive species start penetrating through the coatings and cause volume expansion and subsequently swelling of the coating [123]. Meanwhile, the generation of H_2 gas resulting from the reaction of Mg and water molecules (section 3.4.2) on the metal surface further contributes and results in the emergence of narrow cracks on the SF coating [190]. With the increasing of immersion time, the cracks become broader, resulting in increased metal surface exposure to the media and further corrosion. Nonetheless, the composite SF-CNC coating, owing to the enhanced barrier properties as a results of CNC incorporation can mitigate the penetration of water and corrosive ions through the coating, hence lower the corrosion reaction rate of the underneath Mg substrate. The results of the *In vitro* immersion corrosion tests (section 3.4.2) including the post-corrosion surface SEM images of the coated samples, pH change, and hydrogen evolution measurements were all found to be in agreement with the proposed mechanism.

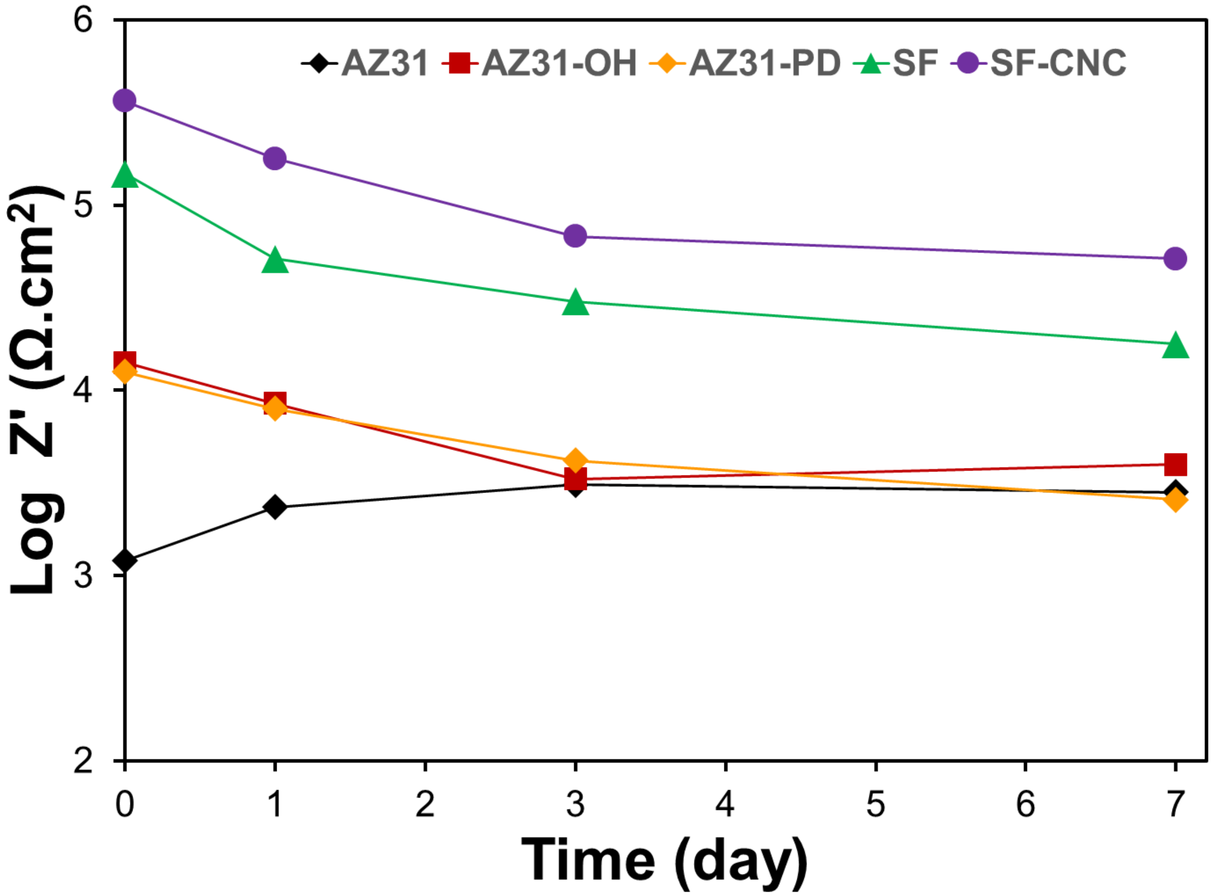

Fig. 3.12. Variation of log $|Z|_{0.01Hz}$ values of the samples over 7 days of immersion in Hank's solution.

3.3.4.2 Immersion Corrosion Tests

Immersion tests were carried out to further study the long-term degradation behavior of the bare and modified Mg alloys over a period of 14 days. Since pH increment of the corrosion media and evolution of hydrogen gas co-occur with the corrosion of Mg alloys (according to following equation), they can be used as reliable corrosion indicators of Mg-based alloys [157].

$$Mg + 2H_2O \rightarrow Mg^{2+} + 2OH^{-} + H_2\ (g)$$

As shown in Figure 3.13A, in the case of bare AZ31, the pH value of the corrosion media at the end of the 14-day immersion test was found to be 11.50 ± 0.20, which was significantly higher than 11.08 ± 0.14 for the AZ31-OH, 10.90 ± 0.07 for the AZ-PD, 9.71 ± 0.19 for the SF, and 9.11 ± 0.26 for the SF-CNC samples, showing a very high reactivity and rapid corrosion of the unmodified AZ31 alloy. A similar trend was observed in the hydrogen evolution measurements (Figure 3.13B). The AZ31 substrate released the highest volume of hydrogen (15.08 ± 0.33 $mL.cm^{-2}$) among all samples after 14 days of immersion, while the final accumulated H_2 volumes were found to be 7.90 ± 0.68 $mL.cm^{-2}$, 8.70 ± 0.40 $mL.cm^{-2}$, 5.51 ± 0.70 $mL.cm^{-2}$, and 3.22 ± 0.31 $mL.cm^{-2}$ for AZ31-OH, AZ31-PD, SF, and SF-CNC, respectively. The results clearly indicated the superior corrosion protection offered by SF-based coatings, which became more significant after incorporation of CNC into the coatings. Like the SF-CNC coating, the pure SF coating was quite effective in slowing down the alkalization and hydrogen evolution, but only during the initial days. By increasing the immersion time, the pH values and the hydrogen generation rates started to increase and deviated from those of SF-CNC samples. Although being able to render a temporary protection as a result of a thick and dense polymer layer, it is evident that the pure SF coating cannot provide a steady and prolonged protection against corrosion.

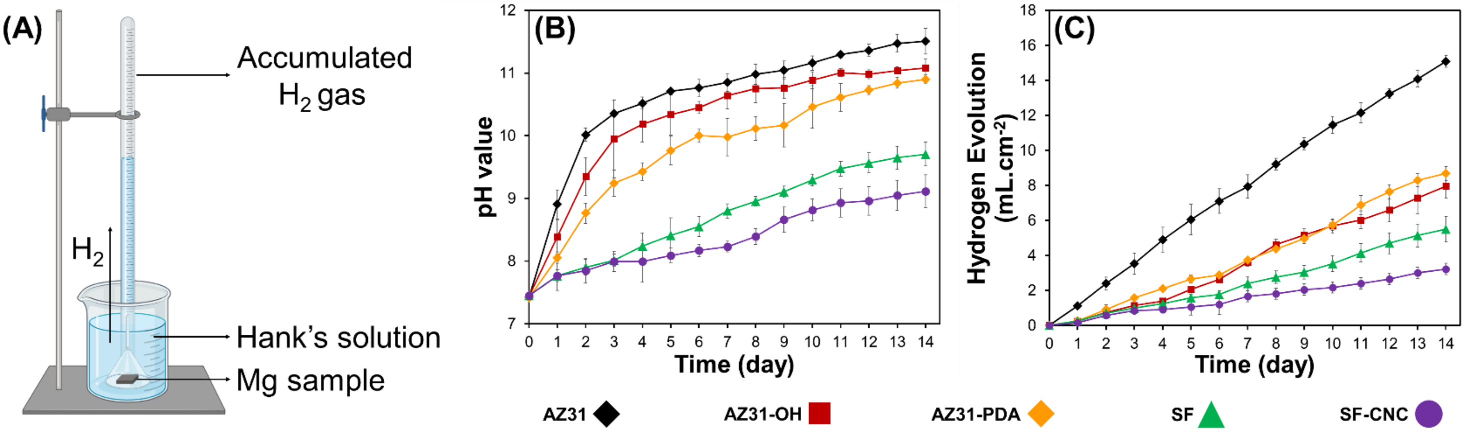

Fig. 3.13. Variation in pH value (A) and hydrogen evolution volume (B) of each group of the samples during immersion in Hank's solution at 37 °C for 14 days.

SEM was employed to observe the post-corrosion surface morphology and comparatively evaluate the severity of corrosion on different samples during 14 days of immersion in Hank's solution (Figure 3.14). The post-corrosion SEM images were found to be in a good agreement with the results of pH and hydrogen evolution measurements. As can be seen, thick layers of corrosion products cumulatively formed on the surfaces of uncoated AZ31, AZ31-OH, AZ31-PD samples after 7 and 14 days of immersion, implying that they severely corroded during the immersion test. For the SF coating, although much smaller amount of corrosion products was found on the surface compared to those of uncoated samples on day 7, there still appeared several cracks on the surface. Emergence of these wide cracks is extremely detrimental for the protective coating, as it weakens the barrier properties in long-term and results in the exposure of the underlying Mg substrate to the corrosive electrolyte [24]. Therefore, severe signs of corrosion were observed on the SF surface after 14 days, like those occurred on the uncoated samples surfaces. In contrast, the SF-CNC presented a more uniform and intact surface with much less apparent corrosion products after 14 days of immersion. Although there were still some tiny cracks appeared on the coating, they were much slender than those appeared on the pure SF coating. This is most likely due to the higher content of β-sheet in the SF-CNC along with the inherent anticorrosion properties of the CNC, which will be discussed in detail in section 3.5. Overall, the results of electrochemical corrosion measurements and *in vitro* immersion study demonstrated that the SF-CNC coating has superior barrier properties and can effectively enhance the corrosion resistance and provide a prolonged protection for the underlying AZ31 substrate against corrosion.

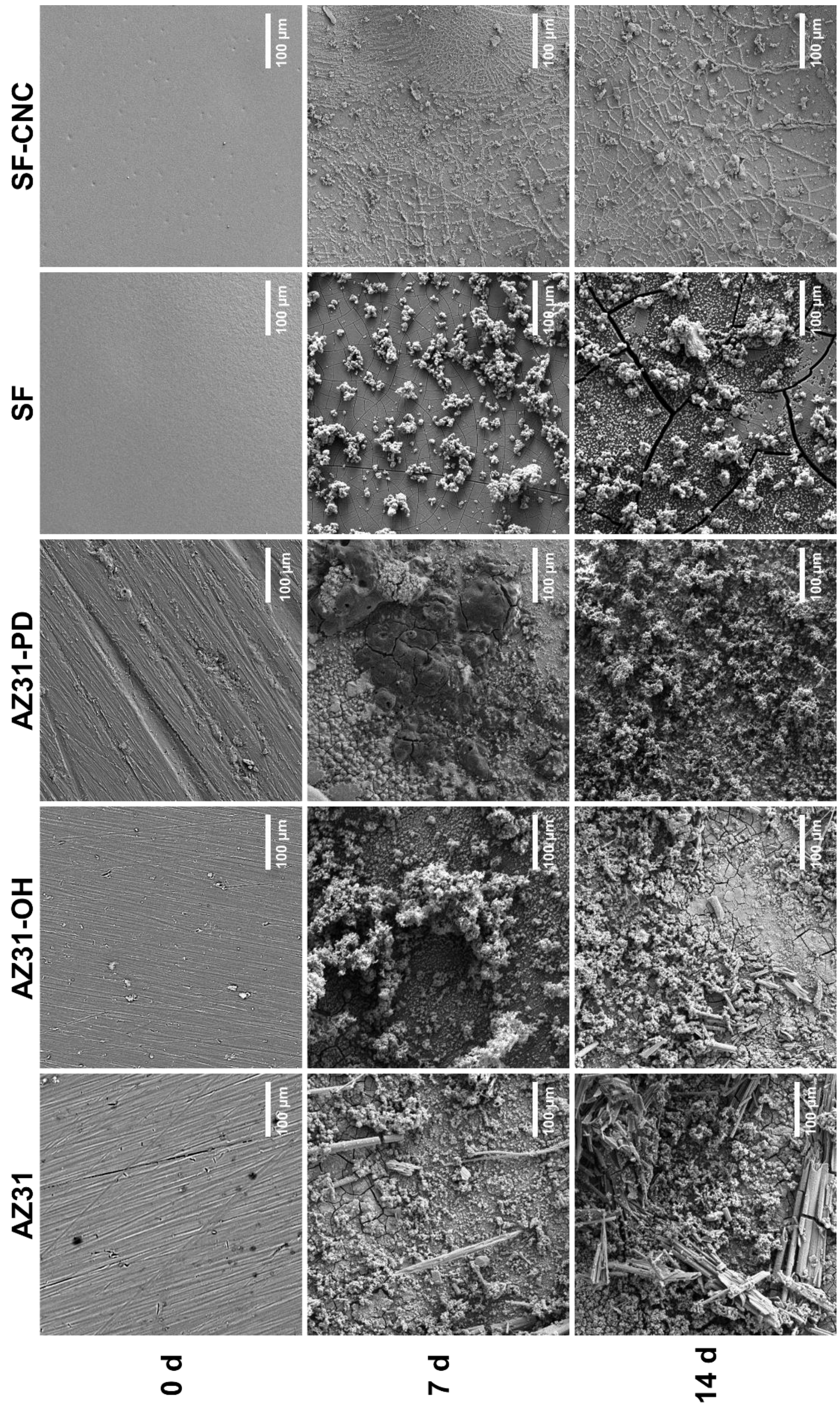

Fig. 3.14. SEM images of bare, pretreated, and coated Mg samples before and after immersion in Hank’s solution for 7 and 14 days at 37 °C.

3.3.5 Mechanism of Corrosion Resistance Enhancement of CNC

Different mechanisms have been proposed to explain the improved corrosion resistance of CNC-containing composite coatings. He et al. has found that the incorporation of CNC into a waterborne hydroxyacrylate-based coating decreased the water uptake capacity of the coating due to the strong hydrogen bonding between CNC and polymeric matrix, and thus retards the penetration of water and corrosive species to the metal surface [168]. Similarly, the results of ATR-FTIR in this study (section 3.2.2) also suggested the presence of strong hydrogen bonding between the SF matrix and CNCs. It was also proposed by the same group that the formation of complexes between the released metal cations and the anionic half ester sulfate groups on CNCs may also contribute in enhancing corrosion resistance [170]. In addition to the all above mentioned mechanisms, the higher crystallinity (β-sheets percentage) of the SF-CNC coating (based on the results of deconvolution analysis) is likely another possible reason behind the improved corrosion resistance properties of this coating compared to the blank SF coating, as the superior water insolubility and corrosion resistance of the SF-based coatings with higher crystallinity percentages have been previously reported in other studies [19, 180, 204].

3.3.6 *In vitro* Cytocompatibility

Biocompatibility is a primary requirement for any material intended to be used as bio-implant. *In vitro* cytocompatibility was investigated as an initial criterion in the assessment of biocompatibility [205] by measuring the viability of hFOB cells exposed to leachates of the samples and observing their morphology after adhesion to the samples. Figure 3.15 presents the viability percentage of hFOBs cultured with the 3-day and 5-day leachates from different samples. For uncoated Mg samples (AZ31, AZ31-OH, and AZ31-PD), the viabilities were relatively low (< 80%) at both intervals, showing that the surfaces were unfavorable for hFOB cell growth.

Moreover, no significant differences in viability percentages of uncoated samples were observed at any time intervals, indicating that none of these surface modifications (alkaline treatment and PD deposition) can remarkably enhance the cytocompatibility of the AZ31 alloy. In contrast, the viabilities of SF and SF-CNC coated samples were significantly higher than those of uncoated samples at both 3-day and 5-day intervals (P-value < 0.001). Having high viabilities (above 100%) at both time points indicated that not only the SF and SF-CNC coatings were not cytotoxic but also, they could support the growth and proliferation of hFOB cells. Besides, no distinct difference between the viability of SF and SF-CNC was observed at any incubation times, suggesting the non-toxic nature of CNC as a bio-safe anticorrosion filler for the SF coating.

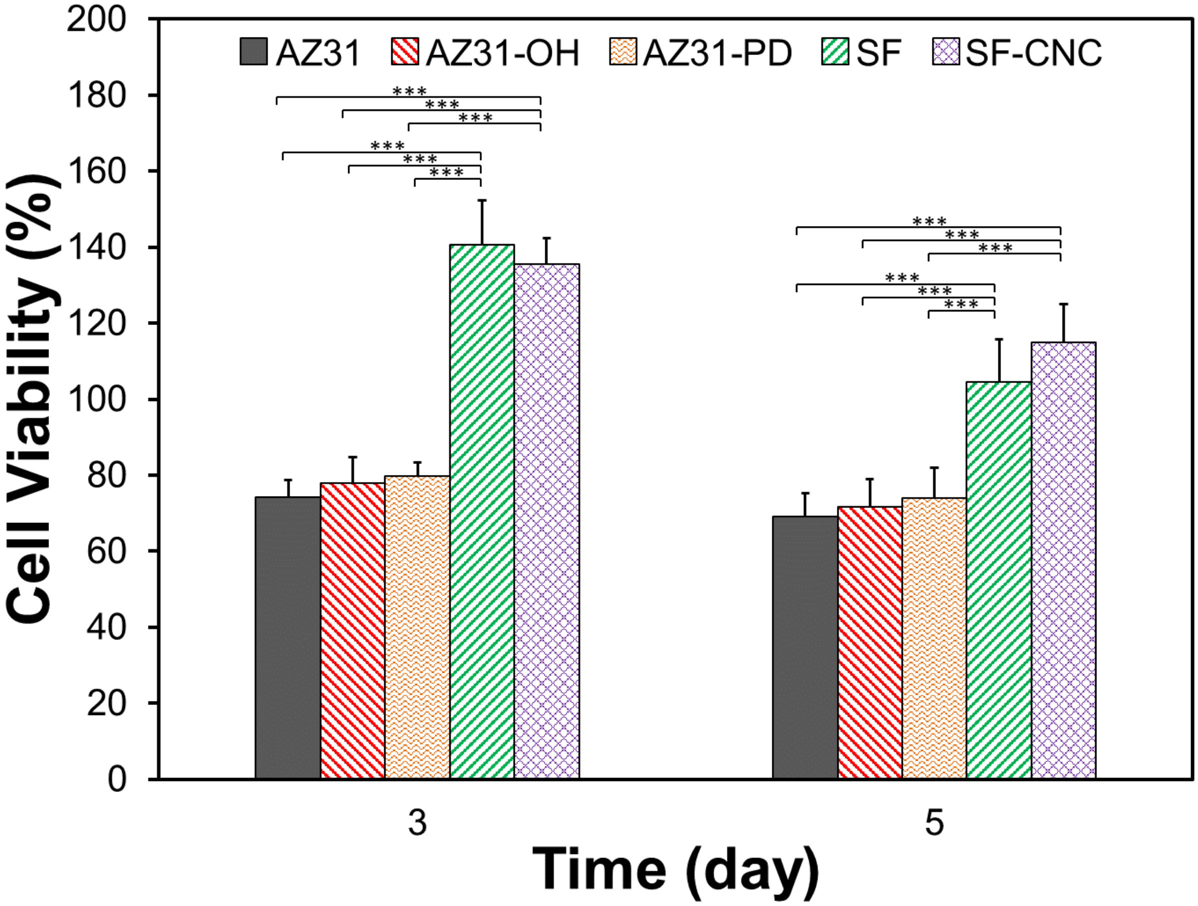

Fig. 3.15. Viability of hFOB cells exposed to sample extracts of 3 and 5 days compared to control cells grown in pure media measured by CCK-8 assay kit; *** indicates P-value < 0.001.

Figure 3.16 shows the fluorescence staining images of hFOB cells cultured on different substrates for 24 h. As can be seen, the number of cells adhered to SF and SF-CNC coatings is much higher compared to those of uncoated samples, almost covering all over the surfaces. Moreover, obvious differences in cellular morphologies were observed on the various surfaces. While the cells adhered and elongated well on the SF and SF-CNC surfaces with extended morphologies, the cells on the uncoated samples exhibited a much less striated or, in some cases, a round-shape morphology. This observation suggested that SF and SF-CNC coatings enhanced cellular adhesion and spreading on the Mg substrates. The improved viability and cellular adhesion of the SF and SF-CNC coatings most likely arises from the hampered rapid degradation of the Mg alloy along with the excellent biocompatibility of the SF itself. The presence of protective coatings prevents the local alkalization, increased concentration of Mg^{2+}, and formation of excessive hydrogen gas within the culture media, which may otherwise damage transport channels of the cell membranes and cause cell necrosis [165]. Moreover, the favorable biocompatibility of SF toward bone cells as being reported previously in several studies [13, 108, 180, 206], likely contributes to the enhanced cellular responses observed in the coated samples. Altogether, the results clearly indicated that coating of AZ31 alloy with the SF and SF-CNC coatings remarkably enhanced the cytocompatibility of the bare Mg substrates both in terms of proliferation and adhesion.

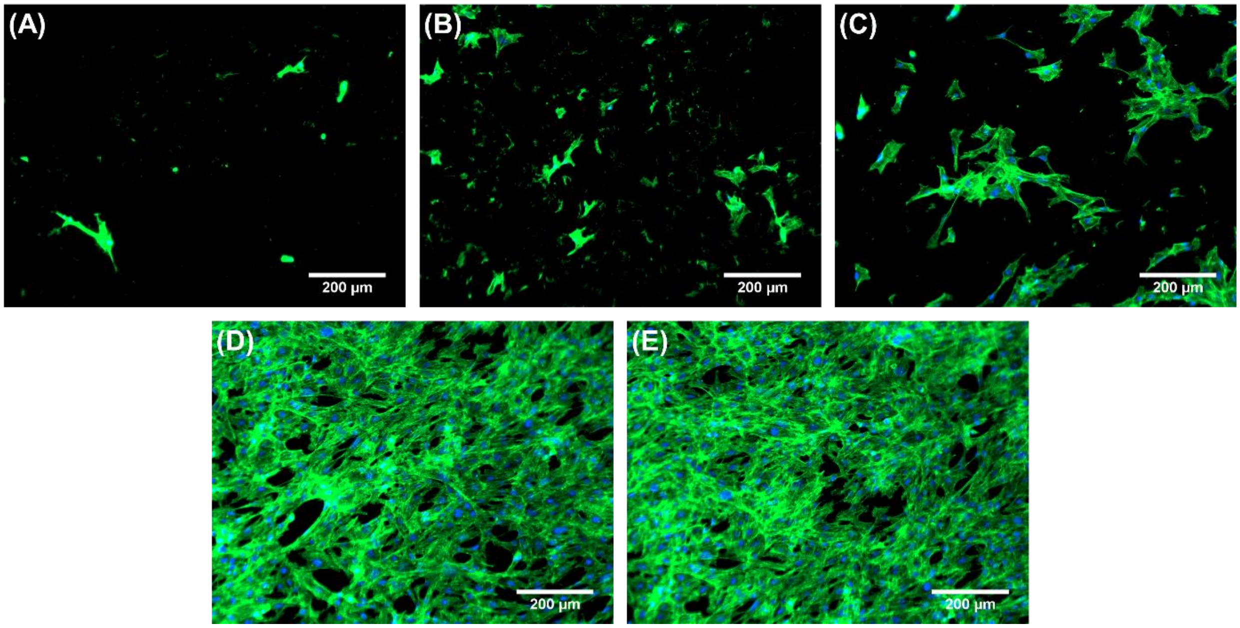

Fig. 3.16. Fluorescence images of actin-nucleus stained hFOB cells cultured on AZ31 (A), AZ31-OH (B), AZ31-PD (C), SF (D), and SF-CNC (E) for 24 h; Blue: DAPI; Green: F-actin.

3.4 Conclusions

In summary, we developed a multifunctional nanocomposite coating by incorporating CNCs into SF and demonstrated that the composite coating significantly improved the barrier and corrosion protection properties. The property enhancement could be attributed to the higher β-sheets content of CNC-reinforced SF coating as well as the intrinsic properties of CNC as an anti-corrosive nanofiller. Surface pretreatment of AZ31 substrate with polydopamine before applying the protective coating was found to be necessary to achieve a notable corrosion protection by the coating. In addition to the corrosion resistance properties, applying SF-CNC coating significantly enhanced the biocompatibility of AZ31 alloy with regards to cell viability and adhesion/spreading toward human fetal osteoblast cells. Taken all together, the natural CNC-reinforced SF coating with excellent biological and enhanced anticorrosion properties holds a great potential as an ideal candidate for surface modification of Mg alloys in bio-implant applications.

3.5. Supplementary Data

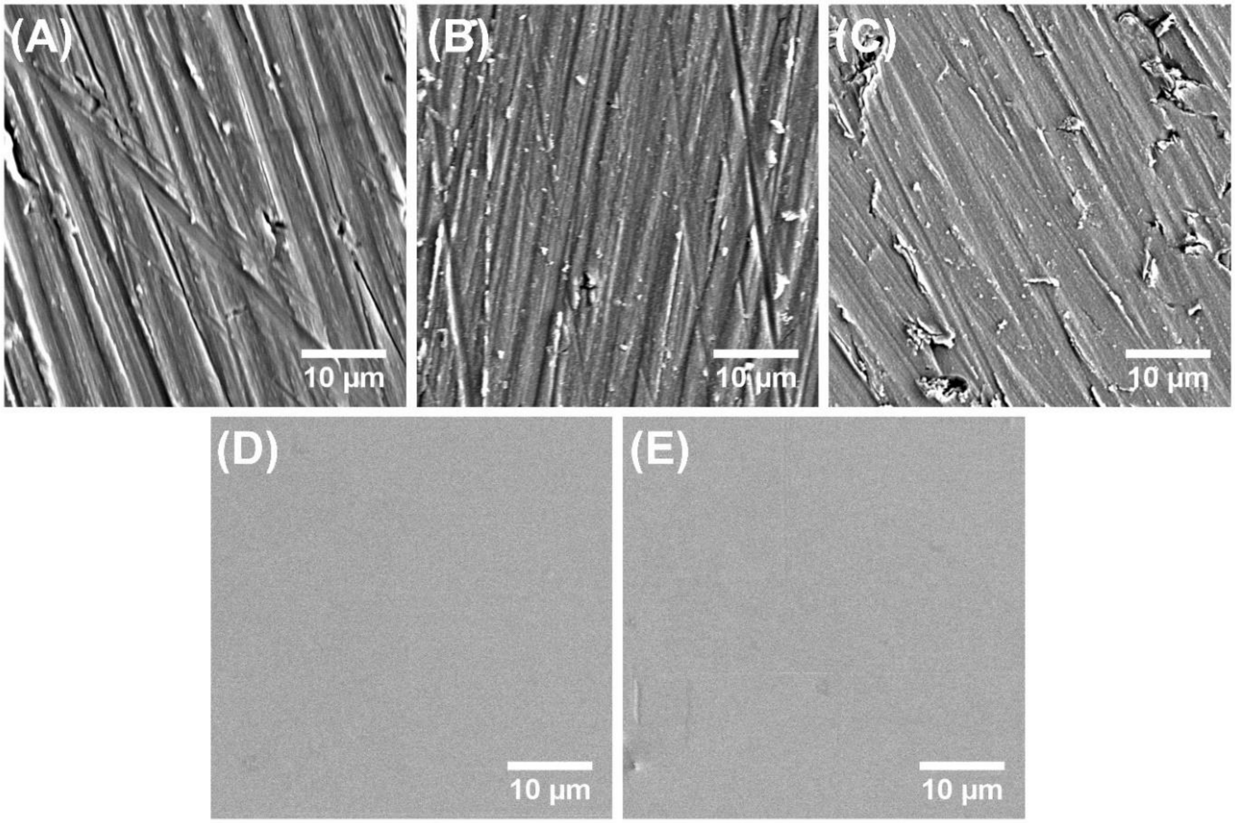

Fig. S3.1. Surface SEM images (higher magnification) of as-prepared AZ31 (A), AZ31-OH (B) AZ31-PD (C), SF (D), and SF-CNC (E).

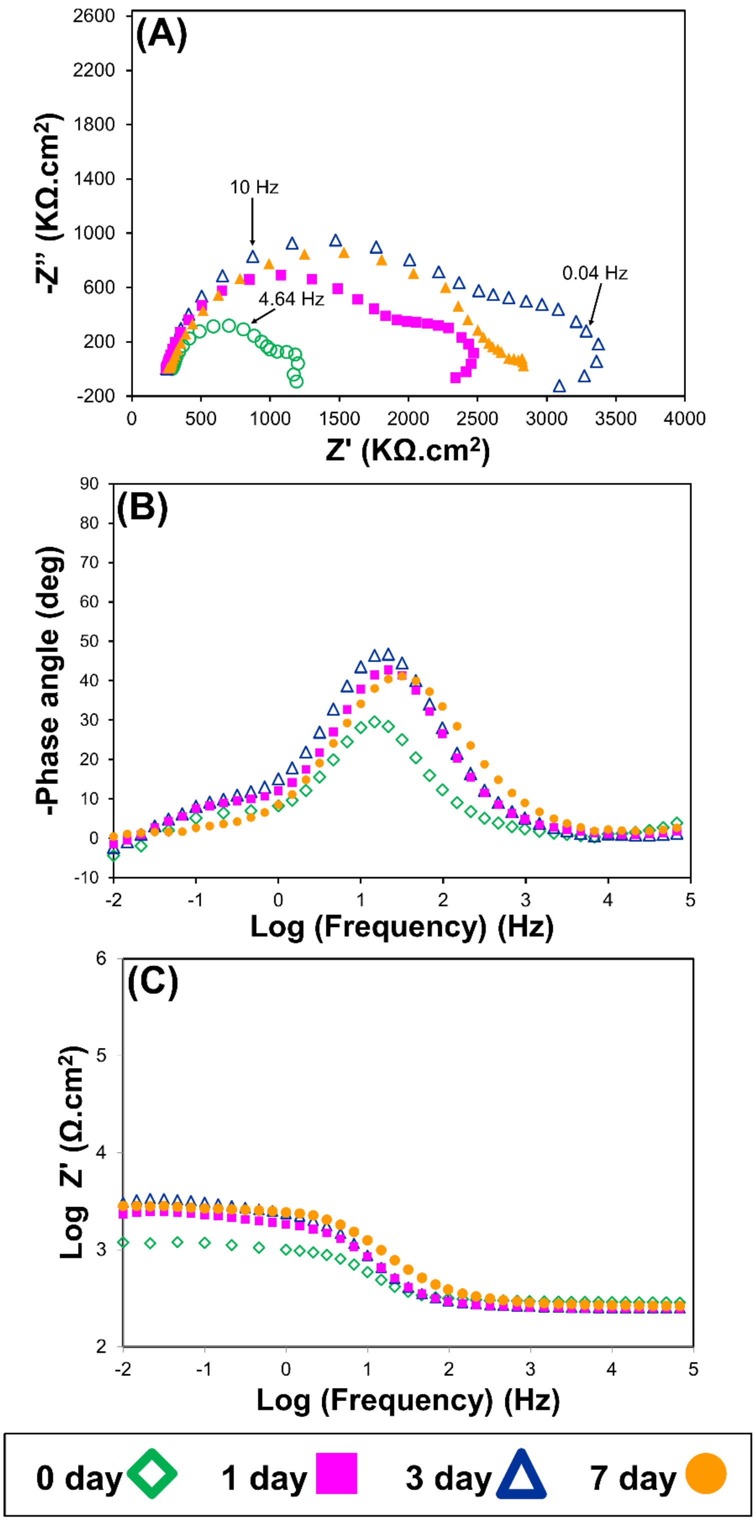

Fig. S3.2. Nyquist (A), Bode-phase (B), and Bode-impedance (C) plots of bare AZ31 at different time intervals during 7 days of immersion in the Hank's solution.

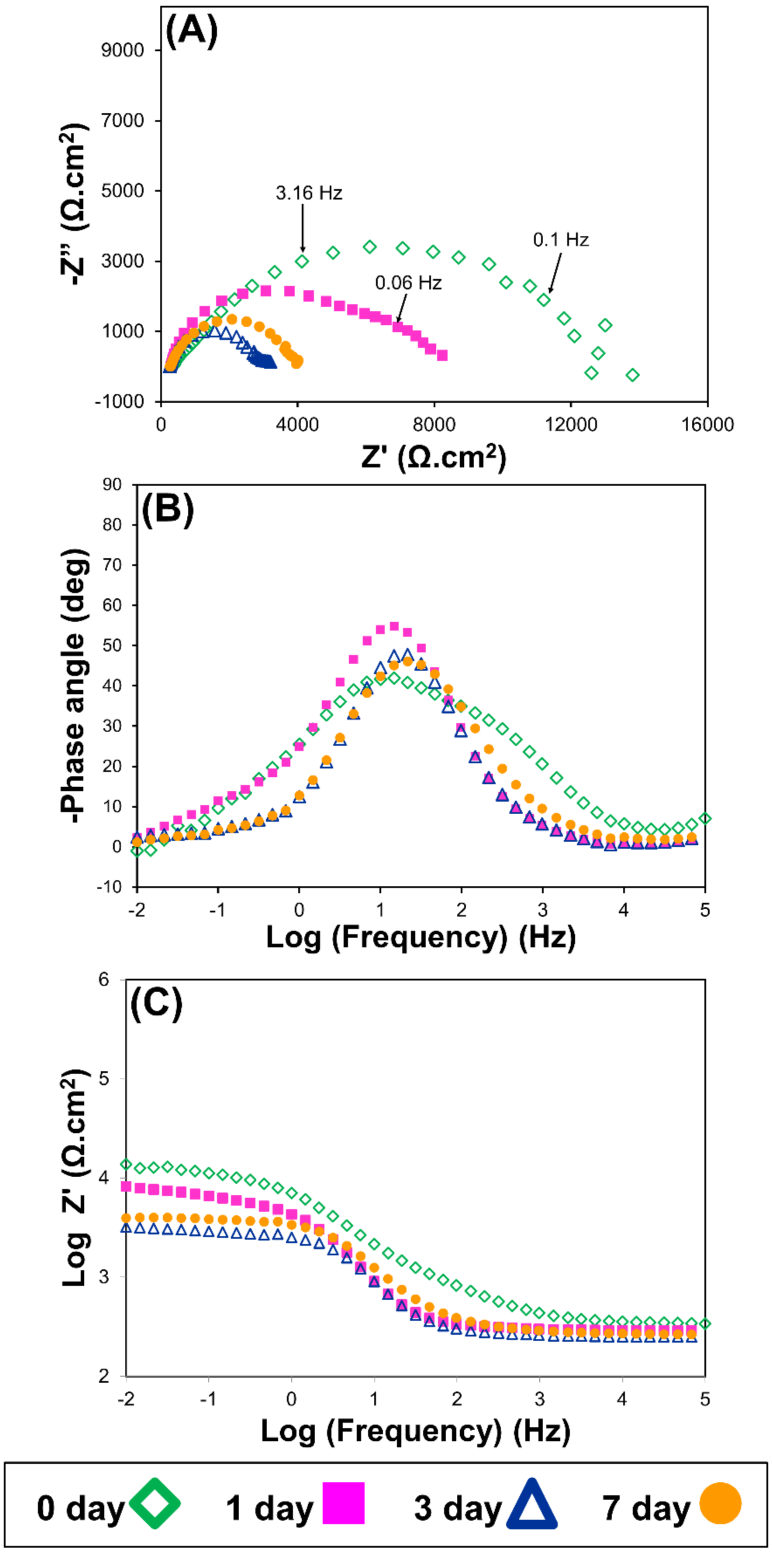

Fig. S3.3. Nyquist (A), Bode-phase (B), and Bode-impedance (C) plots of AZ31-OH at different time intervals during 7 days of immersion in the Hank's solution.

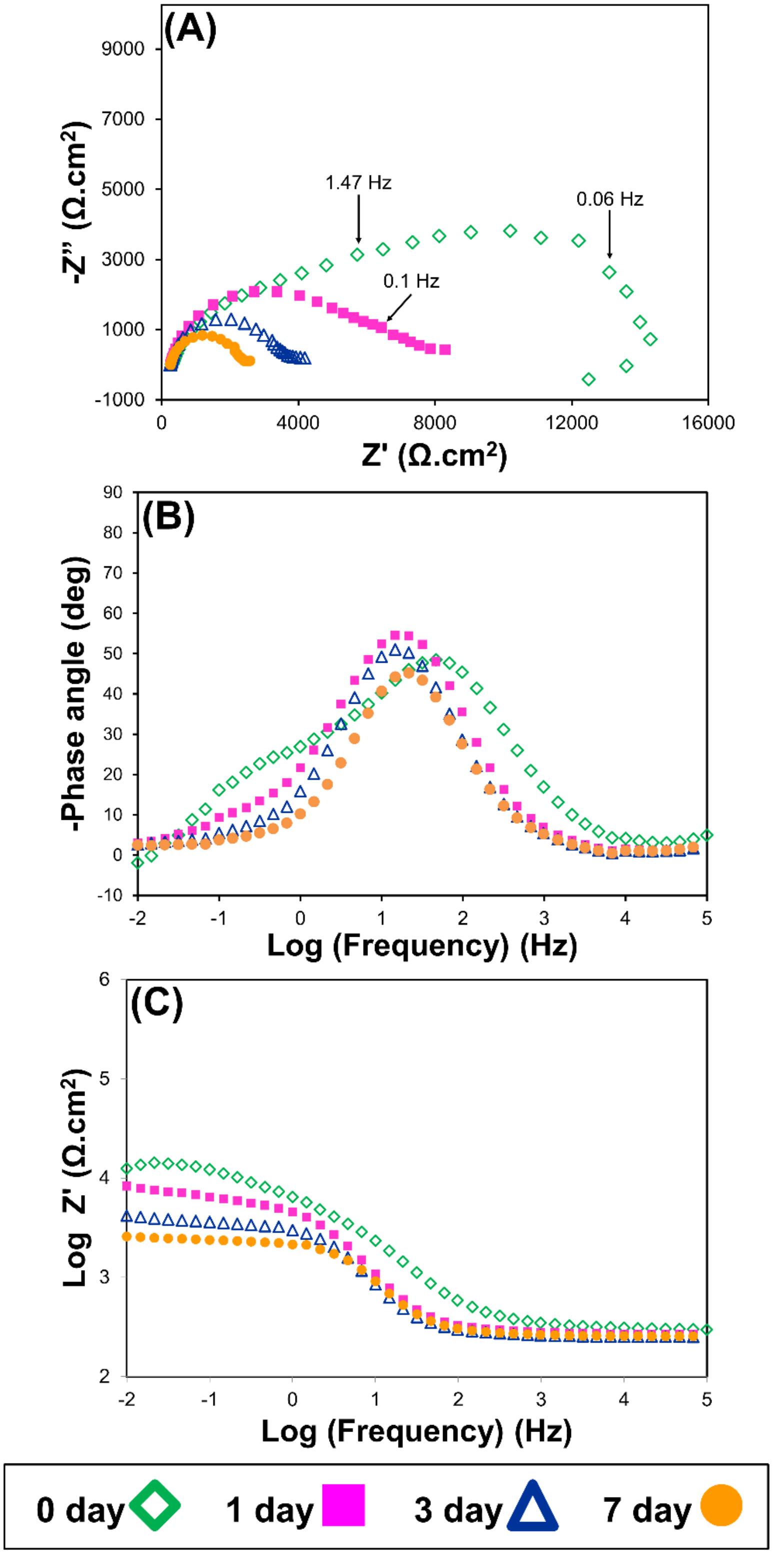

Fig. S3.4. Nyquist (A), Bode-phase (B), and Bode-impedance (C) plots of AZ31-PD at different time intervals during 7 days of immersion in the Hank's solution.

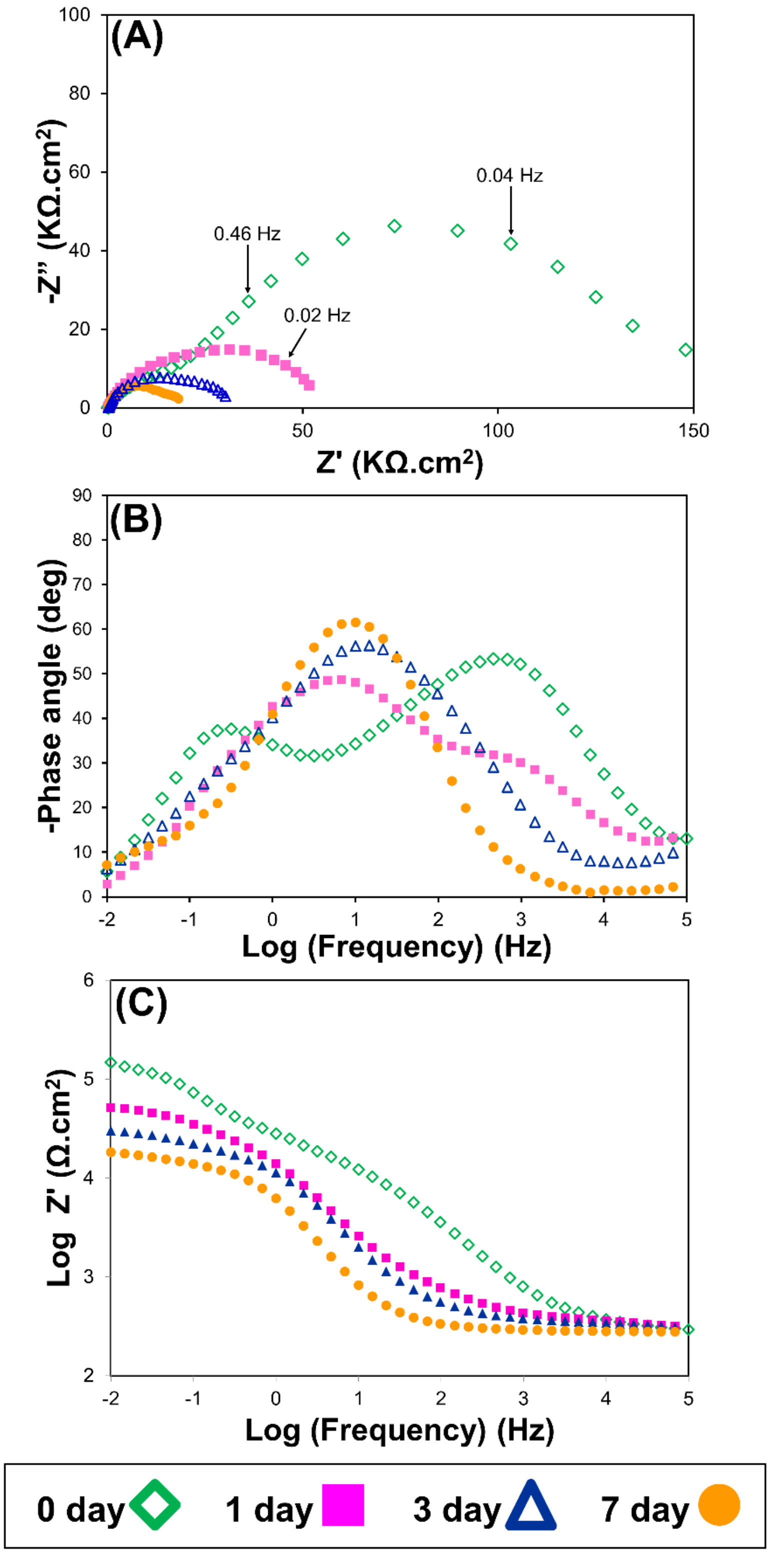

Fig. S3.5. Nyquist (A), Bode-phase (B), and Bode-impedance (C) plots of SF at different time intervals during 7 days of immersion in the Hank's solution.

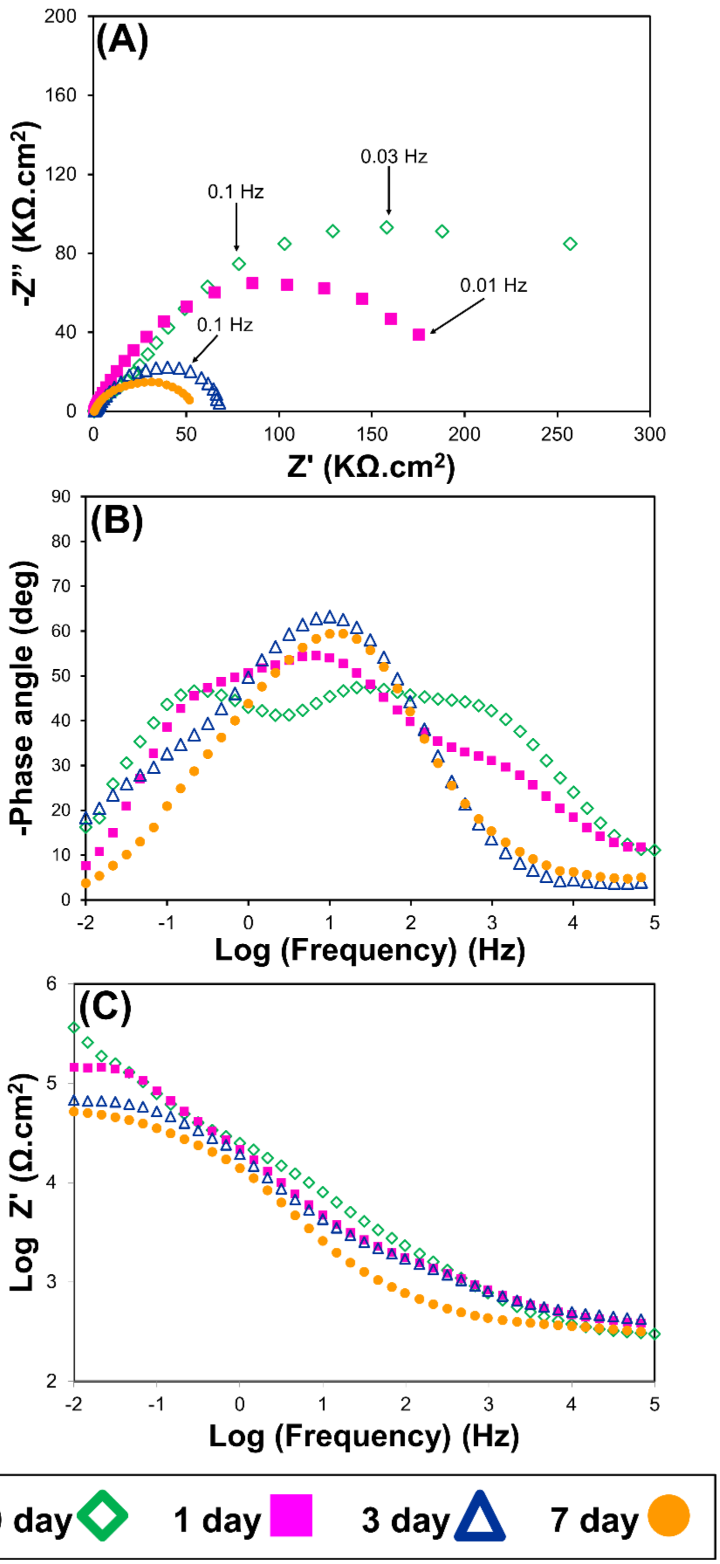

Fig. S3.6. Nyquist (A), Bode-phase (B), and Bode-impedance (C) plots of SF-CNC at different time intervals during 7 days of immersion in the Hank's solution.

CHAPTER 4

MICROBIAL CORROSION OF STAINLESS STEEL DENTAL IMPLANT INDUCED BY STREPTOCOCCUS MUTANS BACTERIUM

Hamid Asadi, Baviththira Suganthan, Or Zolti, Austin Duncan, and Ramaraja P. Ramasamy. To be submitted to Journal of The Electrochemical Society.

Abstract

Stainless steel (SS) is one of most commonly used metals for dental implant application due to its high corrosion resistance and cost-effectiveness. The oral environment is a perfect medium for bacteria growth and colonization on dental implant surfaces. This study investigated the corrosive effect of a common oral pathogen, *Streptococcus mutans (S. mutans)*, on bare 316L and polyurethane (PU) coated SS by various electrochemical and surface examination techniques. The results clearly showed that *S. mutans* negatively affects the corrosion resistance of both bare and PU-coated SS substrates under anaerobic condition. This highlighted the importance of microbiologically influenced corrosion of dental implant materials *in vivo* and the need for approaches for its mitigation.

4.1 Introduction

In the chapters 2 and 3, we focused on the corrosion of Mg alloys and the application of polymeric coatings to improve their corrosion resistance for biodegradable implant application. In this chapter, we shifted our focus from conventional corrosion to microbiologically induced corrosion as another important type of corrosion that implants may undergo in when placed the physiological environment. The application of biomaterials in the oral cavity has increased due to esthetic, surgical, and biofunctional reasons, mainly as elements of dental prosthetics, screws, implants, and orthodontic materials. Metals are mostly used in these applications due to their high tensile strength, ease of sterilization, and fracture toughness [207]. Despite all their advantages, corrosion is a major concern when it comes to metals as it causes the release of metallic ions from the metallic implants. The release of metallic ions into the human body is known to cause several health complications including direct DNA damage, allergies, and cancer [208]. The complex oral environment is a perfect culture medium for the microbial colonization promoting preferential growth of aerobic or anaerobic microorganisms. Microorganisms have a strong tendency to populate on any surfaces including metals, giving rise to a complex and strongly adhering microbial community, called "biofilm". Formation of biofilms has been widely reported to be highly detrimental to the underlying substrates as it may cause an accelerated physical degradation and corrosion of metal surfaces, which is commonly known as microbiologically-induced corrosion (MIC) or bio-corrosion. The role of microorganisms in corrosion has been extensively discussed in the literature for sewage and pipeline industry, however, the number of studies is much lower when it comes to the biological environment, including the dental implant application.

Recently, the application of polymeric coatings has received considerable attention as a promising approach to protect the metallic implant against corrosion and overcome some of the common shortcoming of implant materials such as poor osteointegration and cellular responses. Different kinds of polymers have been applied for dental implants and orthopedic applications including chitosan, polylactide, polycaprolactone, and poly(lactic-co-glycolic acid) [209]. While the abovementioned coatings have been generally reported to enhance the corrosion resistance of the metallic implants, their performance have never been evaluated against MIC.

This study aimed to investigate the effects of *S. mutans* on 316L SS corrosion *in vitro* under anaerobic conditions and in the presence of sucrose to mimic the oral environment. 316L SS has been extensively used in dentistry due to its low cost, low toxicity, and comparably high corrosion resistance. In addition to bare SS, polyurethane (PU), a biocompatible polymer widely used in biomedical applications including bio-implant coatings [210, 211], was used a model coating material on SS to represent a polymeric coated SS substrate in this study. Various electrochemical measurements, surface analysis, and characterization techniques were employed to evaluate the corrosion resistance of SS samples and the effect of *S. mutans* on that.

4.2 Materials and Methods

4.2.1 Materials

Tetrahydrufuran (THF) anhydrous was purchased from TCI Chemicals. All aqueous solutions were prepared using ultrapure water purified with a Milli-Q Millipore system. All other reagents, unless otherwise specified, are of reagent grade.

4.2.2 Preparation of SS Substrates

Commercially available 316L stainless steel sheets ((wt%): Fe: balance; C: <0.03%; Cr: 17%; Ni: 14%; Mo: 2.6%; Mn: 2.0%; Si: 0.5%; N: 0.1%; S: 0.01%) [212] with dimension of 2.75×2.75 cm and thickness of 1 mm were polished by 2500-grit SiC abrasive paper to remove the natural metal oxides layer and obtain a uniform roughness. Then, they were sonicated in absolute ethanol and water each for 5 min to remove any surface contaminations, and finally dried at 60 °C.

4.2.3 Fabrication of the PU coated SS

PU coated SS was prepared by the solution casting method. First, PU solution (4% w/v) was prepared by dissolving PU granules in THF using a magnetic stirrer for 4 h to obtain a homogenous solution. The resulting PU solution (2 mL) was pipetted on SS samples and dried under the hood for 24 h at room temperature. During the drying process, all samples were placed on glass Petri dishes with closed lids to control the solvent evaporation rate. The fabricated sample was labeled as "PU". Meanwhile, specimens coated with pure PU were also prepared as controls under the same condition and denoted as "PU-SS".

4.2.4. Material Characterization

Surface morphologies of the samples were observed using a field emission scanning electron microscope (SEM, FEI Teneo, FEI Co.). All samples were coated with 10 nm of gold layer before SEM observation. Chemical structures of the samples were studied by attenuated total reflectance-Fourier transform Infrared (ATR-FTIR) analysis using a Nicolet 6700 spectrometer (Thermo Electron Corporation, MA, USA). The spectra were recorded over the wavenumber range of 4000-800 cm^{-1} with 64 scans and a resolution of 4 cm^{-1} for each measurement.

4.2.3 Bacteria Strain and Culture

S. mutans ATCC 25175 was taken from a frozen culture medium. The bacteria were grown on agar plates for 48 h at 37 °C. The bacterial cells were inoculated in BHI (1 colony added to 3 mL of liquid culture) and incubated for 18 h at 37 °C and 200 rpm. After incubation, the cells were harvested by centrifugation for 10 min at 4 °C and 5000 rpm and washed twice with AS solution.

The bacterial density was found to be 10^8 CFU/mL in the final solution. All the bacterial cultures were conducted under anerobic conditions using a GasPak anaerobic system in a standard anaerobic jar.

4.2.4 *In vitro* corrosion studies

All the electrochemical and *in vitro* corrosion studies were carried out in Fusayama-Meyer artificial saliva solution containing 0.4 g/L NaCl, 0.4 g/L KCl, 0.906 g/L $CaCl_2{\cdot}H_2O$, 0.69 g/L $NaH_2PO4{\cdot}{}_2H_2O$, 0.005 g/L $Na_2S{\cdot}9H_2O$, and 1 g/L urea. The solution was the enriched with 5 g/L yeast extract and 10 g/L sucrose to simulate eutrophic and high-sugar oral environments, and to provide nutrition for the microorganisms during long-term corrosion experiments and labeled as "AS" [208]. AS was sterilized at 121 ºC for 20 min in an autoclave before further use. For the experiment in the presence of *S. Mutans*, 1 mL of the bacterial solution (10^8 CFU/mL) was added to 6 mL of AS solution under sterile condition and labeled as "AS-*S.mu*" solution

4.2.4.1 Electrochemical Measurements

Electrochemical corrosion tests were performed in a custom-made three-electrode cell consisting of SS samples with an exposing surface area of 2 cm^2 served as working electrode, a silver/silver chloride (Ag/AgCl 3 M) reference electrode, and a platinum wire as the counter electrode connected to an electrochemical workstation (CHI-920c, CH Instruments Inc., Austin, TX). To avoid contamination, electrochemical cells were sterilized in an autoclave machine at 121 ºC for 20 min. Also, the electrodes were sterilized in ethanol before being exposed to the electrolyte. 7 mL of AS or AS-*mu* solutions were used as electrolyte in the experiments. In order to keep the culture alive during the long-term experiments, 2 mL of the electrolyte was replenished with fresh AS every 2 days. The open circuit potential (OCP) plot versus time were recorded over a course of 1 h under no external potential. After OCP stabilized, EIS was run at the OCP over a scanning frequency range of 10^5 to 10^{-2} Hz with an AC amplitude of ± 10 mV. At the end of the immersion test, the specimens were removed from the solution, rinsed thoroughly with water, and dried at 70 °C. The SS samples incubated with *S. mutans* were fixed using glutaraldehyde (2.5% v/v in water) and dehydrated in a dilutional series of ethanol solutions (50-100%). The post-corrosion morphologies of the samples were imaged by SEM. The pH value of the corrosion media was also measured at the end of the corrosion immersion test. After the electrochemical test, a sterile pipette was used to collect the electrolyte mixed with *S. mutans* from the cell. Then, the liquid was plated on agar plate to affirm the viability of microorganisms during the electrochemical study.

4.2.5 Statistical analysis

All data in this study were expressed as mean ± standard deviation with n = 3. One-way analysis of variance (ANOVA) was adopted for statistical analysis, where $P\text{-value} < 0.05$ was considered statistically significant.

4.3 Results

4.3.1 Material Characterization

Figure 4.1 shows the experimental setup used for long-term corrosion experiments. All the electrochemical cells containing AS-*S.mu* were kept in a sealed container with a GasPak to create anerobic environment required for the culture of *S. mutans*. The surface morphologies of bare and PU-coated SS substrates were observed by SEM as shown in Figure 4.2. Uncoated SS substrate showed a quite flat surface with some aligned scratches remained form the mechanical polishing step with SiC papers. The surface morphology of PU-coated SS was smooth and homogenous with no cracks or defects on the surface, suggesting that the coating can fully cover the substrate and protect it against corrosive environment.

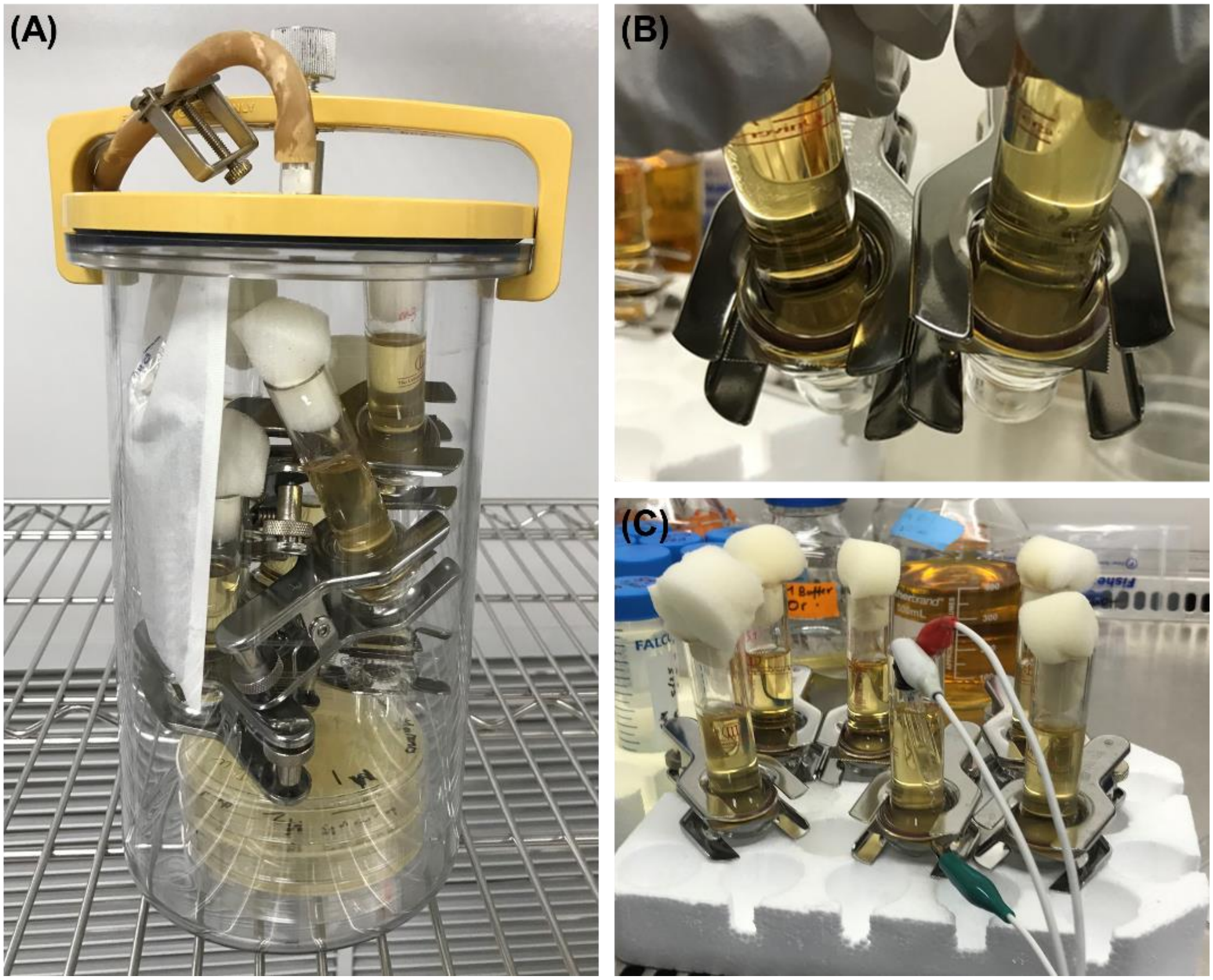

Fig. 4.1. Experimental setup used for electrochemical studies. (A) anerobic chamber with GasPak, (B) electrochemical cells containing sterile AS (left) and AS-*S.mu* (right), (C) electrochemical measurement under sterile hood.

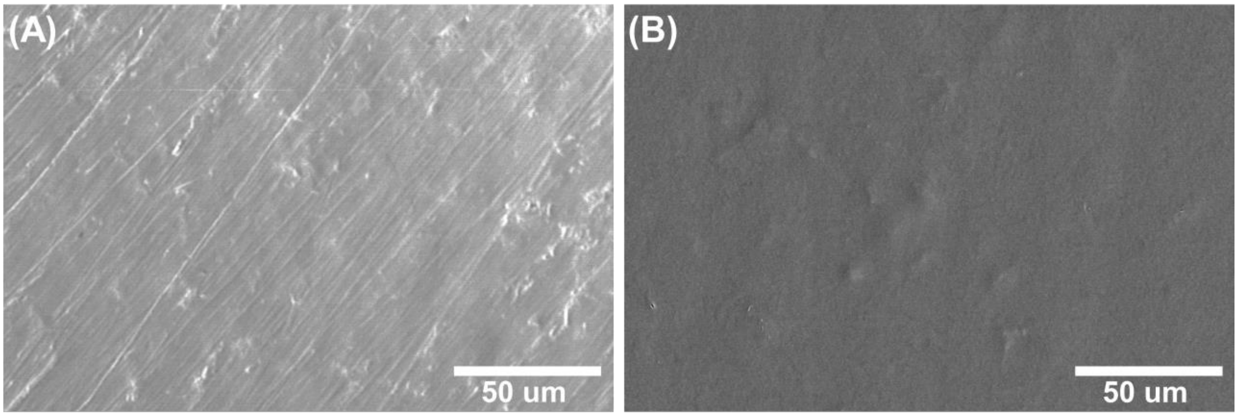

Fig 4.2. Surface SEM images of (A) bare SS and (B) PU-coated SS.

Figure 4.3 displays the ATR-FTIR spectra of the bare and PU-coated SS samples. No distinctive peaks were observed in the spectrum of SS, as there is no functional group on the surface of bare SS. The successful formation of PU coating was confirmed by the emergence peaks at 3314 and 1740, 1703, and 1596 cm^{-1} indicating -hydrogen bonded -NH stretching, carbonyl stretching in hard segments (amide I bond), H-bonding, and binding to C=C benzene ring of PU polymer, respectively [213].

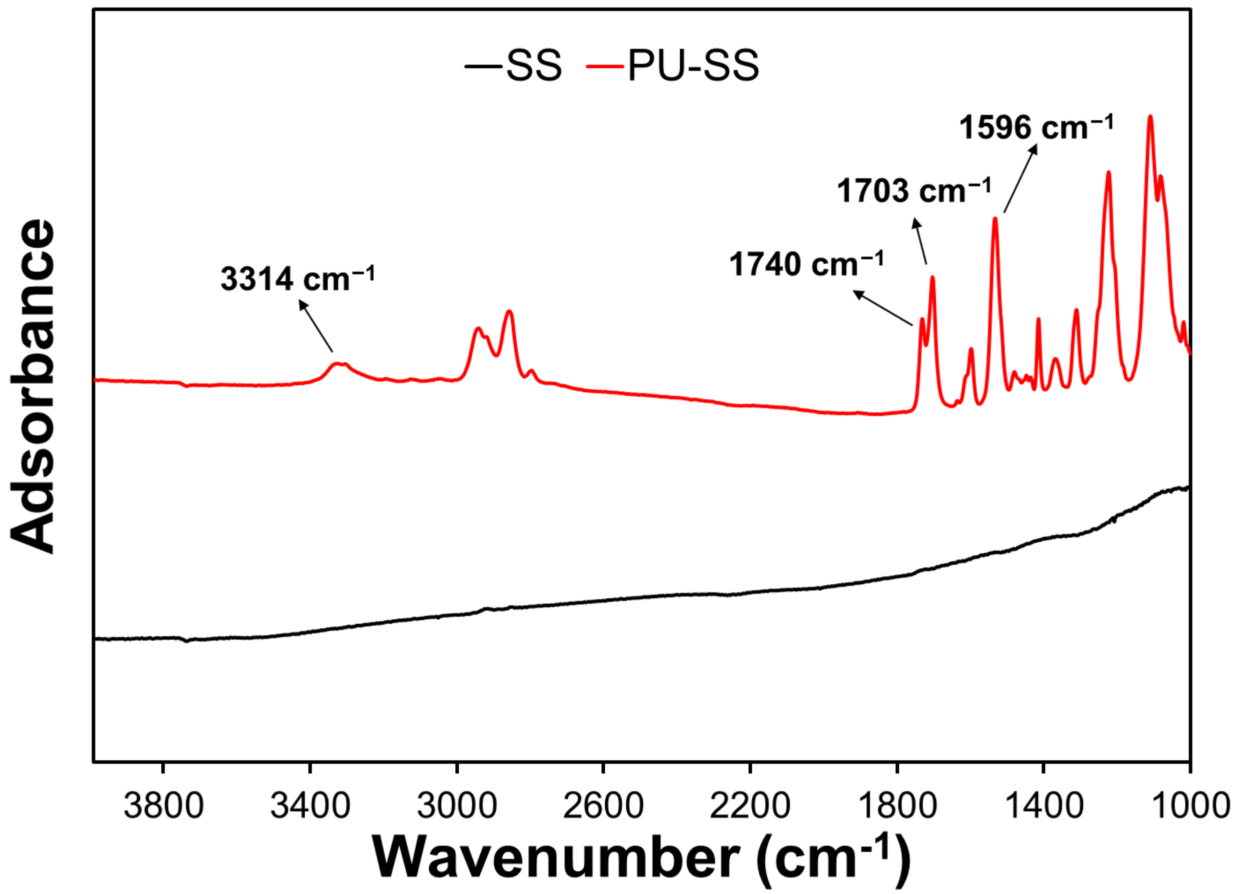

Fig 4.3. ATR-FTIR spectra of bare and PU-coated SS samples.

4.3.2 Biofilm Observation

Figures 4.4 and 4.5 also show the surface SEM images of bare SS and PU-coated SS after being immersed in AS inoculated with *S. mutans* (AS-*S.mu)* for 14 days. The surfaces of both bare and PU-coated SS samples were fully covered with biofilms, and they consisted of dense bacteria colonies and the secreted extracellular polymeric substances (EPS). EPS produced by biofilms could not only act as a contributor to enhance the bio-corrosion of metallic materials, but also make bacteria inside very difficult to eradicate [82].

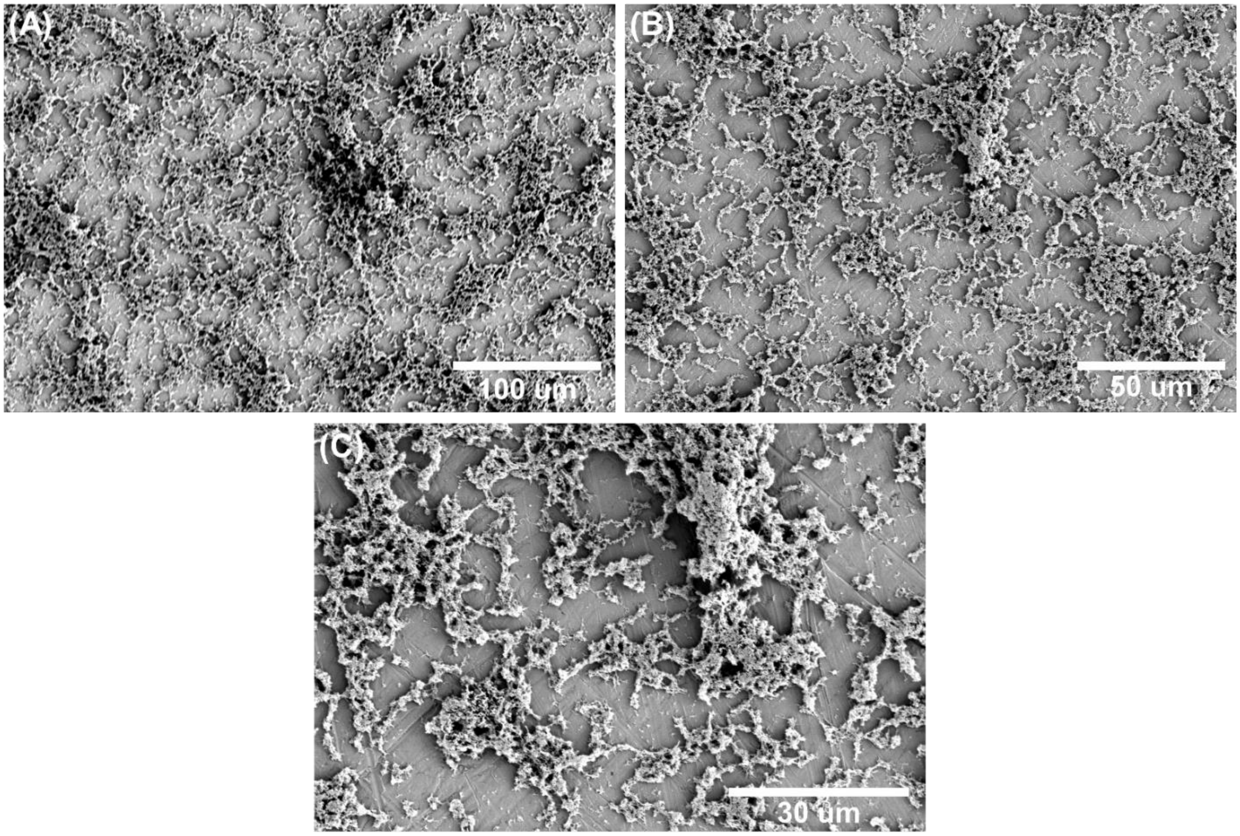

Fig. 4.4. Formation of *S. mutans* Biofilm on SS surface after 14 days of immersion in AS-*S.mu*.

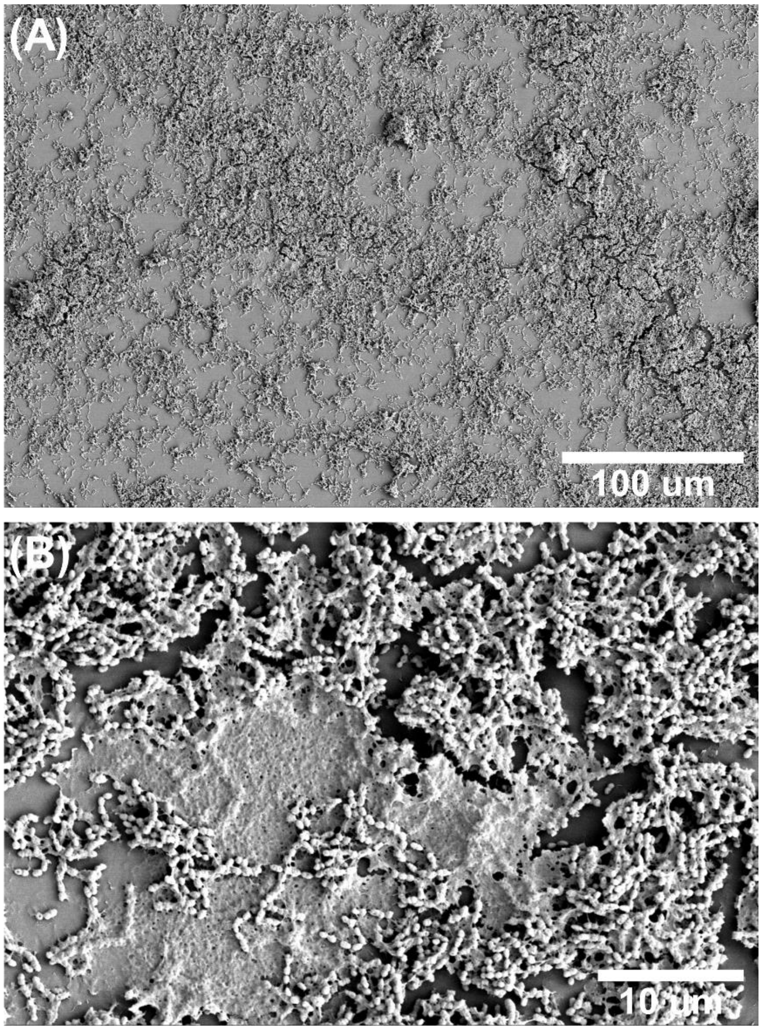

Fig. 4.5. Formation of *S. mutans* Biofilm on PU-SS surface after 14 days of immersion in AS-*S.mu*.

4.3.3 Surface Analysis for MIC

The SS and PU-SS were incubated in AS-*S.mu* for 28 days and their surfaces were imaged with SEM after removing the formed biofilms by mechanical action and sonication in pure ethanol. As displayed in Figure 4.6, the surface of SS immersed in sterile AS solution was almost intact and barely corroded during the immersion test. The scratches from polishing step became shallower most likely because of the formation of corrosion products during the immersion test. However, the SS sample incubated in the presence of *S. mutans* showed a rougher surface with many pits and localized corrosion emerged on its surface. This observation clearly indicated that the presence of *S. mutans* induced the pitting corrosion of SS surface. The similar observation has been previously reported for CoCrMo dental alloy in the presence of *S. mutans* [214]. In the case of PU-coated SS (Figure 4.7), PU-SS did not undergo any obvious changes after immersion in AS for 28 days and only a few scattered corrosion products were found on the surface of PU coating. However, clear signs of coating damage were observed when the same sample was immersed in AS inoculated with *S. mutans*. In the higher magnified SEM images, many tiny cracks and small defects were found on the PU coating surface. The formation of such defects is very detrimental to the underlying substrate as water and other corrosive species can cause metal corrosion by passing through the defects and reaching the metal surface. The results of post-corrosion surface analysis clearly suggested that in the presence of *S. mutans*, the AS solution become much more corrosive as observed by the formation of pits on bare SS and emergence of a high number of cracks/defects on the PU coating. Besides, pH of both AS and AS-*S.mu* solutions was measured after 7 days of incubation using pH test strips (Figure 4.8). As shown in Figure 4.8, the pH of the solution in the presence of *S. mutans* was found to be ~ 5 while the pH of sterile AS solution remained without change at ~ 7. The reduction in pH value is originated from the metabolic activity of *S. mutans* and the secretion of acidic byproducts such as lactic acid to the corrosion media [215].

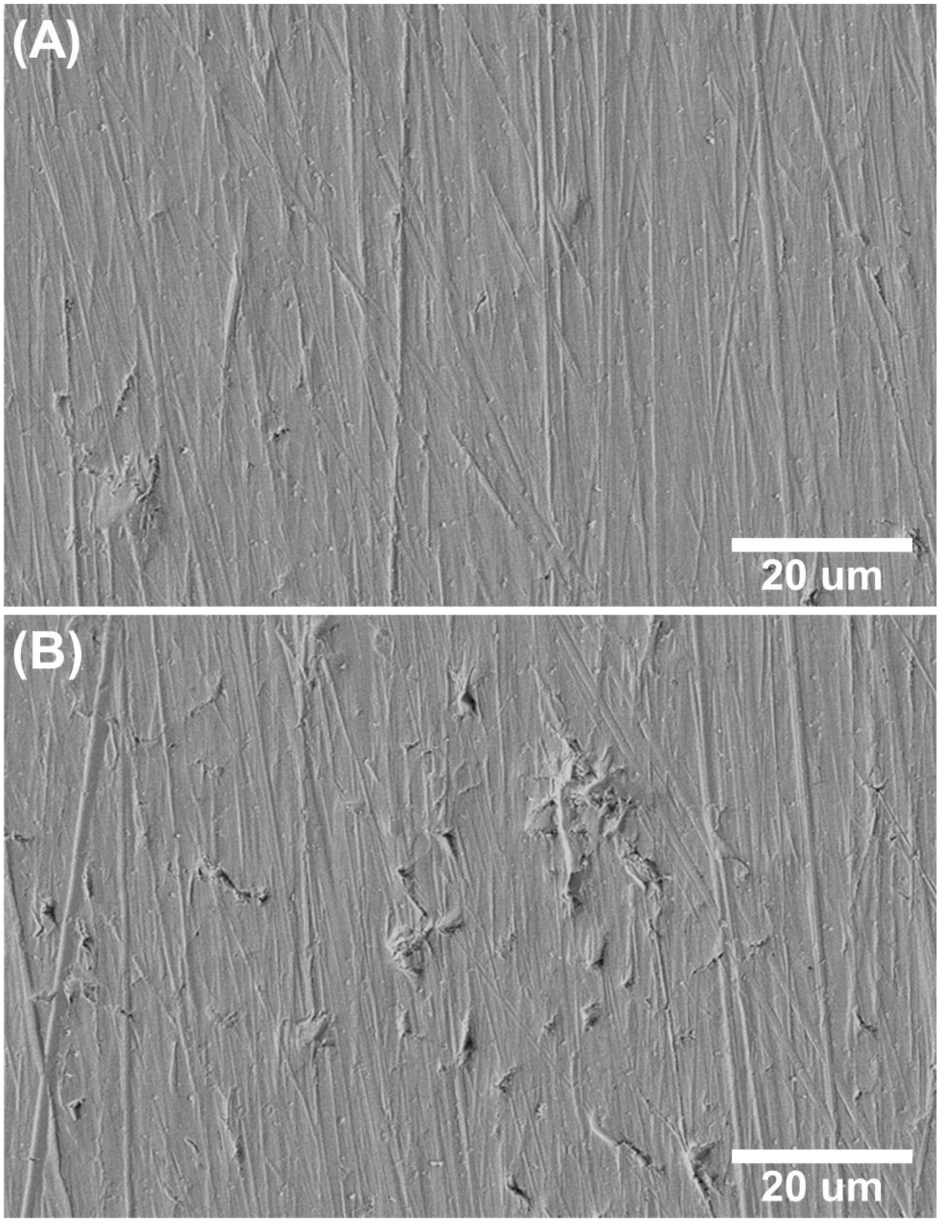

Fig 4.6. Post-corrosion surface morphology of SS immersed in AS (A) and AS-*S.mu* (B) for 28 days after removal of the biofilm.

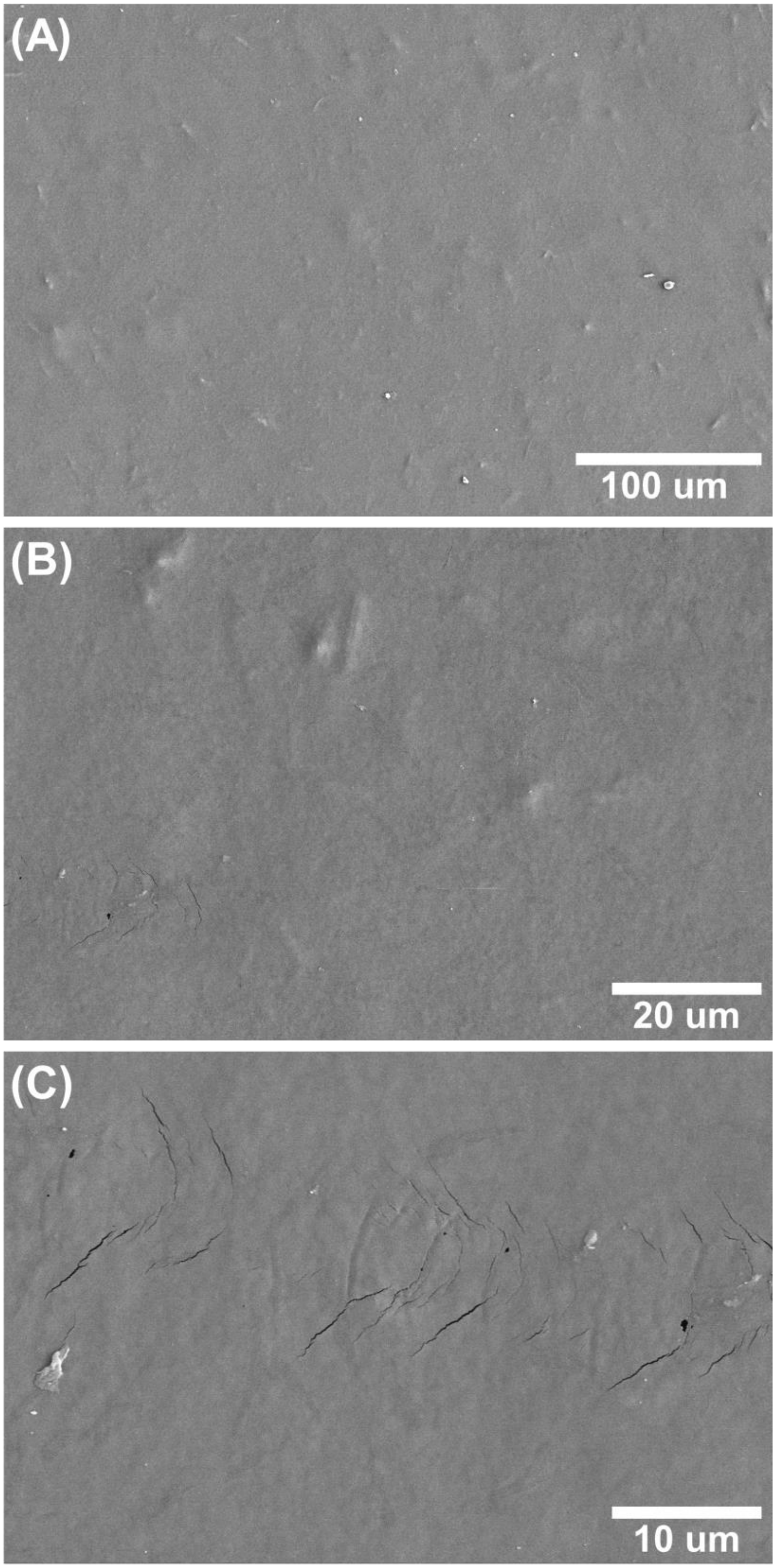

Fig 4.7. Post-corrosion surface morphology of PU-SS immersed in AS (A) and AS-S.mu (B and C) for 28 days after removal of the biofilm.

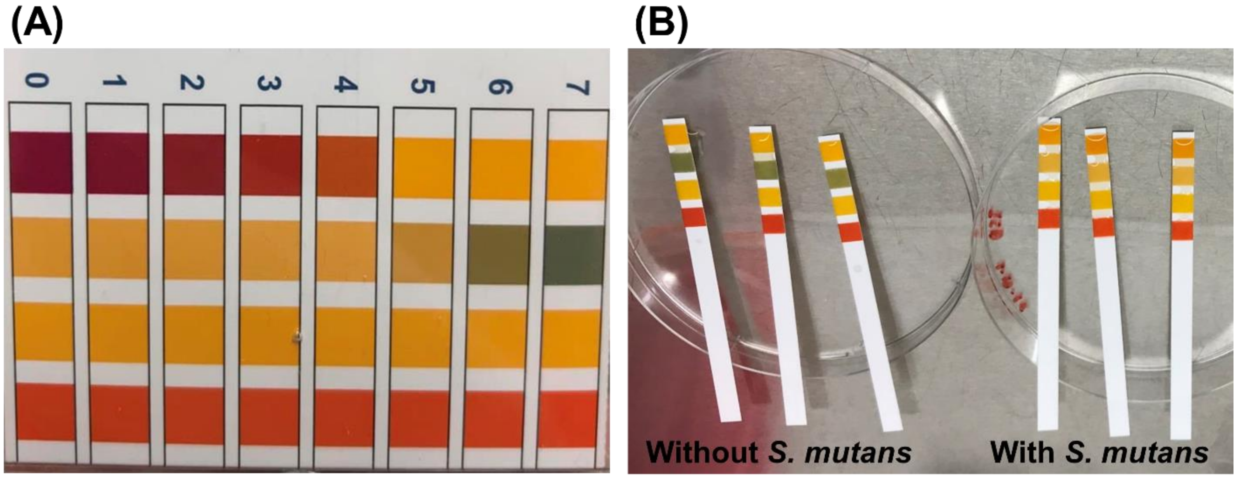

Fig 4.8. pH measurement of the corrosion media after 7 days of immersion.

4.3.4 Electrochemical Measurements

4.3.4.1 Open Circuit Potential

Figure 4.9 shows the OCP values of bare SS in AS and AS-*S.mu* at different time intervals during a 2-week immersion test in AS and AS-*S.mu*. OCP is the potential of the working electrode relative to the reference electrode without any externally applied voltage, reflecting the thermodynamic equilibrium at the interface of metal and solution as a function of time. As a general rule, a more positive OCP value indicates the surface is nobler and therefore, less susceptible to corrosion. The OCP values of bare SS incubated in AS were more positive than those incubated in AS-*S.mu* at all time intervals. This suggested that the introduction of *S. mutans* bacteria aggravated the corrosion behaviors of all SS samples seriously as observed by the reduction of OCP values. In the case of PU samples (Figure 4.10), the OCP values did not follow the same trend that was observed for bare SS samples, which can be due to the presence of the organic coating on SS sample. It’s worth mentioning that the OCP values of PU were found to be more positive compared to the bare SS at all time intervals implying the more stable surface of

PU. This is due to the presence of a thick layer of PU coating with a high physical barrier effect that can mitigate the penetration of the corrosive electrolyte, resulting in enhanced corrosion resistance of the sample [216].

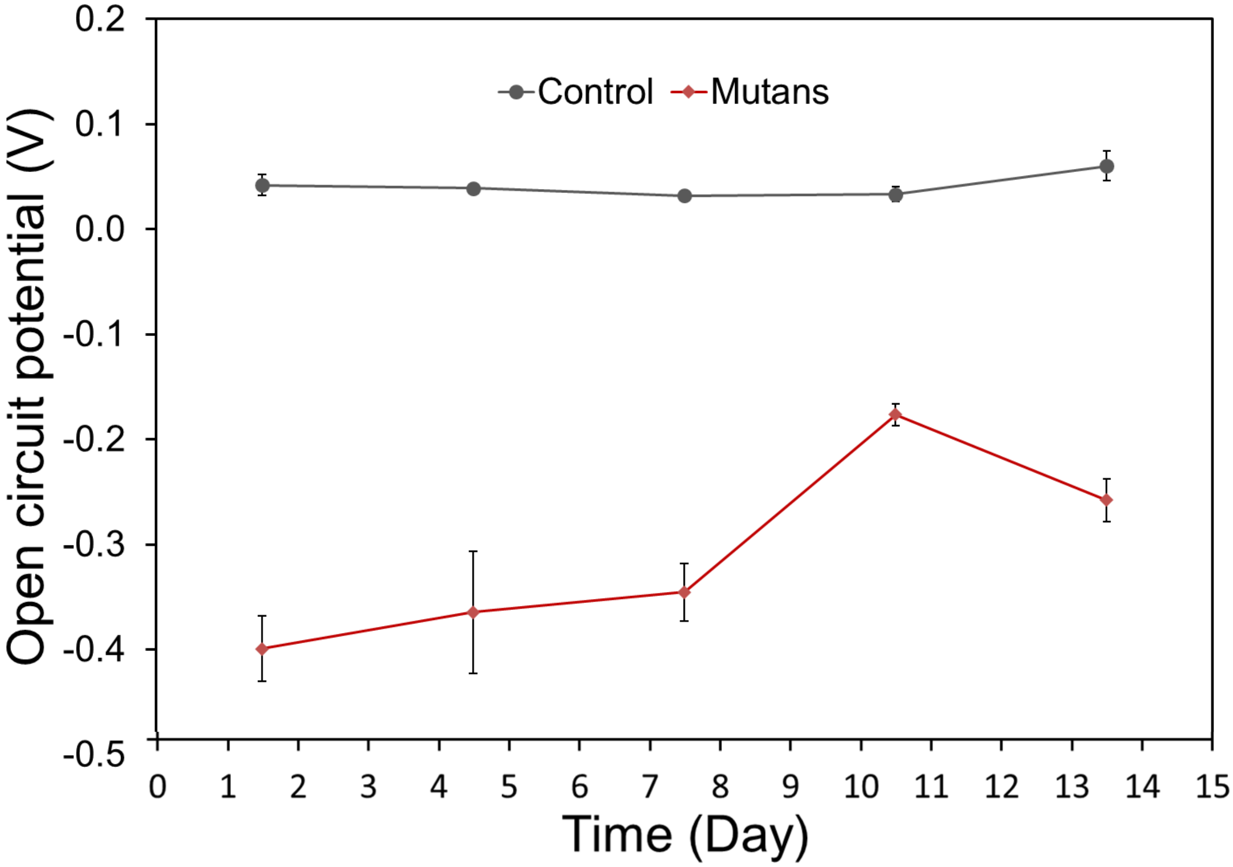

Fig. 4.9. OCP values of SS immersed in AS with and without the presence of *S. mutans*.

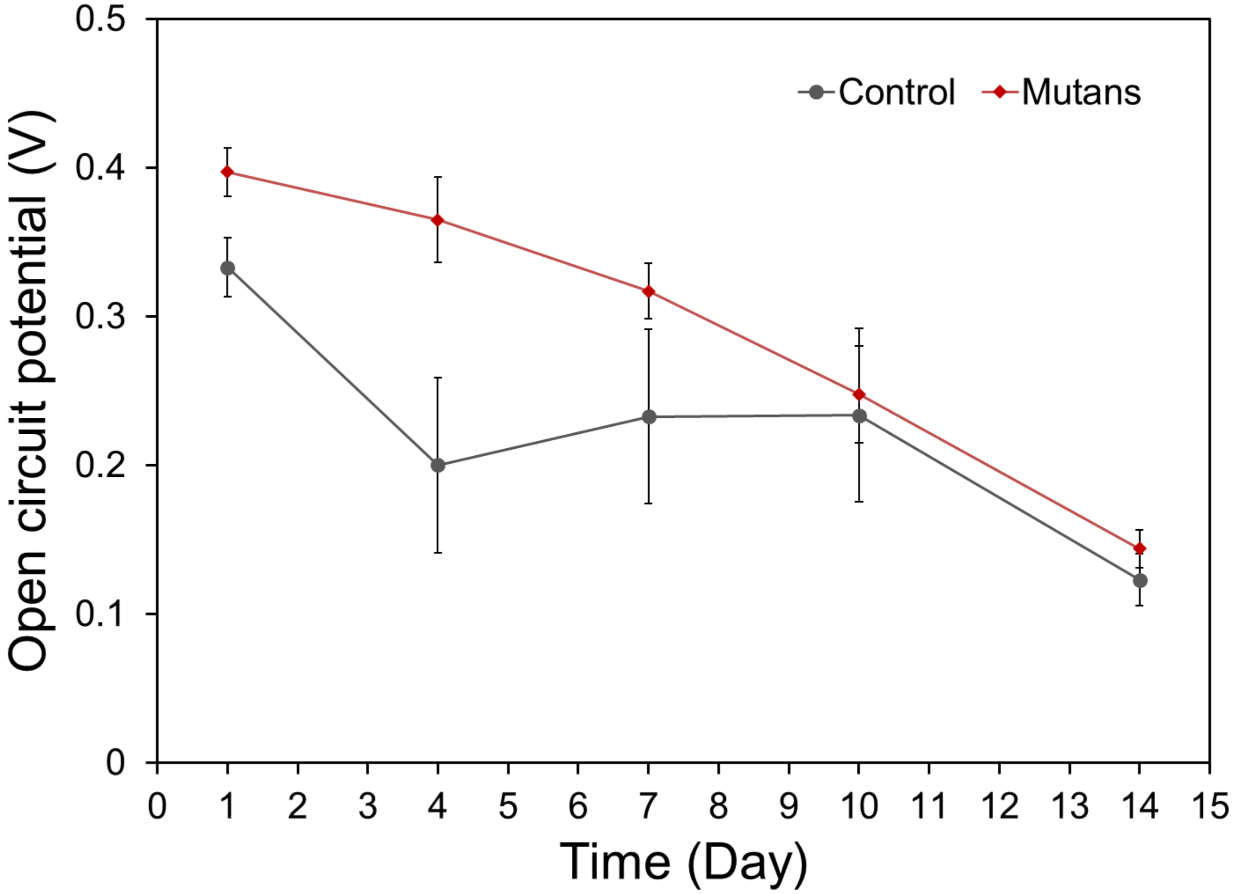

Fig. 4.10. OCP values of PU-SS immersed in AS with and without the presence of S. mutans.

4.3.4.1 Electrochemical Impedance Spectroscopy

EIS was employed as a very powerful technique to further study the corrosive effect of *S. mutans* on the bare and coated SS samples. As opposed to other commonly used electrochemical techniques such polarization tests, the non-destructive nature of EIS allows to monitor the corrosion resistance of a sample in long-term, as it does not perturb the system significantly due to its steady state measurement [78]. From the results of EIS measurements, the value of impedance modulus at the lowest-frequency region ($|Z|_{0.01\ Hz}$) of the Bode impedance plot were extracted and employed to investigate the overall corrosion resistance of the sample at different time intervals. Generally, a higher $|Z|_{0.01Hz}$ value reflects a lower corrosion rate of the corroding metal [217]. Figure 4.11 shows $|Z|_{0.01Hz}$ values of SS immersed in AS solution with and without the presence of *S. mutans* for 1, 3, 7, 10, and 14 days. $|Z|_{0.01Hz}$ remained almost at a same level over the course of EIS study, indicating that SS has strong corrosion resistance against AS solution and its corrosive species and did not undergo a sever corrosion. Addition of *S. mutans* to the AS remarkably reduced $|Z|_{0.01Hz}$ of SS after 1 day mainly because of the production organic acids during the bacterial metabolism. $|Z|_{0.01Hz}$ started to slightly increase after day 1 which is due to the formation of biofilm. Biofilm is often composed of corrosion products embedded in EPS. Polysaccharides and insoluble biomass of biofilm can limit the diffusion of corrosives to the metal surface and slow down the corrosion rate compared to the very initial days after immersion in the biotic solution [218]. It's worth mentioning that SS showed lower $|Z|_{0.01Hz}$ values when immersed in AS-*S.mu*. For PU-SS sample (Figure 4.12), with increase in exposure time, the $|Z|_{0.01Hz}$ of the coated sample continuously dropped during the test both in sterile and S. mutans inoculate AS solutions, indicating the gradual decrease in the barrier properties of the PU coating in both solutions. It should be mentioned that $|Z|_{0.01Hz}$ values of PU-SS in *AS-S.mu* were lower than those obtained in sterile AS in almost all the time intervals with the highest difference at the end of long-term corrosion test (day 14). In general, the results of electrochemical studies were in agreement with surface analysis and pH measurement, both indicating the adverse effect of *S. mutans* on corrosion resistance of SS with/without the presence of an organic protective coating.

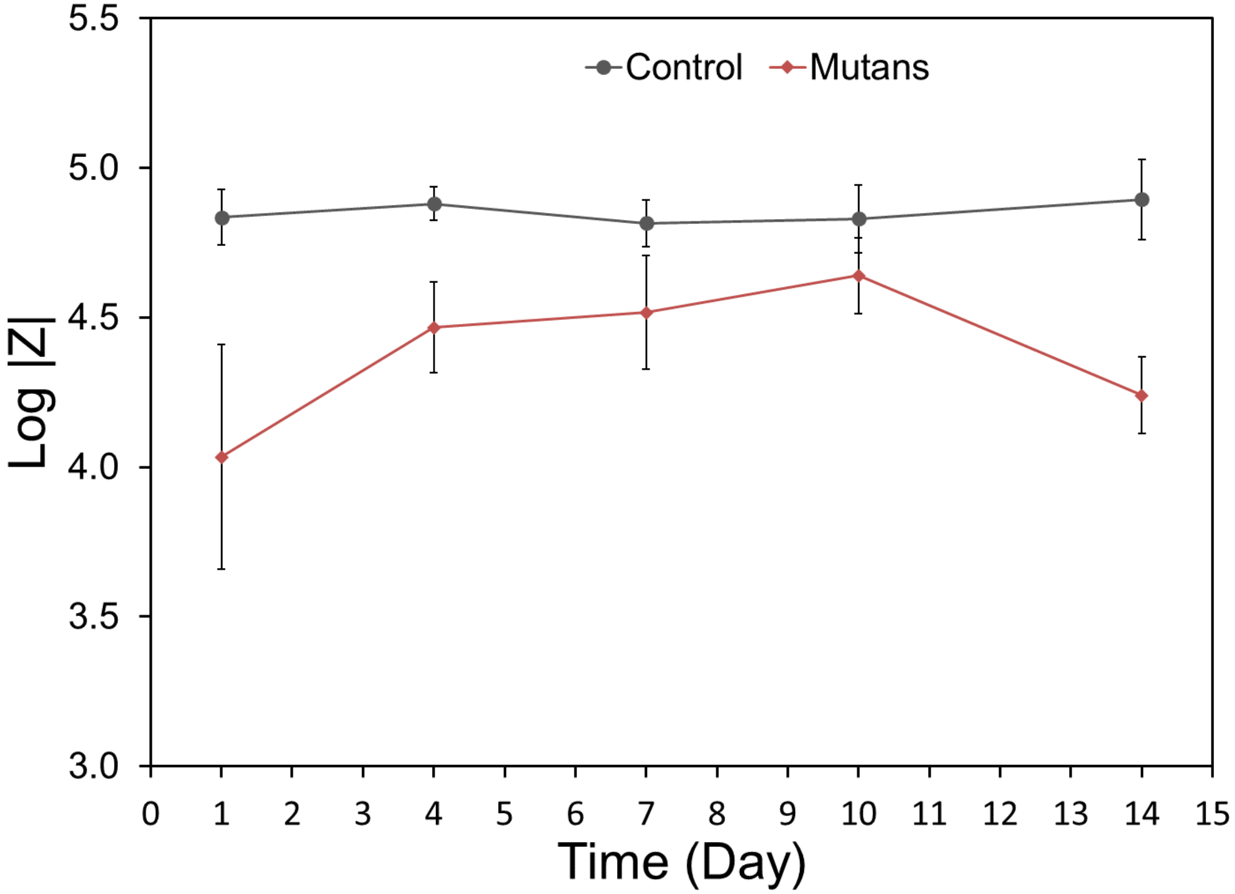

Fig. 4.11. $|Z|_{0.01Hz}$ values of SS immersed in AS with and without the presence of *S. mutans*.

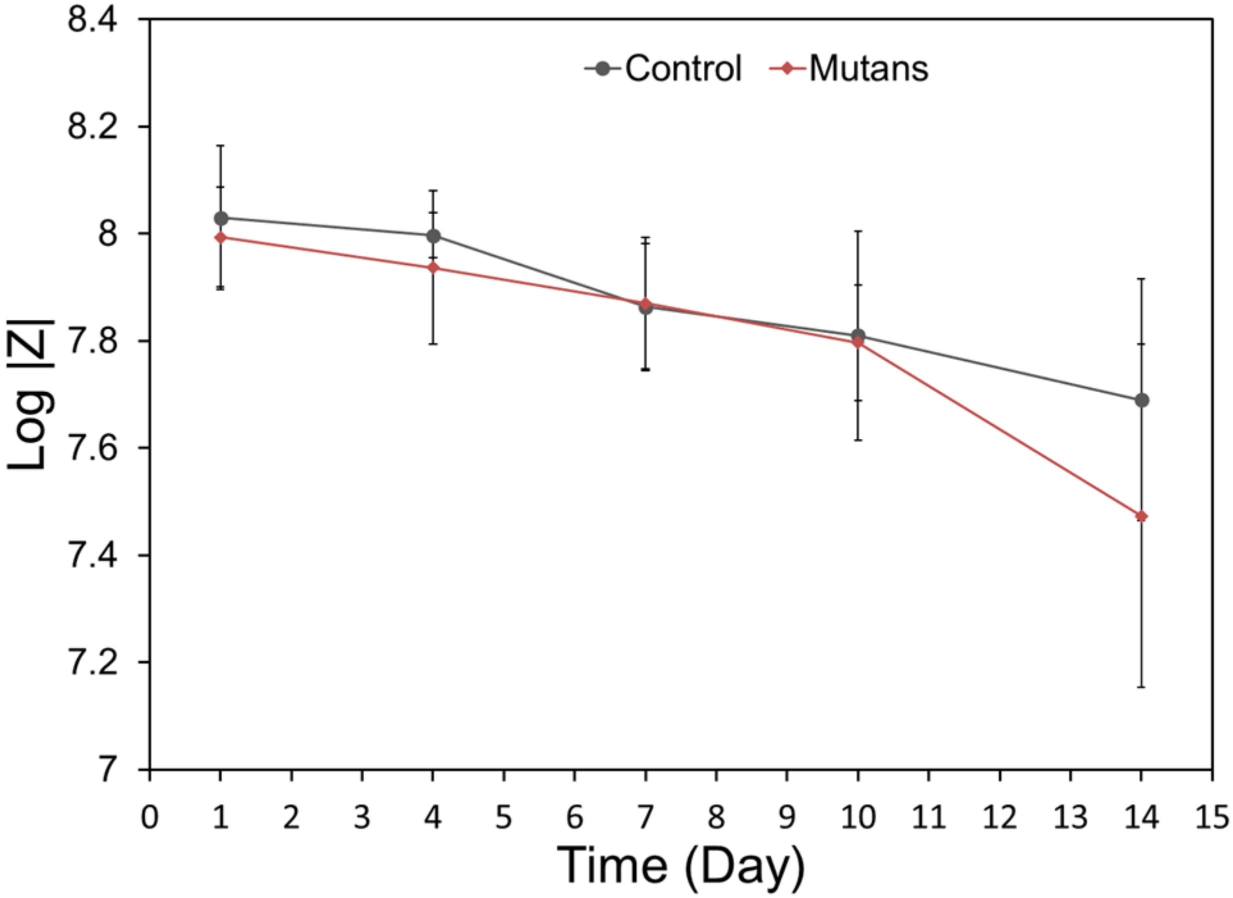

Fig. 4.12. $|Z|_{0.01Hz}$ values of PU-SS immersed in AS with and without the presence of *S. mutans*.

4.4 Conclusion

In this work, the corrosion resistance properties of bare SS and and PU-coated SS immersed in AS solution containing *S. mutans* were examined. The non-coated and coated SS substrates were first characterized by SEM and FTIR analyses. The 28-day immersion test in AS showed that the presence of *S. mutans* in AS causes localized corrosion on bare SS and damages the protective polymeric coating. Electrochemical studies including OCP and EIS measurements confirmed the negative effect of *S. mutans* on the corrosion resistance of the samples. Altogether, the findings of this study show the MIC of SS in the presence of *S. mutans* and emphasize on the importance of new strategies for its mitigation.

CHAPTER 5

CONCLUSION AND FUTURE DIRECTIONS

Despite all the advances the field of metallic biomedical implants and the emergence of new alloy systems with superior corrosion resistance properties, corrosion is still among the most common reasons behind metallic implant failures and therefore, there novel approaches are needed to mitigate corrosion in metallic implants. This dissertation is focused on the development of biocompatible polymeric coatings that not only enhance the corrosion resistance of the metallic substrates, but also provide them with other properties such as enhance cellular response and bactericidal activity which are very desired for bio-implant application. Mg-based biodegradable alloys were chosen as the target metals for the developed coatings toward orthopedic biodegradable/temporary implant applications. In another application, the effect of *S. mutan*, as the main microorganism responsible for oral cavities, on the corrosion resistance of SS-based dental implants was investigated through various immersion and electrochemical tests.

In this dissertation, two novel coating platforms based on naturally derived materials were developed and reported for biodegradable Mg-based implants: 1) a bi-layered coating based on PCL and lawsone and 2) a composite coating based on SF and cellulose nanocrystal CNC. In the first platform, lawsone, a natural dye extracted from the leaves of *Lawsonia inermis* plant, was incorporated into the PCL coating as a corrosion inhibitor to fabricate a polymer/corrosion inhibitor coating. The corrosion protection performance of the coating was investigated by different *in vitro* immersion and electrochemical studies. The results revealed that the incorporation of lawsone into PCL matrix remarkably enhanced the passive corrosion protection of the PCL coating through its strong chelation ability of dissolving Mg^{2+}. Besides, the composite coating showed a strong antibacterial activity against *E. coli* and *S. aureus* bacterial strains, which is helpful in the prevention of microbial infection at early stages after implantation. In the second platform, SF, a natural protein extracted from silkworm cocoons with an excellent biocompatibility and osteogenic potential, was used as a surface coating material. Being a natural polymer, SF has limited barrier properties to serve as an effective corrosion protective coating alone. To address this limitation, CNC, a needle-like nanoparticle produced from acid hydrolysis of various plant sources, was incorporated as an anticorrosion nanofiller to enhance the corrosion protection properties of the SF coating. Through a series of immersion and electrochemical experiments, the incorporation of CNC was found to improve the barrier properties of the SF coating which was attributed to the higher crystallinity of CNC-reinforced SF coating as well as the intrinsic properties of CNC as an anti-corrosive nanofiller. Besides, the cellular response of the Mg substrates toward bone cells was also improved after being coated with the SF-CNC coating. The developed SF-CNC coating benefits from the excellent biological properties of natural SF while possessing an enhanced barrier and corrosion protection properties, comparable to those derived from synthetic polymer-based coatings, as a result of CNC incorporation into the coating. Altogether, the results suggested that the proposed polymeric coatings have great potential as protective coating materials to expand the applicability of Mg alloys for biodegradable implant applications.

Based on the scope of the research discussed in this dissertation, the following path could be taken for future research on these topics.

1) Although extensive *in vitro* immersion tests and electrochemical studies were preformed and all the possible experimental factors including the similarity of corrosion media/electrolyte to the physiological environment and temperature were taken into consideration in all the experiments, still none of these can exactly mimic the physiological environment and predict the degradation behavior of the samples and coatings when implanted in human body. Therefore, performing *in vivo* animal model studies would be very helpful in evaluating the corrosion resistance of the samples and the effect of protective coatings on that. In addition to the corrosion protection performance, the biocompatibility of the coatings will be assessed in a more realistic way when implanted in animal models which has been studied only by *in vitro* cell proliferation and adhesion studies so far. That can give a better insight on the potential of the developed coating for practical applications in clinical settings.
2) In this dissertation, we mainly focused on Mg-based metallic implant for biodegradable/temporary implant application. Here, the main objective was to enhance the corrosion resistance and reduce the corrosion rate of Mg-based alloy by applying the polymeric coatings. However, the developed coatings have the potential to be used as coating materials on other types of biodegradable and/or non-biodegradable metallic implants to enhance their corrosion resistance. Besides, we have shown that the developed coatings are able to impart the underlying substrate with other functionalities such as antibacterial activity, enhanced cytocompatibility, and the ability to load small molecules/therapeutic agents that could be very desired in metallic bio-implant application.
3) Mechanical properties are among the most important factors in biomedical implant application. Most of the commonly used implant materials such as titanium, stainless steel, and Co-Cr are known to have very high elastic modules which are way higher that those observed in natural

bones. This difference in the mechanical properties causes stress shielding issue which will result in the reduction of bone density (osteopenia) as a result of removal of typical stress from the bone by an implant. One of the advantages of Mg alloys over their counterparts is their similar mechanical properties to the natural bones. Similar to biocompatibility, durability, and functionality, mechanical properties of implants are also prone to be adversely affected by corrosion phenomena. Therefore, it's very important to monitor the changes in mechanical properties of the implants during corrosion experiments, for instance by the compression test, to make sure they are able to maintain sufficient mechanical support over the intended implantation period.

4) Regarding the last project on MIC of stainless steel-based implant, we clearly showed the negative effect of MIC on bare and PU coated SS substrates. For the next phase of this study, an antibacterial agent can be incorporated into the polymeric coating to prevent the bacterial growth and biofilm formation on the implant surface, and thus MIC. We have done some preliminary studies by incorporating a Nitric Oxide donor molecule into the PU coating and showed its antibacterial activity against *S. mutans* (Appendix B). However, incorporation of such antibacterial agent directly into the coating compromises the homogeneity and barrier properties of the coating which is not favorable. Therefore, there are still some challenges remained that need to be addressed by optimizing the coating fabrication method and incorporation strategy of the bactericidal agent.

References

1. Davis, R., et al., *A comprehensive review on metallic implant biomaterials and their subtractive manufacturing.* 2022: p. 1-58.
2. Asri, R., et al., *Corrosion and surface modification on biocompatible metals: A review.* 2017. **77**: p. 1261-1274.
3. Eliaz, N. and E. Gileadi, *Physical Electrochemistry: Fundamentals, Techniques, and Applications*. 2019: John Wiley & Sons.
4. Thomsen, P. and L.J.T.b.-b.i. Ericson, *Inflammatory cell response to bone implant surfaces.* 1991. **153**.
5. Eliaz, N.J.M., *Corrosion of metallic biomaterials: a review.* 2019. **12**(3): p. 407.
6. Revathi, A., et al., *Degradation mechanisms and future challenges of titanium and its alloys for dental implant applications in oral environment.* 2017. **76**: p. 1354-1368.
7. Virtanen, S., *Degradation of titanium and its alloys*, in *Degradation of Implant Materials*. 2012, Springer. p. 29-55.
8. Aksakal, B., et al., *Metallurgical failure analysis of various implant materials used in orthopedic applications.* 2004. **4**(3): p. 17-23.
9. Eliaz, N., *Degradation of implant materials*. 2012: Springer Science & Business Media.
10. Willis, J., et al., *Is titanium alloy Ti-6Al-4 V cytotoxic to gingival fibroblasts—A systematic review.* 2021. **7**(6): p. 1037-1044.
11. Asadi, H., et al., *A multifunctional polymeric coating incorporating lawsone with corrosion resistance and antibacterial activity for biomedical Mg alloys.* 2021. **153**: p. 106157.
12. Asadi, H., et al., *A multifunctional polymeric coating incorporating lawsone with corrosion resistance and antibacterial activity for biomedical Mg alloys.* Progress in Organic Coatings, 2021. **153**: p. 106157.
13. Xiong, P., et al., *A pH-sensitive self-healing coating for biodegradable magnesium implants.* Acta biomaterialia, 2019. **98**: p. 160-173.
14. Fang, Y., B. Suganthan, and R.P. Ramasamy, *Electrochemical characterization of aromatic corrosion inhibitors from plant extracts.* Journal of Electroanalytical Chemistry, 2019. **840**: p. 74-83.
15. He, Y., et al., *Comparative study of CNC and CNF as additives in waterborne acrylate-based anti-corrosion coatings.* 2020. **41**(13): p. 2037-2047.
16. Wang, C., et al., *Development of a novel biodegradable and anti-bacterial polyurethane coating for biomedical magnesium rods.* Materials Science and Engineering: C, 2019. **99**: p. 344-356.
17. Xu, W., et al., *Optimized polymer coating for magnesium alloy-based bioresorbable scaffolds for long-lasting drug release and corrosion resistance.* Colloids and Surfaces B: Biointerfaces, 2018. **163**: p. 100-106.
18. Makkar, P., et al., *Development and properties of duplex MgF2/PCL coatings on biodegradable magnesium alloy for biomedical applications.* Plos one, 2018. **13**(4): p. e0193927.
19. Wang, C., et al., *Silk fibroin film-coated MgZnCa alloy with enhanced in vitro and in vivo performance prepared using surface activation.* Acta biomaterialia, 2019. **91**: p. 99-111.
20. Ye, S.-H., et al., *Biodegradable zwitterionic polymer coatings for magnesium alloy stents.* Langmuir, 2018. **35**(5): p. 1421-1429.

21. Li, Y., et al., *Surface engineering of biodegradable magnesium alloys for enhanced orthopedic implants.* Small, 2019. **15**(51): p. 1904486.
22. Hu, T., et al., *Cerium tartrate as a corrosion inhibitor for AA 2024-T3.* Corrosion Science, 2015. **95**: p. 152-161.
23. Wang, X., et al., *Active corrosion protection of super-hydrophobic corrosion inhibitor intercalated Mg–Al layered double hydroxide coating on AZ31 magnesium alloy.* Journal of Magnesium and Alloys, 2020.
24. Abbaspoor, S., A. Ashrafi, and R. Abolfarsi, *Development of self-healing coatings based on ethyl cellulose micro/nano-capsules.* Surface Engineering, 2019. **35**(3): p. 273-280.
25. García, S., H. Fischer, and S. Van Der Zwaag, *A critical appraisal of the potential of self healing polymeric coatings.* Progress in Organic Coatings, 2011. **72**(3): p. 211-221.
26. Calado, L.M., et al., *Novel Smart and Self-Healing Cerium Phosphate-based Corrosion Inhibitor for AZ31 Magnesium Alloy.* Corrosion Science, 2020: p. 108648.
27. Anjum, M.J., et al., *In-situ intercalation of 8-hydroxyquinoline in Mg-Al LDH coating to improve the corrosion resistance of AZ31.* Corrosion Science, 2019. **157**: p. 1-10.
28. Zhang, G., et al., *A novel approach to fabricate protective layered double hydroxide films on the surface of anodized Mg-Al alloy.* Advanced Materials Interfaces, 2017. **4**(12): p. 1700163.
29. Zeng, R.-C., et al., *Corrosion of molybdate intercalated hydrotalcite coating on AZ31 Mg alloy.* Journal of Materials Chemistry A, 2014. **2**(32): p. 13049-13057.
30. Sun, M., et al., *Self-healing plasma electrolytic oxidation coatings doped with benzotriazole loaded halloysite nanotubes on AM50 magnesium alloy.* Corrosion Science, 2016. **111**: p. 753-769.
31. Umoren, S.A., et al., *Exploration of natural polymers for use as green corrosion inhibitors for AZ31 magnesium alloy in saline environment.* Carbohydrate Polymers, 2020. **230**: p. 115466.
32. Shang, W., et al., *Performance evaluation of triethanolamine as corrosion inhibitor for magnesium alloy in 3.5 wt% NaCl solution.* RSC advances, 2016. **6**(115): p. 113967-113980.
33. Oguzie, E.E., *Evaluation of the inhibitive effect of some plant extracts on the acid corrosion of mild steel.* Corrosion science, 2008. **50**(11): p. 2993-2998.
34. Mo, S., H.-Q. Luo, and N.-B. Li, *Plant extracts as "green" corrosion inhibitors for steel in sulphuric acid.* Chemical Papers, 2016. **70**(9): p. 1131-1143.
35. Abdel-Gaber, A., et al., *Inhibitive action of some plant extracts on the corrosion of steel in acidic media.* Corrosion science, 2006. **48**(9): p. 2765-2779.
36. Rahmani, P., A. Shojaei, and N.P. Tavandashti, *Nanodiamond loaded with corrosion inhibitor as efficient nanocarrier to improve anticorrosion behavior of epoxy coating.* Journal of Industrial and Engineering Chemistry, 2020. **83**: p. 153-163.
37. El-Kamel, R.S., A.A. Ghoneim, and A.M. Fekry, *Electrochemical, biodegradation and cytotoxicity of graphene oxide nanoparticles/polythreonine as a novel nano-coating on AZ91E Mg alloy staple in gastrectomy surgery.* Materials Science and Engineering: C, 2019. **103**: p. 109780.
38. Zomorodian, A., et al., *Biofunctional composite coating architectures based on polycaprolactone and nanohydroxyapatite for controlled corrosion activity and enhanced biocompatibility of magnesium AZ31 alloy.* Materials Science and Engineering: C, 2015. **48**: p. 434-443.

39. Guo, Y., et al., *A multifunctional polypyrrole/zinc oxide composite coating on biodegradable magnesium alloys for orthopedic implants.* Colloids and Surfaces B: Biointerfaces, 2020. **194**: p. 111186.
40. Kang, M.-H., et al., *Poly (ether imide)-silica hybrid coatings for tunable corrosion behavior and improved biocompatibility of magnesium implants.* Biomedical Materials, 2016. **11**(3): p. 035003.
41. Nazeer, A.A., et al., *A poly (butyl methacrylate)/graphene oxide/TiO2 nanocomposite coating with superior corrosion protection for AZ31 alloy in chloride solution.* Chemical Engineering Journal, 2019. **361**: p. 485-498.
42. Shi, Y.-j., et al., *Enhanced corrosion resistance and cytocompatibility of biodegradable Mg alloys by introduction of Mg (OH) 2 particles into poly (L-lactic acid) coating.* Scientific reports, 2017. **7**(1): p. 1-11.
43. Li, H., et al., *Layered double hydroxide/poly-dopamine composite coating with surface heparinization on Mg alloys: improved anticorrosion, endothelialization and hemocompatibility.* Biomaterials science, 2018. **6**(7): p. 1846-1858.
44. Huang, J., L. Liu, and J. Yao, *Electrospinning of Bombyx mori silk fibroin nanofiber mats reinforced by cellulose nanowhiskers.* Fibers and Polymers, 2011. **12**(8): p. 1002-1006.
45. Yuan, S., et al., *Antibacterial inorganic− organic hybrid coatings on stainless steel via consecutive surface-initiated atom transfer radical polymerization for biocorrosion prevention.* Langmuir, 2010. **26**(9): p. 6728-6736.
46. Javaherdashti, R., *A review of some characteristics of MIC caused by sulfate-reducing bacteria: past, present and future.* Anti-corrosion methods and materials, 1999.
47. Fukushima, A., et al., *Microbiologically induced corrosive properties of the titanium surface.* Journal of dental research, 2014. **93**(5): p. 525-529.
48. Siddiqui, D.A., et al., *Evaluation of oral microbial corrosion on the surface degradation of dental implant materials.* Journal of periodontology, 2019. **90**(1): p. 72-81.
49. Costa, R.C., et al., *Microbial Corrosion in Titanium-Based Dental Implants: How Tiny Bacteria Can Create a Big Problem?* 2021. **7**(4): p. 1-22.
50. Al-Darbi, M., et al., *Control of microbial corrosion using coatings and natural additives.* Energy Sources, 2002. **24**(11): p. 1009-1018.
51. Herbert, B. and F. Stott, *The Effect of Pressure and Temperature on Bacteria in Oilfield Water Injection Systems.* Microbial Corrosion, 1983: p. 7-17.
52. Alamri, A.H., *Localized Corrosion and Mitigation Approach of Steel Materials Used in Oil and Gas Pipelines-An overview.* Engineering Failure Analysis, 2020: p. 104735.
53. Abdolahi, A., et al., *Application of environmentally-friendly coatings toward inhibiting the microbially influenced corrosion (MIC) of steel: a review.* Polymer Reviews, 2014. **54**(4): p. 702-745.
54. Loto, C., *Microbiological corrosion: mechanism, control and impact—a review.* The International Journal of Advanced Manufacturing Technology, 2017. **92**(9): p. 4241-4252.
55. Rasheed, P.A., et al., *Recent advancements of nanomaterials as coatings and biocides for the inhibition of sulfate reducing bacteria induced corrosion.* 2019. **25**: p. 35-42.
56. Díaz, I., et al., *Corrosion behavior of surface modifications on titanium dental implant. In situ bacteria monitoring by electrochemical techniques.* Journal of Biomedical Materials Research Part B: Applied Biomaterials, 2018. **106**(3): p. 997-1009.

57. Zhang, Y., et al., *Tantalum nitride-decorated titanium with enhanced resistance to microbiologically induced corrosion and mechanical property for dental application.* PLoS One, 2015. **10**(6): p. e0130774.
58. Mystkowska, J., et al., *The role of oral cavity biofilm on metallic biomaterial surface destruction–corrosion and friction aspects.* 2018. **19**(3): p. 743.
59. Schachter, B., *Slimy business—the biotechnology of biofilms.* Nature biotechnology, 2003. **21**(4): p. 361-365.
60. Neoh, K.G. and E.-T. Kang, *Combating bacterial colonization on metals via polymer coatings: relevance to marine and medical applications.* ACS applied materials & interfaces, 2011. **3**(8): p. 2808-2819.
61. Guezennec, J., *Cathodic protection and microbially induced corrosion.* International biodeterioration & biodegradation, 1994. **34**(3-4): p. 275-288.
62. Von Baeckmann, W., W. Schwenk, and W. Prinz, *Handbook of cathodic corrosion protection*. 1997: Elsevier.
63. Little, B., et al., *Microbially influenced corrosion—Any progress?* Corrosion Science, 2020. **170**: p. 108641.
64. Yang, Y., J.D. Scantlebury, and E.V. Koroleva, *A study of calcareous deposits on cathodically protected mild steel in artificial seawater.* Metals, 2015. **5**(1): p. 439-456.
65. Olivares, G.Z., et al. *Sulfate reducing bacteria influence on the cathodic protection of pipelines that transport hydrocarbons*. in *CORROSION 2003*. 2003. OnePetro.
66. Barlo, T. and W. Berry, *An assessment of the current criteria for cathodic protection of buried steel pipelines.* Mater. Performance;(United States), 1984. **23**(9).
67. Pope, D.H. and E. Morris III, *Some experiences with microbiologically influenced corrosion of pipelines.* Materials Performance, 1995. **34**(5).
68. Zuo, R., *Biofilms: strategies for metal corrosion inhibition employing microorganisms.* Applied microbiology and biotechnology, 2007. **76**(6): p. 1245-1253.
69. Sakultantimetha, A., et al., *Acceleration of tributyltin biodegradation by sediment microorganisms under optimized environmental conditions.* International Biodeterioration & Biodegradation, 2010. **64**(6): p. 467-473.
70. Guo, J., et al., *Polymers for combating biocorrosion.* Frontiers in Materials, 2018. **5**: p. 10.
71. Videla, H.A., *Prevention and control of biocorrosion.* International Biodeterioration & Biodegradation, 2002. **49**(4): p. 259-270.
72. Kopteva, Z.P., V. Zanina, and I. Kozlova, *Microbial corrosion of protective coatings.* Surface engineering, 2004. **20**(4): p. 275-280.
73. Rasheed, P.A., et al., *Recent advancements of nanomaterials as coatings and biocides for the inhibition of sulfate reducing bacteria induced corrosion.* Current Opinion in Chemical Engineering, 2019. **25**: p. 35-42.
74. Krishnamurthy, A., et al., *Superiority of graphene over polymer coatings for prevention of microbially induced corrosion.* Scientific reports, 2015. **5**(1): p. 1-12.
75. Carré, G., et al., *TiO2 photocatalysis damages lipids and proteins in Escherichia coli.* Applied and environmental microbiology, 2014. **80**(8): p. 2573-2581.
76. Zhang, S., et al., *Advanced titanium dioxide-polytetrafluorethylene (TiO2-PTFE) nanocomposite coatings on stainless steel surfaces with antibacterial and anti-corrosion properties.* Applied Surface Science, 2019. **490**: p. 231-241.
77. Stobie, N., et al., *Silver doped perfluoropolyether-urethane coatings: antibacterial activity and surface analysis.* Colloids and Surfaces B: Biointerfaces, 2009. **72**(1): p. 62-67.

78. Haque, H., T.J. Cutright, and B.-M.Z. Newby, *Effectiveness of sodium benzoate as a freshwater low toxicity antifoulant when dispersed in solution and entrapped in silicone coatings.* Biofouling, 2005. **21**(2): p. 109-119.
79. Ates, M., *A review on conducting polymer coatings for corrosion protection.* Journal of adhesion science and Technology, 2016. **30**(14): p. 1510-1536.
80. Liu, H., et al., *Preparation of conducting poly N-methylaniline microsphere and its antibacterial performance to sulfate reducing bacteria.* Journal of Wuhan University of Technology-Mater. Sci. Ed., 2008. **23**(4): p. 536-540.
81. Lv, H., et al., *Layer-by-layer self-assembly of minocycline-loaded chitosan/alginate multilayer on titanium substrates to inhibit biofilm formation.* Journal of dentistry, 2014. **42**(11): p. 1464-1472.
82. Zhang, Y., et al., *Tantalum nitride-decorated titanium with enhanced resistance to microbiologically induced corrosion and mechanical property for dental application.* 2015. **10**(6): p. e0130774.
83. Grischke, J., J. Eberhard, and M. Stiesch, *Antimicrobial dental implant functionalization strategies—A systematic review.* Dental Materials Journal, 2016. **35**(4): p. 545-558.
84. Szaraniec, B., et al., *Multifunctional polymer coatings for titanium implants.* Materials Science and Engineering: C, 2018. **93**: p. 950-957.
85. Asri, R., et al., *Corrosion and surface modification on biocompatible metals: A review.* Materials Science and Engineering: C, 2017. **77**: p. 1261-1274.
86. Spange, S.J.C.U.o.T., *Electrochemical Synthesis of Novel Polyaniline-Montmorillonite Nanocomposites and Corrosion Protection of Steel.* 2006.
87. ; Available from: https://pineresearch.com/shop/kb/theory/eis-theory/eis-basics/?msclkid=9efc6773cf3a11ec82b0626fc2185944.
88. Trif, L., A. Shaban, and J.J.C.R. Telegdi, *Electrochemical and surface analytical techniques applied to microbiologically influenced corrosion investigation.* 2018. **36**(4): p. 349-363.
89. Ma, M., et al., *Effect of cerium on the initiation of pitting corrosion of 444-type heat-resistant ferritic stainless steel.* 2020. **39**(1): p. 576-587.
90. Jiang, S., et al., *Effect of alkali/acid pretreatment on the topography and corrosion resistance of as-deposited CaP coating on magnesium alloys.* Journal of Alloys and Compounds, 2019. **793**: p. 202-211.
91. Staiger, M.P., et al., *Magnesium and its alloys as orthopedic biomaterials: a review.* Biomaterials, 2006. **27**(9): p. 1728-1734.
92. Chen, Y., et al., *Recent advances on the development of magnesium alloys for biodegradable implants.* Acta biomaterialia, 2014. **10**(11): p. 4561-4573.
93. Li, Z., et al., *Formation and In vitro evaluation of a deep eutectic solvent conversion film on biodegradable magnesium alloy.* ACS Applied Materials & Interfaces, 2020. **12**(29): p. 33315-33324.
94. Da Conceicao, T., et al., *Surface modification of magnesium alloy AZ31 by hydrofluoric acid treatment and its effect on the corrosion behaviour.* Thin Solid Films, 2010. **518**(18): p. 5209-5218.
95. Guo, Y., et al., *Enhanced corrosion resistance and biocompatibility of biodegradable magnesium alloy modified by calcium phosphate/collagen coating.* Surface and Coatings Technology, 2020. **401**: p. 126318.

96. Cipriano, A.F., et al., *Anodization of magnesium for biomedical applications–Processing, characterization, degradation and cytocompatibility*. Acta biomaterialia, 2017. **62**: p. 397-417.
97. Zhang, R., S. Zhang, and S. Duo, *Influence of phytic acid concentration on coating properties obtained by MAO treatment on magnesium alloys.* Applied Surface Science, 2009. **255**(18): p. 7893-7897.
98. Zhang, R., et al., *Influence of sodium silicate concentration on properties of micro arc oxidation coatings formed on AZ91HP magnesium alloys.* Surface and Coatings Technology, 2012. **206**(24): p. 5072-5079.
99. Kim, J., et al., *Enhanced corrosion resistance and biocompatibility of AZ31 Mg alloy using PCL/ZnO NPs via electrospinning.* Applied Surface Science, 2017. **396**: p. 249-258.
100. Rezk, A.I., et al., *Strategic design of a Mussel-inspired in situ reduced Ag/Au-Nanoparticle Coated Magnesium Alloy for enhanced viability, antibacterial property and decelerated corrosion rates for degradable implant Applications.* Scientific reports, 2019. **9**(1): p. 1-12.
101. Guo, Y., et al., *A Multifunctional Polypyrrole/Zinc Oxide Composite Coating on Biodegradable Magnesium Alloys for Orthopedic Implants.* Colloids and Surfaces B: Biointerfaces, 2020: p. 111186.
102. Zomorodian, A., et al., *Corrosion resistance of a composite polymeric coating applied on biodegradable AZ31 magnesium alloy.* Acta Biomaterialia, 2013. **9**(10): p. 8660-8670.
103. Li, L.-Y., et al., *Advances in functionalized polymer coatings on biodegradable magnesium alloys–a review.* Acta biomaterialia, 2018. **79**: p. 23-36.
104. Shi, P., et al., *Preparation and characterization of PLA coating and PLA/MAO composite coatings on AZ31 magnesium alloy for improvement of corrosion resistance.* Surface and Coatings Technology, 2015. **262**: p. 26-32.
105. Li, J., et al., *In vitro degradation and cell attachment of a PLGA coated biodegradable Mg–6Zn based alloy.* Journal of materials science, 2010. **45**(22): p. 6038-6045.
106. Gu, X., et al., *Surface modification of an Mg-1Ca alloy to slow down its biocorrosion by chitosan.* Biomedical Materials, 2009. **4**(4): p. 044109.
107. Kunjukunju, S., et al., *A layer-by-layer approach to natural polymer-derived bioactive coatings on magnesium alloys.* Acta biomaterialia, 2013. **9**(10): p. 8690-8703.
108. Xiong, P., et al., *Osteogenic and pH stimuli-responsive self-healing coating on biomedical Mg-1Ca alloy.* Acta biomaterialia, 2019. **92**: p. 336-350.
109. Ostovari, A., et al., *Corrosion inhibition of mild steel in 1 M HCl solution by henna extract: A comparative study of the inhibition by henna and its constituents (Lawsone, Gallic acid, α-d-Glucose and Tannic acid).* Corrosion Science, 2009. **51**(9): p. 1935-1949.
110. Motalebi, A., et al., *Improvement of corrosion performance of 316L stainless steel via PVTMS/henna thin film.* Progress in Natural Science: Materials International, 2012. **22**(5): p. 392-400.
111. Odarczenko, M., et al., *Self-protecting epoxy coatings with anticorrosion microcapsules.* ACS omega, 2018. **3**(10): p. 14157-14164.
112. Lamaka, S., et al., *Comprehensive screening of Mg corrosion inhibitors.* Corrosion Science, 2017. **128**: p. 224-240.
113. Nayak, B.S., et al., *The evidence based wound healing activity of Lawsonia inermis Linn.* Phytotherapy Research: An International Journal Devoted to Pharmacological and Toxicological Evaluation of Natural Product Derivatives, 2007. **21**(9): p. 827-831.

114. Ur Rehman, M.A., et al., *Electrophoretic deposition of lawsone loaded bioactive glass (BG)/chitosan composite on polyetheretherketone (PEEK)/BG layers as antibacterial and bioactive coating.* Journal of Biomedical Materials Research Part A, 2018. **106**(12): p. 3111-3122.
115. Barani, M., et al., *Lawsone-loaded Niosome and its antitumor activity in MCF-7 breast Cancer cell line: a Nano-herbal treatment for Cancer.* DARU Journal of Pharmaceutical Sciences, 2018. **26**(1): p. 11-17.
116. Adeli-Sardou, M., et al., *Controlled release of lawsone from polycaprolactone/gelatin electrospun nano fibers for skin tissue regeneration.* International journal of biological macromolecules, 2019. **124**: p. 478-491.
117. Zhang, D., et al., *Advances in antibacterial functionalized coatings on Mg and its alloys for medical use—A review.* Coatings, 2020. **10**(9): p. 828.
118. Zhang, L., et al., *Advances in microarc oxidation coated AZ31 Mg alloys for biomedical applications.* Corrosion Science, 2015. **91**: p. 7-28.
119. Zhang, S., et al., *Research on an Mg–Zn alloy as a degradable biomaterial.* Acta biomaterialia, 2010. **6**(2): p. 626-640.
120. Pan, C.-J., et al., *Effects of self-assembly of 3-phosphonopropionic acid, 3-aminopropyltrimethoxysilane and dopamine on the corrosion behaviors and biocompatibility of a magnesium alloy.* Materials Science and Engineering: C, 2016. **67**: p. 132-143.
121. Choi, J.B., et al., *Effect of composite coating with poly-dopamine/PCL on the corrosion resistance of magnesium.* International Journal of Polymeric Materials and Polymeric Biomaterials, 2019. **68**(6): p. 328-337.
122. Bakhsheshi-Rad, H., et al., *Synthesis and corrosion behavior of a hybrid bioceramic-biopolymer coating on biodegradable Mg alloy for orthopaedic implants.* Journal of Alloys and Compounds, 2015. **648**: p. 1067-1071.
123. Xiong, P., et al., *Biomimetic Ca, Sr/P-doped silk fibroin films on Mg-1Ca alloy with dramatic corrosion resistance and osteogenic activities.* ACS Biomaterials Science & Engineering, 2018. **4**(9): p. 3163-3176.
124. Mohammadi, A., et al., *Aqueous dispersion of polyurethane nanocomposites based on calix [4] arenes modified graphene oxide nanosheets: preparation, characterization, and anti-corrosion properties.* Chemical Engineering Journal, 2018. **349**: p. 466-480.
125. Asadi, H., et al., *Electrospun zein/graphene oxide nanosheet composite nanofibers with controlled drug release as antibacterial wound dressing.* International Journal of Polymeric Materials and Polymeric Biomaterials, 2020. **69**(3): p. 173-185.
126. Wang, P., et al., *A silk-based coating containing GREDVY peptide and heparin on Mg–Zn–Y–Nd alloy: improved corrosion resistance, hemocompatibility and endothelialization.* Journal of Materials Chemistry B, 2018. **6**(6): p. 966-978.
127. Ghalei, S., et al., *Silk Nanoparticles: A Natural Polymeric Platform for Nitric Oxide Delivery in Biomedical Applications.* ACS Applied Materials & Interfaces, 2020.
128. Ghalei, S., et al., *Synergistic Approach to Develop Antibacterial Electrospun Scaffolds Using Honey and S-Nitroso-N-acetyl Penicillamine.* ACS Biomaterials Science & Engineering, 2021.
129. Ghalei, S., et al., *Enhanced cellular response elicited by addition of amniotic fluid to alginate hydrogel-electrospun silk fibroin fibers for potential wound dressing application.* Colloids and Surfaces B: Biointerfaces, 2018. **172**: p. 82-89.

130. Pan, C.-J., et al., *Improving corrosion resistance and biocompatibility of magnesium alloy by sodium hydroxide and hydrofluoric acid treatments.* Applied Sciences, 2017. **7**(1): p. 33.

131. Visan, A.I., et al., *Long-term evaluation of dip-coated pcl-blend-peg coatings in simulated conditions.* Polymers, 2020. **12**(3): p. 717.

132. Liu, H. and T.J. Webster, *Nanomedicine for implants: a review of studies and necessary experimental tools.* Biomaterials, 2007. **28**(2): p. 354-369.

133. Ghalei, S., H. Asadi, and B. Ghalei, *Zein nanoparticle-embedded electrospun PVA nanofibers as wound dressing for topical delivery of anti-inflammatory diclofenac.* Journal of Applied Polymer Science, 2018. **135**(33): p. 46643.

134. Agarwal, S., et al., *Enhanced corrosion protection and biocompatibility of a PLGA–silane coating on AZ31 Mg alloy for orthopaedic applications.* RSC advances, 2016. **6**(115): p. 113871-113883.

135. Ansari, Z., et al., *Polycaprolactone/fluoride substituted-hydroxyapatite (PCL/FHA) nanocomposite coatings prepared by in-situ sol-gel process for dental implant applications.* Progress in Organic Coatings, 2020. **147**: p. 105873.

136. Song, G., et al., *The anodic dissolution of magnesium in chloride and sulphate solutions.* Corrosion science, 1997. **39**(10-11): p. 1981-2004.

137. Eliaz, N., *Corrosion of metallic biomaterials: A review.* Materials, 2019. **12**(3): p. 407.

138. Zhang, W., et al., *Strengthened corrosion control of poly (lactic acid)(PLA) and poly (ε-caprolactone)(PCL) polymer-coated magnesium by imbedded hydrophobic stearic acid (SA) thin layer.* Corrosion Science, 2016. **112**: p. 327-337.

139. Shkirskiy, V., et al., *Revisiting the electrochemical impedance spectroscopy of magnesium with online inductively coupled plasma atomic emission spectroscopy.* ChemPhysChem, 2015. **16**(3): p. 536-539.

140. Shafiee, B.M., et al., *An improvement in corrosion resistance of 316L AISI coated using PCL-gelatin composite by dip-coating method.* Progress in Organic Coatings, 2019. **130**: p. 200-205.

141. Bhattarai, D.P., et al., *A controlled surface geometry of polyaniline doped titania nanotubes biointerface for accelerating MC3T3-E1 cells growth in bone tissue engineering.* Chemical Engineering Journal, 2018. **350**: p. 57-68.

142. Leal, D.A., et al., *Smart coating based on double stimuli-responsive microcapsules containing linseed oil and benzotriazole for active corrosion protection.* Corrosion Science, 2018. **130**: p. 56-63.

143. He, X., et al., *Biocompatibility, corrosion resistance and antibacterial activity of TiO2/CuO coating on titanium.* Ceramics International, 2017. **43**(18): p. 16185-16195.

144. Qian, H., et al., *Dual-action smart coatings with a self-healing superhydrophobic surface and anti-corrosion properties.* Journal of materials chemistry A, 2017. **5**(5): p. 2355-2364.

145. Huang, Y., et al., *Triple-action self-healing protective coatings based on shape memory polymers containing dual-function microspheres.* ACS applied materials & interfaces, 2018. **10**(27): p. 23369-23379.

146. Li, J., et al., *Reinforcement of graphene and its derivatives on the anticorrosive properties of waterborne polyurethane coatings.* Composites Science and Technology, 2016. **129**: p. 30-37.

147. Liu, X., et al., *Improvement of active corrosion protection of carbon steel by water-based epoxy coating with smart CeO2 nanocontainers.* Progress in Organic Coatings, 2018. **115**: p. 195-204.
148. Mingo, B., et al., *Smart Functionalization of Ceramic-coated AZ31 Magnesium Alloy.* ACS Applied Materials & Interfaces, 2020.
149. Plawecka, M., et al., *Self healing ability of inhibitor-containing nanocapsules loaded in epoxy coatings applied on aluminium 5083 and galvanneal substrates.* Electrochimica Acta, 2014. **140**: p. 282-293.
150. Majd, M.T., T. Shahrabi, and B. Ramezanzadeh, *The role of neodymium based thin film on the epoxy/steel interfacial adhesion and corrosion protection promotion.* Applied Surface Science, 2019. **464**: p. 516-533.
151. Feliu, S., *Electrochemical Impedance Spectroscopy for the Measurement of the Corrosion Rate of Magnesium Alloys: Brief Review and Challenges.* Metals, 2020. **10**(6): p. 775.
152. Yeganeh, M., et al., *An investigation on the corrosion behavior of the epoxy coating embedded with mesoporous silica nanocontainer loaded by sulfamethazine inhibitor.* Progress in Organic Coatings, 2019. **128**: p. 75-81.
153. Arrabal, R., et al., *Effect of Nd on the corrosion behaviour of AM50 and AZ91D magnesium alloys in 3.5 wt.% NaCl solution.* Corrosion Science, 2012. **55**: p. 301-312.
154. Majd, M.T., et al., *Construction of a smart active/barrier anti-corrosion system based on epoxy-ester/zinc intercalated kaolin nanocontainer for steel substrate.* Construction and Building Materials, 2020. **247**: p. 118555.
155. Wang, L., et al., *Optimization of the Experimental Parameters Affecting the Corrosion Behavior for Mg–Y–Zn–Mn Alloy via Response Surface Methodology.* 2021. **27**(12): p. 5095-5107.
156. King, A.D., N. Birbilis, and J.R. Scully, *Accurate electrochemical measurement of magnesium corrosion rates; a combined impedance, mass-loss and hydrogen collection study.* Electrochimica Acta, 2014. **121**: p. 394-406.
157. Ghali, E., W. Dietzel, and K.-U. Kainer, *General and localized corrosion of magnesium alloys: a critical review.* Journal of materials engineering and performance, 2004. **13**(1): p. 7-23.
158. Zhang, S., et al., *In vitro degradation, hemolysis and MC3T3-E1 cell adhesion of biodegradable Mg–Zn alloy.* Materials Science and Engineering: C, 2009. **29**(6): p. 1907-1912.
159. Xin, Y., et al., *Corrosion products on biomedical magnesium alloy soaked in simulated body fluids.* Journal of materials research, 2009. **24**(8): p. 2711-2719.
160. Wang, B., et al., *Effect of corrosion product films on the in vitro degradation behavior of Mg-3% Al-1% Zn (in wt%) alloy in hank's solution.* Journal of materials science & technology, 2018. **34**(10): p. 1756-1764.
161. Zou, Y.-H., et al., *Corrosion resistance and antibacterial activity of zinc-loaded montmorillonite coatings on biodegradable magnesium alloy AZ31.* Acta biomaterialia, 2019. **98**: p. 196-214.
162. Dev, V.G., et al., *Dyeing and antimicrobial characteristics of chitosan treated wool fabrics with henna dye.* Carbohydrate Polymers, 2009. **75**(4): p. 646-650.
163. Rahmoun, N., et al., *Antibacterial and antifungal activity of lawsone and novel naphthoquinone derivatives.* Medecine et maladies infectieuses, 2012. **42**(6): p. 270-275.

164. Narayanan, T.S. and M.H. Lee, *A simple strategy to modify the porous structure of plasma electrolytic oxidation coatings on magnesium.* RSC advances, 2016. **6**(19): p. 16100-16114.
165. Bakhsheshi-Rad, H., et al., *In vitro degradation behavior, antibacterial activity and cytotoxicity of TiO2-MAO/ZnHA composite coating on Mg alloy for orthopedic implants.* Surface and Coatings Technology, 2018. **334**: p. 450-460.
166. Heise, S., S. Virtanen, and A.R. Boccaccini, *Tackling Mg alloy corrosion by natural polymer coatings—A review.* Journal of Biomedical Materials Research Part A, 2016. **104**(10): p. 2628-2641.
167. Calvino, C., et al., *Development, processing and applications of bio-sourced cellulose nanocrystal composites.* Progress in Polymer Science, 2020. **103**: p. 101221.
168. He, Y., et al., *Corrosion protective properties of cellulose nanocrystals reinforced waterborne acrylate-based composite coating.* Corrosion Science, 2019. **155**: p. 186-194.
169. Ma, I.A.W., et al., *Anticorrosion properties of epoxy/nanocellulose nanocomposite coating.* Bioresources, 2017. **12**(2): p. 2912-2929.
170. He, Y., et al., *Comparative study of CNC and CNF as additives in waterborne acrylate-based anti-corrosion coatings.* Journal of Dispersion Science and Technology, 2020. **41**(13): p. 2037-2047.
171. Abd El-Fattah, M., et al., *Nanocrystalline cellulose as an eco-friendly reinforcing additive to polyurethane coating for augmented anticorrosive behavior.* Carbohydrate polymers, 2018. **183**: p. 311-318.
172. Chen, Q., et al., *Electrophoretic deposition of cellulose nanocrystals (CNs) and CNs/alginate nanocomposite coatings and free standing membranes.* Colloids and Surfaces B: Biointerfaces, 2014. **118**: p. 41-48.
173. Siavashani, A.Z., et al., *Silk fibroin/sericin 3D sponges: the effect of sericin on structural and biological properties of fibroin.* International journal of biological macromolecules, 2020. **153**: p. 317-326.
174. Mottaghitalab, F., et al., *Silk as a potential candidate for bone tissue engineering.* Journal of controlled release, 2015. **215**: p. 112-128.
175. Thurber, A.E., F.G. Omenetto, and D.L. Kaplan, *In vivo bioresponses to silk proteins.* Biomaterials, 2015. **71**: p. 145-157.
176. He, X., et al., *Layered hydroxide/polydopamine/hyaluronic acid functionalized magnesium alloys for enhanced anticorrosion, biocompatibility and antithrombogenicity in vascular stents.* Journal of biomaterials applications, 2020. **34**(8): p. 1131-1141.
177. Ghalei, S., et al., *Silk Nanoparticles: A Natural Polymeric Platform for Nitric Oxide Delivery in Biomedical Applications.* ACS Applied Materials & Interfaces, 2020. **12**(48): p. 53615-53623.
178. Singer, F., et al., *Corrosion properties of polydopamine coatings formed in one-step immersion process on magnesium.* ACS applied materials & interfaces, 2015. **7**(48): p. 26758-26766.
179. Chakrabarty, A. and Y. Teramoto, *Recent advances in nanocellulose composites with polymers: a guide for choosing partners and how to incorporate them.* Polymers, 2018. **10**(5): p. 517.
180. Wang, C., et al., *Fabrication and characterization of silk fibroin coating on APTES pretreated Mg-Zn-Ca alloy.* Materials Science and Engineering: C, 2020. **110**: p. 110742.

181. Hu, X., D. Kaplan, and P. Cebe, *Determining beta-sheet crystallinity in fibrous proteins by thermal analysis and infrared spectroscopy.* Macromolecules, 2006. **39**(18): p. 6161-6170.
182. Ghalei, S., et al., *Nitric oxide releasing halloysite nanotubes for biomedical applications.* Journal of Colloid and Interface Science, 2021.
183. Mao, H., et al., *Mechanical and water-resistant properties of eco-friendly chitosan membrane reinforced with cellulose nanocrystals.* Polymers, 2019. **11**(1): p. 166.
184. Zhang, L., E.A. Mohammed, and A. Adriaens, *Synthesis and electrochemical behavior of a magnesium fluoride-polydopamine-stearic acid composite coating on AZ31 magnesium alloy.* Surface and Coatings Technology, 2016. **307**: p. 56-64.
185. Yang, X., L. Duan, and X. Ran, *Effect of polydopamine coating on improving photostability of polyphenylene sulfide fiber.* Polymer Bulletin, 2017. **74**(3): p. 641-656.
186. Chakravarty, S., et al., *Silk fibroin–carbon nanoparticle composite scaffolds: a cost effective supramolecular 'turn off'chemiresistor for nitroaromatic explosive vapours.* Journal of Materials Chemistry C, 2016. **4**(38): p. 8920-8929.
187. Liu, L., et al., *Biomimicking the structure of silk fibers via cellulose nanocrystal as β-sheet crystallite.* RSC Advances, 2014. **4**(27): p. 14304-14313.
188. Dorishetty, P., et al., *Tunable biomimetic hydrogels from silk fibroin and nanocellulose.* ACS Sustainable Chemistry & Engineering, 2020. **8**(6): p. 2375-2389.
189. Kim, H.J., et al., *Cellulose–silk fibroin hydrogels prepared in a lithium bromide aqueous solution.* Cellulose, 2017. **24**(11): p. 5079-5088.
190. Fang, H., et al., *Enhanced adhesion and anticorrosion of silk fibroin coated biodegradable Mg-Zn-Ca alloy via a two-step plasma activation.* Corrosion Science, 2020. **168**: p. 108466.
191. Hu, X., D. Kaplan, and P.J.M. Cebe, *Determining beta-sheet crystallinity in fibrous proteins by thermal analysis and infrared spectroscopy.* 2006. **39**(18): p. 6161-6170.
192. Jin, H.-J., et al., *Biomaterial films of Bombyx M ori silk Fibroin with Poly (ethylene oxide).* Biomacromolecules, 2004. **5**(3): p. 711-717.
193. Song, M., et al., *Chemical cross-linked polyvinyl alcohol/cellulose nanocrystal composite films with high structural stability by spraying Fenton reagent as initiator.* International journal of biological macromolecules, 2018. **113**: p. 171-178.
194. Wang, J., et al., *Influence of surface roughness on contact angle hysteresis and spreading work.* Colloid and Polymer Science, 2020. **298**: p. 1107-1112.
195. Hofmann, S., et al., *Silk fibroin as an organic polymer for controlled drug delivery.* Journal of Controlled Release, 2006. **111**(1-2): p. 219-227.
196. Wong, H.M., et al., *Functionalized polymeric membrane with enhanced mechanical and biological properties to control the degradation of magnesium alloy.* Advanced healthcare materials, 2017. **6**(8): p. 1601269.
197. Lee, H., et al., *Mussel-inspired surface chemistry for multifunctional coatings.* science, 2007. **318**(5849): p. 426-430.
198. Yu, H., et al., *Corrosion resistance and infrared emissivity properties of EPDM (EPDM-g-MAH) film on low infrared emissivity PU/Cu coating.* Electrochimica acta, 2010. **55**(5): p. 1843-1847.
199. Yang, C.-W. and G.-K. Wang, *Effect of Hydrothermal (Sr)-Hydroxyapatite Coatings on the Corrosion Resistance and Mg2+ Ion Release to Enhance Osteoblastic Cell Responses of AZ91D Alloy.* Materials, 2020. **13**(3): p. 591.

200. Carangelo, A., A. Acquesta, and T. Monetta, *In-vitro corrosion of AZ31 magnesium alloys by using a polydopamine coating.* Bioactive materials, 2019. **4**: p. 71-78.
201. Wang, C., et al., *A versatile dopamine-induced intermediate layer for polyether imides (PEI) deposition on magnesium to render robust and high inhibition performance.* Corrosion Science, 2017. **122**: p. 32-40.
202. Monetta, T., et al., *Durability of AZ31 magnesium biodegradable alloys polydopamine aided: Part 1.* Journal of magnesium and alloys, 2017. **5**(4): p. 412-422.
203. Li, X., et al., *Corrosion resistance of dicalcium phosphate dihydrate/poly (lactic-co-glycolic acid) hybrid coating on AZ31 magnesium alloy.* Corrosion Science, 2016. **102**: p. 209-221.
204. Lu, Q., et al., *Water-insoluble silk films with silk I structure.* Acta biomaterialia, 2010. **6**(4): p. 1380-1387.
205. Ghalei, S., et al., *Synergistic Approach to Develop Antibacterial Electrospun Scaffolds Using Honey and S-Nitroso-N-acetyl Penicillamine.* ACS Biomaterials Science & Engineering, 2021. **7**(2): p. 517-526.
206. Maleki, H., et al., *Mechanically strong silica-silk fibroin bioaerogel: a hybrid scaffold with ordered honeycomb micromorphology and multiscale porosity for bone regeneration.* ACS applied materials & interfaces, 2019. **11**(19): p. 17256-17269.
207. Saini, M., et al., *Implant biomaterials: A comprehensive review.* 2015. **3**(1): p. 52.
208. Yang, Y., et al., *Streptococcus mutans biofilms induce metabolite-mediated corrosion of 316 L stainless steel in a simulated oral environment.* 2021. **182**: p. 109286.
209. Ansari, Z., et al., *Polycaprolactone/fluoride substituted-hydroxyapatite (PCL/FHA) nanocomposite coatings prepared by in-situ sol-gel process for dental implant applications.* 2020. **147**: p. 105873.
210. Agour, M., et al., *Alkali-Treated Titanium Coated with a Polyurethane, Magnesium and Hydroxyapatite Composite for Bone Tissue Engineering.* 2021. **11**(5): p. 1129.
211. Abdal-hay, A., et al., *Magnesium-particle/polyurethane composite layer coating on titanium surfaces for orthopedic applications.* 2019. **112**: p. 555-568.
212. Liu, Y., et al., *Fretting initiated crevice corrosion of 316LVM stainless steel in physiological phosphate buffered saline: Potential and cycles to initiation.* 2019. **97**: p. 565-577.
213. Abdal-Hay, A., et al., *Electrospun biphasic tubular scaffold with enhanced mechanical properties for vascular tissue engineering.* 2018. **82**: p. 10-18.
214. Mouflih, K., et al., *Chemical, Electrochemical, and Surface Study on Microbial Attack of CoCrMo Dental Alloy by Streptococcus mutans.* 2021. **7**(1): p. 1-10.
215. Zhao, H., et al., *Improved corrosion resistance and biofilm inhibition ability of copper-bearing 304 stainless steel against oral microaerobic Streptococcus mutans.* 2021. **66**: p. 112-120.
216. Shafiee, B.M., et al., *An improvement in corrosion resistance of 316L AISI coated using PCL-gelatin composite by dip-coating method.* 2019. **130**: p. 200-205.
217. Qian, H., et al., *Dual-action smart coatings with a self-healing superhydrophobic surface and anti-corrosion properties.* 2017. **5**(5): p. 2355-2364.
218. Al-Saadi, S., et al., *Graphene coating on a nickel-copper alloy (Monel 400) for microbial corrosion resistance: Electrochemical and surface characterizations.* 2021. **182**: p. 109299.

219. Jayanthi, V.S.A., A.B. Das, and U. Saxena, *Recent advances in biosensor development for the detection of cancer biomarkers.* Biosensors and Bioelectronics, 2017. **91**: p. 15-23.
220. Altintas, Z., et al., *Surface plasmon resonance based immunosensor for the detection of the cancer biomarker carcinoembryonic antigen.* Talanta, 2011. **86**: p. 377-383.
221. Tian, L., et al., *Gold nanoparticles superlattices assembly for electrochemical biosensor detection of microRNA-21.* Biosensors and Bioelectronics, 2018. **99**: p. 564-570.
222. Zhang, A., et al., *Spontaneous implantation of gold nanoparticles on graphene oxide for salivary SERS sensing.* Analytical Methods, 2019. **11**(40): p. 5089-5097.
223. Kangkamano, T., et al., *Pyrrolidinyl PNA polypyrrole/silver nanofoam electrode as a novel label-free electrochemical miRNA-21 biosensor.* Biosensors and Bioelectronics, 2018. **102**: p. 217-225.
224. Lan, H., et al., *MicroRNAs as potential biomarkers in cancer: opportunities and challenges.* BioMed research international, 2015. **2015**.
225. Yin, H., et al., *An electrochemical signal 'off–on' sensing platform for microRNA detection.* Analyst, 2012. **137**(6): p. 1389-1395.
226. Komatsu, S., et al., *Circulating microRNAs in plasma of patients with oesophageal squamous cell carcinoma.* British journal of cancer, 2011. **105**(1): p. 104.
227. Carneiro, M.C., et al., *Homemade 3-carbon electrode system for electrochemical sensing: Application to microRNA detection.* Microchemical Journal, 2018. **138**: p. 35-44.
228. Li, F., et al., *Carbon nanotube-based label-free electrochemical biosensor for sensitive detection of miRNA-24.* Biosensors and Bioelectronics, 2014. **54**: p. 158-164.
229. Zou, D., et al., *Multiplex detection of miRNAs based on aggregation-induced emission luminogen encoded microspheres.* RSC Advances, 2019. **9**(68): p. 39976-39985.
230. Labib, M. and M.V. Berezovski, *Electrochemical sensing of microRNAs: avenues and paradigms.* Biosensors and Bioelectronics, 2015. **68**: p. 83-94.
231. Shabaninejad, Z., et al., *Electrochemical-based biosensors for microRNA detection: Nanotechnology comes into view.* Analytical biochemistry, 2019: p. 113349.
232. Choi, Y.-E., J.-W. Kwak, and J.W. Park, *Nanotechnology for early cancer detection.* Sensors, 2010. **10**(1): p. 428-455.
233. Rahman, M., et al., *Electrochemical DNA hybridization sensors based on conducting polymers.* Sensors, 2015. **15**(2): p. 3801-3829.
234. Rashid, J.I.A. and N.A. Yusof, *The strategies of DNA immobilization and hybridization detection mechanism in the construction of electrochemical DNA sensor: A review.* Sensing and bio-sensing research, 2017. **16**: p. 19-31.
235. Pedano, M. and G. Rivas, *Immobilization of DNA at glassy ccarbon electrodes: A critical study of adsorbed layer.* Sensors, 2005. **5**(6): p. 424-447.
236. Wang, Q., et al., *Hybridization biosensor based on the covalent immobilization of probe DNA on chitosan–mutiwalled carbon nanotubes nanocomposite by using glutaraldehyde as an arm linker.* Sensors and Actuators B: Chemical, 2011. **156**(2): p. 599-605.
237. Rahman, M., et al., *A graphene oxide coated gold nanostar based sensing platform for ultrasensitive electrochemical detection of circulating tumor DNA.* Analytical Methods, 2020. **12**(4): p. 440-447.
238. Su, S., et al., *Dual-mode electrochemical analysis of microRNA-21 using gold nanoparticle-decorated MoS2 nanosheet.* Biosensors and Bioelectronics, 2017. **94**: p. 552-559.

239. Benvidi, A., et al., *Electro-oxidized Monolayer CVD Graphene Film Transducer for Ultrasensitive Impedimetric DNA Biosensor.* Electroanalysis, 2018. **30**(8): p. 1791-1800.
240. Tezerjani, M.D., et al., *A comparative investigation for prostate cancer detection using two electrochemical biosensors based on various nanomaterials and the linker of thioglycolic acid.* Journal of Electroanalytical Chemistry, 2016. **778**: p. 23-31.
241. Benvidi, A., et al., *Ultrasensitive DNA sensor based on gold nanoparticles/reduced graphene oxide/glassy carbon electrode.* Analytical biochemistry, 2015. **484**: p. 24-30.
242. Kesici, E., E. Eksin, and A. Erdem, *An impedimetric biosensor based on ionic liquid-modified graphite electrodes developed for microRNA-34a detection.* Sensors, 2018. **18**(9): p. 2868.
243. Zhang, K., et al., *Label-free impedimetric sensing platform for microRNA-21 based on ZrO 2-reduced graphene oxide nanohybrids coupled with catalytic hairpin assembly amplification.* RSC advances, 2018. **8**(29): p. 16146-16151.
244. Kannan, P., et al., *Nickel-phosphate pompon flowers nanostructured network enables the sensitive detection of microRNA.* Talanta, 2019: p. 120511.
245. Benvidi, A., et al., *Simple and label-free electrochemical impedance Amelogenin gene hybridization biosensing based on reduced graphene oxide.* Biosensors and Bioelectronics, 2014. **58**: p. 145-152.
246. Faria, H.A.M. and V. Zucolotto, *Label-free electrochemical DNA biosensor for zika virus identification.* Biosensors and Bioelectronics, 2019. **131**: p. 149-155.
247. Hizir, M.S., et al., *Simultaneous detection of circulating oncomiRs from body fluids for prostate cancer staging using nanographene oxide.* ACS applied materials & interfaces, 2014. **6**(17): p. 14772-14778.
248. De Silva, D., et al., *Interaction between androgen receptor and coregulator SLIRP is regulated by Ack1 tyrosine kinase and androgen.* Scientific Reports, 2019. **9**(1): p. 1-11.
249. Cai, B., et al., *Ultrasensitive label-free detection of PNA–DNA hybridization by reduced graphene oxide field-effect transistor biosensor.* ACS nano, 2014. **8**(3): p. 2632-2638.
250. Benvidi, A., et al., *Comparison of impedimetric detection of DNA hybridization on the various biosensors based on modified glassy carbon electrodes with PANHS and nanomaterials of RGO and MWCNTs.* Talanta, 2016. **147**: p. 621-627.
251. Zhou, Y., et al., *Charge-directed immobilization of bacteriophage on nanostructured electrode for whole-cell electrochemical biosensors.* Analytical chemistry, 2017. **89**(11): p. 5734-5741.
252. Fang, Y., et al., *Detection of methyl salicylate using bi-enzyme electrochemical sensor consisting salicylate hydroxylase and tyrosinase.* Biosensors and Bioelectronics, 2016. **85**: p. 603-610.
253. Fang, Y., Y. Umasankar, and R.P. Ramasamy, *A novel bi-enzyme electrochemical biosensor for selective and sensitive determination of methyl salicylate.* Biosensors and Bioelectronics, 2016. **81**: p. 39-45.
254. Parimi, N.S., et al., *Kinetic and mechanistic parameters of laccase catalyzed direct electrochemical oxygen reduction reaction.* Acs Catalysis, 2012. **2**(1): p. 38-44.
255. Fang, Y. and R.P. Ramasamy, *Detection of p-ethylphenol, a major plant volatile organic compound, by tyrosinase-based electrochemical biosensor.* ECS Journal of Solid State Science and Technology, 2016. **5**(8): p. M3054.

256. Xu, Y., et al., *Flexible graphene films via the filtration of water-soluble noncovalent functionalized graphene sheets.* Journal of the American Chemical Society, 2008. **130**(18): p. 5856-5857.
257. Ramasamy, R.P., et al., *High electrocatalytic activity of tethered multicopper oxidase–carbon nanotube conjugates.* Chemical Communications, 2010. **46**(33): p. 6045-6047.
258. Jahanbani, S. and A. Benvidi, *A novel electrochemical DNA biosensor based on a modified magnetic bar carbon paste electrode with Fe3O4NPs-reduced graphene oxide/PANHS nanocomposite.* Materials Science and Engineering: C, 2016. **68**: p. 1-8.
259. Zhou, Y., Y. Fang, and R.P. Ramasamy, *Non-covalent functionalization of carbon nanotubes for electrochemical biosensor development.* Sensors, 2019. **19**(2): p. 392.
260. Peña-Bahamonde, J., et al., *Recent advances in graphene-based biosensor technology with applications in life sciences.* Journal of nanobiotechnology, 2018. **16**(1): p. 75.
261. Wang, Z., et al., *Label-free, electrochemical detection of methicillin-resistant staphylococcus aureus DNA with reduced graphene oxide-modified electrodes.* Biosensors and Bioelectronics, 2011. **26**(9): p. 3881-3886.
262. Rasheed, P.A. and N. Sandhyarani, *Graphene-DNA electrochemical sensor for the sensitive detection of BRCA1 gene.* Sensors and Actuators B: Chemical, 2014. **204**: p. 777-782.
263. Singal, S., et al., *Electroactive graphene-multi-walled carbon nanotube hybrid supported impedimetric immunosensor for the detection of human cardiac troponin-I.* Rsc Advances, 2015. **5**(92): p. 74994-75003.
264. Yuan, Y.-H., et al., *Ratiometric electrochemical assay for sensitive detecting microRNA based on dual-amplification mechanism of duplex-specific nuclease and hybridization chain reaction.* Biosensors and Bioelectronics, 2018. **102**: p. 211-216.
265. Wang, Y.-H., et al., *Ultrasensitive supersandwich-type biosensor for enzyme-free amplified microRNA detection based on N-doped graphene/Au nanoparticles and hemin/G-quadruplexes.* Journal of Materials Chemistry B, 2018. **6**(14): p. 2134-2142.
266. Fan, L., et al., *A highly selective electrochemical impedance spectroscopy-based aptasensor for sensitive detection of acetamiprid.* Biosensors and Bioelectronics, 2013. **43**: p. 12-18.
267. Wu, S., et al., *A simple electrochemical biosensor for rapid detection of microRNA based on base stacking technology and enzyme amplification.* Int. J. Electrochem. Sci, 2015. **10**: p. 3848-3858.
268. Tian, L., et al., *A facile DNA strand displacement reaction sensing strategy of electrochemical biosensor based on N-carboxymethyl chitosan/molybdenum carbide nanocomposite for microRNA-21 detection.* Biosensors and Bioelectronics, 2018. **122**: p. 43-50.
269. Keighley, S.D., et al., *Optimization of label-free DNA detection with electrochemical impedance spectroscopy using PNA probes.* Biosensors and Bioelectronics, 2008. **24**(4): p. 906-911.
270. White, R.J., et al., *Optimization of electrochemical aptamer-based sensors via optimization of probe packing density and surface chemistry.* Langmuir, 2008. **24**(18): p. 10513-10518.
271. Congur, G., E. Eksin, and A. Erdem, *Impedimetric detection of miRNA-34a using graphene oxide modified chemically activated graphite electrodes.* Sensors and Actuators A: Physical, 2018. **279**: p. 493-500.

272. Zhou, L., et al., *A label-free electrochemical biosensor for microRNAs detection based on DNA nanomaterial by coupling with Y-shaped DNA structure and non-linear hybridization chain reaction.* Biosensors and Bioelectronics, 2019. **126**: p. 657-663.
273. Tian, L., et al., *Planar intercalated copper (II) complex molecule as small molecule enzyme mimic combined with Fe3O4 nanozyme for bienzyme synergistic catalysis applied to the microRNA biosensor.* Biosensors and Bioelectronics, 2018. **110**: p. 110-117.
274. Li, D., et al., *A colorimetric biosensor for detection of attomolar microRNA with a functional nucleic acid-based amplification machine.* Talanta, 2016. **146**: p. 470-476.
275. Wu, P., S.i. Nakano, and N. Sugimoto, *Temperature dependence of thermodynamic properties for DNA/DNA and RNA/DNA duplex formation.* European journal of biochemistry, 2002. **269**(12): p. 2821-2830.
276. Wong, I.Y. and N.A. Melosh, *An electrostatic model for DNA surface hybridization.* Biophysical journal, 2010. **98**(12): p. 2954-2963.
277. Erdem, A., et al., *Graphene oxide modified chemically activated graphite electrodes for detection of microRNA.* Electroanalysis, 2017. **29**(5): p. 1350-1358.
278. Bettazzi, F., et al., *Electrochemical detection of miRNA-222 by use of a magnetic bead-based bioassay.* Analytical and bioanalytical chemistry, 2013. **405**(2-3): p. 1025-1034.
279. Li, B., et al., *Graphene electrode modified with electrochemically reduced graphene oxide for label-free DNA detection.* Biosensors and Bioelectronics, 2015. **72**: p. 313-319.
280. Zhu, L., L. Luo, and Z. Wang, *DNA electrochemical biosensor based on thionine-graphene nanocomposite.* Biosensors and Bioelectronics, 2012. **35**(1): p. 507-511.
281. Cardoso, A.R., et al., *Novel and simple electrochemical biosensor monitoring attomolar levels of miRNA-155 in breast cancer.* Biosensors and Bioelectronics, 2016. **80**: p. 621-630.
282. Zhang, K., et al., *Sensitive detection of microRNA in complex biological samples by using two stages DSN-assisted target recycling signal amplification method.* Biosensors and Bioelectronics, 2017. **87**: p. 358-364.
283. Azimzadeh, M., et al., *Early detection of Alzheimer's disease using a biosensor based on electrochemically-reduced graphene oxide and gold nanowires for the quantification of serum microRNA-137.* RSC advances, 2017. **7**(88): p. 55709-55719.
284. Zhu, D., et al., *Label-free electrochemical sensing platform for microRNA-21 detection using thionine and gold nanoparticles co-functionalized MoS2 nanosheet.* ACS applied materials & interfaces, 2017. **9**(41): p. 35597-35603.
285. Smith, D.A., et al., *Electrochemical detection of urinary microRNAs via sulfonamide-bound antisense hybridisation.* Sensors and Actuators B: Chemical, 2017. **253**: p. 335-341.
286. Eksin, E., et al., *Chitosan/nitrogen doped reduced graphene oxide modified biosensor for impedimetric detection of microRNA.* Electroanalysis, 2018. **30**(3): p. 551-560.
287. Rafiee-Pour, H.-A., M. Behpour, and M. Keshavarz, *A novel label-free electrochemical miRNA biosensor using methylene blue as redox indicator: application to breast cancer biomarker miRNA-21.* Biosensors and bioelectronics, 2016. **77**: p. 202-207.
288. Azimzadeh, M., et al., *An electrochemical nanobiosensor for plasma miRNA-155, based on graphene oxide and gold nanorod, for early detection of breast cancer.* Biosensors and Bioelectronics, 2016. **77**: p. 99-106.
289. Asadzadeh-Firouzabadi, A. and H.R. Zare, *Preparation and application of AgNPs/SWCNTs nanohybrid as an electroactive label for sensitive detection of miRNA related to lung cancer.* Sensors and Actuators B: Chemical, 2018. **260**: p. 824-831.

290. Voccia, D., et al., *Direct determination of small RNAs using a biotinylated polythiophene impedimetric genosensor*. Biosensors and Bioelectronics, 2017. **87**: p. 1012-1019.
291. Yammouri, G., et al., *Development of an electrochemical label-free biosensor for microRNA-125a detection using pencil graphite electrode modified with different carbon nanomaterials*. Journal of Electroanalytical Chemistry, 2017. **806**: p. 75-81.

APPENDICES

APPENDIX A

GRAPHENE-BASED ELECTROCHEMICAL BIOSENSOR FOR IMPEDIMETRIC DETECTION OF MICRO-RNA AS POTENTIAL CANCER BIOMARKER

This appendix contains text from the following publication:

Hamid Asadi and Ramaraja P. Ramasamy. Journal of The Electrochemical Society 167, no. 16 (2020): 167523.

Reprinted here with permission of the publisher.

Abstract

MicroRNAs (miRNAs) have shown great potential to be used as biomarkers for the screening and clinical diagnosis of cancer. In this study, an electrochemical biosensor based on graphene-modified glassy carbon electrode was developed for the detection of miRNA-21, a well-known biomarker for the early stage of prostate cancer. A novel molecular tethering agent was used for immobilization of single-stranded probe DNA onto the electrode surface. Different parameters related to biosensor fabrication and experimental conditions were optimized to obtain the highest biosensor response. Electrochemical impedance spectroscopy was employed to achieve a sensitive and label-free detection method for miRNA-21 through measuring the change in charge-transfer resistance (R_{ct}) before and after hybridization. Under the optimal conditions, the biosensor showed a linear impedimetric response between ΔR_{ct} and logarithm of miRNA-21 concentration ranging from 10^{-14} to 10^{-8} M with a correlation coefficient of 0.972 and a detection limit of 3 fM. The selectivity of the biosensor was examined against non-complementary miRNA-141. The biosensor showed acceptable reproducibility, regeneration ability and stability as well as remarkable response (recoveries 90-116%) in real plasma samples. The results indicated that the proposed biosensor could be used as a promising alternative to conventional methods in early clinical and point-of-care cancer diagnosis.

Keywords

miRNA cancer biomarkers, Electrochemical biosensors, Electrochemical impedance spectroscopy, Graphene

Introduction

Cancer is the second largest disease worldwide, with an increasing mortality rate over the past few years. Despite recent technological advancements, the survival rate of cancer patients is still low, mainly because of the diagnosis of cancer at very late stages [219]. Conventional cancer diagnosis methods such as ultrasound, magnetic resonance imaging, and biopsy are inefficient for early-stage cancer detection as these methods depend on the phenotypic properties of the tumor [220]. Cancer biomarkers can remarkably improve early detection capability and subsequent treatment of cancer before it proceeds into advanced stages. Such biomarkers can be found in most bodily fluids like blood serum, urine and, saliva, which makes them promising targets for the diagnosis, prognosis, and treatment of cancer [221, 222].

MicroRNAs (miRNAs) are naturally occurring, single-stranded non-coding RNAs with 19-25 nucleotides in length, which play an essential role in regulating gene expression and various physiological processes. Recently, they have been receiving much attention as clinically-significant molecular biomarkers for early cancer screening. Clinical studies have revealed that aberrant expression of miRNAs compared to the basal level can be closely associated with the initiation, progression, and metastasis of cancer [223]. Additionally, miRNAs are highly stable in the circulation system and can withstand severe conditions like boiling, low or high pH levels, extended storage, and freeze−thaw cycles without degradation [224]. All these advantages have made miRNAs ideal biomarkers for clinical diagnosis cancer biomarkers. Despite miRNA's great diagnostic value, direct and real-time detection of miRNA from patient samples is still challenging due to their exceptionally short length, similarity with multitude of other small nucleotide sequences, and quite low levels of expression (1×10-14 M to 9×10-10 M) [225, 226].

The most widely used methods for miRNA analysis include northern blotting, quantitative real-time polymerase chain reaction (qRT-PCR), and microarray [227]. These methods have some intrinsic limitations, including the need for tedious procedures, a large sample requirement, need for highly specialized experts, expensive instrumentation, and extended analysis time, limiting their potential use in point of care (POC) diagnostics [228].

Biosensors offer significant prospects for POC testing, by enabling fast results and requiring minimal sample pretreatment. They could overcome some of the limitations of conventional molecular methods such as the ability to provide multiplexed detection [229], real-time measurement, and high throughput [230]. Among different types of biosensors for miRNA detection, electrochemical biosensors (EC) have shown great promise due to their high sensitivity, rapidity, low-cost, wide dynamic range, and compatibility with the miniaturization [231]. In EC biosensor, the hybridization event between the immobilized nucleotide probe and target miRNA is converted to a quantifiable electrochemical signal (current, potential or impedance), which is proportional to the concentration of the target miRNA [227].

One of the most crucial steps in the construction of any EC biosensor is the immobilization of DNA probe on the transducer surface, which is responsible for selectively interacting with the analyte [232]. Several DNA probe immobilization techniques, including physical adsorption and covalent bonding, have been used in the fabrication of electrochemical nucleotide biosensors [233]. Physical adsorption techniques offer a rapid and straightforward immobilization strategy with less usage of chemical reagents. However, the physically-adsorbed DNA probe could easily be desorbed from the electrode surface even with slight changes in pH, ionic strength, or temperature [234]. Moreover, it has been reported that physical adsorption of probe DNA will create a randomly oriented DNA monolayer on the electrode surface with a significant compromise of the bases of adsorbed DNA, making further hybridization difficult [235]. In contrast, covalent bonding techniques can form a vertically oriented DNA monolayer with high binding strength and stability, resulting in a more reactive and flexible probe layer and consequently higher hybridization efficiency [236].

Recently, different types of nanomaterials have been used in the fabrication of EC DNA biosensors with the goals of improving the limit of detection (LOD) and detection sensitivity [237]. Nanomaterials as immobilization supports can remarkably improve the performance of DNA biosensors by increasing the electrode surface area and the rate of probe immobilization [238]. Graphene, composed of a two-dimensional sheet of sp^2-bonded carbon atoms, has attracted much attention as an ideal transducer material for the construction of electrochemical biosensors [222, 239]. Owing to its unique properties including large surface area, excellent electrical conductivity, enhanced electrochemical behavior, fast heterogeneous electron transfer, and high mechanical adhesion, graphene has a great potential for fabrication of EC sensing platforms [240].

Electrochemical impedance spectroscopy (EIS) is a promising technique for analysis of the electrode surface. The method is highly sensitive to any change in the electrical properties of the electrode surface [241], and has been used previously for the detection of miRNAs [242-244]. As a label-free detection method, EIS eliminates the need for labeling target miRNA with markers such as fluorescent dyes, enzymes, or other redox labels, which is often costly and time-consuming [245]. During EIS measurement, the hybridization of the complementary miRNA with the immobilized capture probe changes the charge-transfer resistance (R_{ct}) of the system. This variation in R_{ct} values before and after hybridization will be used as an impedimetric signal for the detection of miRNA binding [246].

In this work, we present a novel label-free electrochemical biosensor for the detection of miRNA as a potential cancer biomarker. As the model analyte, miRNA-21 was selected due to its overexpression in the early stage of prostate cancer, the second leading cause of cancer death in men in the US [247, 248]. Owing to the advantages of molecular tethering for covalent immobilization of biomolecules, we used 1-pyrenebutyric acid-N-hydroxysuccinimide ester (PBSE) as a molecular linker to immobilize probe DNA on the graphene-modified electrode. Using PBSE and graphene provides a suitable platform for a stable and reproducible immobilization of probe DNA strands on the electrode surface. Additionally, it simplifies the whole electrode preparation processes by eliminating the activation steps usually needed in other methods like EDC/NHS coupling. The resulting biosensor was used for the detection of miRNA-21 using EIS as the detection technique under optimized experimental conditions (loading mass of graphene, probe DNA concentration, hybridization time, and hybridization temperature). The biosensor response measurement is based on the monitoring of the change in the charge-transfer resistance consequent to the hybridization. We also examined non-complementary miRNA sequences as negative controls to verify the selectivity of the biosensor. Finally, the applicability of the biosensor for measuring miRNA-21 in blood plasma samples was also evaluated.

Experimental

Reagents and chemicals

The following chemicals were reagent grade and used as received: sodium phosphate dibasic anhydrous (Na_2HPO_4) and sodium chloride (NaCl) from EMD chemicals; 1-pyrenebutanoic acid succinimidyl ester (PBSE), ethanolamine, and 20× saline-sodium citrate (SSC) buffer from Sigma-Aldrich; dimethylformamide (DMF) from Acros; potassium ferricyanide ($K_3[Fe(CN)_6]$) (from AMRESCO Inc); potassium ferrocyanide ($K_4[Fe(CN)_6]$) and magnesium chloride hexahydrate ($MgCl_2.6H_2O$) (from MP Biomedicals); ethylenediamine tetraacetic acid (EDTA), potassium chloride (KCl), potassium dihydrogen phosphate (KH_2PO_4), and sodium phosphate monobasic anhydrous (NaH_2PO_4) from BDH® and Tris-HCl (from Promega™ Corporation). Graphene (X & Y Dimensions: > 2 um and average thickness: 8-15 nm) were obtained from Cheap Tubes Inc.

All aqueous solutions were prepared using ultrapure water purified with a Milli-Q Millipore system (resistivity = 18 MΩ.cm). DNA and RNA oligonucleotides were synthesized by Eurofins Genomics. Stock solutions of oligonucleotides (100 μM) were prepared in TE buffer (10 mM Tris + 0.1 mM EDTA, pH 8.0) and stored at -80 °C. Several working aliquots were prepared from stock solutions to avoid repeated freeze/thaw cycles and kept at −20 °C before each experiment. Dispensable DNase/RNase-free microtubes and pipette tips were used. All surfaces and vials that come into contact with DNA and RNA were decontaminated with RNaseZap® Solution. The following DNA/RNA sequences were used in this study:

Anti-miRNA-21 (probe DNA strands): 5'-NH_2-C_6-TCA ACA TCA GTC TGA TAA GCT A-3'

Target miRNA-21: 5'-UAG CUU AUC AGA CUG AUG UUG A-3'

Non-complementary miRNA-141: 5'-UAA CAC UGU CUG GUA AAG AUG G-3'

The following buffers were used in the experiments: Phosphate buffer (PB) - 10 mM Na_2HPO_4/NaH_2PO_4 (pH 7.4) used as washing buffer; Immobilization buffer - PB + 0.15 M NaCl; Hybridization buffer - 10 mM PB + 1 M NaCl + 20 mM $MgCl_2$; Regeneration buffer - 0.1× SSC buffer containing 15 mM NaCl and 1.5 mM trisodium citrate.

Electrochemical Characterization

Electrochemical characterization was conducted using CHI-920c model potentiostat (CH Instruments Inc., Austin, TX). A conventional three-electrode cell (a 3mm glassy carbon (GC) working electrode (CH Instruments Inc., Austin, TX), a 3 M Ag/AgCl reference electrode, and a Pt wire counter electrode) were used for electrochemical measurements. All tests were carried out at room temperature with 0.1 M KCl electrolyte solution containing 5 mM $Fe(CN)_6^{3-/4-}$ (1:1) as redox active species. Cyclic voltammograms (CV) were obtained between -0.2 to 0.6 V with a scan rate of 20 mV/s, and a sampling interval of 0.001 V. EIS measurement was conducted at a DC potential of 0.21 V between frequencies of 0.1 Hz to 100 kHz with an AC amplitude of ±5 mV. For all experiments, ΔR_{ct} was defined as the change in impedimetric signal upon probe hybridization as below:

$$\Delta R_{ct} = R_{ct,\ \text{After hybridization with miRNA-21}} - R_{ct,\ \text{Before hybridization with miRNA-21}}$$

Fabrication of Probe DNA Immobilized Electrode

A glassy carbon electrode (GCE) was polished to a mirror-like finish with 0.3 μm and 0.05 μm alumina powder before each experiment, and then bath-sonicated for 5 min in DI water to remove any adhered polishing powder. After that, the electrode was rigorously rinsed with DI water and kept at 70 °C for 30 min to completely dry the electrode surface and then allowed to cool down at room temperature. Graphene dispersion was prepared by adding 1 mg of graphene to 10 mL DMF and ultrasonication (Omni Sonic Ruptor 250, Omni International) of the mixture at 20 W for 30 min to form a homogenous dispersion. For modification of the electrode, 1 mL of graphene dispersion was dropped on the GCE surface and allowed to dry at room temperature for 2 hours to form a thin film. Drying at room temperature prevents coating shrinkage during the evaporation of DMF and leads to the formation of more uniform graphene coating. PBSE was used as a molecular tethering agent for probe DNA immobilization. For this purpose, 2 μL of 10 mM PBSE in DMF was pipetted on graphene-modified GCE and incubated for 15 min to allow the non-covalent binding between the aromatic pyrene moieties of PBSE and graphene sheets. To remove excess unreacted PBSE molecules, the electrode was washed with DMF and PB, sequentially. Single-stranded probe DNA-immobilized electrode was fabricated by dropping 30 μL of DNA solution (1 μM in immobilization buffer) on the electrode surface and incubation for 1 hour at room temperature. The electrode was exposed to ethanolamine solution (100 mM in PB) for 30 min at room temperature to inactivate un-reacted PBSE molecules [249] and finally rinsed with PB to remove any loosely bound DNA strands.

miRNA Hybridization

Hybridization reaction was carried out by pipetting 30 μL of miRNA-21 solutions, prepared in hybridization buffer, on the probe DNA immobilized electrode. Before hybridization, target miRNA-21 solutions were heated at 80 °C for 5 min and cooled down to room temperature to unfold all miRNA strands and facilitate hybridization. After 1 hour, the electrode was rinsed with PB to remove the non-hybridized physically adsorbed miRNAs. The same procedure was applied to evaluate the hybridization of the biosensor with non-complementary miRNA-141 sequences. All steps of electrode preparation were monitored using cyclic voltammetry (CV) and EIS analyses.

Results and Discussion

Fabrication and working principle of the biosensor

The proposed approach for immobilization of probe DNA and miRNA detection is schematically presented in Fig. 1. A GCE was used as the base substrate and modified with a thin layer of graphene by drop-casting. Graphene has two main roles in the biosensor. First, it serves as a platform for immobilization of single-stranded DNAas the bio-recognition element. Second, incorporation of graphene can enhance electronic properties, provide higher surface area, and rapid electrode kinetics, which contribute to a wider linear range and a lower LOD [250]. Capture DNA probes were covalently immobilized onto the graphene-modified electrode using PBSE, the cross-linking chemistry of which has been previously reported by our group [251-255]. Briefly, graphene surface was first functionalized with PBSE molecule. Aromatic pyrene moieties of PBSE have a strong affinity to attach to the base plane of graphene sheets through irreversible π-π stacking [256, 257]. Then, the PBSE-functionalized graphene surface was allowed to react with amine-terminated DNA strands. N-hydroxyl succinimidyl ester groups of PBSE molecule can form a covalent amide bond with amine groups of DNA strands through nucleophilic substitution [258, 259]. After the immobilization step, the probe DNA-immobilized electrode was incubated with different concentrations of miRNA-21. Finally, miRNA-21 detection was achieved through EIS by measuring the change in R_{ct} before and after hybridization between target miRNA-21 and the immobilized complementary probe DNA strands.

Using PBSE as a covalent linker for immobilization of probe DNA onto graphene offers several advantages over the commonly used methods, EDC/NHS coupling reaction and physisorption [260]. Although being used as a popular and well-established method in the fabrication of DNA biosensors, EDC/NHS chemistry often involves extra steps to activate functional groups of the surface prior to DNA immobilization. In case of graphene, as it lacks carboxyl/hydroxyl groups, mostly its derivatives (graphene oxide and reduced graphene oxide) are being used as immobilization platform, which lack the intrinsic electrical and stability properties of graphene, resulting in a compromised performance of the biosensor. On the other hand, there are serious stability concerns over physical immobilization of DNA onto graphene-based surfaces through π–π stacking or hydrogen bonding interactions. Physical immobilization methods are highly susceptible to slight changes in the experimental condition such as pH, ionic strength, and temperature. Additionally, it has been also reported that non-covalently immobilized ssDNA layer becomes even less stable after formation of duplex structure upon hybridization with a target strand, making these methods extremely unreliable for miRNA biosensor applications. Taken together, immobilization using PBSE not only shortens electrode fabrication procedure, but also can result in formation of a highly stable probe DNA layer on the electrode surface [261, 262].

Electrochemical characterization of the miRNA biosensor

All surface modifications, immobilization, and hybridization events were investigated by CV and EIS analyses, carried out in a redox solution of 5 mM $[Fe(CN)_6]^{3-/4-}$ (1:1), prepared in 0.1 M KCl solution. Fig. 2A shows the stepwise CV responses of the electrode after each step. Bare GCE showed a pair of reversible redox peaks of $[Fe(CN)_6]^{3-/4-}$ with peak-to-peak separation of 110 mV, indicating a clean and active GCE surface. After modification with graphene, the redox peak current densities increased notably owing to the excellent conductivity and high surface area of graphene, which results in more rapid electron transfer. The current density response decreased after activation of the electrode with PBSE. As a hydrophobic molecule, PBSE forms a physical barrier between the redox couple and the electrode surface, thus leading to hampered electron transfer [263]. Immobilization of probe DNA resulted in a notable decrease in current density response and a shift in peak potentials. The immobilized DNA layer can hinder the electron transfer rate between the electrode and the redox couple and therefore reduces the peak current density

[264]. Incubation of DNA-immobilized electrode with target miRNA further decreased peak current densities and caused a greater shift in peak potentials. It was suggested that the formation of double helix structures increases the electrostatic repulsion between the negatively charged DNA/miR backbone and repels the diffusion of $[Fe\ (CN)_6]^{3-/4-}$ toward the electrode surface [265].

The charge transfer properties of the electrode were further investigated by EIS. Fig. 2B shows the impedance spectra of the electrode recorded after each modification step in the form of Nyquist plots. A typical Nyquist plot consists of a semi-circle at higher frequencies related to the electron-transfer-limiting process and a straight line at lower frequencies, corresponding to diffusion-limited electrochemical reaction. All EIS data were fitted to Randle's equivalent circuit which includes four following elements, ohmic resistance of the electrolyte solution (R_s), charge transfer resistance (R_{ct}) which is inversely proportional to the rate of electron transfer, Warburg impedance (Z_w) related to the diffusion of ions from the bulk electrolyte to the electrode interface, and double-layer capacitance (C_{dl}) attributed to the surface characteristics of the electrode [266]. R_{ct} value is often directly determined by measuring the diameter of the semi-circle and can be used to define the interfacial electron-transfer properties of the electrode. The CHI software based equivalent circuit fitting was used to obtain the values of R_{ct} and other equivalent circuit parameters. Bare GCE exhibited a small semi-circle impedance spectrum with R_{ct} of 9.12 $\Omega.cm^2$ and a linear part indicating a diffusion limiting process in the lower frequency region. Graphene-modified GCE displayed a smaller semi-circle in the high-frequency region, and R_{ct} value decreased to 3.49 $\Omega.cm^2$ due to the excellent conductivity of graphene. When the electrode was activated by PBSE, R_{ct} was increased to 6.40 $\Omega.cm^2$ due to the insulating nature of PBSE. After incubation with capture DNA, the R_{ct} value increased significantly to 39.56 $\Omega.cm^2$, demonstrating the successful immobilization of probe DNA on electrode through PBSE linker. Negatively charged DNA backbone could make it difficult for $[Fe(CN)_6]^{3-/4-}$ ions to reach the electrode surface through electrostatic repulsions and spatial blockage [267]. In the last step, hybridization with miRNA-21 resulted in higher R_{ct} values of 77.00 $\Omega.cm^2$ due to further charge blocking by miRNA-21 bound to the probe DNA on the electrode surface [268]. Overall, CV and EIS results were consistent and confirmed the successful fabrication of the sensing interface.

Optimization of experimental condition

Different variables related to biosensor fabrication and experimental conditions, including loading mass of graphene, probe DNA concentration, hybridization time, and hybridization temperature, were investigated to acquire the highest biosensor response and the shortest detection time. To investigate the effect of graphene loading, GCE was modified with different graphene loading masses. As can be seen in Fig. 3A, the hybridization signal decreases with increasing the loading mass of graphene. Excess amount of graphene loading on the electrode surface makes the electrode too conductive and diminishes the hybridization signal. Therefore, 1.41 mg/cm^2 of graphene loading mass was used for modification of GCE surface.

The amount of accessible DNA probe on the electrode surface is considered a major factor affecting the efficiency of hybridization [269]. To find the optimal probe DNA loading, several electrodes were fabricated using different probe DNA solutions with concentrations ranging from 0.1 to 2 μM. The prepared electrodes with varying DNA loadings were hybridized with 10^{-10} M miRNA-21 for 60 min at 25 °C. The result of Fig. 3B shows that the highest impedimetric signal was observed when the DNA concentration was 1 μM. Higher probe DNA loading on the electrode surface suppressed the response of the biosensor. This might be due to the extremely high packing density of probe DNA on the surface, which prevents efficient hybridization [270]. Therefore, 1 μM was selected as the optimal probe DNA concentration to fabricate biosensor.

The influences of hybridization time and hybridization temperature on the biosensor response were also assessed. As shown in Fig. 3C, the biosensor response increased with increasing hybridization time up to 60 min and then decreased at 120 min possibly due to miRNA degradation by a minimum amount of ubiquitous RNase present on surfaces or in solutions [228]. Similar observations have also been reported in other studies [271, 272]. Therefore, 60 min was selected as the optimal hybridization time for the rest of the experiments.

Regarding hybridization temperature, Fig. 3D revealed that R_{ct} increases with increasing temperature up to about 37 °C and then decreases with a further increase in temperature. Higher temperatures can lead to the uncoiling of the probe and target strands, making them more accessible to each other and thereby improving hybridization efficiency. A similar trend has been reported previously in other studies [273, 274]. However, at a higher temperature (50 °C), a decrease in impedimetric signal was observed, which is most likely due to the change in thermodynamic properties of DNA/miRNA duplex formation [275]. Moreover, the increase in temperature might cause the partial removal of probe DNA from the electrode surface [250]. Therefore, 25 °C was adopted as the optimum hybridization temperature.

Analytical performance

Analytical performance of the present biosensors was evaluated by incubation of biosensor with different concentrations of miRNA-21 under optimal condition. Fig. 4A shows the Nyquist plots of the biosensor with different miRNA-21 concentrations. The diameter of the semi-circle in the Nyquist plot increased with increasing concentrations of miRNA-21 due to hybridization reactions. Fig. 4B shows the calibration curve of the biosensor plotted based on the average of ΔR_{ct} versus the logarithmic value of miRNA-21 concentration. Linear regression was observed within a concentration range from 10^{-14} to 10^{-8} M, with a regression coefficient of 0.972. At concentrations higher than 10^{-8} M, R_{ct} was decreased most likely due to electrostatic hindrance of miRNA strands on the electrode surface [276]. Similar observations have also been reported in other studies [271, 277]. A detection limit of 3 fM was calculated using the following equation: 3 s/m, where s is the standard deviation from three blank electrodes without target miRNA, and m is the slope of the linear regression. The analytical performance of the biosensor was compared with some of the previously published studies on miRNA detection using electrochemical biosensors, as summarized in Table 1. The obtained LOD of 3 fM is superior than LODs in most of the cited works. Although there are some studies that have reported lower LODs, our proposed biosensor provided a satisfactory LOD which is low enough to detect miRNA-21 present in human blood plasma and serum samples with typical concentrations of 10 fM to 0.9 nM [226]. It is also worth mentioning that the design and working principle of the present biosensor are much simpler than those biosensors with lower reported LODs, and do not require tedious multiple reactions. Moreover, the obtained linear range of detection was comparable to or wider than other reported biosensors.

Selectivity of the biosensor

To verify the selectivity of the biosensor towards miRNA-21, a hybridization reaction was carried out with non-complementary miRNA-141, and the obtained impedimetric response was compared with complementary miRNA-21 at the same concentration of 10^{-10} M (Fig. 5). As expected, a noticeable increase in R_{ct} value was observed after hybridization with miRNA-21 due to the sequence-specific formation of double helix between probe DNA immobilized on the electrode and complementary miRNA-21. In contrast, the increase in R_{ct} value for miRNA-141 was ~80 % lower than that of the complementary strand. Although binding events are mostly dominated by the bio-recognition of the target miRNA via DNA probes, a small increase in R_{ct}

value by the non-complementary miRNA-141 can be attributed to non-specific adsorption of miRNA-141 on the electrode surface [278]. These results confirm the biosensor has expected level of selectivity, while offering some room for improvement. The selectivity could be further enhanced by minimizing the non-specific adsorption of non-complementary RNA strands on to the probe DNA, and could be a scope for future work.

Stability, regeneration, and reproducibility of the biosensor

To evaluate the storage stability, the fabricated biosensor was stored in the immobilization buffer at 4 °C over a period of 14 days and its response was measured toward miRNA-21 at two concentrations of 10^{-9} M and 10^{-13} M on different time intervals. As shown in Fig. 6, the proposed biosensor was able to maintain more than 90 % of its initial ability for detection of miRNA-21 for a wide range of concentrations after being stored in the buffer for 14 days. The storage ability obtained in this study is significantly higher than what previously reported for a physically immobilized DNA onto a graphene-based biosensor, which experiences a notable probe DNA desorption only after 3 hours of storage in buffer [279]. The fabricated biosensor also exhibited a remarkably higher stability compared to a covalently attached probe DNA onto a graphene/thionine surface using glutaraldehyde cross-linker with 71 % of its initial response after 5 days of storage [280]. The results suggested that the covalent immobilization approach based on PBSE and graphene results in a highly stable probe DNA layer with an excellent activity for hybridization even after 2 weeks of storage. The reusability of a biosensor is extremely essential for practical applications. Therefore, the regeneration ability of the biosensor after hybridization with miRNA-21 was evaluated. To do so, the electrode was immersed in the regeneration buffer at 60 °C for 15 min and then washed with DI water [281]. As can be seen in Fig. 7, Nyquist spectrum of the regenerated biosensor exactly matches the original spectra before hybridization.

Besides, biosensor retained more than 96 % of its initial responses even after three repeated hybridizations. This excellent performance confirmed the steady immobilization and reactivity of the DNA probes. The reproducibility of the biosensor was examined by measuring the response of three parallel-made biosensors to 10^{-10} μM miRNA-21. The relative standard deviation (RSD) of the resulted impedimetric responses was 10 %, indicating the satisfactory reproducibility of the biosensor.

Quantitative detection of miRNA-21 in plasma samples

To validate the applicability of the developed biosensor for analyzing circulating miRNA biomarker, its detection capability was evaluated in a complex biological matrix that simulate a real sample. To achieve this, diluted plasma samples (1:50 ratio with Hybridization buffer) were spiked with different concentrations of miRNA-21 (triplicate samples) and tested with the biosensor under the same optimized experimental conditions as discussed before. To minimize the matrix effect (non-specific adsorption of plasma components onto the electrode surface), prior to miRNA detection, the biosensor was first incubated with the blank diluted plasma for 30 min. After rinsing the electrode surface with washing buffer, EIS measurement was conducted and the result served as the baseline for further measurements. As listed in Table 2, the obtained recovery values in real plasma samples varied from 90.38 to 116.50%, and the corresponding relative errors were all below 14%. The obtained recoveries (%) were all within the clinically acceptable recovery range of 80-120% [282]. These results clearly demonstrated that the proposed biosensor holds a great potential to be used as sensitive and reliable miRNA detection method in clinical diagnostics.

Conclusions

An ultrasensitive electrochemical biosensor was fabricated for the detection of prostate cancer-related miRNA-21. The sensor was prepared by immobilizing complementary probe DNA strands on a graphene-modified glassy carbon electrode using a molecular linker. The covalently immobilized probe showed high stability and reactivity towards hybridization of the target miRNA-21. EIS was employed for direct impedimetric detection and quantification of miRNA-21. Low detection limit of 3 fM was achieved in buffer with no need for any target labeling step or signal amplification. The biosensor displayed high selectivity toward complementary miRNA-21 along with remarkable reproducibility, regeneration ability, stability, and applicability in real plasma samples. All results indicate that the biosensor proposed in this study can be used for quantitative measurement of miRNAs and has great potential in early screening and clinical diagnosis of cancer in a point-of-care setting.

Table 2. Comparison of the developed biosensor with other reported electrochemical biosensors for miRNA detection.

Electrode	Recognition element	Target	Signaling element	Electrochemical technique	LOD (M)	Linear range (M)	Ref
ERGO/AuNW	SH-ssDNA	miRNA-137	Doxorubicin	DPV	1.7×10^{-15}	5×10^{-15}-7.5×10^{-13}	[283]
MoS_2/Thi/AuNP	SH-ssDNA	miRNA-21	Thionine	SWV	2.6×10^{-13}	1×10^{-12}-1×10^{-8}	[284]
Naphthalene sulfonic acid	NH_2-ssDNA	miRNA-21	$Fe(CN)_6^{3-/4-}$	Coulometry	2×10^{-14}	1×10^{-14}-1×10^{-8}	[285]
Chit/NRGO	NH_2-ssDNA	miRNA-660	$Fe(CN)_6^{3-/4-}$	EIS	2.8×10^{-11}	8.2×10^{-11}-3.2×10^{-10}	[286]
MWCNT	NH_2-ssDNA	miRNA-21	Methylene blue	DPV	8.4×10^{-14}	1×10^{-13}-5×10^{-10}	[287]
GO/GNR	SH-ssDNA	miRNA-155	Oracet blue	DPV	6×10^{-16}	2×10^{-15}-8×10^{-12}	[288]
Cys-AuNP	NH_2-ssDNA	miRNA-25	AgNP/SWCNT	DPV	3.1×10^{-13}	1×10^{-12}-1×10^{-8}	[289]
Biotinylated polythiophene/ streptavidin	Biotynilated-DNA	miRNA-221	$Fe(CN)_6^{3-/4-}$	EIS	7×10^{-13}	1×10^{-12}-1×10^{-10}	[290]
ZrO_2/RGO/PAA	NH_2-hairpin DNA	miRNA-21	$Fe(CN)_6^{3-/4-}$	EIS	4.3×10^{-15}	1×10^{-14}-1×10^{-10}	[243]
Carbon black	ssDNA	miRNA-125	$Fe(CN)_6^{3-/4-}$	EIS	1×10^{-11}	1×10^{-9}-1.98×10^{-6}	[291]
Graphene/PBSE	ssDNA	miRNA-21	$Fe(CN)_6^{3-/4-}$	EIS	3×10^{-15}	1×10^{-14}-1×10^{-8}	**This work**

ERGO, electrochemically-reduced graphene oxide; AuNW, gold nanowires; SH-ssDNA, thiolated single-stranded DNA; DPV, differential pulse voltammetry; Thi, thionine; AUNP, gold nanoparticle; SWV, square-wave voltammetry; NH_2-ssDNA, aminated single-stranded DNA; Chit, chitosan; NRGO, nitrogen doped graphene oxide; GO, graphene oxide; GNR, gold nanorod; Cys-AuNPs, cysteamine-capped gold nanoparticle; AgNP, silver nanoparticle; SWCNT, single-wall carbon nanotube; RGO, reduced graphene oxide; PAA, poly(acrylic acid).

Table 2. Detection of miRNA-21 in plasma samples (n=3) by the developed biosensor.

Sample	Added miRNA-21	Detected miRNA-21	Recovery (%)	RSD (%)
1	100 fM	105.68 fM	105.68	8.07
2	10 pM	11.65 pM	116.50	13.22
3	1 nM	0.90 nM	90.38	5.84

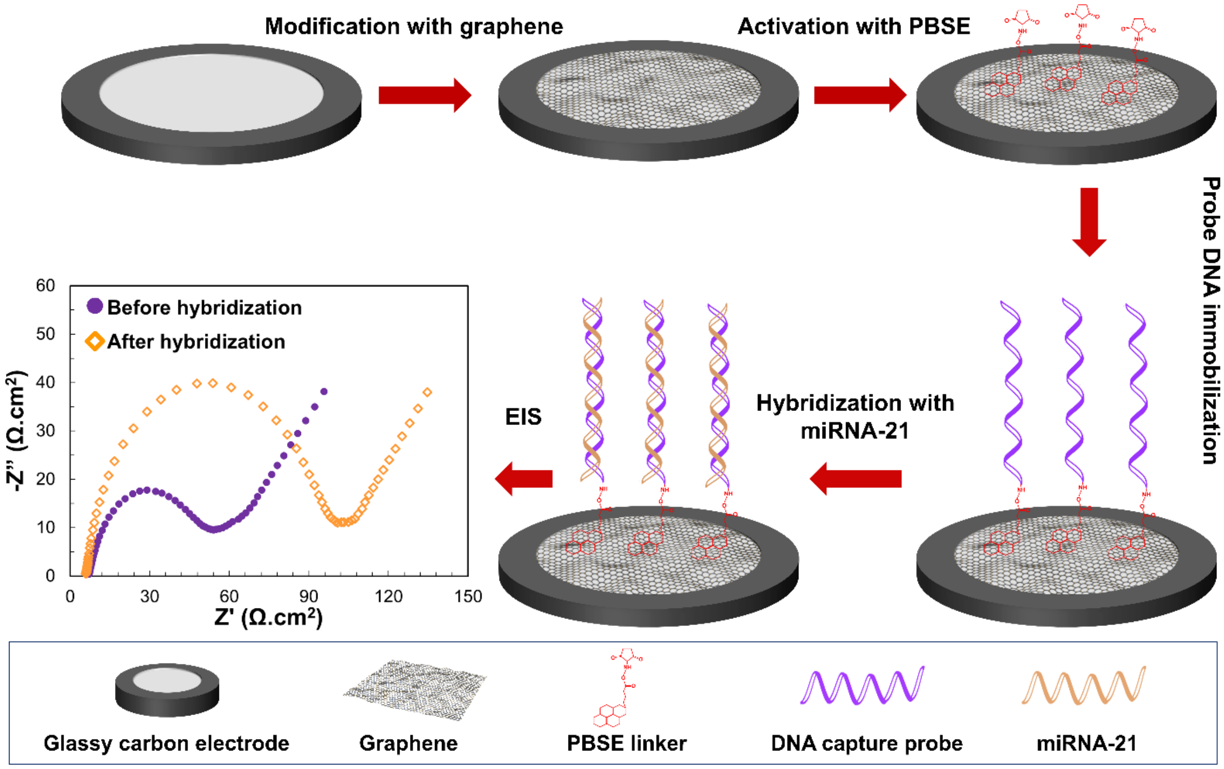

Fig. 1. Schematic representation of the fabrication and detection principle of the biosensor

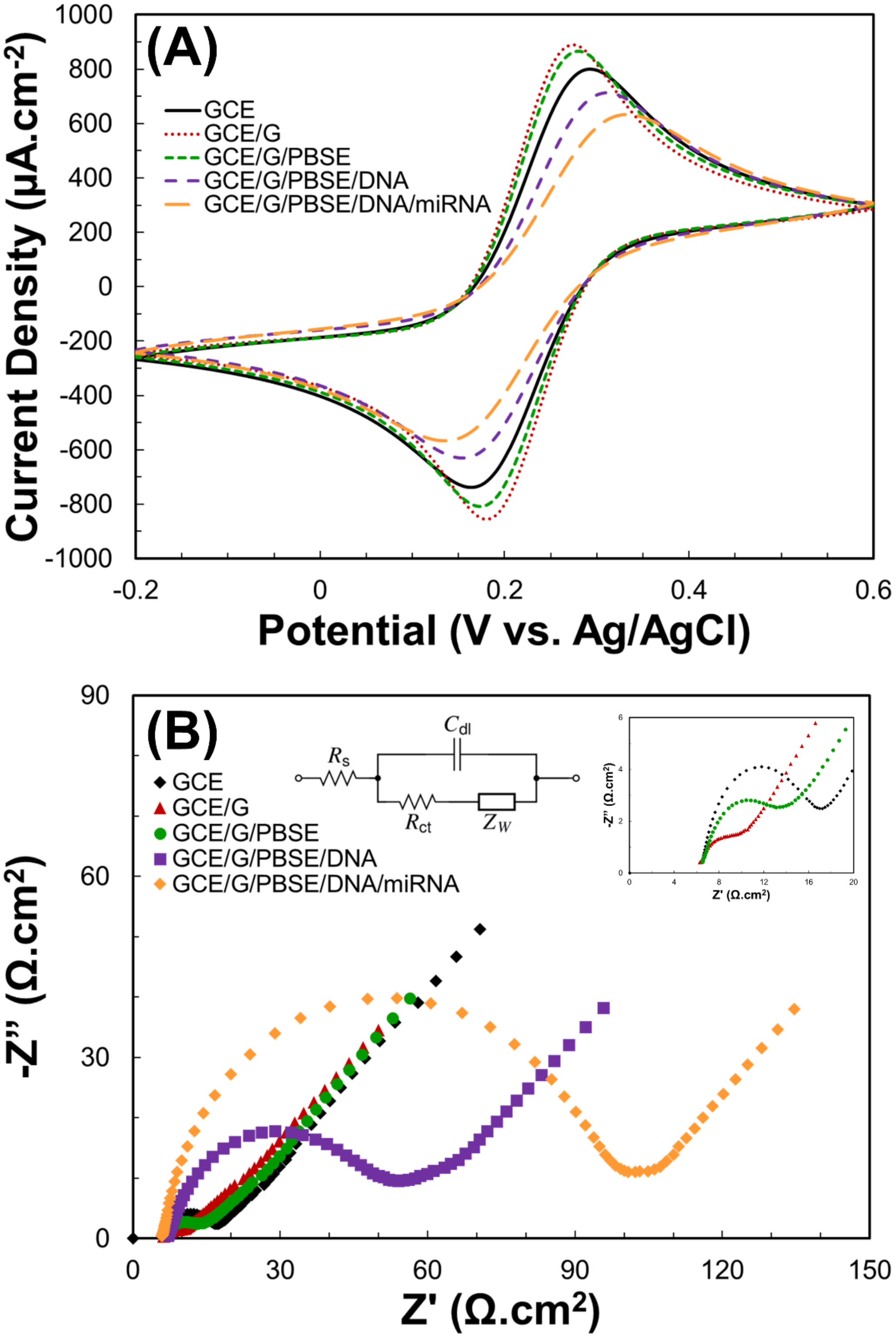

Fig. 2. CV (A) and Nyquist plots (B) of different modified electrode surfaces performed in 0.1 M KCl containing 5.0 mM $[Fe(CN)6]^{-/4-}$. The inset shows the equivalent circuit used for fitting EIS data.

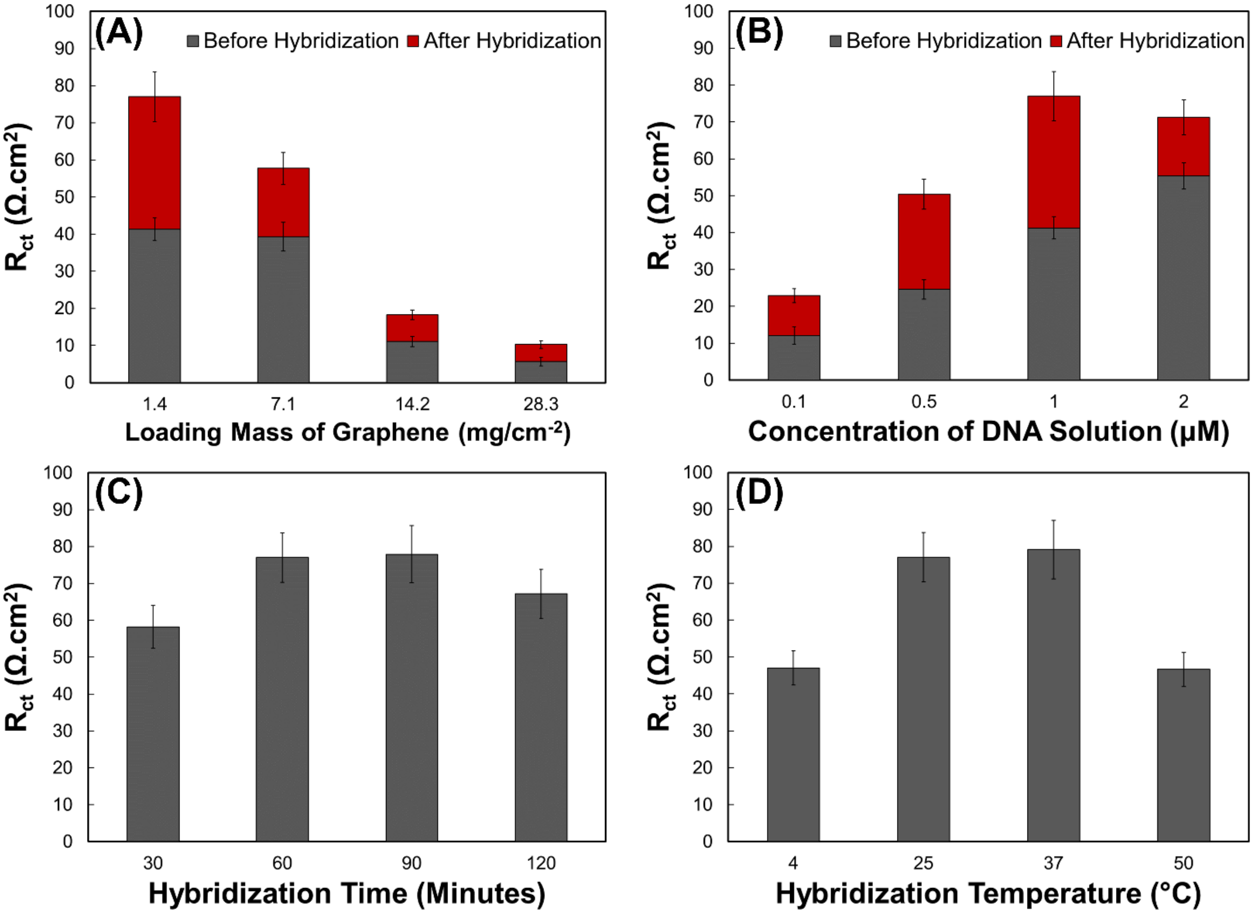

Fig. 3. The effect of concentration of graphene dispersion used for electrode modification (A), concentration of DNA solution used for probe immobilization (B), hybridization time (C), and hybridization temperature (D) on the biosensor response. The concentration of miRNA-21 was set to 10^{-10} M in all experiments.

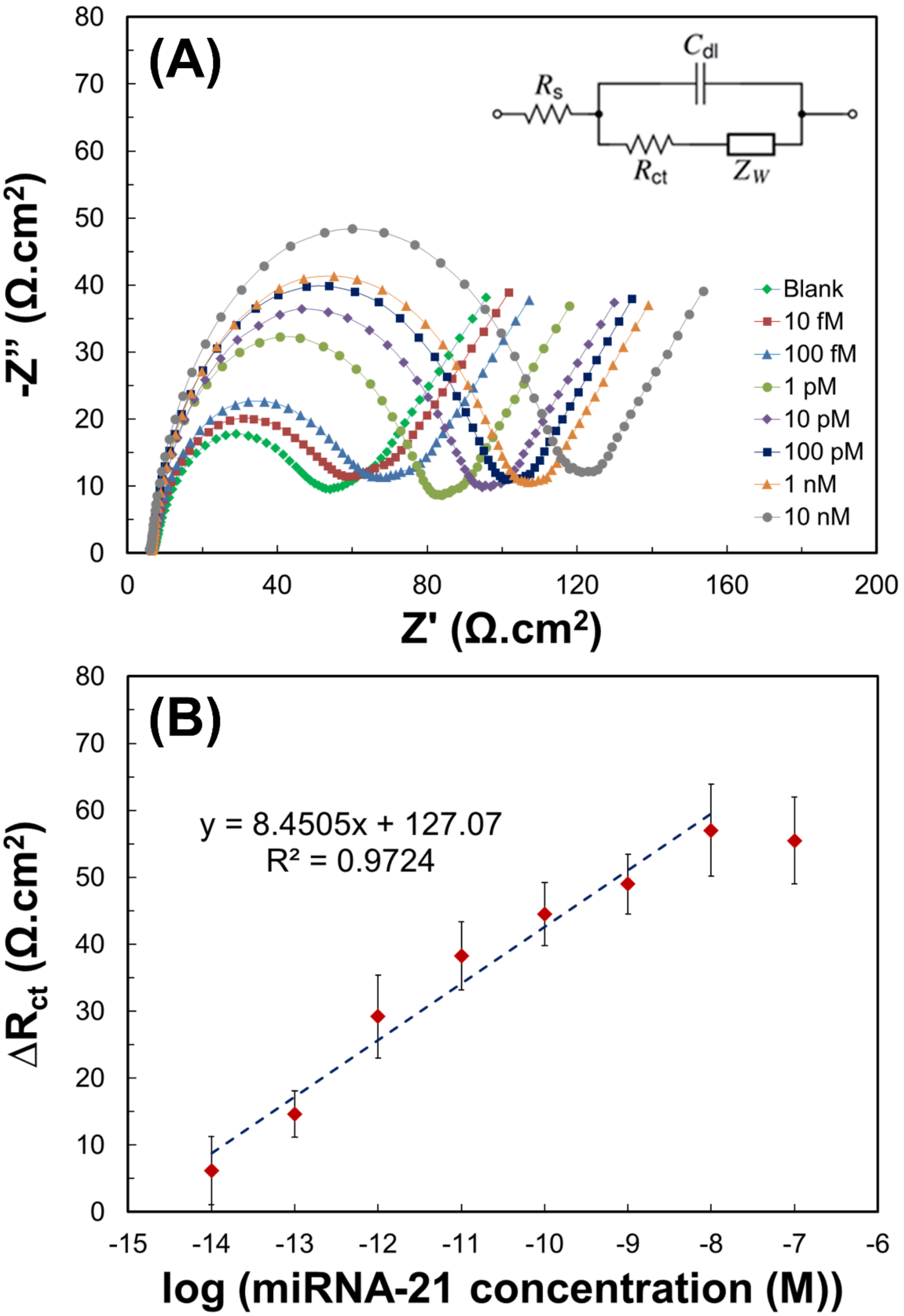

Fig. 4. (A) Nyquist plots of DNA probe-immobilized electrode incubated with different concentrations of miRNA-21 performed in 0.1 M KCl containing 5.0 mM $[Fe(CN)6]^{3-/4-}$ and (B) the corresponding calibration curve based on ΔR_{ct} vs. the log concentration of miRNA-21.

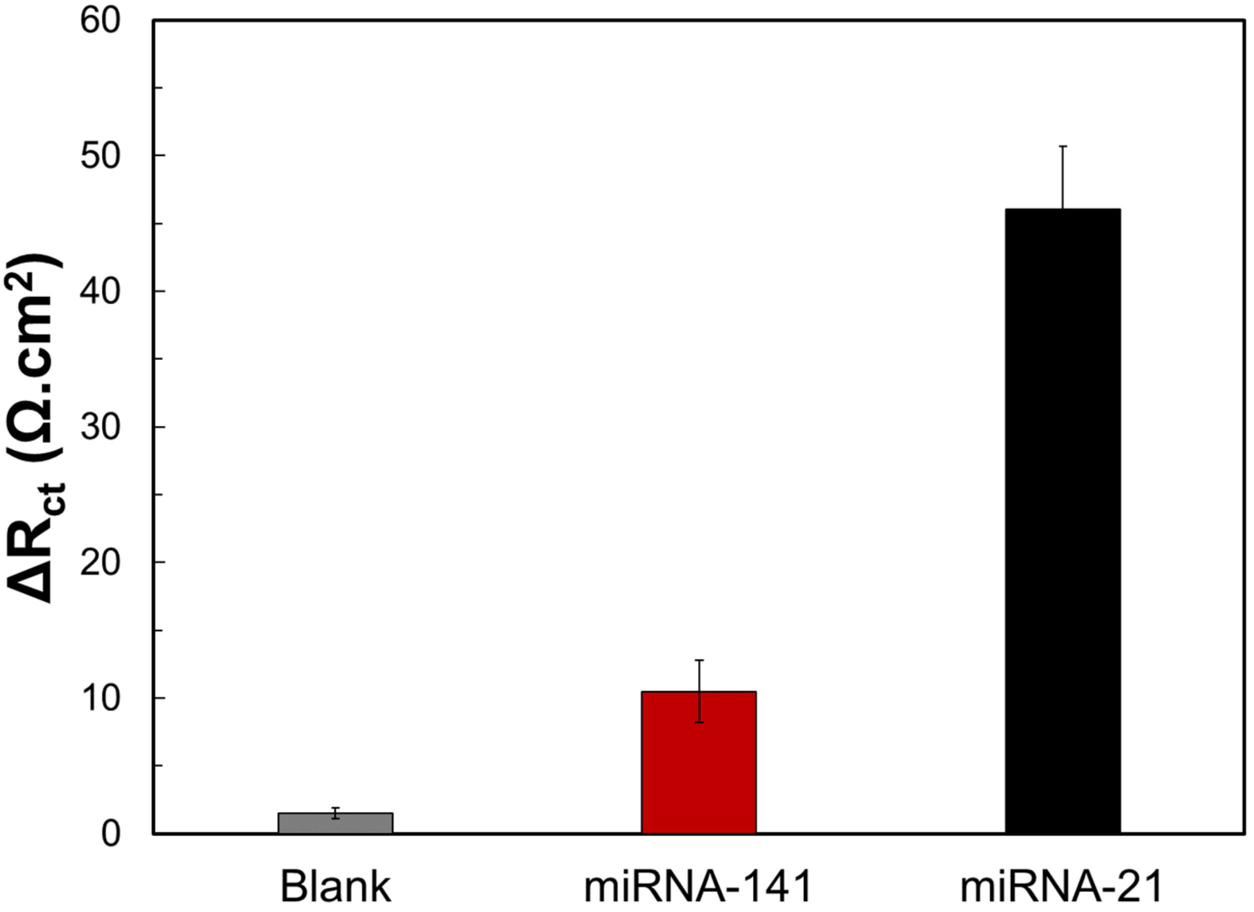

Fig. 5. Responses of the DNA probe-immobilized electrode toward blank buffer, non-complementary miRNA-141 and target miRNA-21. The concentrations of miRNAs were all 10^{-10} M.

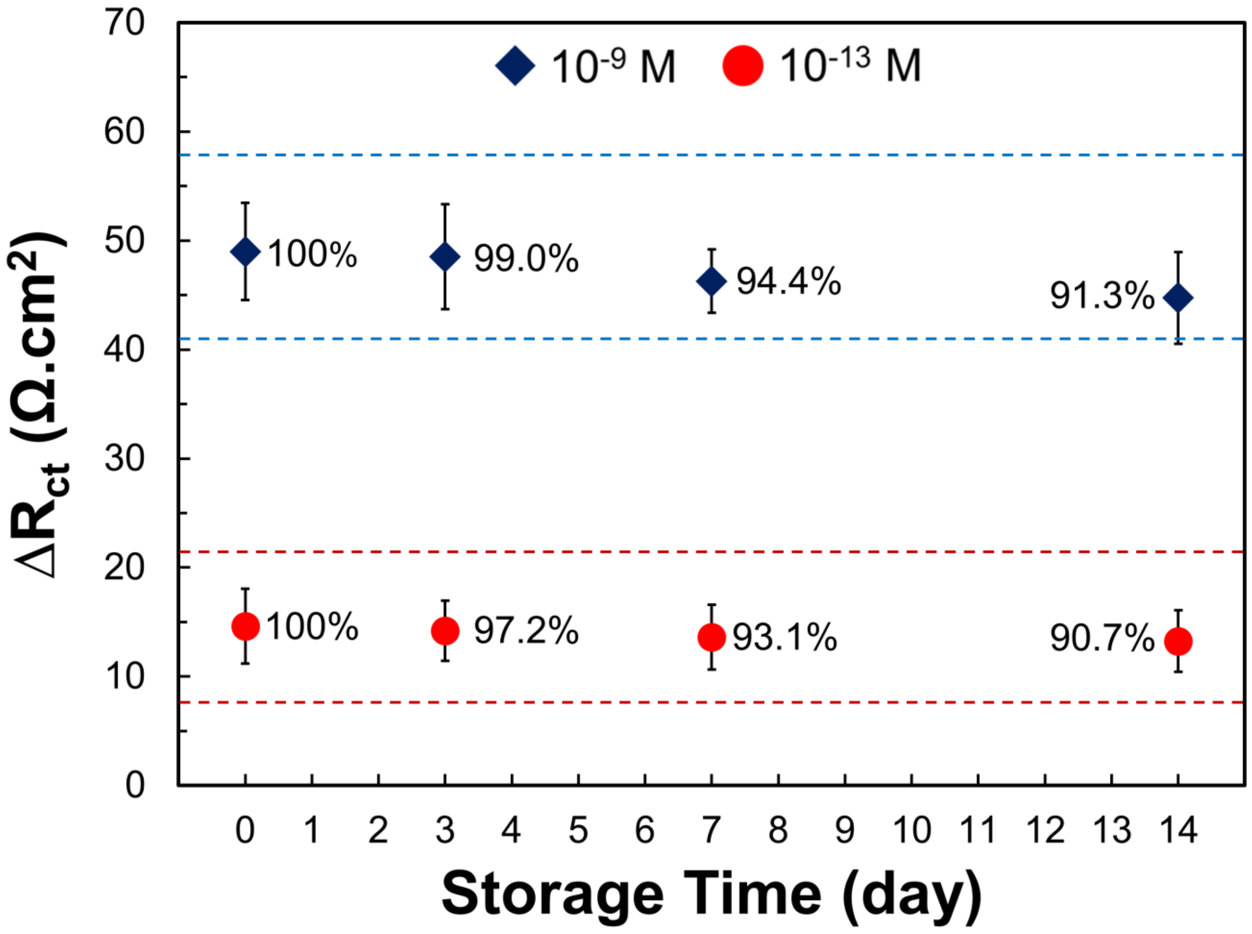

Fig. 6. Impedimetric response of the biosensor toward miRNA-21 at different concentrations after storage in the immobilization buffer at 4 °C. The number next to each data point represents the average percent of response compared to freshly prepared biosensor. Dashed lines were set at ±2 × SD of the mean ΔR_{ct} values measured with freshly prepared biosensors.

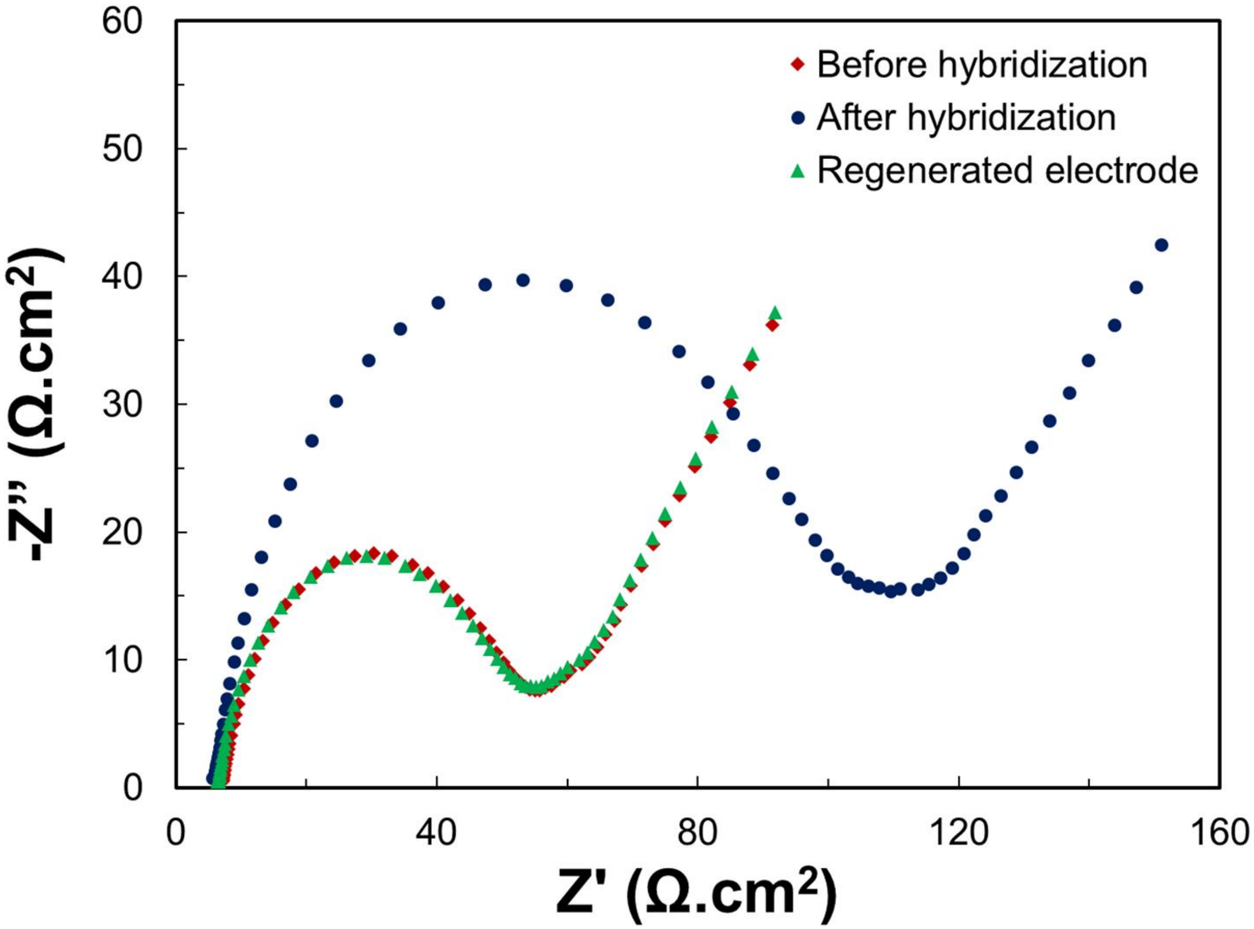

Fig. 7. Regeneration of the biosensor using 0.1× SSC buffer at 60 °C for 15 min, monitored by EIS performed in 0.1 M KCl containing 5.0 mM $[Fe(CN)6]^{3-/4-}$. The concentration of hybridized miRNA-21 was 10^{-10} M.

Supplementary Data

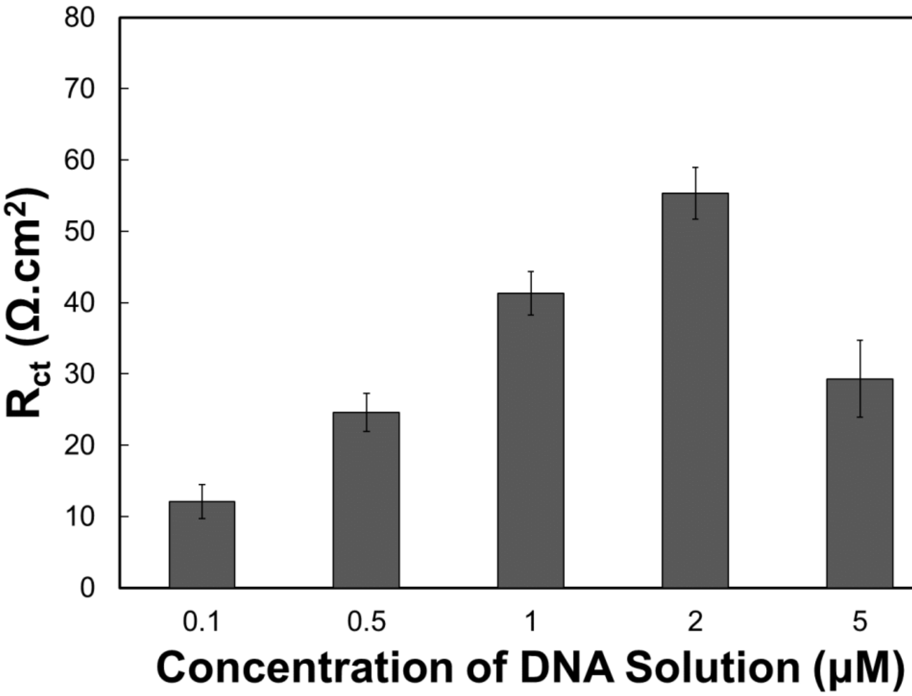

Figure S1. Charge transfer resistance (R_{ct}) of the electrode as a function of concentration of DNA solution. The immobilization time was 60 min in all experiments. R_{ct} increased with the increase of concentration of probe DNA solution up to 2 μM. At higher concentrations, the repulsion between probes is predominant over surface covalent attachment, and the immobilization efficiency is reduced. 2 μM is the highest concentration of DNA solution that could be used for sensor fabrication.

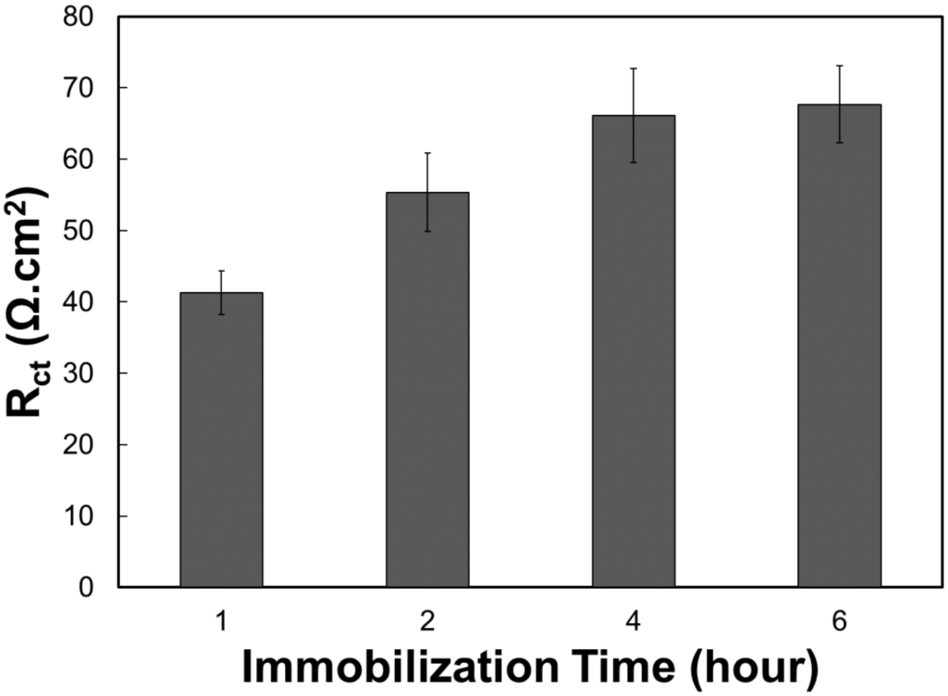

Figure S2. Charge transfer resistance (Rct) of the electrode as a function of immobilization time. The concentration of DNA solution was 1 μM in all experiments. Rct values increased with the increase of the probe immobilization time up to 4 hours and then started to level off after that due to the full coverage of the electrode surface by the DNA probes within the first 4 hours of incubation.

APPENDIX B

Nitric-oxide Releasing Coatings on Stainless Steel Samples

Fabrication of PU-NO coated sample:

PU-NO coated SS was prepared by a combination of the solution casting and spin coating methods. First, PU solution (4% w/v) was prepared by dissolving PU granules in THF using a magnetic stirrer for 4 h. SNAP powder was added to the PU solution and stirred to obtain a homogenous greenish solution with 10% w/w of SNAP with respect to PU weight. The resulting PU/SNAP solution (2 mL) was pipetted on SS samples and dried under the hood for 24 h at room temperature. During the drying process, all samples were placed on glass Petri dishes with closed lids to control the solvent evaporation rate. Besides, a cardboard box was places on the SNAP containing samples to minimize light exposure and unwanted NO release from the samples. To prepare the top coating, a pure PCL solution (1 mL) was pipetted on the samples and spin coated at 500 rpm and 3100 rpm for 15s and 25s, respectively. This process was repeated for three times to obtain a thick and fully covering top coating. The SNAP containing samples were labeled as "PU-NO". PU-NO samples were kept in freezer until use.

Zone of inhibition test:

S. mutans bacterial strain was used to study the antibacterial activities of the coatings using the Kirby-Bauer disk diffusion test [125]. Briefly, a pure bacterial culture is suspended in a phosphate buffer saline (pH 7.4), adjusted to a turbidity of 0.5 McFarland standard, and swabbed uniformly across a culture plate. SS samples were sterilized under UV light for 15 min each side and placed on the culture plates. After, incubating the plates at 37 °C for 24 h under anerobic condition, the antibacterial activity was evaluated by measuring the diameter of the inhibitory zone formed around the samples.

Results:

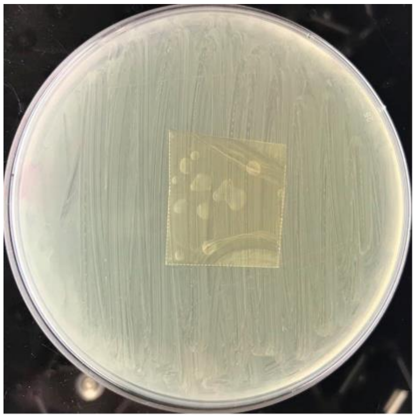

Bare stainless steel (SS)

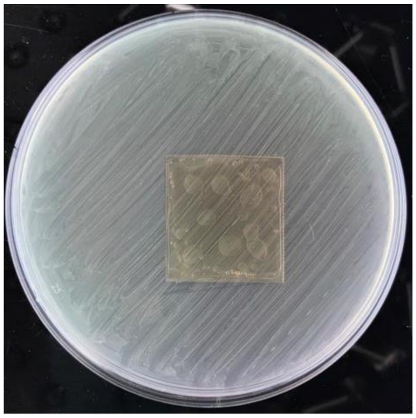

PU coating

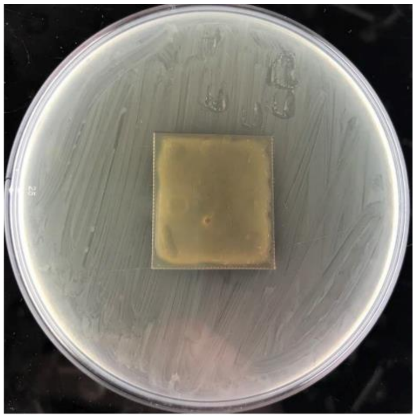

PU-NO coating

S. mutans culture was able to grow on bare and PU coated SS samples. Culture growth is apparent as the parallel lines remained from inoculation of plates (using a swab) continues from one side to the other side of the plates and fully cover the surfaces of SS and PU samples. Such parallel culture lines were not observed on the PU-NO sample surface indicating its bactericidal activity. Besides, a small inhibitory zone was observed around PU-NO sample separating it from the culture plate. Contrary, SS and PU samples are fully covered by the culture do not possess such an inhibitory zone.

APPENDIX C

Fixation of Biological Samples

Materials required:

- 3% glutaraldehyde solution (prepared in PBS, otherwise with DI water it can get acidic and damage cells)
- 50, 60, 70, 80, 90, 100% ethanol solutions prepared in DI water
- Hexamethyldisilazane (HMDS) prepared in 100% ethanol

Procedure:

1. Washing step: Samples are gently rinsed with PBS (gently pipette 1mL of PBS on the sample)
2. Fixation step: The rinsed samples are then soaked in 3% glutaraldehyde overnight to allow complete fixation of the biomass.
3. Dehydration step: Once fixed, samples are dehydrated using increasing concentrations of ethanol for 15 min each (50, 60, 70, 80, 90, and 100%).
4. Drying step: The samples are then immediately transferred to a 2:1 ratio solution of 100% ethanol: HMDS. After 20 min, these samples are then transferred to and soaked in 1:2 ratio of 100% ethanol: HMDS for 20 min. Finally, samples are transferred to 100% HMDS (for 20 min) and allowed to dry overnight in the fume hood.
5. Sputter coating step: The dried samples are then sputter coated (Leica sputter coater) in 10 nm thickness of gold-palladium for SEM imaging.

APPENDIX D

Bacterial Zone of Inhibition Test

Bacterial Suspension Preparation

- Isolate a colony forming unit (CFU) of bacteria from the streak plate containing bacteria and gently scrape it off using an inoculation loop

- Add the CFU into a culture tube containing 3 mL of appropriate media by swirling the inoculation loop in the media

- Grow the bacteria by placing the Falcon tube containing the single inoculated CFU on the shaker

- Clean out bacteria hood, spray/wipe down with 70% ethanol and turn on UV light

Exposing Bacteria to Sample

Preparation for the actual experiment

Prepare **larger 90 mm sterile agar plates** based on the number of sample types to plate

Plating bacteria and samples

- Bring samples on weigh boats into the biosafety hood

- Expose the samples under UV light for 15 minutes on each side OR prepare in completely sterile environment

- Pipet **500uL** of bacteria (in media) onto an agar petri dish, repeat for each plate

I) Make sure the OD of the bacteria is < 1 (if OD is > 1, discard falcon tube and start over OR re-inoculate)

- Use a **swab** to evenly distribute the bacteria across the petri dish, repeat for each plate

- Gently place sample in center of petri plate, press lightly to ensure it is securely on the agar and place lid on the petri dish

- Wrap the petri dishes using parafilm

- Place the petri dishes inverted (with the agar on the top) inside the incubator (non-shaker) for 24 hours at 37 ^{O}C

- Clean out bacteria hood, spray/wipe down with 70% ethanol and turn on UV light